Optimalisering van een geïntegreerde optische isolator
gebaseerd op een halfgeleiderversterker
met een ferromagnetisch metaalcontact

Optimization of an Integrated Optical Isolator
Based on a Semiconductor Amplifier
with a Ferromagnetic Metal Contact

Wouter Van Parys

Promotoren: prof. dr. ir. R. Baets, prof. dr. ir. D. Van Thourhout
Proefschrift ingediend tot het behalen van de graad van
Doctor in de Ingenieurswetenschappen: Fotonica

Vakgroep Informatietechnologie
Voorzitter: prof. dr. ir. D. De Zutter
Faculteit Ingenieurswetenschappen
Academiejaar 2008 - 2009

UNIVERSITEIT
GENT

ISBN 978-90-8578-265-0
NUR 959, 926
Wettelijk depot: D/2009/10.500/23

Promotoren:

Prof. dr. ir. R. Baets	Universiteit Gent, INTEC
Prof. dr. ir. D. Van Thourhout	Universiteit Gent, INTEC

Examencommissie:

Prof. dr. ir. R. Van De Walle (voorzitter)	Universiteit Gent, ELIS
Prof. dr. ir. R. Baets (promotor)	Universiteit Gent, INTEC
Dr. ir. L. Lagae	IMEC vzw, Leuven
Prof. dr. ir. G. Morthier (secretaris)	Universiteit Gent, INTEC
Prof. dr. ir. K. Neyts	Universiteit Gent, ELIS
Dr. J.J.G.M. van der Tol	TU/e, Eindhoven
Prof. dr. ir. D. Van Thourhout (promotor)	Universiteit Gent, INTEC
Dr. ir. M. Vanwolleghem	IEF-CNRS, Universit*é* Paris-Sud

Universiteit Gent
Faculteit Ingenieurswetenschappen

Vakgroep Informatietechnologie (INTEC)
Sint-Pietersnieuwstraat 41
B-9000 Gent
België

Tel.: +32-9-264.33.35
Fax: +32-9-264.35.93

Dankwoord

Doctoreren is een bijzondere job; het is in alle vrijheid zoeken naar het antwoord op de moeilijkste vragen. Die vrijheid is uiteraard een luxe, je bepaalt zelf je agenda, je komt en je gaat min of meer wanneer je wil, je mag het gaan uitleggen op conferenties aan de andere kant van de grote plas. Die vrijheid heeft ook zijn uitdagende kanten; je leeft een beetje op een eiland, binnen je directe omgeving zijn er weinigen die echt weten waaraan je werkt, laat staan jouw vragen kunnen beantwoorden. Het is ook een heel individuele job, jij en enkel jij bent verantwoordelijk voor het afronden van je eigen project. Maar het is mooi geweest, het was een fascinerende tocht, het voelt zelfs een beetje vreemd aan om er een punt achter te zetten.

Het begin van dit boek is de perfecte plaats om een aantal mensen te bedanken die een bijzondere rol hebben gespeeld tijdens deze 5 jaar. Vooreerst moet het gezegd dat een doctoraat zonder promotor een stuurloos schip is. Roel en Dries, bedankt, voor al die keren dat ik zomaar jullie bureau kon binnenwandelen op zoek naar een uitleg voor weer eens een vreemd experimenteel resultaat. Daarnaast ook een dikke merci aan Steven en Liesbet voor de precisie waarmee die magnetische lasertjes gemaakt werden. Een deel van de fabricatie werd gedaan in IMEC. Tijdens mijn aperiodieke trips naar Leuven kon ik altijd terecht bij Liesbet om mij, photonieker van nature, in te wijden in de mysteries van het magnetisme. Celso, thanks also to you, for the amusing talks on football during the waiting hours.

Tijdens het Europees Isolaser-project, waarin de basis werd gelegd voor dit werk, heb ik de liefde voor projectmanagement ontdekt. In team aan een quasi-onmogelijke opdracht werken bleek zeer inspirerend. Van een projectvergaderingen kwam ik telkens supergemotiveerd terug met een vat vol nieuwe ideeën. Dans ce projet j'ai eu la chance de rencontrer des scientifiques enthousiasmants. Pierre, Beatrice et Bruno, merci pour la collaboration et les discussions approfondies.
Furthermore, I have had the opportunity to work together with the founding fathers of the amplifying waveguide optical isolator at Tokyo University. Yoshi and Hiromasa, I would like to thank you for the warm welcome I have experienced in Japan and for the numerous fruitful discussions during my time in your lab.

Een speciale vermelding voor mijn – intussen ex – collega's; een groepje ongeregeld dat uitgegroeid is tot zo veel meer dan enkel collega's, mede dankzij enkele memorabele *5-to-5* avonden. Mathias in de eerste plaats, ik blijf het fascinerend vinden hoe onze ietwat bizarre tandem liep als een trein. Hendrik, bureaugenoot gedurende vele jaren, voor het delen van lief en leed. Rein, voor de gezellige babbels bij het betere trappistenwerk. Sam, voor brood en pintjes tijdens

de spontane vrijdagse feestjes. Kristof 'KriKri', voor de muziek en andere inspiratiebronnen. Jon, voor de taboeloze discussies. Dave en Lieven, voor de nooit aflatende ambiance in de gang en ver daarbuiten. Wout, Koen, Peter en Joost voor alle uren fun, overdag en soms ook 's nachts. Pieter, D'Oos, Gunther, Gino en Jos om na 5 jaar studies nog eens 5 jaar samen te kunnen doorbrengen. En dan zijn er nog de andere twee derden van de heilige Drievuldigheid, Katrien en Peter, later uitgebreid tot een viertal met Stijn – het was magie in dat kleine hokje op het einde van gang. Ik zal jullie missen!

Uiteraard stopt een doctoraat niet aan de poorten van het labo. Ook daarbuiten zijn er een aantal mensen die een belangrijke invloed hebben gehad op mij en dus op dit werk. Steven, voor de vriendschap, vaak bezegeld met een flesje Schots water. Joost, voor de talloze discussies over de zin en onzin van wiskunde en fysica. Dennis, voor zon en zee in Spanje; had je niet beloofd nog es naar Gent te komen als mijn doctoraat af was? Niet te vergeten is mijn familie, voor hun onvoorwaardelijke steun en liefde, mama, papa, zusjes en aanverwanten, merci!
Een heel speciale vermelding voor iemand die er op elk moment is voor mij, al negen jaar. Annelies, het zou teveel woorden kosten om te beschrijven wat je betekent voor mij, misschien komt dit nog het dichtst in de buurt: ik zie je graag!

Het ga jullie goed!

"Turn the light out say goodnight,
No thinking for a little while,
Let's not try to figure out everything at once..."

Matt Beringer

"It was the future reflecting, it felt familiar..."

Andrew VanWyngaerden

"A, B, C... One, Two, Three... Make sure to keep it simple..."

Daan Stuyven

"Black mirror knows no reflection..."

Win Butler

"Whoo! Alright - Yeah UhHuh"

Luke Jenner

Contents

Samenvatting

EEN optische isolator vermijdt één van de belangrijkste bronnen van ruis in een optisch communicatiesysteem door optische terugkoppeling in de laserbron te blokkeren. De huidige commerciële optische isolatoren zijn bulk componenten die collimerende lenzen en dure aligneringtechnieken vereisen bij toepassing in een laserdiode module. Een geïntergreerd laser-isolator systeem is dus uiterst gewenst aangezien dit de kost en de afmetingen van de laserdiode module zou verminderen en de thermische en mechanische stabiliteit zou verhogen. De kostreductie van een laserdiode kan het belangrijkst zijn bij direct gemoduleerde lasers die opereren bij een golflengte van 1300nm.
Traditioneel is het onderzoek geconcentreerd op het gebruik van ferrimagnetische granaten om de niet-reciprociteit te induceren. De interesse voor deze klasse van materialen komt door hun unieke combinatie van lage optische verliezen bij telecommunicatiegolflengtes en een aanzienlijk sterk magneto-optisch effect, de bron van de niet-reciprociteit. Alleenstaande componenten met goede optische isolatie werden eerder gerapporteerd. Echter, de integratie met III-V halfgeleidermateriaal blijft een probleem. Het best gerapporteerde resultaat beschrijft een isolatie niet hoger dan 5dB in een component van enkele millimeter lang.

Een totaal andere onderzoeksbenadering vertrekt van de vereiste dat voor monolithische integratie de isolatorstructuur zeer gelijkaardig moet zijn aan de laser waarmee deze geïntegreerd wordt. Wanneer in een standaard halfgeleider optische versterker een gemagnetizeerd ferromagnetisch metaal in de directe omgeving van de geleidende laag wordt geplaatst, introduceert het magneto-optisch

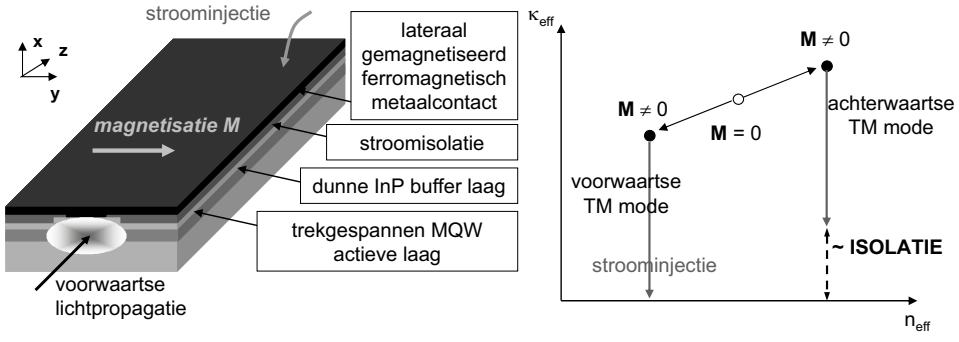

Figuur 1: Schematische lay-out en werkingsprincipe van de transversaal magnetische golfgeleider optische isolator.

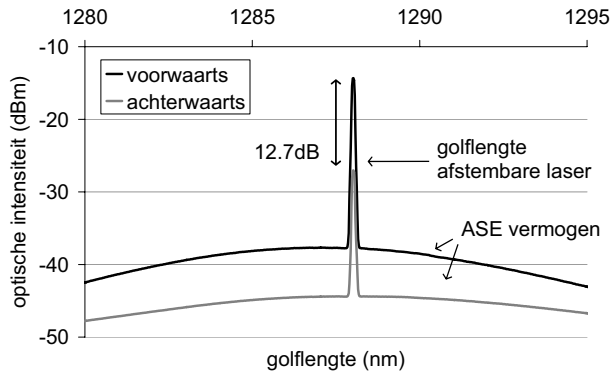

Figuur 2: Transmissie experiment op een 2.1mm lange anti-reflectie gecoatede isolator met 12.7dB optische isolatie; gemeten met 160mA stroominjectie. Met het totale verlies lager dan de koppelverliezen is dit de eerste demonstratie van een transparante isolator gebaseerd op een halfgeleider optische versterker.

Kerr effect een niet-reciproke verandering van de complexe effectieve index van de geleide mode. Met andere woorden, de modale absorptie is verschillend in beide propagatierichtingen. Het overblijvende verlies in de voorwaartse richting kan gecompenseerd worden door stroominjectie in het versterkende materiaal. Het resultaat is een component die, aangezien hij transparant of versterkend is in de ene richting en verlies vertoont in de tegenovergestelde richting, isolerend werkt en die bovendien mo-nolithisch geïntegreerd kan worden met InP-gebaseerde actieve fotonische componenten. Configuraties voor zowel transversaal elektrische als transversaal magnetische polarizatie werden gerapporteerd. In dit werk concentreren we ons op deze laatste structuur, die intrinsiek eleganter is aangezien de ferromagnetische metaalfilm dienst doet zowel als de bron van de niet-reciprociteit en als het ohms elektrisch contact van de onderliggende optische versterker. Figuur 1 illustreert de lay-out en het werkingsprincipe van de transversaal magnetische golfgeleider optische isolator. Voorafgaand aan dit werk werd het concept van deze golfgeleider optische isolator experimenteel gedemonstreerd, het resultaat van gezamelijk onderzoek met Vanwolleghem. Verder werden reeds een serie verbeteringen geimplementeerd, maar het kan worden gesteld dat bij de start van dit onderzoek de isolatorconfiguratie veeleer een (veelbelovende) academische curiositeit was.

Het logische eerste objectief was dan ook om de performantie van de transversaal magnetische golfgeleider optische isolator naar een hoger niveau te tillen, en te evolueren naar een praktische component. Daarom is heel wat inspanning geleverd om de verschillende mechanismen die de optische isolator bepalen diepgaand te begrijpen. Een uitgebreide studie werd gemaakt van de interactie van de evanescente staart van de geleide mode met het gemagnetizeerd ferromagnetisch metaalcontact. De complexe interactie tussen de magneto-optische parameters van het metaal en de brekingindices van het metaal en de omliggende materialen die de grootte van het niet-reciproke effect bepaalt, werd bestudeerd en fundamentele ontwerpsregels konden worden opgesteld. Belangrijke aspecten

van de component, zoals de keuze van het ferromagnetische metaalcompositie en het ontwerp van een ohmse me-taal-halfgeleider contactstructuur, werden behandeld op basis van deze bevindingen. Met berekeningen aan de hand van een eerste-orde perturbatieformule werd de eigenlijke lagenstructuur van de transversaal magnetische golfgeleider optische isolator ontworpen. Belangrijk is een gepaste keuze van de kostenfunctie om de performantie van een bepaald ontwerp te evalueren. Praktische kostenfuncties zijn de stroom vereist voor voorwaartse transparantie van de isolator en het produkt van de stroom en de lengte van de component, beiden grootheden die geminimaliseerd moeten worden. De meest geoptimaliseerde component opererend bij een golflengte van 1300nm is een InAlGaAs-InP versterkende structuur bestaande uit 9 quantumlagen met ingebouwde trekspanning, elektrisch gecontacteerd via een equiatomaire $Co_{50}Fe_{50}$ ferromagnetische metaalfilm. De ohmse contactstructuur is een sterk p-type gedopeerde hybride InGaAs-InGaAsP tweelagenstructuur waarvan de dimensies geoptimaliseerd werden zodat het ohms elektrisch gedrag gegarandeerd is en er terzelfdertijd slechts een minimale vermindering is van de magneto-optische sterkte van de component. De diktes van de mantellagen rondom de versterkende kern werden zo gekozen dat de hoogste performantie wordt bereikt. Voor een 25dB isolator komt dit neer op een 5mm lange component die 78.5mA stroom verbruikt (per micrometer ribbreedte) of een structuur van 2.5mm met een transparantiestroom van 117mA (per micrometer ribbreedte), afhankelijk van de kostenfunctie die gebruikt wordt in de berekeningen.
Isolatordemonstratoren in alle stadia van het optimaliseringsproces werden gefabriceerd en vervolgens gekarakteriseerd. Het belangrijkste en finale resultaat wordt geïllustreerd in figuur 2. Het getransmitteerde vermogen van een externe afstembare laser varieert met 12.7dB wanneer de propagatierichting van het licht in een 2.1mm lange component omgedraaid wordt. Een beperkte stroominjectie (155mA) volstaat om het overblijvende verlies in de voorwaartse propagatierichting te compenseren. Dit resultaat is de eerste – en voorlopig enige – demonstratie van een transparante, monolithisch integreerbare optische isolator. Door interpolatie van de stroom nodig voor transparantie is het mogelijk dit resultaat te vergelijken met dat van het allereerste experiment. Sindsdien is de performantie met meer dan een factor 80 gestegen. Er werd een uitgebreide studie gemaakt van andere aspecten van deze component zoals het golflengtegedrag en de invloed van de stroominjectie op de geobserveerde optische isolatie. Een mathematisch model gebaseerd op versterkervergelijkingen werd ontwikkeld dat de relatie tussen de optische isolatie en de geïnjecteerde elektrische stroom en de toename van de optische isolatie met de intensiteit van het ingangssignaal accuraat reproduceert. Het blijkt dat de aanwezigheid van spontane emissie een grote invloed heeft op de werking van de component.

Eén van de belangrijke aspecten van dit type isolatoren is de magnetizatie van de ferromagnetische metaalfilm. De zeer hoge aspectratio van de lengte van de film tot zijn breedte resulteert in een zeer lage remanente magnetizatie van de film, als gevolg van grote demagnetizatievelden. Eén van de oplossingen voor dit probleem bestaat erin een magneet te integreren met de isolator. Een tweede belangrijk deel van dit werk was daarom de realizatie van een transversaal magnetische golfgeleider optische isolator met een geïntegreerde elektromagneet. Deze magneet

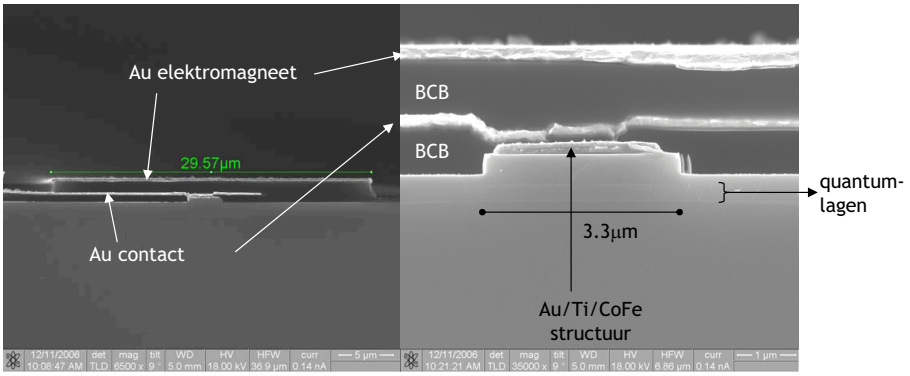

Figuur 3: Afbeeldingen van een onder een elektronenmicroscoop bekeken dwarsdoorsnede van de golfgeleider optische isolator met geïntegreerde elektromagneet. Deze illustreren de succesvolle fabricage van deze component.

is een strook goud gedeponeerd langs de longitudinale richting van de isolator in de directe omgeving van de ferromagnetische film. Stroom die doorheen de goudlaag vloeit in de longitudinale richting induceert een lateraal magneetveld dat het magneto-optisch Kerr effect genereert. Naast het feit dat dit een oplossing levert voor de moeilijkheden in verband met magnetizatie is een dergelijke geïntegreerde elektromagneet ook interessant doordat deze de mogelijkheid biedt een magnetisch veld te genereren met een arbitraire veldrichting. Dit kan bijvoorbeeld gebruikt worden om het radiale magneetveld op te wekken nodig in een ringresonator-gebaseerde isolator. Verder merken we ook op dat met een dergelijke golfgeleider optische isolator met geïntegreerde elektromagneet het mogelijk wordt om het intern verlies in een halfgeleider optische versterker dynamisch en niet-reciprook te wijzigen.
Een eerste generatie isolatoren met geïntegreerde elektromagneet werd ontworpen, gefabriceerd en getest, met als resultaat de succesvolle demonstratie van het principe. Figuur 3 toont afbeeldingen van een onder een elektronenmicroscoop bekeken dwarsdoorsnede van deze component. Zoals reeds te verwachten op basis van magneetveldberekeningen is het stroomniveau nodig om een magneetveld te genereren dat sterk genoeg is om de magneto-optische film te satureren minstens een orde te hoog voor praktische toepassingen. We konden echter een elegant concept identificeren dat een grote verbetering belooft. Door de ferromagnetische film niet enkel als het ohms contact voor de onderliggende versterker te gebruiken maar ook als elektromagneet – door een longitudinale stroom door het metaal te sturen – verlaagt de elektromagneetstroom nodig om een bepaald niveau van niet-reciprociteit te behalen drastisch. Het achterliggende mechanisme is dat het genereerde magnetizatieprofiel veel gunstiger is dan het geval met een externe elektromagneet. Dit fenomeen werd in detail theoretisch uitgewerkt en de theorie werd gestaafd door een experimenteel resultaat.

Het fundamentele voordeel van de versterker-gebaseerde isolator boven de granaat-gebaseerde aanpak is dat deze monolithisch kan worden geïntegreerd met zijn laserbron. Een derde doelstelling van dit werk was de ontwikkeling van

een dergelijke geïntegreerde laser-isolator component. De structuur werd gerealizeerd in een begraven ribgolfgeleiderontwerp, een standaard technologie voor DFB-lasers. De lagenstructuur is gebaseerd op de ééndimen-sionale structuur van eerder geteste ondiep geëtste ribgolfgeleiderisolatoren en de effecten van het hoge laterale indexcontrast tussen de versterkende kern en de InP mantel werd berekend via magneto-optische perturbatierekening van de exacte tweedimensionale dwarsdoorsnede. Dankzij de verhoogde modale opsluiting kan de breedte van de geleidende kern beperkt worden tot 1μm, wat de transparantiestroom gevoelig verlaagt in vergelijking met de ribgolfgeleidercomponenten. Monolithisch geintegreerde laser-isolator testcomponenten werden gefabriceerd. Het DFB-laser gedeelte bleek van goede en reproduceerbare kwaliteit. Voor de isolatorsectie vereiste het bijkomende studie en procesaanpassingen vooraleer niet-reciprociteit kon worden gedemonstreerd. De performantie bleef echter beperkt. Bovendien vertoont de geïntegreerde component elektrische een lekstroom wat de demonstratie van de eigenlijke monolithisch geïntegreerde laser-isolator component verhinderde. Dusdanig kan er worden van uitgegaan dat enkel door uitgebreid onderzoek van het metaal-halfgeleider grensvlak en van de elektrische scheiding van het laser en isolatorgedeelte deze problemen kunnen worden opgelost en de performantie kan worden verhoogd.

Het laatste onderdeel van dit werk behelste een studie van andere niet-reciproke componenten waarvan de golfgeleiderisolator de bouwsteen is. De focus lag op de ontwikkeling van ring resonator-gebaseerde optische isolatoren en op passieve niet-reciproke componenten. Resonantie van licht in een ringvormige en gemagnetizeerde golfgeleider bedekt met een ferromagnetisch metaal kan gebruikt worden om een hoogperformante optische isolator te realizeren. In een droppoort configuratie is de versterking van de optische isolatie te danken aan het feit dat resonerend licht meerdere malen door de caviteit propageert vooraleer gekoppeld te worden naar een uitgangsgolfgeleider. Via de passpoort krijgen we grote optische isolatie ten gevolge van het verschil in intern verlies tussen voorwaarts en achterwaarts – wijzerzin en tegenwijzerzin – propagerend licht in de resonator. Een grondige theoretische studie werd gemaakt en volledige actieve ringgebaseerde isolatoren werden ontworpen. Een set maskers voor contactlithografie werd ontwikkeld en gebruikt voor de fabricage van de eerste testcomponenten. Door inferieure kwaliteit van de fabricage kon echter het experimentele bewijs van het principe niet worden bereikt.
Passieve niet-reciproke componenten gebaseerd op ferromagnetische metalen zijn aantrekkelijk voor toepassingen waarbij optische transparantie geen vereiste is, zoals een magneetveldsensor. Het voor de hand liggende materiaalsysteem is silicium-op-isolator (SOI), gekarakteriseerd door een hoog indexcontrast tussen kern en de omringende mantel. Voor dit materiaal is het reële deel van het magneto-optisch effect het dominant niet-reciprook effect. Simulaties tonen aan dat de verhouding tussen de niet-reciproke fase shift en de absorptie in het metaal echter veel te laag zijn voor praktische implementatie.

Summary

AN optical isolator allows to avoid one of the main noise sources in an optical communication system by blocking optical feedback to the laser source. Current commercial isolators are bulk components, requiring collimating lenses and expensive alignment techniques when applied in a laser diode package. An integrated laser-isolator system is highly desirable as it would reduce cost and size and enhance the mechanical and thermal stability. The cost reduction of a laser diode package would be the largest with directly modulated lasers, operating at 1300nm.
Traditional research focuses on applying ferrimagnetic garnets to induce non-reciprocity. The interest in this class of materials comes from their unique combination of low optical loss at telecom wavelengths and a considerably strong magnetooptic effect, the source of the non-reciprocity. Stand-alone devices with good isolating performance have been reported. The integration with III-V host material however remains an issue. In the best reported result isolation not higher than 5dB has been demonstrated in a device with a length of several millimeters.

A different research approach starts from the requirement that for monolithic integration the isolator structure should be very similar to that of the laser it is to be integrated with. If in a standard semiconductor optical amplifier (SOA) an adequately magnetized ferromagnetic metal is placed very close to the guiding region, the magnetooptic Kerr effect induces a non-reciprocal shift of the complex effective index of the guided mode. In other words, the modal absorption is different in both propagation directions. The remaining loss in the forward

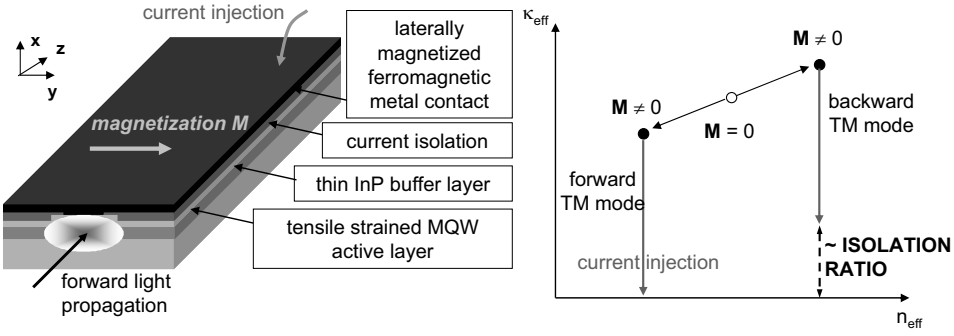

Figure 4: Schematic layout and operation principle of the TM-mode amplifying waveguide optical isolator.

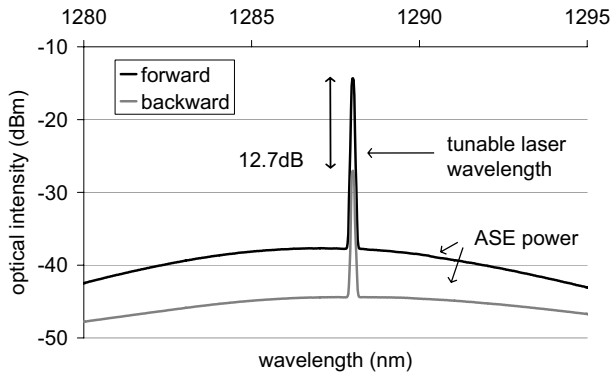

Figure 5: Transmission experiment on a 2mm long AR-coated isolator showing 12.7dB optical isolation; measured with 160mA bias current. With the total insertion loss lower than the coupling losses this is the first demonstration of a transparent amplifying waveguide optical isolator.

direction can be compensated by current injection in the active material. The result is a component which, being transparent or amplifying in one direction while providing loss in the opposite direction, is isolating and which can be monolithically integrated with InP-based active photonic devices. Configurations for both transverse electric (TE) and transverse magnetic (TM) polarization have been proposed. In this work, we focus on the latter structure, which is more elegant, as the ferromagnetic metal film serves both as the source of the non-reciprocity and as the ohmic electrical contact of the underlying SOA. Figure 4 illustrates the layout and operation principle of the TM-mode amplifying waveguide optical isolator. Prior to this work, the concept of an amplifying waveguide optical isolator had been experimentally demonstrated, the result of joint research together with Vanwolleghem. Furthermore, a series of improvements had been implemented, but it can be stated that at the start of the current research the device was, while very promising, still an academic curiosity.

The logical first objective was therefore to bring the performance of the TM-mode amplifying waveguide optical isolator to a higher level and to evolve towards a practical device. To this purpose, a lot of effort has been spend to truly understand the different mechanisms that determine the optical isolator. More in particular, an extensive study has been made on the interaction of the evanescent tail of a guided mode with a magnetized ferromagnetic metal cladding. The complex interaction between the magnetooptic parameters of the metal and the refractive indices of the metal and the surrounding materials, which determines the magnitude of the non-reciprocal effect, has been uncovered and fundamental design rules could be established. Main device issues such as the choice of the ferromagnetic metal and the development of an ohmic metal-semiconductor contact structure have been resolved on the basis of these findings. With calculations based on a first-order perturbation formula the actual design of the TM-mode isolator layer structure has been done. A proper choice of the figure of merit (FoM) to evaluate a performance of a certain design is important. Practical device FoM-functions are the current required for forward transparency of the isolator and

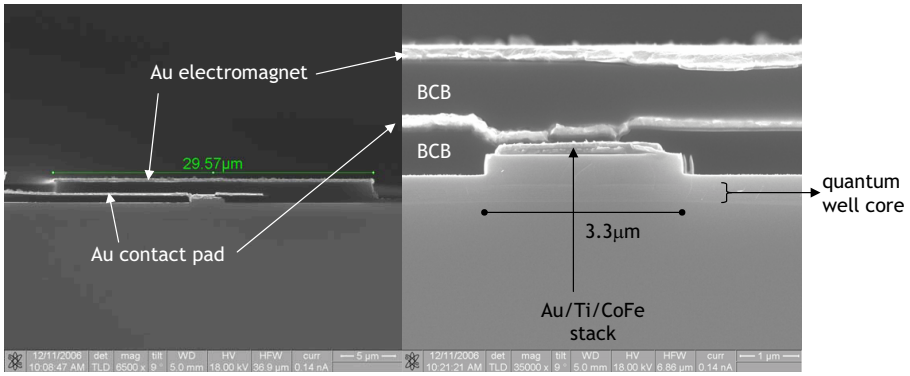

Figure 6: Electron microscope images of the cross-section of the amplifying waveguide optical isolator with integrated electromagnet, illustrating the successful fabrication.

the product of the current and the device length, both of which should obviously be minimized. The most optimized device operating at 1300nm wavelength is a InAlGaAs-InP tensile strained multiple quantum wells (9 wells) structure with an equiatomic $Co_{50}Fe_{50}$ ferromagnetic metal film on top. The ohmic contact structure is a heavily p-doped hybrid InGaAs-InGaAsP bilayer with properly chosen dimensions so as to guarantee ohmic electrical behavior whilst only minimally decreasing the magnetooptic quality. With optimized thickness of the cladding layers the best obtainable performance for a 25dB waveguide isolator is either a device of 5mm-length consuming 78.5mA (per micrometer ridge width) or a device of 2.5mm-length consuming 117mA of current (per micrometer ridge width), depending on the FoM that is used in the calculations.
Isolator demonstrators in all stadia of the optimization process have been fabricated and characterized. The most important and final result is illustrated in figure 5. The transmitted power from an external (tunable) laser varies by 12.7dB as the propagation direction of light through the 2.1mm-long device is reversed. Moderate electrical injection (155mA) suffices to compensate the remaining loss in the forward direction. This result is the first – and so far only – worldwide demonstration of a transparent monolithically integratable waveguide optical isolator. Through interpolation of the current required for forward transparency it is possible to compare this result to the first proof-of-principle experiment. Since then the performance level has been increased by more than a factor 80. In addition, an extensive study of other device aspects such as the spectral behavior and the current dependence of the optical isolation has been performed. A rate equations model of the amplifier-based isolator has been developed, which accurately reproduces the relation between the optical isolation and the injected electrical current and the increase of the optical isolation with the intensity of the input signal. Apparently the presence of spontaneous emission has a large influence on the isolator operation.

One of the main issues for this kind of isolator is the magnetization of the ferromagnetic metal film. The very high aspect ratio of the length of the film to its width results in very low remanent magnetization of the film due to large demag-

netizing fields. One of the solutions to this problem is to have a magnet integrated with the isolator. The second main focus of this research was therefore the realization of a TM-mode amplifying waveguide isolator with an integrated electromagnet. This magnet is a gold strip deposited along the longitudinal direction of the isolator in close vicinity to the ferromagnetic film. Current flowing through the gold strip from one facet to the other induces a lateral magnetic field which generates the magnetooptic Kerr effect. Apart from being a solution for the magnetization difficulties, such an integrated electromagnet is interesting as it enables to generate a magnetic field with an arbitrary field direction. This can for example be used to create the radially oriented magnetic field needed in a ring resonator based isolator. Furthermore, we remark that with an amplifying waveguide optical isolator with an integrated electromagnet it is possible to modify the internal loss of a semiconductor optical amplifier in a non-reciprocal and dynamic way.
A first generation of isolators with an integrated electromagnet has been designed, fabricated and tested, resulting in the successful demonstration of the proof-of-principle. In figure 6 electron microscope images of a cross-section of an amplifying waveguide optical isolator with an integrated electromagnet are shown. As already indicated by magnetic field calculations, the current level needed to generate a magnetic field strong enough to saturate the magnetooptic film exceeds the practical levels by at least an order of magnitude. We have however identified an elegant concept for a major improvement. Using the ferromagnetic metal film not only as the ohmic contact for the underlying amplifier but also as an electromagnet – by sending a longitudinal current through the metal strip – the electromagnet current required to obtain a certain level of non-reciprocal effect decreases drastically. The origin is the much more favorable magnetization profile in the metal film compared to the case of an external electromagnet. This phenomenon has been theoretically elaborated in detail and the theory is supported by an experimental result.

The fundamental advantage of the amplifying waveguide optical isolator over the traditional garnet-based approach is that the isolator can straightforwardly be integrated with its laser source in a monolithic way. The development of such a monolithically integrated laser-isolator component was the third objective of this work. The structure is realized in a buried ridge stripe design, which is a standard technology for DFB-lasers. The layer structure is based on the slab structure of previously tested shallowly etched ridge waveguide isolators, and the effects of the high lateral index contrast between the amplifying core and the surrounding InP cladding are calculated via magnetooptic perturbation calculations of the exact two-dimensional cross section. Thanks to the enhanced modal confinement the guiding core width can be limited to 1μm, which largely reduces the forward transparency current of the isolator as compared to the ridge waveguide devices. Monolithically integrated laser-isolator test components have been fabricated. Good and reproducible quality of the DFB-laser part has been observed. For the isolator section, it took us additional study and subsequent processing adaptations before non-reciprocity could be demonstrated. Even then, the performance level remains limited. Moreover, the integrated device suffers from electrical current leakage phenomena, obstructing the demonstration of the actual monolithically integrated laser-isolator component. As such, it is expected

that only extensive investigation of the metal-semiconductor interfaces and the laser-isolator contact separation can solve these problems and enhance the performance.

The last objective of this work was to investigate the application of the basic amplifying waveguide isolator configuration as a building block for other non-reciprocal devices. The main focus has been on the development of ring resonator-based optical isolators and on passive non-reciprocal devices. Resonance of light in a ring-shaped magnetized metal-clad waveguide can be exploited to realize a high performance optical isolator. In a drop port configuration enhancement of the optical isolation originates from the fact that resonating light travels multiple roundtrips in the cavity before being coupled to the bus waveguide. Using the pass port on the other hand results in a very large optical isolation at the resonance wavelength due to the difference in internal loss of forward and backward – or clockwise and counterclockwise – propagating light in the resonator. A thorough theoretical study has been made and all-active ring-based isolators have been designed. A contact lithography mask set has been developed and used for the fabrication of the first test devices. Due to inferior fabrication quality the experimental proof-of-principle could not be achieved.
Passive metal-clad non-reciprocal devices are attractive for applications where the optical transparency is not a requirement, such as a magnetic field sensor. The obvious material system is silicon-on-insulator (SOI), characterized by a large index contrast between the core and the surrounding cladding. For this material system it is the real part of the magnetooptic effect that is the dominant non-reciprocal effect. Still, simulations show that the ratio of the non-reciprocal phase shift to the absorption in the metal is far too low for practical implementation.

1 Introduction

THE subject of this work is the development of a planar, waveguide-based non-reciprocal component, more specifically an optical isolator. We start this introductory chapter by giving the rationale behind this work. We define an optical isolator and point out how important this component is in optical telecommunication systems. We then motivate why a planar, waveguide version of this device would imply an enormous cost reduction of active optical components. Being a prominent research topic for more than thirty years, it is worth to list the milestones in the waveguide optical isolator history. We give an overview of the important isolator configurations and material systems, we discuss the state-of-the-art, and motivate the relevance of our research.
Throughout this work, we focus on one specific configuration. In the last section of this chapter, its operation principle is elaborated, the different research initiatives related to this concept are listed, and our position within the research community is discussed.

1.1 Context

An optical isolator plays an important role in fiber optic systems. Its purpose is to protect an optical source from reflections and backscattering that cause output instabilities or unwanted changes in the output spectrum. An isolator can do this because it is a non-reciprocal device, meaning that its transmission characteristics depend on the direction of the light propagating through it. Isolators act as one-way light valves that allow the efficient injection of optical signals into a system while preventing unwanted feedback from returning to the optical source. Reflections in optical systems can emerge from a variety of sources, including Fresnel reflections at connectors, splices, fiber ends, bulk optics interfaces, detector surfaces, and even Rayleigh backscattering from the fiber may add up to a substantial return signal.
There are a large number of effects which occur when a semiconductor laser diode is operated in the presence of optical feedback. Different feedback regimes have been identified, depending on the level of the optical feedback and on the distance to the reflection [1, 2]. One regime, termed the coherence collapse state, is of particular importance since the range of feedback levels is likely to be encountered in an optical communication system. In the coherence collapse state, chaotic behavior of the laser causes a dramatic broadening of the laser linewidth, a large increase in relative intensity noise (RIN), and a degradation of the the dynamic performance of laser diode (LD) modules [3], which rises with the data rate. For example 20 to 30dB of cutoff ratio (= isolation) to external optical feedback is known to be sufficient for keeping 2.5Gbs^{-1} DFB-LD modules far from the coherence collapse regime.

Ever since the burst of the dot-com bubble the market pressure on the selling prices of optical telecom equipment is very strong, leading to a reduction of the average unit price of telecom lasers and transceivers by a factor 7 [4, 5]. As a matter of fact, this is still the trend to date, mid-2008, as is illustrated in figure

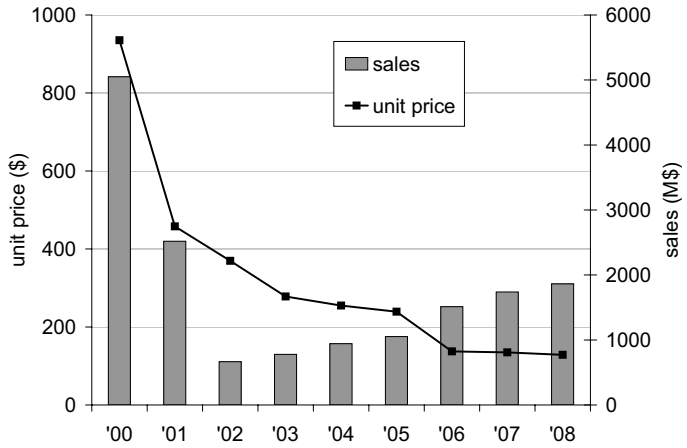

Figure 1.1: Evolution of the annual sales (M$) and unit price ($) of telecom diode-lasers [4, 5].

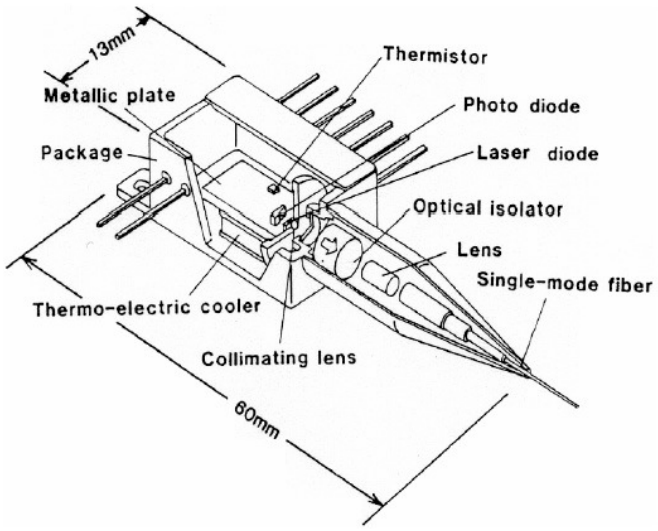

Figure 1.2: Three-dimensional view of a DFB-laser diode configuration inside a hermetically sealed 14-pin butterfly package with a single-mode fiber pigtail (after [8]).

1.1. While the volume of telecom diode-lasers has exceeded that of the year 2000 already two years ago, the average price continues to decline, with consequently a slow increase of the turnover. Telecom laser and receiver prices could stabilize if supply would ever be restricted but there are still no signs of that happening. In fact, profits are still sorely lacking among the several large suppliers with excess capacity. This is obviously a situation that cannot be sustained unlimitedly. The only way out is to reduce the actual fabrication cost of the laser modules.
But there is another important element that speaks in favor of cost reduction. The current growth of the optical network hardware sales is fueled by the rapid increase of customers' demand for voice, video and data traffic. Today's market for active components is therefore mostly Metro and FTTx (fiber to the home / node / business) in nature, with cost rather than performance being the main driver [6, 7]. If high-bandwidth services are to become really widely deployed, further innovations are required to achieve lower costs.

The major contribution to the cost of a laser diode is the packaging cost, rather than the expenses of the individual elements in the module. Indeed, the cost of the individual subcomponents can be estimated in order of tens of Dollars – the typical fabrication cost of a laser chip is around 5$ – while the cost of a high-speed transceiver is several thousands of Dollars. This can be explained as follows. Wafer scale fabrication of the subcomponents, especially the laser diode itself, allows for mass production. Parallel processing is however not possible for the assembly of the discrete elements in the package, due to the requirement of submicron-alignment precision. In a high-speed (2.5Gb/s and more) telecom laser module at least four discrete elements need to be aligned: a laser diode, a rear facet monitoring photodiode, an optical isolator and the output fiber. As is illustrated in figure 1.2 these different discrete components are optically coupled

through a high-aperture lens. Precise coupling happens via time-consuming active alignment techniques. Each additional element in the package, such as an external modulator or a wavelength tuning etalon, requires an additional alignment step and possibly an extra lens. To achieve temperature control and stabilization a thermo-electric cooler must be added to the laser module, which increases the total power consumption, hence the operation cost of the system.
We can distinguish three distinct routes towards cost reduction:

- *Reducing the costs of individual subcomponents* - Device miniaturization obviously enhances the materials utilization, essentially lowering the cost of the component. In transceivers especially the traditional bulk isolator has the most potential for size reduction. Recently, commercial nanofabricated isolators entered the market, lowering the price of individual isolators below 1$ [9]. While this innovation reduces the package size and improves the coupling efficiency to the output fiber, the problem of serial submicron-alignment remains.

- *Integration of subcomponents* - Integration of subcomponents, either in a hybrid or a monolithic manner, lowers the number of discrete parts, which essentially simplifies the alignment. This leads to a major cost reduction due to the higher yield and reduced packaging time. It also significantly reduces the component alignment sensitivity which complicates transceiver manufacture. Moreover, integration holds the promise of reduced footprint size, which would enable higher density within the system rack. Additional advantages of integration are the enhancement of thermal and mechanical stability. Last but certainly not least, for (future[1]) photonic lightwave circuits (PLC) assembling several functions onto one chip, it is essential that fundamental operations such as modulation and non-reciprocal behavior can be executed by waveguide-based components.

- *Simplification of the laser module* - Examples of this are the operation of the laser diode under uncooled conditions [11], isolator-free [12], or directly modulated [13]. Avoiding the need for cooling and temperature stabilization reduces the power consumption of the transmitter. Furthermore, operating without an isolator or external modulator obviously reduces the number of components in the package, which directly results in cost reduction. However, application-specific demands, such as wavelength channel spacing and data rate, impose stringent restrictions on the possible degree of simplification. For example, due to the strong dependence of the output wavelength on the temperature, uncooled laser diodes cannot be applied in a dense wavelength division multiplexing (DWDM) technology with a typical channel spacing of 100GHz.

There are obviously arguments for each of these three paths to be followed. Integration seems to be the preferred solution but it might introduce extra (optical

[1] Although 'future' might be a wrongful term, as recently a commercial PLC-based transceiver platform for FTTx applications became available incorporating advanced wavelength filtering functions onto the chip [10].

and/or electrical) boundary conditions which are not present when the discrete components are assembled in a free-space manner. Furthermore, technological difficulties might cause integration to actually be the most expensive option, while it essentially reduces the packaging cost. In any case, there is a strong consensus that an optical isolator that is compatible with waveguide integration is highly desirable. As a matter of fact, non-reciprocal devices, of which an isolator is one important example, can be considered as the only class of components that is not available in integrated form [14]. The search for a waveguide version of non-reciprocal components is actually almost as old as integrated optics itself [15]. In the next section we give a short historical overview of the main developments and derive the most straightforward way to continue this research.

In this work we target a waveguide optical isolator that operates in a spectral region close to 1310nm. After all, the cost reduction would be the highest for uncooled directly-modulated transmitters, with the standard wavelength of 1310nm [16]. In the end however, in any application that requires a low noise figure an integrated isolator is desired. Extension of the integrated isolator concept towards the 1550nm wavelength window is therefore an important next step in this research.[2] One market segment where integrated optical isolators operating at 1310nm could play a prominent role is that of FTTx applications. Currently, the optical network unit (ONU) at the subscriber 'home' in FTTx networks does not contain an optical isolator, essentially limiting the speed of upstream data traffic (at 1310nm wavelength) in contrast to the transceiver for downstream communication in the optical line terminals (OLT) at operator base stations. Keeping in mind that for FTTH deployments the ONU typically accounts for 80% of the system cost [17], the cost reduction inherent to the integration of laser and isolator is expected to lead to low-cost/high-speed ONU transceivers, meeting the demand for high-speed transmission in FTTH networks.

We end this section with the remark that in addition to source protection, isolators also play an increasingly important role within fiber optic transmission systems. Reflections between components or interfaces within such systems can result in serious degradations in system performance. For example, multiple reflections within a transmission system can cause the interferometric conversion of laser phase noise to intensity noise. In systems containing optical amplifiers, reflections can produce increased noise and can even cause lasing, thus limiting the levels of amplifier gain and component reflectivity that can be allowed. Clearly, then, there is a need for isolators to control reflections throughout optical transmission systems to avoid degraded performance.
For amplifiers in general and amplifiers for the metropolitan network environment specifically, most implementations today still use individual discrete passive components instead of waveguide-based technology. This is due in part to the lack of an integrated optical isolator, as has been the conclusion of a workshop on the requirements and implementation of the network elements in the metropolitan environment, held at OFC 2003 [6]; *"It seems clear from the discussion that there are*

[2]We believe that extension of the waveguide isolator configuration studied here towards 1550nm is mainly a matter of developing strong TM-gain selective material emitting at 1550nm. While this is a particularly challenging task, from a pure isolator point of view, no new elements are expected to enter the picture.

still opportunities for improvement and cost reduction in the component, subsystem and amplifier designs – including integration and waveguide structures. One specific technical challenge that was identified is the need for an optical isolator that is compatible with waveguide integration."

1.2 Waveguide optical isolator: state-of-the-art

1.2.1 Introduction: bulk Faraday isolator

Bulk optical isolators are all based on the magnetooptic effect of Faraday rotation. When linearly polarized light passes through a magnetooptically active material that is subjected to a magnetic field $\boldsymbol{H}$ in a direction parallel to this field $\boldsymbol{H}$, the plane of polarization rotates. The angle of rotation θ is proportional to the magnitude of $\boldsymbol{H}$ and the distance traveled through the medium:

$$\theta = VHL, \tag{1.1}$$

with V the Verdet constant of the material. A positive Verdet constant corresponds to counterclockwise rotation[3] when the direction of propagation is parallel to the magnetic field and to clockwise rotation when the direction of propagation is antiparallel. Thus, if a ray of light is passed through a material and reflected back through it, the rotation doubles. This phenomenologically differentiates the Faraday effect from the effect of natural optical activity. We elaborate the origin of magnetooptic effects more in detail in chapter 2.

The principle of a bulk optical isolator is shown in figure 1.3. Incoming, 'forward' light is linearly polarized by a first polarizer. The plane of polarization is rotated at 45° by the Faraday rotator. A second polarizer, set at 45° with respect to the first one, lets the light pass. The plane of polarization of reflected, 'backward' light traversing the Faraday rotator is rotated by another 45°, hence is blocked by the first polarizer. This isolator configuration is obviously polarization dependent. This simple scheme is therefore only used in laser packages. The protection of active components in fiber-optic systems requires polarization independence. A variety of polarization independent isolator designs exist [18], but the heart of the system remains a Faraday rotator. The important material characteristics for a Faraday rotator are obviously a high Verdet constant and low optical absorption. In the telecom wavelength window yttrium iron garnet (YIG) or bismuth-substituted iron garnet (BIG) crystals are traditionally used. Faraday isolators are commercially available since the mid-80's. The typical requirements to a polarization independent single-stage free-space isolator are displayed in table 1.2.1. The wavelength range of isolators is typically 40nm, which is limited by the material dispersion of the Verdet constant. PDL and PMD stand for polarization dependent loss and polarization mode dispersion, respectively. The return loss denotes the amount of reflection from the isolator itself; light which is always coupled back to the source. The different central wavelengths refer to operation in

[3] When looking into the beam

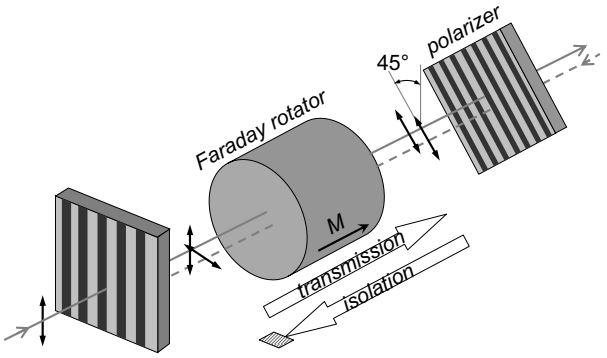

Figure 1.3: Schematic layout of a bulk Faraday optical isolator.

Central Wavelength (nm)	1310, 1480, 1550 or 1585
Peak Isolation (dB)	≥ 40
Minimal Isolation (dB)*	≥ 30
Insertion Loss (dB)	0.5
Bandwidth (nm)	20
Return Loss	≥ 60
PDL (dB)	≤ 0.1
PMD (ps)	≥ 0.2
Operating Temperature (°C)	-20 to +70

* at 23°C over $\pm$20nm

Table 1.1: Typical performance specifications of a free-space single stage optical isolator.

the O-, S-, C-, and L-band of the infrared spectrum.[4] Nowadays standard telecommunication packages use a dual stage isolator with a total isolation of 40dB, i.e. two stages of 20dB.

1.2.2 The history of a waveguide optical isolator

The development of an integrated optical isolator is a quest that is going on for more than 35 years now. Ever since the first proposal by Wang [19] a multitude of concepts have been developed and studied theoretically and experimentally, with different kinds of non-reciprocal effects exploited. In the next paragraphs we will concisely discuss the long history of the waveguide optical isolators, but first we will review the candidate materials for integrated magnetooptics at telecom

[4]In telecommunications several transmission bands have been defined and standardized. O-band: 1260nm-1360nm, S-band: 1460nm-1530nm, C-band: 1530-1565, L-band: 1565-1625. (Dense) wavelength demultiplexing (DWDM) systems mainly operate in the C-band, although for small distances (<10km) the O-band is also used. For Course WDM (CWDM), the low-cost version of WDM, the S-, C-, and L-band are currently used, but extensions towards the O-band is possible. FTTH technologies, based on passive optical networks (PON) use different wavelengths for upstream and downstream data traffic. For example the bandwidth allocation for GPON requires 1260nm-1360nm upstream, 1440nm-1500nm downstream, and 1550nm-1560nm for video (CATV).

wavelengths. For an in-depth description of the state-of-the-art of (garnet-based) magnetooptic waveguides we refer to the recent review article by Dötsch [20].

1.2.2.1 Magnetooptic materials

For decades the only material system that received attention is that of ferrimagnetic garnets. These crystals have the general formula $C_3A_2D_3O_{12}$ in which *C* presents a large rare earth (most frequently bismuth, BIG) or yttrium ion (YIG) in dodecahedral coordination, and *A* and *D*, in magnetooptic garnets, are usually iron ions in octahedral and tetrahedral coordination, respectively. Given the flexible chemistry of this structure many substitutions can be made, which allows for tailoring of the growth and properties of the material. The two iron sublattices are usually antiferromagnetically coupled to each other. Most of the work to date on garnets involve films (YIG or BIG) grown epitaxially onto garnet substrates, typically gadolinium- or lanthanum-gallium garnets (GGG or LGG), depending on the best lattice match. A detailed description of magnetooptic garnets can be found in literature [21, 22]. The interest in this class of materials for optical isolators comes from their unique combination of low optical absorption and a relatively high Verdet constant at telecom wavelengths. The most popular magnetooptic garnet is Ce-substituted YIG, with a specific Faraday rotation[5] of 4500°/cm at 1550nm. However, garnets have the large drawback that integration onto semiconductor host substrates and waveguides, which are the integration platforms for practically all optical devices, is difficult. The main hurdle for direct growth of garnets onto semiconductor lays in their large difference in thermal expansion. Just recently Stadler [23, 24] has demonstrated YIG waveguides and polarizers grown on a variety of substrates. Hutchings on the other hand has reported on a Ce-substituted YIG layer sputter-deposited on a GaAs-AlGaAs waveguide structure [25]. Other attempts involve direct wafer bonding to combine garnets and semiconductor materials, both on InP-related hosts [26, 27] and on silicon-on-insulator (SOI) [28, 29].

A class of materials that has only entered the picture for integrated magnetooptics less than a decade ago is that of the transition metals and their alloys. The reason for this is straightforward, namely that at telecom wavelengths their extinction coefficient is high, causing unacceptable levels of optical loss, at least for passive non-reciprocal devices. However, for magnetooptic recording transition metal alloys, mainly based on cobalt (Co), iron (Fe) and/or nickel (Ni), have always been and still are the materials of interest [30]. Their intrinsic advantages are the ease of deposition on basically any substrate combined with a rather strong magnetooptic effect, although this varies significantly with the specific composition of the alloy. At infrared wavelengths the Co_xFe_{1-x}-alloy system is likely to perform best. Section 3.2 is devoted to the study of the optical and magnetooptic properties of these metals. Other (semi-)metals that have been studied for integrated magnetooptics are Mn-based compounds such as MnAs [31] and MnSb [32]. These can either be sputtered of be epitaxially grown on III-V semiconductors.

About ten years ago, quite some attention went to composite materials with mag-

[5] The Faraday rotation per unit length at magnetic saturation, $\theta_{spec} = VH_{sat}$

netic particles or nanoclusters embedded in a non-magnetic matrix. Examples are GaMnAs/AlAs [33] and MnAs/GaAs superlattices [34, 35]. One other experiment is particularly remarkable. Baba [36] reported on the demonstration of ferromagnetic particles composite films in which Fe powder is homogenously dispersed in a (non-magnetic) polymer matrix. In accordance to the Maxwell-Garnet theory, the optical loss was shown to be significantly lower than those of bulk Fe layers with the same volume of Fe. The Faraday effect however seems to remain the same in both cases. This result suggests a major enhancement of the magnetooptic effect relative to the optical absorption. There is however considerable skepticism towards this result. After all, the paper is now more than 10 years old, but there has been no confirmation of this result or sign of continuation of this research. In addition, while it is known that magnetooptic effects can be enhanced by exploiting surface plasmon resonance phenomena in nanoparticles, the optical loss is expected to enhance simultaneously [37, 38].

Diluted magnetic semiconductors – also called semimagnetic semiconductors – are another interesting class of materials, combining the properties of ordinary and magnetic semiconductors. These materials include semiconductor crystals doped with 3d ions of transition metals and solid solutions containing a magnetic component. The most prominent material that has been studied for non-reciprocal applications is $Cd_{1-x}Mn_xTe$ [39]. As this material shares the zinc-blende crystal structure with III-V semiconductor materials it can directly be grown on GaAs or InP substrates. Furthermore, the $Cd_{1-x}Mn_xTe$-system exhibits a relatively large specific Faraday rotation near the absorption edge, θ_{spec} = 470°/cm at 740nm, and has a low loss in the wavelength range of 600nm to 800nm. Substitution of Cd with Hg can extend the wavelength range to telecom wavelengths [40]. However, the fundamental drawback – and the reason why it is unlikely that a $Cd_{1-x}Mn_xTe$ isolator will ever be commercialized – is that this material is highly poisonous.

Recently, very efficient Faraday rotation has been demonstrated in polythiophene films [41]. These conjugated polymeric materials are transparent at infrared wavelengths and have the major advantage that they can easily be deposited on any substrate by way of spin-coating. A specific Faraday rotation of 400°/cm has been reported.

1.2.2.2 Waveguide Faraday rotator

The first logical step towards an integrated isolator was to try to develop a waveguide version of a Faraday isolator. As defined earlier, the Faraday effect causes a non-reciprocal rotation of the polarization plane. When adapting this free-space isolator approach to a waveguide-based structure, there are however three principle challenges to be faced. First, the planar format of optical waveguides breaks the symmetry of bulk optical devices. This leads to a structurally-induced birefringence with linearly polarized eigenstates – transverse electric (TE) and transverse magnetic (TM) modes – which are phase mismatched, $\beta_{TE} \neq \beta_{TM}$, with β the propagation constant of the mode. As a result, there is an incomplete, periodical power exchange between these modes. In other words, for a complete TE-TM mode conversion perfect phase matching is required. Numerous attempts have been made to solve this problem, a comprehensive overview of which is given in

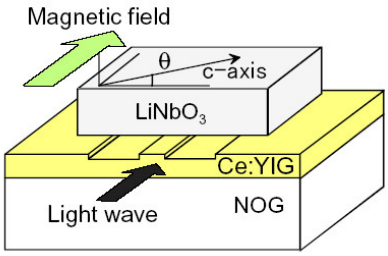

Figure 1.4: Schematic layout of a garnet waveguide Faraday isolator. The $LiNbO_3$ cladding serves as the reciprocal polarization rotation element. The substrate is a substituted non-magnetic garnet $(GdCa)_3(GaMgZr)_5O_{12}$ (NOG).

reference [20]. The most elegant way to remove the restriction in the obtainable polarization rotation is to use a quasi-phase-matching approach, by a periodic reversal of the applied magnetic field every beat length [25].

Secondly, in addition to polarization rotation, the standard method of using the Faraday effect for optical isolation additionally requires two polarizers, normally set at 45° to each other. Generally, planar waveguides have a polarization dependence that can be used for TE-TM selectivity. The most obvious way is to rely on the higher penetration of TM-modes in the waveguide cladding, hence the higher TM-absorption if a metal cladding is used. However, it is not obvious how to obtain a polarization selectivity at alternative angles. The solution is to integrate a reciprocal 45° polarization rotator in combination with the non-reciprocal Faraday rotator. The most straightforward way is to use a (naturally) anisotropic material, for example $LiNbO_3$, as the top cladding layer of a garnet waveguide, with the optical axis in the plane of the film and rotated with respect to the TE-direction (see figure 1.4). By a proper choice of this offset angle the magnetooptic mode conversion in the forward direction can be canceled, while it is still present for backward propagation. This concept was historically the first attempt to obtain an integrated optical isolator [42, 43]. Back in the seventies it has never worked, mainly due to a bad interface quality between the garnet core and the $LiNbO_3$ layer. Mizumoto picked up this old idea, experimentally demonstrated the concept in 2001 [44], and last year an isolation of 20dB in a 1.6mm-long device at 1550nm wavelength was reported, but with a high insertion loss of 8dB [45]. Ando [46], in the late eighties, successfully used another way to introduce a reciprocal polarization rotation, based on the (reciprocal) magnetooptic Cotton-Mouton effect [47]. This can be considered to be the first demonstration of a waveguide optical isolator. A third possibility is to introduce the necessary quarter-wave plate functionality with an asymmetric ridge waveguide. In such a structure the fundamental modes are of mixed polarization, hence launching light of either pure TE or TM polarization results in periodical rotation of the polarization between TE and TM. Several examples of such polarization rotators have been reported, two of which are illustrated in figure 1.5. In the left picture the asymmetry is caused by an angled sidewall [48, 49], the right structure uses the phenomenon of reactive ion etching lag (RIE Lag) [50].

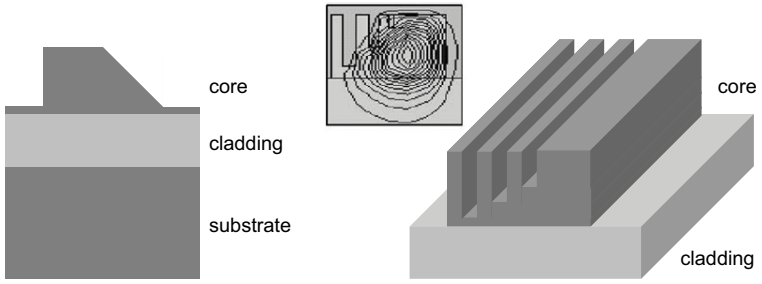

Figure 1.5: Two examples of an asymmetrical rib waveguide which provides a reciprocal polarization rotation.

The third challenge relates to the integration of the waveguide Faraday isolator with a semiconductor laser. This is a severe problem that is actually twofold. First of all, there is the integration of the different materials onto the the same carrier. As discussed earlier in section 1.2.2.1, a variety of solutions are being investigated. Another main issue that arises for garnet waveguides is the fact that at telecom wavelengths the refractive index of garnets is around 2.2 whereas that of semiconductors is in the range of 3.2-3.5. If the magnetooptic garnet is to form the waveguide core, this requires a film of even lower refractive index and sufficient thickness to form the cladding. A solution for this integration problem would be to create an air gap between the garnet core and the semiconductor substrate, as demonstrated by Izuhara [27]. However, the submicron precision horizontal alignment of the patterned garnet film with the features on the semiconductor chip, such as a laser diode, poses serious difficulties. An alternative scheme that solves this issue is to use a magnetooptic film as a top cladding of a waveguide. In this configuration the Faraday effect only affects the evanescent tail of the waveguide mode, hence the same non-reciprocal polarization rotation requires a longer device. TE-TM mode conversion on a garnet-clad GaAs-AlGaAs waveguide has recently been demonstrated by Hutchings [25], however with only 12% efficiency in an 8mm long device.

The major research effort on waveguide versions of a Faraday isolator took place from the end of the seventies until the beginning of the nineties. Broadband isolation of more than 30dB has been achieved on a 3.4mm-long chip with an insertion loss not exceeding 2dB [51]. Nevertheless, the enormous difficulties of achieving precise phase matching has led to the investigation of other isolator concepts. It is however striking that lately the idea of an integrated Faraday isolator re-entered the picture. This is mainly due to the progress in fabrication techniques, such as surface activation wafer bonding between $LiNbO_3$ [45] and sputter deposition of garnets onto semiconductors [25].

1.2.2.3 Non-reciprocal phase shift

The second major research approach relies on a different magnetooptic effect. If a transversely magnetized – perpendicular to the propagation direction of the light – magnetooptic material is the cladding layer of a waveguide structure, the effec-

tive indices of forward and backward propagating modes are shifted with respect to one another.[6] The origin of this non-reciprocal phenomenon will extensively be elaborated in chapter 2. Important is that this magnetooptic effect does not cause a coupling between TE and TM polarization. Using this effect, a waveguide Mach-Zehnder interferometer (MZI) can be designed such that in the forward direction the modes in the two arms are in phase, yielding constructive interference, whereas in the backward direction the modes are out of phase by 180° causing destructive interference. This elegant configuration has already been proposed in 1975 [53], but only gained interest by the end of the nineties, when the limitations on the waveguide Faraday isolator concept had become clear. Nevertheless, an isolator based on the non-reciprocal phase shift overcomes two of the intrinsic challenges of the Faraday rotator approach; there is no need for phase-matching between TE and TM polarization, and no reciprocal polarization rotators are required.

In its simplest scheme, one arm of the MZI contains a magnetized element with a proper length that introduces a non-reciprocal phase shift of $\pm 90°$ with the sign depending on the propagation direction. In the other arm a reciprocal phase shift of 90° is built-in, by adjusting the length difference between the arms. A length reduction can be obtained by introducing a $\pm 45°$ non-reciprocal shift in one arm and a $\mp 45°$ non-reciprocal shift in the other. Configurations operating for TE [54, 55] and TM-polarization [56, 57] have been studied. In 2000 Fujita published the first experimental demonstration of a (TM-mode) garnet waveguide MZI optical isolator [58]. Isolation of 19dB with an insertion loss of 2dB around a wavelength of 1530nm has been achieved on an all-garnet waveguide structure. The corresponding interferometer length is as large as 8mm. Since then a variety of alternative structures has been studied, mainly on a theoretical basis, including polarization independent isolators [59, 60], non-reciprocal multimode imaging devices [61, 62], and recently isolators based on microring resonators [63]. However, the experimental result of Fujita [58] could not be improved.

Shortly after the demonstration of an all-garnet interferometric isolator research focussed on the integration with semiconductors. Yokoi came up with the idea of wafer bonding a garnet film onto a patterned semiconductor chip [64]. The first experimental demonstration followed shortly afterwards [65]. A Ce:YIG layer is attached through direct-bonding techniques to a InGaAsP-InP MZI, as illustrated in figure 1.6. The measured optical isolation was however limited to 4.9dB in a device of several millimeters long. Yokoi attributed this to the asymmetry of the waveguide problem. As the bottom cladding (n_{InP} = *3.17 at 1550nm*) has a refractive index much higher than that of the garnet ($n_{Ce:YIG}$ = *2.22 at 1550nm*) only a small fraction of the light is coupled in the magnetooptic layer, resulting in a small non-reciprocal phase shift. Recently, it has been demonstrated by the same research institute that a solution can be to include a selectively oxidized AlInAs layer between the InGaAsP core and the InP substrate, with a refractive index close to that of Ce:YIG (n_{AlInAs} = *2.45*) [66]. Furthermore, they have successfully fabricated a Fabry-Pérot laser, monolithically integrated with a passive optical

[6] While this is a valid statement, it can be proven that for an asymmetric waveguide with a magnetooptic core and different materials for the upper and lower cladding, there is also a non-reciprocal phase shift [52].

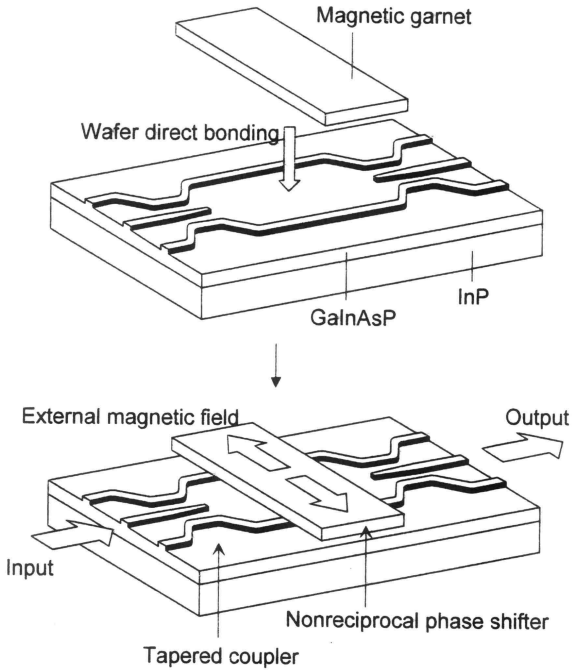

Figure 1.6: Schematic layout of the non-reciprocal phase shifter based on a Mach-Zehnder interferometer.

waveguide by means of selective area epitaxy [67]. With this, in principle, the last hurdle has been cleared for the realization of a fully integrated laser-isolator device, based on a garnet-clad non-reciprocal phase shifter. However, with the (hydroxyl) wafer bonding technique used earlier a high temperature annealing step is essential to obtain a strong bonding [68], and this is not compatible with active devices. Two possible solutions are being investigated. One is to use surface activation bonding, which does not require the high temperature annealing step. The other is to use wafer bonding on silicon-on-insulator (SOI). The laser diode can then be incorporated after the bonding of the garnet film. Moreover, using SOI, with its high index contrast between the Si core (n_{Si} = *3.48* at 1550nm) and the SiO_2 lower cladding (n_{SiO_2} = *1.44* at 1550nm), as a guiding layer solves the issue of asymmetric waveguiding, reducing the isolator length to a few hundreds of micrometers [28].

While the non-reciprocal phase shifter has obvious advantages with respect to the Faraday isolator, its disadvantages should not be minimized. A lot of these issues have been studied lately and solutions have been proposed. Due to the interferometric nature of the device, its bandwidth is limited and is much smaller than the wavelength range of Faraday isolators which is determined by material dispersion of the Verdet constant. Shoji has proposed an ultra-wideband design of a MZI isolator, based on an adjustment of the reciprocal phase shift [69].
Secondly, for designs operating for either TE or TM polarization, the basic non-

reciprocal phase shifter is transparent in the backward direction for the other polarization.[7] As demonstrated by Yokoi [70], light of opposite polarization can be filtered out by properly designing the reciprocal phase shifter so as to obtain a shift of 90° for the isolator polarization and 180° for the other, provided two directional couplers are used for the MZI (see figure 1.6).
A third issue is the fact that the external magnetic field is to be applied antiparallel with respect to the interferometer arms to achieve a push-pull non-reciprocal phase shift, as illustrated in figure 1.6, which obviously complicates fabrication. This difficulty has also been addressed by Yokoi [71]. He proved both theoretically and experimentally that by creating a difference in the layer structure of both arms, an interferometric isolator that operates in a unidirectional magnetic field can be obtained.

1.2.2.4 Magnetophotonic crystals

In recent years, a new research direction has entered the picture, that of magnetophotonic crystals. One-dimensional magnetophotonic crystals – comprising a periodic stack of magnetic and non-magnetic layers with one or more defects – have been studied since the late nineties [72, 73]. It has been shown that for frequencies associated with a defect resonance the specific Faraday rotation in such a magnetophotonic crystal structure can be largely enhanced. The origin is a difference in the resonance frequency of left- and right-hand circular polarization.
Currently, research is concentrated on two-dimensional magnetophotonic crystals. The idea is to modify the band dispersion relations $\omega(\boldsymbol{k})$ of a photonic crystal such that strong spectral asymmetry $\omega(\boldsymbol{k}) \neq \omega(-\boldsymbol{k})$ is created [74]. If zero group velocity can be achieved in the backward propagation direction such a structure acts as an isolator. Kono [75] has theoretically studied a garnet-based photonic crystal waveguide, with an asymmetry in the bandstructure originating from asymmetry in the magnetization profile. Takeda [76] has proposed a similar configuration composed of a magnetooptic EuO layer sandwiched between two reciprocal Si-based photonic crystal claddings. Another solution to introduce a non-reciprocal bandstructure is to modify the geometrical symmetry of the photonic crystal itself, as proposed by Vanwolleghem [77].

1.2.2.5 Conclusion

In summary, two main integrated isolator concepts have been studied extensively throughout history: a Faraday isolator and a non-reciprocal phase shifter. They have in common that nearly all research has focussed on ferrimagnetic garnet material as the source of the non-reciprocal effect. In both configurations stand-alone (all-garnet) isolators have been demonstrated with high isolation and limited insertion loss. However, the integration with semiconductor hosts or waveguides remains an issue. Therefore, at the end of the millennium another idea entered the picture. This is the configuration our work is based upon, and it is elaborated in the next section.

[7] Actually in both propagation directions but obviously only backward propagating light needs to be blocked.

To finalize this study of garnet-based isolators we remark that in recent years, the old ideas have regained attention, an evolution that is mainly due to improved fabrication techniques, such as surface activation wafer bonding and sputter deposition of garnet material.

1.2.3 Amplifying waveguide optical isolator

1.2.3.1 Theoretical concept

Given the serious issues raised with respect to the integration of garnet layers onto semiconductor materials, the problem can also be approached from a different perspective, namely, starting from a structure that can be integrated with III-V active devices and trying to introduce non-reciprocity into it. Therefore, consider a semiconductor optical amplifier (SOA), i.e. a diode laser without feedback mechanism, and use a ferromagnetic metal layer instead of the common Au or PtAu film to provide the electrical contact for current injection in the device. Furthermore, reduce the buffer layer that separates the active core from the metal, such that the guided mode overlaps with the metal. In the presence of a magnetic field applied in the lateral direction – perpendicular to the longitudinal propagation direction and parallel to the layer surfaces – magnetooptic phenomena generate a non-reciprocal phase shift on the TM-polarized guided modes. As a result of the high optical absorption of ferromagnetic metals in the infrared spectrum, the non-reciprocal phase shift is of complex nature, contrary to a garnet-clad device. In other words, both the effective index n_{eff} and the effective extinction coefficient κ_{eff} ($\sim$ absorption) differ for oppositely propagating light. This principle is illustrated with the diagram of figure 1.7. The physics behind this mechanism are the focus of chapter 2.
Apart from non-reciprocal behavior, an isolator requires optical transparency for forward propagating light. The overall loss level in the metal-clad SOA can obviously be lowered by electrical pumping of the SOA. With sufficient optical gain the forward modal loss can entirely be compensated, while in the backward direction the guided mode remains (partially) absorbed. In the simplest configuration, the ferromagnetic metal acts both as the source of the magnetooptic effect and as the electrical contact. Such a device is schematically drawn in figure 1.7.
This elegant concept, which we will term as 'amplifying waveguide optical isolator' throughout this work, was almost simultaneously proposed by Nakano [78] and Ando [79]. Actually, it was Hammer who first proposed to use ferromagnetic metals, although in a Faraday rotator configuration [80]. Based on theoretical calculations Nakano and Ando predicted very high optical isolation ratios in the order of 10-20dB/mm, and transparency gain levels of 1500cm^{-1}. Although these theoretical calculations should only be considered as a feasibility study, these numbers show that the idea is not unrealistic.

As it is basically a non-reciprocal phase shifter, the amplifying waveguide isolator scheme has all the corresponding advantages, but in addition it solves basically all the problems of the garnet-clad interferometric isolator. The main advantage is obviously the integratability. As the isolator has essentially the same structure as the active device it is to be integrated with, monolithic integration is possible and no degradation of the isolating performance is expected. Further-

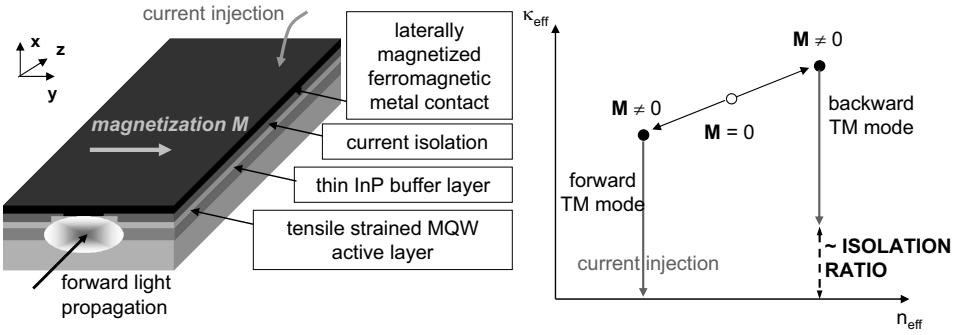

Figure 1.7: Schematic layout and operation principle of the TM-mode amplifying waveguide optical isolator.

more, as the magnetooptic metal layer can be sputter-deposi-ted on the semiconductor interface, this isolator can be fabricated using standard InP-SOA processing techniques. As the operation of this device doesn't rely on interfering signals, the high wavelength sensitivity of the MZI isolator doesn't apply to this configuration. Instead, the dominating factor is expected to be the gain spectrum of the active material of the isolator – and of the source protected by the isolator. In addition the high degree of polarization selectivity of the tensile strained multiple quantum well active region (see chapter 3) ensures that the component is opaque for TE-polarized light. Another advantage with respect to ferrimagnetic garnet-based device is that the magnetooptic strip can, provided its dimensions are properly designed, act as a permanent magnet. As such, there is no need to integrate an extra micromagnet on top of the isolator.
Of course these features come at a certain price. The disadvantages of the amplifying waveguide optical isolator are related to the fact that the isolator itself is an active component. The amplified spontaneous emission (ASE) generated along the device adds to the noise in the signal, hence might deteriorate the optical signal-to-noise ratio (OSNR). In addition, the backward propagating ASE couples into the source, hence the isolator itself causes optical feedback to the active device it protects. However, ASE is not coherent, hence will not interfere with the lasing mode. In addition, as the isolator requires electrical pumping, its operation increases the power consumption of the system.

1.2.3.2 State-of-the-art

The configuration of an amplifying waveguide optical isolator has received a lot of attention in recent years. In this section we review the current state-of-the-art and indicate our position within the research community. It is important to stress that this work is the continuation of research initiated by Mathias Vanwolleghem. This obviously causes some overlap between both research projects. Instead of trying to define the overlap at this point, we will mention it throughout this document. For now it suffices to mention that together with Vanwolleghem, we have performed the first experimental demonstration of the amplifying waveguide op-

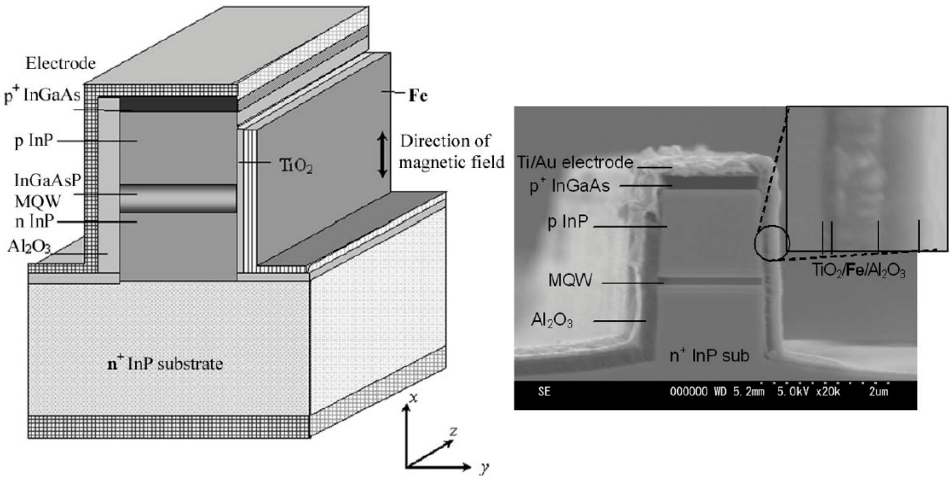

Figure 1.8: Schematic layout and cross-sectional electron microscope image of the TE-mode amplifying waveguide optical isolator (after [82]).

tical isolator configuration [81].
Apart from this (partially joint) research, two other groups have been working on the development of an isolator based on the non-reciprocal loss shift in ferromagnetic materials. In the group of Nakano, two routes have been investigated. Shimizu has proposed a configuration operating for TE-polarization [82]. The basic principle is analogous, only the orientation of the ferromagnetic metal and the magnetization are different. As illustrated in figure 1.8, an iron film is deposited on one of the side walls of a ridge waveguide and magnetized along the transverse direction. An isolation ratio of 14.7dB/mm has been achieved, but with a high insertion loss above 10.0dB/mm even at an injection current of 150mA. This structure suffers from two problems. First of all, in a ridge waveguide configuration, etching through the quantum well layers is required, which introduces surface defects, hence enhances the modal loss. A solution could be a buried heterostructure device. Another issue is how to realize the transverse magnetization in the absence of an external magnetic field. As will be discussed in chapter 2 the intrinsically low ratio of the length to the width of this metal stripe makes it virtually impossible to obtain remanent magnetization. On the other hand, the TE-configuration provides a simple scheme for an integrated laser-isolator device. The idea is that for a wide ridge width the optical mode does not overlap with the ferromagnetic metal, hence the device is reciprocal, acting as a SOA, or a laser if a feedback mechanism is provided. An integrated laser-isolator device therefore consists of a part with a narrow ridge, the isolator, and a laser part with a large ridge width. This scheme has been proposed and demonstrated by Shimizu [83]. In a proof-of-principle experiment, 4dB of isolation has been achieved, making this the first monolithically integrated laser-isolator device. Researchers from the same group have demonstrated an isolator based on the amplifying waveguide isolator principle where the optical isolation is generated by a ferromag-

netic manganese-compound such as MnAs [31] and MnSb [32]. These materials can be grown epitaxially onto InP substrates. The best result, an isolation ratio of 12.0dB/mm combined with an insertion loss of 42dB/mm at 80mA current injection, has been obtained with a MnSb cladding. The authors claim that the advantage of Mn-based materials over elemental ferromagnetic metals such as Fe and Ni is that the latter yield a high electrical contact resistance when used as the contact metal of SOAs. We refute this point in chapter 3, where we show that with the appropriate choice of the semiconductor contact layers an ohmic electrical contact can be realized with $Co_{90}Fe_{10}$ and similar alloys. Moreover, we prove that at infrared wavelengths MnAs and MnSb have inferior magnetooptic properties compared to the Co_xFe_{1-x}-alloy system studied throughout this work.
The other group that is studying the amplifying waveguide optical isolator concept is the one by Zayets and Ando. They have mainly investigated the device from a theoretical point of view. On the experimental side, 1dB of non-reciprocal propagation has been reported, on a passive $Ga_{1-x}Al_xAs$ waveguide structure [84].
To indicate where we stand with respect to these research initiatives, we mention here the specifications of our best performing devices; we have demonstrated a monolithically integratable isolator with completely compensated forward loss, showing an isolation ratio of 6.35dB/mm. This is the first transparent optical isolator of this type and as such it is fair to state that we are world-leading in the field of semiconductor-based waveguide optical isolators.

1.3 Outline of this work

The purpose of this work can be considered fourfold. The first objective is to bring the performance of the TM-mode amplifying waveguide optical isolator to a higher level, to evolve from an academic curiosity towards a practical device. The second main focus of this research lays on the realization of an optical isolator with an integrated electromagnet. Thirdly, there is the development and demonstration of a monolithically integrated laser-isolator component. The last objective is to investigate the application of the basic amplifying waveguide isolator configuration as a building block for other non-reciprocal devices, such as a ring resonator based isolator.

In chapter 2 we study non-reciprocal phenomena, and more specifically the origin of the complex non-reciprocal phase shift in metal-clad waveguides. Furthermore, the calculation methods for magnetooptic layer structures will be discussed. A third main part of this chapter concentrates on the derivation of general design rules for metal-clad non-reciprocal devices. At the end of the chapter, the magnetic properties of the isolator device will be discussed.
Chapter 3 is devoted to the development of a TM-mode amplifying waveguide optical isolator. The building blocks of this component are optimized, both from a theoretical and an experimental point of view. In a second part, magnetooptic slab waveguide simulation techniques are used to calculate the ideal isolator layer structure and an extensive tolerance study is performed.
In chapter 4 we will focus on the fabrication and characterization of non-reciprocal

components. A chronological overview will be given and we will show how the performance has improved by a factor 80 between the first demonstration of the principle and the current device. A second part of the chapter discusses the development of an optical isolator with an integrated electromagnet.
A monolithically integrated laser-isolator component is the subject of chapter 5. The design, fabrication and characterization will subsequently be elaborated.
Chapter 6 studies alternative isolator configurations and other non-reciprocal devices, where we stick to ferromagnetic metals as the source of the non-reciprocity. To this end we rely on the theoretical study of chapters 2 and 3 and on the experimental results of chapter 4.
The last chapter summarizes the conclusion of this work and gives prospects for the future.

1.4 Publications

The scientific output of our research has been published in a number of international journals and has been presented at several national and international conferences. The following list gives an overview.

1.4.1 International Journals

1. W. Van Parys, D. Van Thourhout, R. Baets, B. Dagens, J. Decobert, O. Le Gouezigou, D. Make, and L. Lagae, 'Transparent AlGaInAs/InP Amplifying Waveguide Optical Isolator', submitted to *Journal of Lightwave Technology*.

2. W. Van Parys, D. Van Thourhout, R. Baets, B. Dagens, J. Decobert, O. Le Gouezigou, D. Make, and L. Lagae, 'Amplifying Waveguide Optical Isolator With an Integrated Electromagnet', *IEEE Photonics Technology Letters*, 19(24), p.1949-1951 (2007).

3. W. Van Parys, M. Vanwolleghem, D. Van Thourhout, R. Baets, F. Lelarge, B. Thedrez, and L. Lagae, 'Study of a Magnetooptic Contact for an Amplifying Waveguide Optical Isolator', *Photonics Technology Letters*, 19(9), p.659-661 (2007).

4. M. Vanwolleghem, W. Van Parys, P. Gogol, P. Beauvillain, and R. Baets, 'Design and optimization of a monolithically integratable InP-based optical waveguide isolator', *Journal of the Optical Society of America B*, 24(1), p.94-105 (2007).

5. W. Van Parys, B. Moeyersoon, D. Van Thourhout, R. Baets, M. Vanwolleghem, B. Dagens, J. Decobert, O. Le Gouezigou, D. Make, R. Vanheertum, and L. Lagae, 'Transverse magnetic mode nonreciprocal propagation in an amplifying', *Applied Physics Letters*, 88, p.071115 (2006).

6. F. Lelarge, B. Dagens, C. Cuisin, O. Le Gouezigou, G. Patriarche, W. Van Parys, M. Vanwolleghem, R. Baets, and J.L. Gentner, 'GSMBE growth of GaInAsP/InP 1.3 μm-TM-lasers for monolithic integration with optical waveguide isolator', *Journal of Crystal Growth*, 278(1-4), p.709-713 (2005).

7. M. Vanwolleghem, W. Van Parys, D. Van Thourhout, R. Baets, F. Lelarge, O. Gauthier-Lafaye, B. Thedrez, R. Wirix-Speetjens, and L. Lagae, 'Experimental demonstration of nonreciprocal amplified spontaneous emission in a CoFe clad semiconductor optical amplifier for use as an integrated optical isolator', *Applied Physics Letters*, 85(18), pp.3980-3982 (2004).

1.4.2 Conference Proceedings

8. W. Van Parys, D. Van Thourhout, R. Baets, B. Dagens, J. Decobert, O. Le Gouezigou, D. Make, R. Vanheertum, and L. Lagae, 'Low-Loss, InP-Based Integrated Optical Isolators', *Conference on Lasers and Electro-Optics 2008*, California (USA), p.1-2 (2008).

9. W. Van Parys, D. Van Thourhout, and R. Baets, 'Amplifying Waveguide Optical Isolator with an Integrated Electromagnet', *IEEE/LEOS Symposium Benelux Chapter, 2007*, Belgium, p.7-10 (2007).

10. H. Shimizu, W. Van Parys, R. Baets, and Y. Nakano, 'Characterization of nonlinear nonreciprocal propagation in semiconductor amplifying waveguide optical isolators', *68th Autumn Meeting of the Japan Society of Applied Physics*, Japan, p.4p-P3-21 (2007).

11. W. Van Parys, D. Van Thourhout, and R. Baets, 'Optimization of a TM-mode Amplifying Waveguide', *IEEE/LEOS Benelux Annual Workshop 2007*, Netherlands, p.23-24 (2007).

12. W. Van Parys, D. Van Thourhout, R. Baets, B. Dagens, J. Decobert, O. Le Gouezigou, D. Make, and L. Lagae, 'Amplifying Waveguide Optical Isolator with Integrated Electromagnet', *ECIO 2007*, Denmark, p.ThA5 (2007).

13. W. Van Parys, D. Van Thourhout, R. Baets, B. Dagens, and L. Lagae, 'Transparent amplifying waveguide optical isolator', *ePIXnet Winterschool 2007*, Switzerland, p.93 (2007).

14. W. Van Parys, D. Van Thourhout, R. Baets, M. Vanwolleghem, B. Thedrez, F. Lelarge, L. Lagae, and R. Wirix-Speetjens, 'Magneto-optic Contact for Application in an Amplifying Waveguide Optical Isolator', *2006 IEEE LEOS Annual Meeting*, Canada, p.679-680 (2006).

15. W. Van Parys, D. Van Thourhout, R. Baets, B. Dagens, J. Decobert, O. Le Gouezigou, D. Make, R. Vanheertum, and L. Lagae, 'TM-mode AlGaInAs/InP Amplifying Waveguide Optical Isolator with 12.7dB Isolation', *Integrated Photonics Research and Applications*, United States, p.ITuG3 (2006).

16. W. Van Parys, D. Van Thourhout, R. Baets, B. Dagens, J. Decobert, O. Le Gouezigou, D. Make, R. Vanheertum, and L. Lagae, '11.4dB Isolation on an Amplifying AlGaInAs/InP Optical Waveguide Isolator', *Optical Fiber Conference 2006*, United States, p.OFA2 (2006).

17. W. Van Parys, D. Van Thourhout, R. Baets, B. Dagens, J. Decobert, O. Le Gouezigou, D. Make, R. Vanheertum, and L. Lagae, 'Amplifying AlGaInAs/InP Waveguide Optical Isolator with 99dB/cm Non-reciprocal Propagation', *IEEE/LEOS Benelux Chapter, 2005*, Belgium, p.83-86 (2005).

18. M. Vanwolleghem, W. Van Parys, P. Gogol, R. Baets, and P. Beauvillain, 'Optimisation d'un isolateur magneto-optique integré pour diode laser à la longeur d'onde de 1.3μm, *Horizons de l'Optique 2005*, France, p.135-136 (2005).

19. M. Vanwolleghem, W. Van Parys, P. Gogol, R. Baets, and P. Beauvillain, 'Optimization of a monolithically integrated ferromagnetic-metal-clad InP-based optical waveguide isolator', *10ième colloque Louis Neel*, France, p.VI.35 (2005).

20. L. Lagae, W. Van Parys, B. Moeyersoon, D. Van Thourhout, R. Baets, R. Vanheertum, B. Dagens, J. Decobert, O. Le Gouezigou, and D. Make, 'Magneto-optical waveguide isolator with 104 dB/cm non-reciprocal propagation', *Moscow International Symposium on Magnetism*, Russia, p.114 (2005).

21. W. Van Parys, and R. Baets, 'InP-based optical waveguide isolator', *IEEE/LEOS Benelux Annual Workshop 2005*, Netherlands, p.4 (2005).

22. W. Van Parys, M. Vanwolleghem, D. Van Thourhout, R. Baets, J. Decobert, B. Dagens, B. Thedrez, L. Lagae, and R. Wirix-Speetjens, 'Demonstration of 81dB/cm isolation on an InP-based optical waveguide isolator', *ECIO 2005*, France, p.33-36 (2005).

23. W. Van Parys, D. Van Thourhout, and R. Baets, 'InP-based Monolithically Integratable Optical Waveguide Isolator', *5e UGent-FTW Doctoraatssymposium*, Belgium, (2004).

24. W. Van Parys, M. Vanwolleghem, D. Van Thourhout, R. Baets, J. Decobert, B. Dagens, B. Thedrez, R. Wirix-Speetjens, and L. Lagae, 'InP-Based Monolithically Integrated Optical Waveguide Isolator with 32 dB/cm Isolation', *2004 IEEE LEOS Annual Meeting*, Puerto Rico, p.386-387 (2004).

25. W. Van Parys, M. Vanwolleghem, D. Van Thourhout, R. Baets, R. Wirix-Speetjens, L. Lagae, B. Thedrez, F. Lelarge, and O. Gauthier-Lafaye, 'Experimental Verification of a Novel Integrated Optical Isolator Concept', *Bianisotropics 2004*, Belgium, p.224-227 (2004).

26. F. Lelarge, B. Dagens, C. Cuisin, O. Le Gouezigou, G. Patriarche, W. Van Parys, M. Vanwolleghem, R. Baets, and J.L. Gentner, 'GSMBE growth of GaInAsP/InP 1.3μm-TM-lasers for monolithic integration with optical waveguide isolator', *13th International Conference on Molecular Beam Epitaxy(IC-MBE),* p. ThA2.2, Edinburgh, Scotland, August 2004.

27. W. Van Parys, 'Demonstration of a Novel Integrated Isolator Concept', *IEEE/LEOS Benelux Chapter Workshop on Photonic Materials and Technology*, Netherlands, p.12 (2004).

28. M. Vanwolleghem, W. Van Parys, D. Van Thourhout, R. Baets, O. Gauthier-Lafaye, F. Lelarge, B. Thedrez, R. Wirix-Speetjens, and J. De Boeck, 'First Experimental Demonstration of a monolithically integrated InP-based waveguide isolator', *OFC 2004*, United States, p.TuE6 (2004).

29. M. Vanwolleghem, W. Van Parys, D. Van Thourhout, R. Baets, F. Lelarge, O. Gauthier-Lafaye, B. Thedrez, R. Wirix-Speetjens, and J. De Boeck, 'Experimental verification of a novel integrated isolator concept',*ECOC-IOOC, 6*, Italy, p.78-79 (2003).

30. M. Vanwolleghem, W. Van Parys, S. Verstuyft, R. Wirix-Speetjens, L. Lagae, J. De Boeck, and R. Baets, 'Ferromagnetic-metal-based InGaAs(P)/InP optical waveguide isolator: electrical and magneto-optical characterisation', *2002 Annual Symposium of the IEEE/LEOS Benelux Chapter*, Netherlands, p.282-285 (2002).

The first experimental success was also reported in the periodical newsletter of the IMEC research institute:

- W. Van Parys, and M. Vanwolleghem, 'Experimental demonstration of a novel type of optical isolator.' *IMEC Newsletter* vol. 39, p. 7, July 2004.

At the 2005 European Conference on Integrated Optics (ECIO) in Grenoble (6-8 April 2005), the paper by Wouter Van Parys et al. was attributed with the Best Paper 2nd Prize.

Bibliography

[1] D. Lenstra, B.H. Verbeek, and A.J. Den Boef "Coherence Collapse in Single-Mode Semiconductor Lasers Due to Optical Feedback." *J. Quant. Electron.,* 21(6), pp.674-679 (1985).

[2] H. Li, J. Ye, and J.G. McInerney, "Detailed Analysis of Coherence Collapse in Semiconductor Lasers." *J. Quant. Electron.,* 29(9), pp.2421-2432 (1993).

[3] B.R. Clarke, "The Effect of Reflections on the System Performance of Intensity Modulated Laser Diodes." *J. Lightwave Technol.,* 9(6), pp.741-749 (1991).

[4] R.V. Steele, "Review and forecast of the laser markets: Part II: Diode lasers." *Laser Focus World,* February 2004.

[5] R.V. Steele, "Laser Marketplace 2008: Diode lasers track long-term trend." *Laser Focus World,* February 2008.

[6] J. Livas, and J. Zhou "Amplifiers and Network Elements in the Metro Environment." *J. Lightwave Technol.,* 22(1), pp.290-293 (2004)

[7] S. Hardy "Optical market looks to build on 2007 momentum." *Lightwave Europe,* January 2008.

[8] A. Takemoto, H. Watanabe, Y. Nakajima, Y. Sakakibara, S. Kakimoto, J. Yamashita, T. Hatta, and Y. Miyake, "Distributed Feedback Laser Diode and Module for CATV Systems." *IEEE Journal of Selected Areas in Communications* 8, pp.1359-1364 (1990).

[9] "NanoOpto announces new optical isolator." *Fiber Optics Weekly Update,* March 25, 2005.

[10] M. Pearson, "FTTx technologies: planar lightwave circuits revolutionize photonics." *Laser Focus World,* June 2007.

[11] K. Sakai, H. Aruga, S.I. Takagi, M. Kawano, M. Negishi, Y. Kondoh, and S.I. Kaneko, "1.3-μm uncooled DFB laser-diode module with a coupled differential feed for 10-Gb/s ethernet applications." *J. Lightwave Technol.,* 22(2), pp.574-581 (2004).

[12] "Eblana Photonics announces first shipments of ultra-narrow linewidth, low noise laser diodes emitting at lambda = 1310 nm and 1550 nm." *Press release on http://www.eblanaphotonics.com,* September 2007.

[13] K. Sato, S. Kuwahara, Y. Miyamoto, and N. Shimizu, "40 Gbit/s direct modulation of distributed feedback laser for very-short-reach optical links," *Electron. Lett.,* 38(15), pp.816817 (2002).

[14] L. Eldada, "Integrated optics need magnets *www.EETimes.com,* September 2001.

[15] P.K. Tien "Integrated optics and new wave phenomena in optical waveguides." *Rev. Mod. Phys.* 49, pp.361-420 (1977).

[16] J. Hecht "Uncooled devices challenge designers." *Laser Focus World,* July 2003.

[17] "Ethernet Passive Optical Networks." *IEC Web ProForums,* http://www.iec.org/online/tutorials/epon/index.html.

[18] K.W. Chang, and W.V. Sorin, "Polarization Independent Isolator Using Spatial Walkoff Polarizers." *IEEE Photon. Technol. Lett.,* 1(3), pp.68-70 (1989).

[19] S. Wang, M. Shah, and J.D. Crow, "Studies of use of gyrotropic and anisotropic materials for mode conversion on thin-film optical-waveguide applications." *J. Appl. Phys.* 43(4), pp.1861-1875 (1972).

[20] H. Dötsch, N. Bahlmann, O. Zhuromskyy, M. Hammer, L. Wilkens, R. Gerhardt, P. Hertel, and A.F. Popkov, "Applications of magneto-optical waveguides in integrated optics: review." *J. Opt. Soc. Am. B,* vol. 22(1), pp.240-253 (2005).

[21] A. K. Zvezdin, and V. A. Kotov, *chapter 9* in "Modern Magnetooptics and Magnetooptical Materials." *Institute of Physics Publishing, Philadelphia, USA* (1997).

[22] V.J. Fratello, and R. Wolfe, in "Magnetic Film Devices." ed. M.H. Francombe, and J.D. Adam, *Volume 4* of "Handbook of Thin Film Devices: Frontiers of Research, Technology and Applications." *New York: Academic Press,* pp.93-139 (2000).

[23] S.-Y. Sung, X. Qi, and B.J.H. Stadler, "Integrating Yttrium Iron Garnet onto Non-Garnet Substrates with Faster Deposition Rates and High Reliability," Appl. Phys. Lett. 87, pp.121111 (2005).

[24] S.K. Mondal, and B.J.H. Stadler, "Novel Designs for Integrating YIG/Air Photonic Crystal Slab Polarizers With Waveguide Faraday Rotators," *IEEE Photon. Techn. Lett.*, 17(1), pp.127-129 (2005).

[25] B.M. Holmes, and D.C. Huchings, "Demonstration of quasi-phase-matched nonreciprocal polarization rotation in III-V semiconductor waveguides incorporating magneto-optic upper claddings." *Appl. Phys. Lett.*, 88, p061116 (2006).

[26] H. Yokoi, T. Mizumoto, K. Maru, and Y. Naito, "Direct bonding between InP and rare-earth iron-garnet grown on $Gd_3Ga_5O_{12}$ substrate by liquid-phase epitaxy." *Electron. Lett.*, vol. 31(18), pp.1612-1613 (1995).

[27] T. Izuhara, J. Fujita, M. Levy, and R.M. Osgood, "Integration of Magnetooptical Waveguides Onto a III-V Semiconductor Surface" *IEEE Photon. Technol. Lett.*, 14(2), pp.167-169 (2002).

[28] H. Yokoi, T. Mizumoto, and Y. Shoji, "Optical nonreciprocal devices with a silicon guiding layer fabricated by wafer bonding." *Appl. Opt.*, vol. 42(33), pp.6605-6612 (2003).

[29] L. Richard, T. Izuhara, M-C Tsai, R. Osgood, and H. Dotsch, "Magneto-optical nonreciprocal phase shift in garnet/silicon-on-insulator waveguides" *Optics Letters*, 29(9), pp.941-943 (2004).

[30] A. K. Zvezdin, and V. A. Kotov, *chapter 14* in "Modern Magnetooptics and Magnetooptical Materials." *Institute of Physics Publishing, Philadelphia, USA* (1997).

[31] T. Amemiya, H. Shimizu, Y. Nalano, P.N. Hai, M. Yokoyama, and M. Tanaka, "Semiconductor waveguide optical isolator based on nonreciprocal loss induced by ferromagnetic MnAs." *Appl. Phys. Lett.*, 89, pp.021104 (2006).

[32] T. Amemiya, Y. Ogawa, H. Shimizu, H. Munekata, and Y. Nakano, "Semiconductor Waveguide Optical Isolator Incorportating Ferromagnetic Epitaxial MnSb for High Temperature Operation." *App. Phys. Express*, 1, pp.022002 (2008).

[33] T. Hayashi, M. Tanaka, K. Seta, T. Nishinaga, and K. Ando, "III-V based magnetic(GaMnAs)/nonmagnetic(AlAs) semiconductor superlattices." *Appl. Phys. Lett.*, 71(13), pp.1825-1827 (1997).

[34] H. Akinaga, S. Miyanishi, K. Tanaka, W. Van Roy, and K. Onodera, "Magneto-optical properties and the potential application of GaAs with magnetic MnAs nanoclusters." *Appl. Phys. Lett.*, 76(1), pp.97-99 (2000).

[35] H. Shimizu, and M. Tanaka, "Magneto-optical properties of semiconductor-based superlattices having GaAs with MnAs nanoclusters." *J. Appl. Phys.*, 89(11), pp.7281-7283 (2001).

[36] K. Baba, F. Takase, and M. Miyagi, "Ferromagnetic particle composite films for glass and semiconductor substrates." *Opt. Commun.*, 139, pp.35-38 (1997).

[37] J.L. Menendez, B.Bescos, and G.Armelles, "Optical and magneto-optical properties of Fe nanoparticles." *Phys. Rev. B*, 65, pp.205413 (2002).

[38] M. Abe, and T. Suwa, "Surface plasma resonance and magneto-optical enhancement in composites containing multicore-shell structured nanoparticles." *Phys. Rev. B*, 70, pp.235103 (2004).

[39] V. Zayets, M.C. Debnath, and K. Ando, "Optical isolation in $Cd_{1-x}Mn_xTe$ magneto-optical waveguide grown on GaAs substrate." *J. Opt. Soc. Am. B*, 22(1), pp.281-285 (2005).

[40] J.F. Dillon, J.K. Furdyna, U. Debska, and A. Mycielski, "Faraday rotation in $Hg_{1-x}Mn_xTe$ at 1.3 and 1.55μm." *J. Appl. Phys.*, 67, pp.4917-4919 (1990).

[41] P. Gangopadhyay, S. Foerier, G. Koeckelberghs, M. Vangheluwe, A. Persoons, and T. Verbiest, "Efficient Faraday rotation in conjugated polymers." *Proc. of SPIE* 6331, pp.63310Z (2006). in "Linear and Nonlinear Optics of Organic Materials VI." *edited by Robert A. Norwood.*

[42] J. Warner, "Nonreciprocal Magnetooptic Waveguides." *IEEE Trans. Microwave Theory Tech.*, MTT-23(1), pp.70-78 (1975).

[43] S. Yamamoto, Y. Okamura, and T. Makimoto, "Analysis and design of semileaky-type thin-film optical waveguide isolator." *IEEE J. Quantum Electron.*, QE-12(12), pp.764-770 (1976).

[44] T. Mizumoto, H. Yokoi, and M. Shimizu, "Demonstration of semi-leaky isolator fabricated by wafer bonding of magnetic garnet and lithium niobate." *OECC/IOOC Conf. Proc.*, WH4, pp.339-340 (2001).

[45] T. Mizumoto, and H. Saito, "Semi-leaky waveguide optical isolator." *2007 Optical Fiber Communication Conference (OFC2007), Anaheim, California*, pp.OThU4 (2007).

[46] K. Ando, T. Okoshi, and N. Koshizuka, "Waveguide magneto-optic isolator fabricated by laser annealing." *Appl. Phys. Lett.,* 53(1), pp.4-6 (1988).

[47] A. K. Zvezdin, and V. A. Kotov, *chapter 3* in "Modern Magnetooptics and Magnetooptical Materials." *Institute of Physics Publishing, Philadelphia, USA* (1997).

[48] J.J.G.M. van der Tol, F. Hakimzadeh, J.W. Pedersen, D. Li, and H. van Brug, "A New Short and Low-Loss Passive Polarization Converter on InP." *IEEE Photon. Technol. Lett.,* 7(1), pp.32-34 (1995).

[49] J.Z. Huang, R. Scarmozzino, G. Nagy, M.J. Steel, and R.M. Osgood, Jr., "Realization of a Compact and Single-Mode Optical Passive Polarization Converter." *IEEE Photon. Technol. Lett.,* 12(3), pp.317-319 (2000).

[50] B.M. Holmes, and D.C. Hutchings, "Realization of Novel Low-Loss Monolithically Integrated Passive Waveguide Mode Converters." *IEEE Photon. Technol. Lett.,* 18(1), pp.43-45 (2006).

[51] R. Wolfe, J.F. Dillon,Jr., R.A. Lieberman, and V.J. Fratello, "Broadband magneto-optic waveguide isolator." *Appl. Phys. Lett.,* 57(10), pp. 960-962 (1990).

[52] D. Marcuse, "Influence of Position of Magnetooptic Layer on Differential Phase Shift of Slab Waveguide." *IEEE J. Quant. Electron.,* QE-23(8), pp.1268-1272 (1987).

[53] F. Auracher, and H.H. Witte, "A new design for an integrated optical isolator." *Opt. Commun.,* 13, pp.435-438 (1975).

[54] A.F. Popkov, M. Fehndrich, M. Lohmeyer, and H. Dötsch, "Nonreciprocal TE-mode phase shift by domain walls in magnetooptic rib waveguides." *Appl. Phys. Lett.,* 72(20), pp.2508-2510 (1998).

[55] N. Bahlmann, M. Lohmeyer, H. Dötsch, and P. Hertel, "Integrated magneto-optic Mach-Zehnder isolator for TE modes." *Electron. Lett.,* 34, pp.2122-2123 (1998).

[56] M. Shamonin, and P. Hertel, "Analysis of nonreciprocal mode propagation in magneto-optic rib-waveguide structures with the spectral-index method." *Appl. Opt.,* 33(27), pp.6415-6421 (1994).

[57] J. Fujita, M. Levy, R.U. Ahmad, R.M. Osgood, Jr., M. Randles, C. Gutierrez, and R. Villareal, "Observation of optical isolation based on nonreciprocal phase shift in a Mach-Zehnder interferometer." *Appl. Phys. Lett.,* 75(7), pp.998-1000 (1999).

[58] J. Fujita, M. Levy, R. M. Osgood, Jr., L. Wilkens, and H. Dötsch "Waveguide optical isolator based on MachZehnder interferometer." *Appl. Phys. Lett.,* 76(16), pp.2158-2160 (2000).

[59] O. Zhuromskyy, M. Lohmeyer, N. Bahlmann, H. Dötsch, P. Hertel, and A.F. Popkov, "Analysis of Polarization Independent Mach-Zehnder-Type Integrated Optical Isolator." *J. Lightwave Technol.* 17(7), pp.1200-1205 (1999).

[60] J. Fujita, M. Levy, R.M. Osgood, Jr., L. Wilkens, and H. Dötsch, "Polarization-Independent Waveguide Optical Isolator Based on Nonreciprocal Phase Shift." *IEEE Photon. Technol. Lett.,* 12(11), pp.1510-1512 (2000).

[61] O. Zhuromskyy, M. Lohmeyer, N. Bahlmann, P. Hertel, H. Dötsch, and A.F. Popkov, "Analysis of nonreciprocal light propagation in multimode imaging devices." *Opt. and Quant. Electron.,* 32, pp.885-897 (2000).

[62] M. Lohmeyer, L. Wilkens, O. Zhuromskyy, H. Dötsch, and P. Hertel, "Integrated magnetooptic cross strip isolator." *Opt. Commun.,* 189, pp.251-259 (2001).

[63] N. Kono, K. Kakihara, K. Saitoh, and M. Koshiba, "Nonreciprocal microresonators for the miniaturization of optical waveguide isolators." *Opt. Express,* 15(12), pp.7737-7751 (2007).

[64] H. Yokoi, and T. Mizumoto, "Proposed configuration of integrated optical isolator employing wafer-direct bonding technique." *Electron. Lett.,* 33, pp.1787-1788 (1997).

[65] H. Yokoi, T. Mizumoto, N. Shinjo, N. Futakuchi N, and Y. Nakano, 'Demonstration of an optical isolator with a semiconductor guiding layer that was obtained by use of a nonreciprocal phase shift." *Appl. Opt.,* 39(33), pp. 6158-6164 (2000).

[66] Y. Shoji, H. Yokoi, T. Mizumoto, "Enhancement of Magneto-optic Effect in Optical Isolator with GaInAsP guiding layer by Selective Oxidation of AlInAs." *Jpn. J. Appl. Phys.,* 43(2), pp.590-593 (2004).

[67] K. Sakurai, H. Yokoi, T. Mizumoto, D. Miyashita, and Y. Nakano, "Fabrication of Semiconductor Laser for Integration with Optical Isolator." *Jpn. J. Appl. Phys.,* 43(4A), pp.1388-1392 (2004).

[68] T.Mizumoto, K.Sakurai, Y.Shoji, and H.Saito, "(Invited) Waveguide optical isolator integratable to photonic devices." *in Proc. Integrated Photonics Research and Applications Topical Meeting (IPRA-2006), Uncasville, Connecticut*, pp.ITuG1 (2006).

[69] Y. Shoji, and T. Mizumoto, "Ultra-wideband design of waveguide magneto-optical isolator operating in 1.31μm and 1.55μm." *Opt. Express*, 15(2), pp.639-645 (2007).

[70] H. Yokoi, T. Mizumoto, S. Kuroda, T. Ohtsuka, and Y. Nakano, "Elimintation of a back-reflected TE mode in a TM-mode optical isolator with a Mach-Zehnder interferometer." *Appl. Opt.*, 41(33), pp.7045-7051

[71] H. Yokoi, Y. Shoji, E. Shin, and T. Mizumoto, "Interferometric optical isolator employing a nonreciprocal phase shift operated in a unidirectional magnetic field." *Appl. Opt.*, 43(24), pp.4745-4752 (2004).

[72] M. Inoue, K. Arai, T. Fujii, M. Abe, "One-dimensional magnetophotonic crystals." *J. Appl. Phys.*, 85(8), pp. 5768-5770 (1999).

[73] M.J. Steel, M. Levy, and R.M. Osgood, "Photonic Bandgaps with Defects and the Enhancement of Faraday Rotation." *J. Lightwave Technol.*, 18(9), pp. 1297-1308 (2000).

[74] A. Figotin, and I. Vitebsky, "Nonreciprocal photonic crystals." *Phys. Review E*, 63, pp. 066609 (2001).

[75] N. Kono, and M. Koshiba, "Three-dimensional finite element analysis of nonreciprocal phase shifts in magneto-photonic crystal waveguides." *Opt. Express*, 13(23), pp. 9155-9166 (2005).

[76] H. Takeda, and S. John, "Compact Optical One-way Waveguide Isolators for Photonic-band-gap Microchips." *Phys. Review A*, 78, pp. 023804 (2008).

[77] M. Vanwolleghem, P. Gogol, P. Beauvillain, and J.M. Lourtioz, "First Theoretical Evidence of Optical Non-Reciprocity and Band Gap Tunability in Two-Dimensional Magneto-Photonic Crystals." *Proc. CLEO/QELS Conference 2006*, 1, pp. QTuC2 (2006).

[78] M. Takenaka, and Y. Nakano, "Proposal of a Novel Monolithically-Integratable Optical Waveguide Isolator." *in Proc. 11th International Conference on Indium Phosphide and Related Materials, Davos, Switzerland*, pp. 298-292 (1999).

[79] W. Zaets, and K. Ando, "Optical waveguide isolator based on nonreciprocal loss/gain of amplifier covered by ferromagnetic layer." *IEEE Photon. Technol. Lett.*, 11(8), pp.1012-1014 (1999).

[80] J.M. Hammer, J.H. Abeles, and D.J. Channin, "Polycrystalline-Metal-Ferromagnetic Optical Waveguide Isolator (POWI) for Monolithic-Integration with Diode-Laser Diodes." *IEEE Photon. Technol. Lett.*, 9(5), pp.631-633 (1997).

[81] M. Vanwolleghem, W. Van Parys, D. Van Thourhout, R. Baets, F. Lelarge, O. Gauthier-Lafaye, B. Thedrez, R. Wirix-Speetjens, and L. Lagae "Experimental demonstration of nonreciprocal amplified spontaneous emission in a CoFe clad semiconductor optical amplifier for use as an integrated optical isolator." *Appl. Phys. Lett.*, 85, pp. 3980-3982 (2004).

[82] H. Shimizu, and Y. Nakano, "Fabrication and Characterization of an InGaAsP/InP Active Waveguide Optical Isolator With 14.7 dB/mm TE Mode Nonreciprocal Attenuation." *J. Lightwave Technol.* 24, pp.38-43 (2006).

[83] H. Shimizu, and Y. Nakano, "Monolithic Integration of a Waveguide Optical Isolator With a Distributed Feedback Laser Diode in the 1.5μm Wavelength Range." *IEEE Photon. Technol. Lett.*, 19(24), pp.1973-1975 (2007).

[84] V. Zayets, and K. Ando, "Isolation effect in ferromagnetic-metal/semiconductor hybrid optical waveguide." *Appl. Phys. Lett.* 86, pp.261105261107 (2005).

2

Theoretical study of non-reciprocity

THE amplifying waveguide optical isolator – and practically all configurations of non-reciprocal devices – is based on the interaction of light with a magnetized medium. This is the field of magnetooptics. In this chapter the magnetooptic part of the isolator is extensively studied. We start with basic magnetooptic theory applied to bulk media and progressively build up to come to the transversely magnetized metal-clad optical isolator. The calculation of the isolator performance is treated, including a detailed discussion of a suitable figure-of-merit for the component. Furthermore, we design a metal-clad waveguide optical isolator from a purely theoretical point of view, that is, neglecting issues such as the choice of the ferromagnetic metal and the strength of the amplifying core material in terms of gain per unit of current injection. We end the chapter with a concise overview of the magnetic properties of ferromagnets and ferromagnetic metal stripes.

2.1 Magnetooptics and magnetooptic waveguides

In this section we discuss the basic principles of magnetooptics and its application in magnetooptic waveguides. We start by highlighting the effect of a magnetic field on the propagation of light in bulk matter – bulk magnetooptics. More in particular we focus on the reflection of light at the interface between a magnetic and a non-magnetic medium. Using geometric optics the equations of bulk magnetooptics can be used to get a feel of magnetooptic waveguides, as is done on a three-layer slab waveguide in section 2.1.2.1. The obtained results are then confirmed through rigorous analytical calculation of this metal-clad magnetooptic three-layer slab waveguide.

2.1.1 Bulk magnetooptics

2.1.1.1 Introduction

Magnetooptics deals with phenomena arising as a result of interaction between light and matter when the latter is subjected to a magnetic field. In the case of magnetically ordered matters, such as ferromagnets and ferrimagnets, magnetooptic effects may appear in the absence of an external magnetic field as well. The presence of a magnetic field changes the dispersion curves of the absorption coefficient and leads to the appearance or variation of optical anisotropy. All magnetooptic effects are the direct or indirect outcome of the splitting of system energy levels in a magnetic field, the so-called Zeeman effect. It is well known that right or left circularly polarized photons excite electronic transitions, which in accordance to the law of angular momentum conservation, change the appropriate projection of the quantum system's angular momentum by $\Delta m = \pm 1$. The Zeeman effect causes a difference in the frequencies of the 'right' and 'left' transitions, which in turn results in a difference in the polarizabilities of the system in the field of right and left circularly polarized waves. The implementation of this simple idea depends strongly on the character of the electron wave functions and the electron energy spectrum. In this work we will limit ourselves to a phenomenological treatment of magnetooptics instead of exploring the corresponding quantum-mechanical mechanisms, for which we refer to text books [1].
Basically, magnetooptic phenomena can be classified according to the relative orientation of the wave vector of the light $\boldsymbol{k}$ and the magnetic field $\boldsymbol{H}$; two basic geometries can be distinguished:

- Faraday geometry: light travels along the field direction: $\boldsymbol{k} \parallel \boldsymbol{H}$
- Voigt geometry: light travels perpendicularly to the field direction: $\boldsymbol{k} \perp \boldsymbol{H}$

The Zeeman effect manifests itself as dichroism, that is as a difference in the absorption coefficient for the two orthogonal polarizations of the medium the light is traveling through. In the case of Faraday geometry this is a difference in absorption between right and left circular polarization, so-called magnetic circular dichroism (MCD). In the Voigt geometry it is an absorption difference between the components parallel and perpendicular to the magnetic field, magnetic linear dichroism (MLD). From the Kramers-Kronig relations it follows that the splitting

of the dispersion curves of the absorption coefficient, i.e. MCD and MLD, is connected to a splitting of the dispersion curves of the refractive index of the propagating light, the so-called magnetic circular birefringence or Faraday effect and magnetic linear birefringence or Cotton-Mouton/Voigt effect respectively.
The Faraday effect implies that the refractive indices, n_+ and n_-, of left-hand and right-hand circularly polarized light in the case of an originally inactive material become different. In section 2.1.1.3 we highlight how this manifests itself as a non-reciprocal rotation of the polarization plane, combined with a non-reciprocal change of the ellipticity in the case of dissipative media.
Both the Faraday and the Voigt effect are transmission effects, i.e. if the light travels through a magnetooptic medium the dispersion curves are being altered. Apart from these effects optical anisotropy of a magnetized medium manifests itself also in the reflection of light at its surface. The effects associated with this reflection are called magnetooptic Kerr effects. A more detailed discussion of the reflection at a magnetooptic medium is given in section 2.1.1.4.

2.1.1.2 Constitutive relationships

A linear device is characterized by a linear relationship between the electric field strength $\boldsymbol{E}$ and the magnetic field strength $\boldsymbol{H}$ of a light wave and the corresponding dielectric displacement and magnetic induction, $\boldsymbol{D}$ and $\boldsymbol{B}$ respectively. This relationship may be written as $\boldsymbol{D} = \hat{\epsilon}\boldsymbol{E}$ and $\boldsymbol{B} = \hat{\mu}\boldsymbol{H}$. For optical frequencies the $\hat{\mu}$-tensor reduces to the vacuum permeability μ_0. The permittivity $\hat{\epsilon}$ is described by a dimensionless tensor. This tensor not only depends on the light wavelength λ, the temperature and mechanical stress, but also on quasi-static external electric or magnetic fields. As such, in a macroscopical theory of magnetooptic phenomena – which we restrict ourselves to here – the response of a light wave to a magnetized medium can entirely be described with the permittivity $\hat{\epsilon}$ tensor.
Non-reciprocal effects in linear materials are caused by contributions to $\hat{\epsilon}$ of odd order in the external, quasi-static magnetic field or in the magnetization $\boldsymbol{M}$ (for ferromagnetic or anti-ferromagnetic substances). The reciprocity theorem is based on the observation that under a time reversal transformation:

$$\begin{aligned} \mathbf{E}(t,x,y,z) &\rightarrow \mathbf{E}(-t,x,y,z) \\ \mathbf{H}(t,x,y,z) &\rightarrow -\mathbf{H}(-t,x,y,z) \end{aligned} \tag{2.1}$$

the Maxwell equations are left unchanged. In other words, out of a forward propagating solution, a backward propagating solution with the same properties can be generated by the above transformation. However, in the presence of a quasi-static external magnetic field or magnetization the time reversal symmetry of the Maxwell equations is broken and non-reciprocal effects arise. Consider for example a ferromagnetic substance magnetized along the y-axis and assume that the material is optically isotropic in the demagnetized state.[1] The presence of the

[1] This is valid for most practical ferromagnets for example because the sputtered film is polycrystalline.

magnetization reduces the isotropic spherical symmetry of the material to an uniaxial rotational symmetry around the y-axis and the permittivity tensor of this substance takes the following form:[2]

$$\hat{\epsilon} = \epsilon_0 \begin{pmatrix} \epsilon^1 & 0 & 0 \\ 0 & \epsilon^0 & 0 \\ 0 & 0 & \epsilon^1 \end{pmatrix} + \epsilon_0 \begin{pmatrix} 0 & 0 & -jg \\ 0 & 0 & 0 \\ jg & 0 & 0 \end{pmatrix} \tag{2.2}$$

with ϵ_0 the permittivity of the vacuum and ϵ^0 the relative permittivity of the medium in the demagnetized state ($\boldsymbol{M}$ = 0). For the optically isotropic ferromagnet the electrical induction can then be calculated as:

$$\mathbf{D} = \epsilon_0 \left[\epsilon^0 \mathbf{E} - j[\mathbf{g} \times \mathbf{E}] + b(\mathbf{E} - \mathbf{m}(\mathbf{m} \cdot \mathbf{E}))\right] \tag{2.3}$$

with $\boldsymbol{m}$ = $\boldsymbol{M}/M$, $b(M)$ = ϵ^1-ϵ^0 and $\boldsymbol{g}$ the gyration vector with $g(\boldsymbol{M})$ the gyro-electric constant. In the case of absorption ϵ^0, b and g are fully complex.
Using Onsager's principle [2] ($\epsilon_{ij}(\boldsymbol{M}) = \epsilon_{ji}(-\boldsymbol{M})$) one can prove that the gyro-electric constant $g(\boldsymbol{M})$ is a linear function of $\boldsymbol{M}$ and the diagonal magnetooptic element $b(\boldsymbol{M})$ is a quadratic function of $\boldsymbol{M}$. As such, the second term of equation (2.3) describes the gyrotropic effects, i.e. magnetic circular birefringence and magnetic circular dichroism, while the last term describes the magnetic linear birefringence and the magnetic linear dichroism. The magnetooptic Voigt parameter Q is defined as:

$$Q = Q' - jQ'' = \frac{g}{\epsilon^1} \tag{2.4}$$

In practice $|Q| \ll 1$. The gyrotropy of the magnetic permeability tensor is normally described in terms of the equivalent parameter Q_M. As the magnetic permeability at optical frequencies is practically zero ($\hat{\mu} \approx \mu_0$), Q_M can also be considered negligible throughout this work.

The form of the permittivity tensor $\hat{\epsilon}$ for a magnetooptic substance (equation 2.2) can also easily be derived from an extended version of the microscopic Drude free carrier theory [3]. Here we elaborate this theory for magnetooptic metals, but it can directly be extended to magnetooptic semiconductors. In the absence of a magnetic field, the equation of motion of electrons in an optically isotropic metal reads:

$$m\frac{\partial^2 \mathbf{x}}{\partial t^2} = -\frac{m}{\tau}\frac{\partial \mathbf{x}}{\partial t} - e\mathbf{E}, \tag{2.5}$$

with e and m the electron charge and the free-carrier optical mass and τ the average collision time of the electrons with metal ions, called the relaxation time. The first term of the right side of the equation of motion is the damping term, the second term the driving term with $\boldsymbol{E}$ the electric field that accelerates the electrons. The source of magnetooptic effects is associated with the influence of a magnetic

[2] This can straightforwardly be derived on the basis of symmetry considerations, Onsager's principle [2] ($\epsilon_{ij}(\boldsymbol{M}) = \epsilon_{ji}(-\boldsymbol{M})$) and the requirement of hermiticity ($\epsilon_{ij} = \epsilon_{ji}^*$) of the permittivity tensor for lossless materials.

field or a magnetic ordering on the orbital motion of electrons. A constant external magnetic field $\boldsymbol{H} = H(h_x,h_y,h_z)$ induces an extra (Lorentz) force on the carriers traveling at a speed $\boldsymbol{v} = \frac{\partial \boldsymbol{x}}{\partial t}$:

$$\mathbf{F}_{lorentz} = -e\mu_0 H(\mathbf{v} \times \mathbf{h}) \tag{2.6}$$

which causes a 'swirling' effect on the electron trajectories. In magnetically ordered metals – such as ferromagnetic metals – the spin-orbit interaction yields a substantially stronger 'swirling' effect. This can be understood qualitatively as follows. The effect of spin-orbital interaction can be described by using the effective axial field:

$$\mathbf{H}_{SL} = \frac{1}{2\mu_B}\lambda\langle S\rangle \tag{2.7}$$

with $\lambda\langle S\rangle$ the average value of the spin momentum, λ the spin-orbit interaction constant and μ_B the Bohr magneton. For example in d metals $H_{SL} \sim 10^6$ *Oe*. In what follows we use $\boldsymbol{H}$ as the symbol for the magnetic field vector, whatever the origin of this field (external of spin-orbital). The equation of motion hence becomes:

$$-\frac{m}{e}\left(\frac{\partial}{\partial t} + \frac{1}{\tau}\right)\mathbf{v} = \mathbf{E} + \mu_0 H(\mathbf{v} \times \mathbf{h}). \tag{2.8}$$

Introducing the electron current $\boldsymbol{j} = -eN\boldsymbol{v}$, with N the carrier density, and assuming a harmonic plane-wave solution for $\boldsymbol{v}$, we get:

$$-\frac{m}{e}\left(j\omega + \frac{1}{\tau}\right)\frac{\mathbf{j}}{-eN} = \mathbf{E} + \frac{\mu_0 H}{-eN}(\mathbf{j} \times \mathbf{h}), \tag{2.9}$$

which can be rewritten as:

$$\left[\frac{m}{e^2 N}\left(j\omega + \frac{1}{\tau}\right)\hat{I} + \frac{\mu_0 H}{eN}\begin{pmatrix} 0 & h_z & -h_y \\ -h_z & 0 & h_x \\ h_y & -h_x & 0 \end{pmatrix}\right]\mathbf{j} = \mathbf{E}, \tag{2.10}$$

with $\hat{I}$ the unity tensor. From this equation the magnetooptic contribution to the permittivity tensor $\hat{\epsilon}$ can be obtained using Ohm's law $\boldsymbol{j} = \hat{\sigma}\boldsymbol{E}$ and keeping in mind the expression relating the conductivity tensor $\hat{\sigma}$ to the permittivity tensor of a material:

$$\hat{\epsilon}(\omega) = \epsilon_0\left(\hat{I} + \hat{\chi}(\omega) - \frac{j}{\epsilon_0\omega}\hat{\sigma}(\omega)\right), \tag{2.11}$$

with $\hat{\chi}$ the susceptibility tensor of the medium associated with the inter-band transitions. The dispersion of the medium is explicitly written down. The permittivity tensor of the magnetized metal hence reads:

$$\hat{\epsilon}(\omega) = \epsilon_0\left(\hat{I} + \hat{\chi}(\omega) + \omega_p^2\left[\left(-\omega^2 + \frac{j\omega}{\tau}\right)\hat{I} - j\omega\omega_c\begin{pmatrix} 0 & h_z & -h_y \\ -h_z & 0 & h_x \\ h_y & -h_x & 0 \end{pmatrix}\right]^{-1}\right), \tag{2.12}$$

where the plasma frequency ω_p is defined as:

$$\omega_p \equiv \sqrt{\frac{Ne^2}{m\epsilon_0}}, \tag{2.13}$$

which depends on the free-carrier concentration N and the free-carrier mass m. The free-carrier cyclotron frequency ω_c

$$\omega_c \equiv \frac{-e\mu_0 H}{m}, \tag{2.14}$$

depends on the free-carrier mass m and is proportional to the magnitude of the magnetic field. In the demagnetized case ($H = 0$) equation 2.12 reduces to the classical Drude formula.
From expression 2.12 it can directly be seen that the presence of a magnetic field $\boldsymbol{H}$ results in a contribution to the permittivity tensor that is described by an antisymmetric tensor. In other words, the magnetic field causes symmetry breaking in the material response to a light wave. Now, consider the special case of an optically isotropic medium with a fixed magnetic field applied along the y-direction $\boldsymbol{H} = H(0,1,0)$. The corresponding permittivity tensor can be calculated as:

$$\hat{\epsilon}(\omega) = \epsilon_0 \begin{pmatrix} 1+\chi+\frac{\omega_p^2\left(-\omega+\frac{j}{\tau}\right)}{\omega\left[\left(-\omega+\frac{j}{\tau}\right)^2-\omega_c^2\right]} & 0 & \frac{j\omega_c\omega_p^2}{\omega\left[\left(-\omega+\frac{j}{\tau}\right)^2-\omega_c^2\right]} \\ 0 & 1+\chi+\frac{\omega_p^2}{\omega\left(-\omega+\frac{j}{\tau}\right)} & 0 \\ -\frac{j\omega_c\omega_p^2}{\omega\left[\left(-\omega+\frac{j}{\tau}\right)^2-\omega_c^2\right]} & 0 & 1+\chi+\frac{\omega_p^2\left(-\omega+\frac{j}{\tau}\right)}{\omega\left[\left(-\omega+\frac{j}{\tau}\right)^2-\omega_c^2\right]} \end{pmatrix}. \tag{2.15}$$

This can directly be rewritten in the form of expression 2.2; the diagonal element ϵ_{yy} remains unchanged with respect to the demagnetized state, the diagonal elements ϵ_{zz} and ϵ_{zz} are modified by a contribution quadratic in the magnetic field H, and the antisymmetric tensor elements ϵ_{xz} and ϵ_{zx} occur. These depend quasi-linearly on the magnetic field H.
It should be remarked that this model based on the Drude free-carrier theory is only a simplified phenomenological model used here to illustrate the nature of magnetooptic effect. A correct description of the magnetooptic properties of materials requires ab initio quantum-mechanical calculations.

2.1.1.3 Normal modes and Fresnel equations

The Maxwell equations directly lead to the following general wave equation:

$$-\nabla^2\mathbf{E} + \nabla(\nabla\cdot\mathbf{E}) = \frac{-1}{c^2\epsilon_0}\frac{\partial^2\mathbf{D}}{\partial t^2}. \tag{2.16}$$

In an anisotropic medium, such as a magnetized medium, the base orthogonal polarization states by which the propagation of an arbitrary polarized beam can be described are unique and have a different phase velocity. These base states are

called normal modes and they have a harmonic dependence on time and coordinates:

$$\mathbf{E} \sim exp[j(\omega t - \mathbf{k} \cdot \mathbf{r})] \tag{2.17}$$

For these normal modes the wave equation becomes:

$$n^2\mathbf{E} - \mathbf{n}(\mathbf{n} \cdot \mathbf{E}) = \frac{\hat{\epsilon}}{\epsilon_0}\mathbf{E} \tag{2.18}$$

where $\boldsymbol{n} = (c/\omega)\boldsymbol{k}$ is the refraction vector. This eigenvalue problem has a non-trivial solution if the determinant of the coefficients vanishes:

$$det\left[n^2\delta_{ik} - n_i n_k - \frac{\epsilon_{ik}(\omega)}{\epsilon_0}\right] = 0 \tag{2.19}$$

Equation 2.19 is called the Fresnel equation and it determines the refraction vector $\boldsymbol{n} = \boldsymbol{n}(\omega)$ of the normal modes. Substitution of a solution into the wave equation 2.18 gives the corresponding eigenvector $\boldsymbol{E}$ of the mode. In general the modes are elliptically polarized. In a gyrotropic medium – $g \neq 0$ – the refraction vector depends on the handedness of the elliptical mode. This left-right anisotropy – $n_+ \neq n_-$ – is called the gyrotropy of the medium.

Let us now consider the special case of the Faraday geometry, i.e. the gyration vector $\boldsymbol{g}$, hence the magnetization, is parallel to the propagation vector $\boldsymbol{k}$ or, equivalently, the refraction vector $\boldsymbol{n}$. Consider the magnetization and the propagation along the y-direction, i.e. $\boldsymbol{g} = (0,g,0)$ and $\boldsymbol{n} = (0,n,0)$. The corresponding solutions of equation 2.19 read:

$$n_\pm^2 = \epsilon^1(1 \pm Q), \tag{2.20}$$

where the signs $\pm$ correspond to the left-handed and right-handed elliptical polarization. The corresponding eigenvectors $\boldsymbol{E}$ of the normal modes are found to be:

$$\mathbf{E}_\pm = \frac{1}{\sqrt{2}}\begin{pmatrix} 1 \\ 0 \\ \pm j \end{pmatrix} exp(j\omega t - j\frac{\omega}{c}n_\pm y). \tag{2.21}$$

with the $1/\sqrt{2}$-factor introduced for normalization. This clearly shows that the non-reciprocity in the Faraday geometry manifests itself as a difference of the propagation velocity of the circularly polarized normal modes. As an illustration of how this influences transmitted light we consider a linearly polarized – along the x-axis – electromagnetic wave traveling along the y-direction of magnetization, entering the medium with an amplitude E_0 at $y = 0$. We assume a lossless medium with ϵ^1 and Q real. The wave excites the two normal modes $\boldsymbol{E}_\pm$ to a certain extent:

$$\mathbf{E} = c_+\mathbf{E}_+ + c_-\mathbf{E}_-, \tag{2.22}$$

where the constants can be found from the boundary conditions at $y = 0$: $E_x = E_0$, $E_y = 0$;

$$c_+ + c_- = \sqrt{2}E_0, \qquad j(c_+ - c_-) = 0, \tag{2.23}$$

which yields $c_+ = c_- = E_0/\sqrt{2}$. For $y > 0$ we get:

$$\begin{aligned} \mathbf{E}(y) &= \frac{1}{\sqrt{2}}E_0\mathbf{E}_+ + \frac{1}{\sqrt{2}}E_0\mathbf{E}_- \\ &= E_0 \begin{pmatrix} cos\left(\frac{\omega}{c}\Delta n y\right) \\ 0 \\ sin\left(\frac{\omega}{c}\Delta n y\right) \end{pmatrix} exp(j\omega t - j\frac{\omega}{c}n_0 y). \end{aligned} \tag{2.24}$$

with $n_0 = (n_+ + n_-)/2$ and $\Delta n = (n_+ - n_-)/2$. In the first order approximation in Q – which is valid in practical cases due to the small magnitude of Q – this becomes:

$$n_0 = \epsilon^1, \qquad \Delta n = \frac{1}{2}n_0 Q. \tag{2.25}$$

With propagation through the (transparent) magnetized medium the electromagnetic wave remains linearly polarized and the magnetooptic effect causes a rotation of the plane of polarization. This phenomenon is the Faraday rotation. It is well known that the rotation angle θ is described by:

$$tan(2\theta) = \frac{2Re[\chi]}{1 - |\chi|^2}, \tag{2.26}$$

with χ the polarization factor:

$$\chi = \frac{E_z}{E_x}. \tag{2.27}$$

As such the rotation angle reads:

$$\theta = \frac{\omega}{c}\Delta n y \approx \frac{\omega n_0}{2c}Qy \equiv \Phi_F y \tag{2.28}$$

with $\Phi_F = \pi n_0 Q/\lambda$ the specific Faraday rotation, i.e. the rotation of the polarization plane per unit length of the sample. Equation 2.28 shows that inversion of the propagation direction of the light *($y \rightarrow$ -y)* inverses the rotation direction (when looking into the beam). This shows the non-reciprocity of the magnetooptic Faraday effect.
In the case of an absorbing medium, both the permittivity ϵ^1 and the gyration g have an imaginary part. The refraction coefficients of the normal modes $n_\pm$ then read:

$$n_\pm = n_0 \pm \frac{1}{2}\frac{g'}{n_0} \; + \; j\left(k \pm \frac{1}{2}\frac{g''}{n_0}\right), \tag{2.29}$$

in the approximation that $|\epsilon'| >> max(|\epsilon''|,|g'|,|g''|)$. $n_0^2 = \epsilon^1$ and k is the extinction coefficient, which is equal to $k = \epsilon''/2n_0$ in this approximation. If a magnetized medium exhibits absorption, the imaginary part of the refraction coefficient

– which is proportional to the absorption coefficient – is therefore different for right and left-handed circularly polarized light. This effect is called magnetic circular dichroism (MCD). The direct effect on a linearly polarized electromagnetic wave traveling through the medium is the introduction of a certain degree of ellipticity, i.e. the polarization is changed from linear to elliptical. The ellipticity ψ is calculated as:

$$sin(2\psi) = \frac{2Im[\chi]}{1+|\chi|^2}, \tag{2.30}$$

with χ defined by equation 2.27.

Another special case is the Voigt geometry with the gyration vector ***g***, hence the magnetization, perpendicular to the propagation vector ***k*** or the refraction vector ***n***. Consider the magnetization along the *y*-direction, i.e. ***g*** = *(0,g,0)*. The eigenvalues can directly be calculated as:

$$\begin{aligned} n_s^2 &= \epsilon^0 \\ n_p^2 &= \epsilon^1(1-Q^2). \end{aligned} \tag{2.31}$$

In other words, in the linear approximation in Q the propagation constant in a bulk medium magnetized along the transverse direction remains unaffected by the magnetic field. The corresponding normal modes are the s-wave (TE)

$$H_x \neq 0, \qquad H_y = 0, \qquad H_z \neq 0, \tag{2.32}$$

and the p-wave (TM)

$$H_x = 0, \qquad H_y \neq 0, \qquad H_z = 0. \tag{2.33}$$

2.1.1.4 Reflection at a magnetized medium

The amplifying waveguide optical isolator basically is an optical waveguide with a magnetooptic metal cladding. From a geometric optics point of view the light travels with a zigzag trace through the waveguide core and the interaction with the metal is through reflection at the semiconductor-metal interface. It is therefore interesting to study how linearly polarized light, traveling through a non-magnetic material, interacts with the interface between a non-magnetic medium and a magnetic medium. The non-reciprocal effects that are associated with reflection at a magnetooptic medium are called magnetooptic Kerr effects. Different Kerr effects can be distinguished depending on the orientation of the magnetization with respect to the direction of the wave propagation and the normal to the surface. The various geometries are illustrated in figure 2.1. The polar effect (figure 2.1(a)) occurs if the magnetization ***M*** is oriented perpendicularly to the reflective surface and parallel to the plane of incidence. In the longitudinal Kerr configuration figure 2.1(b) ***M*** is parallel to both the medium interface and the plane of incidence. The general feature of the polar and the longitudinal effects is the presence of a non-zero projection of the wave vector ***k*** of the electromagnetic wave on the magnetization direction ***M***. The influence of the magnetization in both these

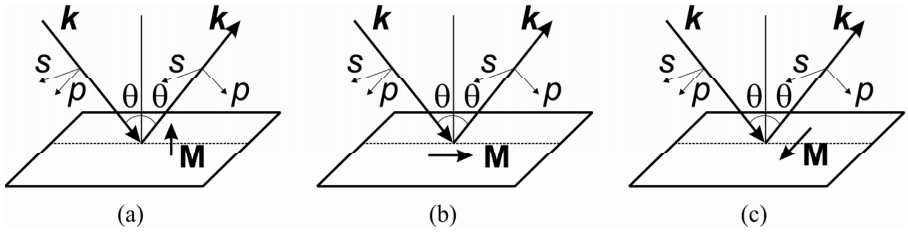

Figure 2.1: Magnetooptic Kerr effects taking place when light is reflected from the surface of a magnetized material: (a) polar, (b) longitudinal (meridional) and (c) transverse (equatorial) effects. The subscripts p *and* s *in* E_p *and* E_s *indicate* p *and s polarization of the light wave.*

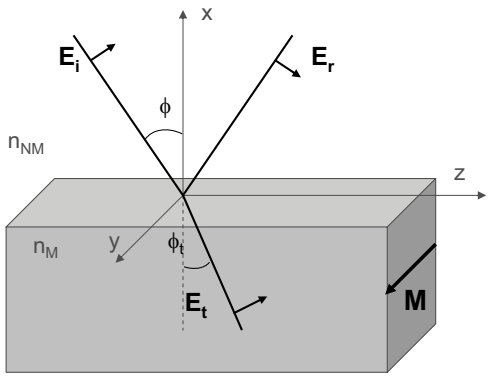

Figure 2.2: Schematic diagram of the transmission of light through an interface between a nonmagnetic medium and a transversely magnetized medium.

effects is a rotation of the plane of polarization and the appearance of ellipticity of the reflected light. Especially the rotation of the polarization plane due to the polar Kerr effect is important in the field of data storage, since it is the basis of the reading process of magnetooptic disks. As a direct consequence, for the class of materials used in magnetooptic recording – transition metal alloys – the most prominently tabulated quantity in literature is the Kerr rotation angle (at the blue side of the visible wavelength spectrum):

$$\Phi_K = -Im\left(\frac{Qn}{n^2-1}\right). \tag{2.34}$$

The third possible Kerr geometry is that in which the transverse or equatorial Kerr effect occurs, depicted in figure 2.1(c). It is observed when the magnetization vector is oriented perpendicularly to the plane of incidence of the light, and it manifests itself in the change of the intensity and phase of the linearly polarized light reflected by the magnetized medium. In the rest of this section we limit ourselves to this case of the transverse Kerr geometry, as this is the configuration relevant for the optical isolator. A more detailed picture is given in figure 2.2.

Consider first a TM-polarized, or p-polarized, plane wave incident on the interface between non-magnetic and magnetic medium. The electric field vectors of incident and reflected wave can be written in terms of the projection on the coordinate axes as:

$$\begin{aligned} \mathbf{E}_i &= E_i \begin{pmatrix} sin\phi \\ 0 \\ cos\phi \end{pmatrix} exp(j\omega t - j\frac{\omega}{c}\mathbf{n}_i \cdot \mathbf{r}) \\ \mathbf{E}_r &= E_r \begin{pmatrix} -sin\phi \\ 0 \\ cos\phi \end{pmatrix} exp(j\omega t - j\frac{\omega}{c}\mathbf{n}_r \cdot \mathbf{r}). \end{aligned} \tag{2.35}$$

where

$$\mathbf{n}_i = n_{NM}(-cos\phi, 0, sin\phi), \qquad \mathbf{n}_r = n_{NM}(cos\phi, 0, sin\phi). \tag{2.36}$$

Apart from the reflected wave there is obviously also a transmitted wave traveling through the magnetized medium. If a p-wave is incident on the interface this transmitted wave is the p-polarized normal mode of this medium (equation 2.33). The corresponding refraction vector reads:

$$\mathbf{n}_t = n_t(-cos\phi_t, 0, sin\phi_t). \tag{2.37}$$

with, according to equation 2.31:

$$n_t = n_M(1 - Q^2)^{\frac{1}{2}} \approx n_M \qquad (linear\ approximation\ in\ Q) \tag{2.38}$$

and $sin\phi_t$ is defined by Snell's law:

$$sin\phi_t = \frac{n_{NM}}{n_M} sin\phi, \qquad cos\phi_t = (1 - \frac{n_{NM}^2}{n_M^2} sin^2\phi)^{\frac{1}{2}}. \tag{2.39}$$

The electric field of the transmitted wave can be derived from the wave equation 2.18, where we limit ourselves to a linear approximation in Q as $|Q| \ll 1$:

$$\mathbf{E}_t = E_t \begin{pmatrix} sin\phi_t + jQ/cos\phi_t \\ 0 \\ cos\phi_t \end{pmatrix} exp(j\omega t - j\frac{\omega}{c}\mathbf{n}_t \cdot \mathbf{r}) \tag{2.40}$$

The wave described by the equation 2.40 is elliptically polarized in the plane of incidence; in addition to the ordinary transverse component present in the absence of magnetization, it contains an extra field component along the x-direction, shifted in phase and proportional to Q, hence to the magnetization. In what follows we will show how this extra field component gives rise to non-reciprocity of the reflection and transmission coefficients of the light at the interface between non-magnetic and magnetic medium. This phenomenon is called the transverse magnetooptic Kerr effect.
The magnetic fields of the three waves can easily be derived from the Maxwell curl equation

$$\nabla \times \mathbf{E} = -j\omega\mu_0\mathbf{H} \tag{2.41}$$

which in this case takes the form

$$\epsilon_0 c\ \mathbf{n} \times \mathbf{E} = \mathbf{H}. \tag{2.42}$$

From this and from equations 2.35 and 2.40 the magnetic fields can readily be found:

$$\mathbf{H}_{i,r,t} = (0, H_{i,r,t}, 0) exp(j\omega t - j\frac{\omega}{c}\mathbf{n}_{i,r,t} \cdot \mathbf{r}) \tag{2.43}$$

with

$$H_i = \epsilon_0 c n_{NM} E_i, \qquad H_r = -\epsilon_0 c n_{NM} E_r, \qquad H_t = \epsilon_0 c n_M (1 + jQ\ tan\phi_t) E_t.$$

Now from the Maxwell equations the boundary conditions for the electric and magnetic field components at the interface between the two media can be derived, stating that the tangential components of ***E*** and ***H***-field are continuous:

$$E_{iz} + E_{rz} = E_{tz}, \qquad H_{iy} + H_{ry} = H_{ty}. \tag{2.44}$$

Substitution of equations 2.35 to 2.43 into equation 2.44 gives:

$$\begin{aligned} (E_i + E_r) cos\phi &= E_t\ cos\phi_t \\ n_{NM}(E_i - E_r) &= n_M\ E_t(1 + jQ\ tan\phi_t). \end{aligned} \tag{2.45}$$

Now we can readily determine the formulas for the reflection r^p and transmission t^p coefficients at the interface between a non-magnetic and a magnetic medium.

$$\begin{aligned} r^p = \frac{E_r}{E_i} &= \frac{cos\phi_t - \eta\ cos\phi(1 + jQ\ tan\phi_t)}{cos\phi_t + \eta\ cos\phi(1 + jQ\ tan\phi_t)} \\ t^p = \frac{E_t}{E_i} &= \frac{2cos\phi}{cos\phi_t + \eta cos\phi(1 + jQ\ tan\phi_t)}, \end{aligned} \tag{2.46}$$

with $\eta = \frac{n_M}{n_{NM}}$. Using a linear approximation in Q the magnetic and non-magnetic contribution can be separated:

$$\begin{aligned} r^p &= r_0^p + j\delta r^p \\ t^p &= t_0^p + j\delta t^p, \end{aligned} \tag{2.47}$$

with

$$\begin{aligned} \delta r^p &= \frac{-2sin\phi cos\phi}{(\eta\ cos\phi + cos\phi_t)^2} Q \\ \delta t^p &= \frac{2\eta\ cos\phi^2 tan\phi_t}{(\eta\ cos\phi + cos\phi_t)^2} Q \end{aligned} \tag{2.48}$$

and r_0^p and t_0^p the conventional Fresnel coefficients

$$\begin{aligned} r_0^p &= \frac{cos\phi_t - \eta\, cos\phi}{cos\phi_t + \eta\, cos\phi} \\ t_0^p &= \frac{2cos\phi}{cos\phi_t + \eta\, cos\phi}. \end{aligned} \tag{2.49}$$

The magnetooptic effect manifests itself as a modification of the reflection and transmission coefficients at the interface between a non-magnetic and a magnetic medium. This change is linear in Q hence in the magnetization. This implies that switching the direction of the magnetization switches the sign of δr^p and δt^p. In the next paragraph we elaborate how the modification of the reflection and transmission coefficients gives rise to the non-reciprocal loss shift that is the basis of the amplifying waveguide optical isolator studied in this work.
So far we have considered a p-polarized wave incident on the interface. If the incident wave is s-polarized (TE-polarization), the electric field vectors of incident and reflected wave read:

$$\begin{aligned} \mathbf{E}_i &= E_i \begin{pmatrix} 0 \\ 1 \\ 0 \end{pmatrix} exp(j\omega t - j\frac{\omega}{c}\mathbf{n}_i \cdot \mathbf{r}) \\ \mathbf{E}_r &= E_r \begin{pmatrix} 0 \\ 1 \\ 0 \end{pmatrix} exp(j\omega t - j\frac{\omega}{c}\mathbf{n}_r \cdot \mathbf{r}). \end{aligned} \tag{2.50}$$

with $\boldsymbol{n}_i$ and $\boldsymbol{n}_r$ as defined in equation 2.36. The s-polarized wave gives rise to a wave propagating through the magnetized medium with refraction vector $\boldsymbol{n}_t$ = n_t(-cosϕ_t,0,sinϕ_t) with n_t defined by equation 2.31. The corresponding electric field can be found from the wave equation 2.18:

$$\mathbf{E}_t = E_t \begin{pmatrix} 0 \\ 1 \\ 0 \end{pmatrix} exp(j\omega t - j\frac{\omega}{c}\mathbf{n}_t \cdot \mathbf{r}). \tag{2.51}$$

The transmitted wave is purely s-polarized, hence the presence of the magnetization has, in a linear approximation in Q, no influence on the TE-polarized light. The corresponding reflection and transmission coefficients are therefore equal to the conventional Fresnel coefficients. The situation changes when gyromagnetic effects must be taken into account (Q_M) which cause a transverse Kerr effect for TE-polarized light interacting with the interface between a non-magnetic and a magnetic medium.

2.1.2 Three-layer slab with a magnetooptic cladding

In this section we discuss the special case of a three-layer slab with a laterally magnetized magnetooptic cladding – with the magnetization $\boldsymbol{M}$ along the y-direction – as depicted in figure 2.3. It consists of a non-magnetic substrate, a non-magnetic guiding core and a magnetic metal top layer. While this is a simplified version

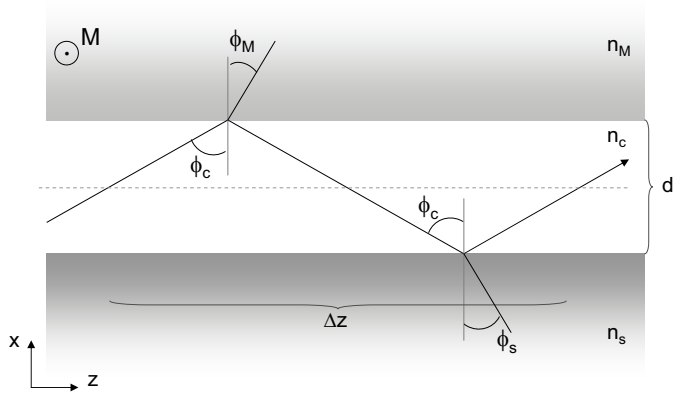

Figure 2.3: Schematic drawing of a slab waveguide, with indication of the symbols used in the theoretical elaboration.

of the real isolator structure, the basic principles remain the same, hence it is instructive to perform this exercise. The main advantage is that this structure can straightforwardly be calculated rigorously by solving the Maxwell equations. This is elaborated in paragraph 2.1.2.2. On the other hand, geometric optics can be used to gain physical insight in the operation of the metal-clad optical isolator; in the next paragraph it is shown how the magnetooptic reflection coefficient translates to a non-reciprocal change of the modal propagation constant. In the last paragraph 2.1.2.3 of this section we investigate how the non-reciprocal effect in a three-layer slab waveguide can be associated with the magnetooptic Faraday effect and magnetic circular dichroism.

2.1.2.1 Geometric optics approach

A waveguide mode of the structure of figure 2.3 can be represented by a superposition of two plane waves. One of the plane waves may be considered as the incident wave, whereas the other may be viewed as the reflected one. If the superposition represents a guided mode, confined in the waveguide core, the plane waves experience total internal reflection at both interfaces with substrate and (magnetized) superstrate. However, the condition of total internal reflection is only a necessary condition for a guided mode, but not all rays trapped by total internal reflection constitute a mode. A mode, by definition, must have a unique propagation constant and a well-defined field amplitude at each point in space and time. A mode $\boldsymbol{E}_m(x,z,t) = E_0(x)\ exp(j(\omega t - \beta z))$ can be represented by a zigzagging plane wave of the form:

$$\mathbf{E}_m = \mathbf{E}_0\ exp(j(\omega t - \beta z - hx)), \tag{2.52}$$

with $\boldsymbol{E}_0$ a constant vector, β the propagation constant and h the transverse wave number in the core:

$$h = \frac{\omega}{c} n_c \, cos\phi_c = \left[\left(\frac{n_c \omega}{c} \right)^2 - \beta^2 \right]^{\frac{1}{2}}. \tag{2.53}$$

Now, call Δz the longitudinal distance traveled by the plane wave in one zigzag during a time Δt. With ϕ_M and ϕ_s the – possibly complex – phase shifts encountered by the plane wave upon reflection at the upper and lower interface respectively, the total phase shift after one zigzag equals:

$$\omega \Delta t - \beta \Delta z - 2hd + \phi_M + \phi_s. \tag{2.54}$$

with *d* the thickness of the core layer (figure 2.3). Now, a guided mode ***E***$_m$*(x,z,t)* = $E_0(x)$ *exp(j($\omega t - \beta z$))* traveling along the z-direction will gain a phase shift of $\omega \Delta t$ - $\beta \Delta z$. Consequently, the condition for a zigzagging plane wave to be a guided mode is that the extra transverse phase shift is equal to an integral multiple of 2π, that is,

$$-2hd + \phi_M + \phi_s = -2m\pi \tag{2.55}$$

with m an integer. The minus sign preceding $2m\pi$ is chosen such that m corresponds to the TE$_m$ and TM$_m$ modes of the waveguide. In order to solve this equation – that is, finding the propagation constant β – the phase shifts ϕ_M and ϕ_s need to be expressed in terms of β. Let us first consider the case of a TM-polarized guided wave. The phase shifts $\phi_{M,s}$ are obviously related to the reflection coefficient at the interface between the two media through $r_{M,s}$ = *exp(j$\phi_{M,s}$)*. For the reciprocal interface between core and substrate the reflection coefficient r_s is given by the Fresnel formulas:

$$r_s = \frac{cos\phi_s - \eta \, cos\phi_c}{cos\phi_s + \eta \, cos\phi_c}. \tag{2.56}$$

For the non-reciprocal interface between core and magnetized superstrate the reflection coefficient r_M is expressed by formula 2.46:[3]

$$r_M = \frac{cos\phi_M - \eta \, cos\phi_c (1 - jQ \, tan\phi_M)}{cos\phi_M + \eta \, cos\phi_c (1 - jQ \, tan\phi_M)}. \tag{2.57}$$

Now, define the $\bar{p}$ and $\bar{q}$ parameters as:

$$\bar{p} \equiv j \frac{n_c^2}{n_M^2} \frac{\omega}{c} n_M \, cos(\phi_M) \qquad \bar{q} \equiv j \frac{n_c^2}{n_s^2} \frac{\omega}{c} n_s \, cos(\phi_s). \tag{2.58}$$

As such, $\bar{p}$ and $\bar{q}$ are proportional to the transverse components of the wave vector ***k*** or the refraction vector ***n***=*(c/ω)****k*** in the superstrate and the substrate respectively. In terms of the h, $\bar{p}$ and $\bar{q}$ parameters the reflection coefficients read:

[3]Notice the change of the sign of the non-reciprocal term with respect to formula 2.46, which is due to the different orientation of the coordinate axes in the current example. This is the mathematical analogy of the fact that the sign of the magnetooptic effect in the case a magnetic superstrate is opposite to that for a magnetic substrate, at a fixed magnetization direction. This originates from the difference in sign of the modal longitudinal field component in the superstrate and the substrate.

$$\begin{aligned} r_s &= \frac{j\bar{q}+h}{j\bar{q}-h} \\ r_M &= \frac{j\bar{p}+h(1+\frac{Q\beta}{\bar{p}}\frac{n_c^2}{n_M^2})}{j\bar{p}-h(1+\frac{Q\beta}{\bar{p}}\frac{n_c^2}{n_M^2})}. \end{aligned} \tag{2.59}$$

The corresponding phase shifts ϕ_M and ϕ_s are the (complex) arguments of r_M and r_s respectively and can be calculated as:

$$\begin{aligned} \phi_s &= 2tan^{-1}\left(\frac{\bar{q}}{h}\right) \\ \phi_M &= 2tan^{-1}\left(\frac{\bar{p}}{h(1+\frac{Q\beta}{\bar{p}}\frac{n_c^2}{n_M^2})}\right). \end{aligned} \tag{2.60}$$

In the expression for the phase shift ϕ_M at reflection at the magnetized medium an extra term linear in the propagation constant β appears. This implies that this phase shift depends on the propagation direction of the light; $\beta_{forward}$ = -$\beta_{backward}$. This is the direct proof of the presence of non-reciprocity.
With equations 2.60 expressing the phase shifts at the interfaces substrate-core and core-magnetic material in terms of the complex propagation constant of the traveling mode β, the guided mode condition (equation 2.55) can be solved in the complex propagation constant β of the non-reciprocal slab waveguide. With the aid of the mathematical identity:

$$tan^{-1}(x)+tan^{-1}(y)=tan^{-1}\left(\frac{x+y}{1-xy}\right) \tag{2.61}$$

for *-1 < x,y < 1*, the eigenvalue equation of the three-layer slab is obtained:

$$tan(hd)=\frac{h\left(\bar{q}+\frac{\bar{p}}{1+\frac{Q\beta}{\bar{p}}\frac{n_c^2}{n_M^2}}\right)}{h^2-\bar{q}\frac{\bar{p}}{1+\frac{Q\beta}{\bar{p}}\frac{n_c^2}{n_M^2}}}. \tag{2.62}$$

This shows that the non-reciprocal phase shift at the core-magnetic material interface translates to a change of the (TM-polarized) modal propagation constant, and this change is non-reciprocal. It needs to be remarked that for realistic values of the *Q*-parameter the magnetooptic term in the denominator of equation 2.60 is small compared to 1, hence the phase change due to the magnetooptic effect is quasi-symmetric around the non-magnetic value (*Q = 0*).
We illustrate the non-reciprocity by calculating a three-layer magnetooptic waveguide consisting of an InP substrate (n_{substr} = *3.2* at λ = 1300nm), an InGaAlAs core (n_{core} = *3.57* at λ = 1300nm) and a $Co_{50}Fe_{50}$ superstrate. The optical and magnetooptic parameters of $Co_{50}Fe_{50}$ have experimentally been determined, as elaborated in chapter 3: $n_{Co_{50}Fe_{50}}$ = *3.2-4.5j* and $g_{Co_{50}Fe_{50}}$ = *-1.7+1.7j*. In figure 2.4 the real and imaginary part of the effective indices of a forward (top) and

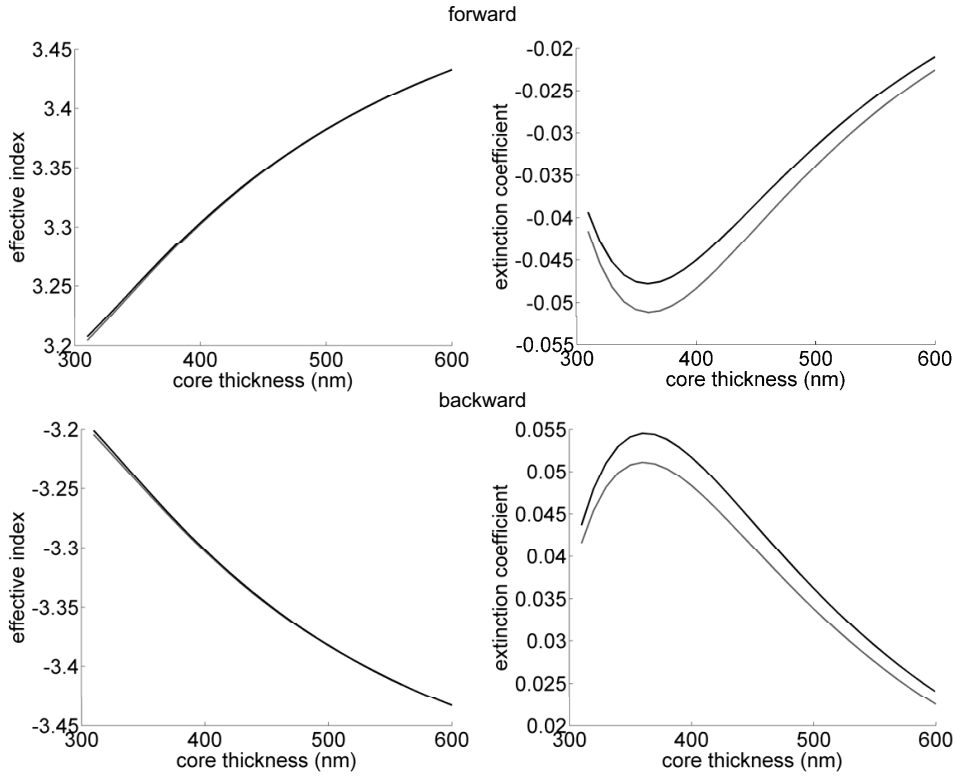

Figure 2.4: At propagation through a magnetized waveguide the complex effective index of a guided mode changes non-reciprocally. In black the TM modal propagation constant of a magnetized waveguide is plotted, while the grey curves represent the non-magnetic situation.

backward (bottom) traveling mode are plotted as a function of the thickness d of the waveguide core. The grey curve shows the non-magnetic situation, the black graph the case of a magnetized superstrate. For the chosen set of waveguide parameters a forward mode undergoes a (slight) increase of the real part of its effective index and a significant decrease of the extinction coefficient – hence of the modal absorption $\alpha = \frac{4\pi}{\lambda}|k|$ – while for a backward mode the (absolute value of the) effective index decreases and the modal absorption increases. In other words, the presence of a magnetooptic effect generates non-reciprocity of the propagation constant of the guided mode. The ratio between the real and the imaginary part of the non-reciprocal effect is heavily determined by the material choice of the layers comprising the waveguide.

For a TE-polarized guided wave propagating in a laterally magnetized waveguide, no magnetooptic terms linear in the propagation constant appear in the reflection coefficients, as calculated in section 2.1.1.4. From this it directly follows that there is no non-reciprocal change of the propagation constant.

2.1.2.2 Analytical calculation

The special case of a three-layer (magnetooptic) slab can straightforwardly be solved rigorously. Again we consider the configuration illustrated in figure 2.3. The Maxwell curl equations in each layer read:

$$\begin{aligned} \nabla \times \mathbf{E} &= -j\omega\mu_0\mathbf{H}, \\ \nabla \times \mathbf{H} &= j\omega\hat{\epsilon}_i\mathbf{E}. \end{aligned} \tag{2.63}$$

with $\hat{\epsilon}_i$ the permittivity tensor of the corresponding medium. All fields f are of the form:

$$f(x,y,z,t) = F(x,y)exp(j\omega t - j\beta z), \tag{2.64}$$

with β the – possibly complex – propagation constant. In the case of a slab waveguide the electromagnetic fields are invariant in the y-direction hence the field expressions are independent of the y-coordinate. It is well known that a slab waveguide with a diagonal permittivity tensor carries either transverse electric (TE) or transverse magnetic (TM) modes. The non-vanishing fields for TE-polarization are then E_y, H_x and H_z, whereas for TM-polarization E_x, H_y and E_z are non-zero. Contributions ϵ_{xy} or ϵ_{yz} to the permittivity tensor of a medium thus would couple the TE and TM modes. An example is a gyrotropic medium that is magnetized along the propagation direction of the light, an effect which is applied in the waveguide version of a Faraday rotator. If on the other hand, the only nonvanishing off-diagonal elements of the permittivity tensor are ϵ_{xz} and ϵ_{zx}, then the eigenmodes of the structure retain their TE or TM character. This is the case for the laterally magnetized medium considered here, for which the permittivity tensor reads:

$$\hat{\epsilon}_M = \epsilon_0 \begin{pmatrix} \epsilon^M & 0 & -jg \\ 0 & \epsilon^M & 0 \\ jg & 0 & \epsilon^M \end{pmatrix} \tag{2.65}$$

with $\epsilon^M = n_M^2$. We neglect here the second-order magnetooptic contributions to the diagonal elements of the permittivity tensor. The material response to the electric fields in the waveguide core and the substrate are described by:

$$\hat{\epsilon}_{c,s} = \epsilon_0\epsilon^{c,s} \begin{pmatrix} 1 & 0 & 0 \\ 0 & 1 & 0 \\ 0 & 0 & 1 \end{pmatrix}. \tag{2.66}$$

with $\epsilon^{c,s} = n_{c,s}^2$. Hence, the solutions of the three-layer slab isolator of figure 2.3 are pure TE and TM modes. The general solution for TM modes is:

$$\begin{aligned} \mathbf{E}(x,z,t) &= [E_x, 0, E_z]\ exp(j\omega t - j\beta z), \\ \mathbf{H}(x,z,t) &= [0, H_y, 0]\ exp(j\omega t - j\beta z). \end{aligned} \tag{2.67}$$

Substituting equations 2.67 into equations 2.63 results in a differential equation describing the (transverse) magnetic field H_y in the magnetooptic medium:

$$\frac{\partial^2 H_y}{\partial x^2} + \left[k_0^2 \frac{\epsilon^{M^2} - g^2}{\epsilon^{M^2}} - \beta^2 \right] H_y = 0, \tag{2.68}$$

which, in a linear approximation in the gyrotropy constant g, reduces to:

$$\frac{\partial^2 H_y}{\partial x^2} + \left[k_0^2 \epsilon^{M^2} - \beta^2 \right] H_y = 0. \tag{2.69}$$

As such, in a first order approximation the non-reciprocal term does not appear in the differential equation, but instead in a continuity requirement at interfaces between adjacent media, as will be proven later. This is the mathematical equivalence of the fact that for a bulk medium in the Voigt geometry ($\boldsymbol{k} \perp \boldsymbol{M}$), for which the normal modes are the TE and TM linearly polarized waves, the magnetooptic effects are quadratic in the gyrotropy, hence reciprocal of nature. For the waveguide core and substrate the differential equations expressing the magnetic field equivalently read:

$$\frac{\partial^2 H_y}{\partial x^2} + \left[k_0^2 \epsilon^{c,s^2} - \beta^2 \right] H_y = 0. \tag{2.70}$$

The solution of the differential equations 2.69 and 2.70 for the three-layer slab isolator – in a linear approximation in g – can be written as:

$$H_y(x) = \begin{cases} C\left[\frac{h}{\bar{q}} cos(hd) + sin(hd) \right] exp(-p[x-d]) & d \leq x \\ C\left[\frac{h}{\bar{q}} cos(hx) + sin(hx) \right] & 0 \leq x \leq d \\ \frac{h}{\bar{q}} C exp(qx) & x \leq 0 \end{cases} \tag{2.71}$$

with d the thickness of the waveguide core, C a normalization constant and h, p, $\bar{p}$, q and $\bar{q}$ defined as:

$$\begin{aligned} h &= \left[\left(\frac{n_c \omega}{c} \right)^2 - \beta^2 \right]^{\frac{1}{2}}, \\ p &= \left[\beta^2 - \left(\frac{n_M \omega}{c} \right)^2 \right]^{\frac{1}{2}}, \quad \bar{p} = \frac{n_c^2}{n_M^2} p, \\ q &= \left[\beta^2 - \left(\frac{n_s \omega}{c} \right)^2 \right]^{\frac{1}{2}}, \quad \bar{q} = \frac{n_c^2}{n_s^2} q. \end{aligned} \tag{2.72}$$

Obviously these parameters h, $\bar{p}$ and $\bar{q}$ are identical to ones defined in equations 2.53 and 2.58. The boundary conditions at the layer interfaces require that the tangential field components H_y and E_z are continuous. The expression for the longitudinal field E_z can directly be found from the Maxwell curl equations 2.63:

$$E_z(x) = \frac{-j}{\omega \epsilon_0 \epsilon^M} \left[\frac{\partial H_y}{\partial x} + \frac{g}{\epsilon^M} \beta H_y \right] \tag{2.73}$$

for the magnetooptic superstrate and:

$$E_z(x) = \frac{-j}{\omega\epsilon_0\epsilon^{c,s}}\frac{\partial H_y}{\partial x} \tag{2.74}$$

for the waveguide core and substrate. Expressions 2.71 are written such that the boundary condition of H_y continuous is automatically fulfilled at both interfaces and that E_z is continuous at the core-substrate interface. The eigenvalue equation that yields the solution of the three-layer slab hence follows from the requirement that E_z is continuous at the interface between core and (magnetooptic) superstrate:

$$tan(hd) = \frac{h\left(\bar{q} + \bar{p}\left[1 - \frac{Q\beta}{\bar{p}}\frac{n_c^2}{n_M^2}\right]\right)}{h^2 - \bar{q}\bar{p}\left[1 - \frac{Q\beta}{\bar{p}}\frac{n_c^2}{n_M^2}\right]}, \tag{2.75}$$

with $Q = g/\epsilon^M$. This eigenvalue equation involves a linear term in the propagation constant β. Therefore, the equation has a non-reciprocal solution in β.
Obviously, this equation must be identical to the one derived on the basis of geometric optics (formula 2.62). Using the Maclaurin series expansion:

$$\frac{1}{1-x} = 1 + x + x^2 + ... \tag{2.76}$$

for $-1 < x < 1$, equations 2.62 and 2.75 indeed become identical in a first order approximation in the magnetooptic parameter Q.

For TE polarized light the eigenvalue equation that can be obtained by solving the Maxwell equations is:

$$tan(hd) = \frac{h(p+q)}{h^2 - pq}, \tag{2.77}$$

again in a first order approximation of the non-reciprocal effect. As no linear terms in β appear in the eigenvalue equation, TE modes are reciprocal.

2.1.2.3 Faraday rotation and magnetic circular dichroism

An intriguing question is whether the non-reciprocal effect that occurs in the metal-clad waveguide optical isolator can be traced back to the Faraday effect or the Voigt effect, combined with magnetic circular dichroism (MCD) respectively magnetic linear dichroism (MLD) in dissipative media [4]. Remember that the Faraday effect manifests itself as a difference of the effective refractive indices n_+ and n_- of left-hand and right-hand circularly polarized light in a magnetized medium. MCD states that the absorption of these two circular polarizations is different. The Voigt effect and MLD are the analogies for linearly polarized light.

Again, consider the slab waveguide of figure 2.3; the Maxwell equations that describe the TM-mode field components are:

$$\begin{aligned} h_y(x,z,t) &= H_y(x)exp(j\omega t - j\beta z) \\ e_x(x,z,t) &= \frac{j}{\omega\epsilon_0\epsilon^i}\frac{\partial h_y}{\partial z} = \frac{\beta}{\omega\epsilon_0\epsilon^i}H_y(x)exp(j\omega t - j\beta z) \\ e_z(x,z,t) &= \frac{-j}{\omega\epsilon_0\epsilon^i}\frac{\partial h_y}{\partial x}, \end{aligned} \tag{2.78}$$

with ϵ^i the relative permittivity of the corresponding medium. It is well known that the solution for the magnetic field amplitude H_y in the top cladding layer of the slab reads:

$$H_y(x) = Cexp(-jk_x[x-a]), \tag{2.79}$$

with

$$k_x = \left(k_0^2 n^2 - \beta^2\right)^{\frac{1}{2}} \tag{2.80}$$

the transverse component of the propagation vector in the top cladding, n the refractive index of the top cladding material, C a normalization constant and a the coordinate of the interface with the underlying layer. Analogous considerations can be made for the bottom cladding. Furthermore, the Maxwell equations 2.78 yield the following relation between the longitudinal and the transverse electric field components:

$$e_z(x,z,t) = \frac{-j}{\beta}\frac{\partial e_x(x,z,t)}{\partial x} \tag{2.81}$$

or, with

$$e_x(x,z,t) = E_x(x)exp(j\omega t - j\beta z), \qquad e_z(x,z,t) = E_z(x)exp(j\omega t - j\beta z), \tag{2.82}$$

$$E_z(x) = \frac{-j}{\beta}\frac{\partial E_x(x)}{\partial x}. \tag{2.83}$$

Substitution of the expression for the magnetic field (2.78) leads to a very simple formula relating the longitudinal and the transverse electric field amplitudes in the top cladding of a slab waveguide:

$$E_z(x) = \frac{k_x}{\beta}E_x(x). \tag{2.84}$$

This shows that in the top cladding layer (and in the bottom layer) of a TM-mode slab waveguide the ratio between longitudinal and transverse electric field is constant. This ratio is exactly the polarization factor χ as defined in equation 2.27:[4]

$$\chi \equiv \frac{E_z}{E_x} = \frac{k_x}{\beta}, \tag{2.87}$$

which can directly be rewritten as:

$$\chi = \pm\sqrt{\frac{n_M^2}{n_{eff}^2} - 1}. \tag{2.88}$$

with n_M the refractive index of the cladding material and n_{eff} the effective index of the guided mode and the plus and minus sign for respectively forward and backward propagating light.

Assume for a moment that the three-layer slab waveguide consists only of non-dissipative media. For this structure the effective index of a guided mode is obviously purely real and obeys the relation:

$$\epsilon_{core} > \epsilon_{eff} > max(\epsilon_{cladding}) \tag{2.89}$$

with $\epsilon_{eff} = n_{eff}^2$. As such, the polarization factor for a TM-polarized mode χ is purely imaginary[5] with a magnitude between 0 and 1. In other words, the TM-guided mode in the magnetooptic cladding is elliptically polarized in the *xz*-plane, with a different handedness for modes propagating in opposite directions ($n_{eff} \rightarrow$ -n_{eff}). Now, because an elliptically polarized light wave can be decomposed into a left and right circularly polarized component, the amplitude of the electric field vector in the magnetooptic top cladding can be expressed as:

$$\begin{aligned} \mathbf{E}_0(x) &= E_x(x) \begin{pmatrix} 1 \\ 0 \\ \pm j|\chi| \end{pmatrix} \\ &= c_1 \frac{1}{\sqrt{2}} \begin{pmatrix} 1 \\ 0 \\ j \end{pmatrix} + c_2 \frac{1}{\sqrt{2}} \begin{pmatrix} 1 \\ 0 \\ -j \end{pmatrix}, \end{aligned} \tag{2.90}$$

[4]The polarization factor χ completely describes the polarization state. Indeed, the orientation of the major axis of the polarization ellipse θ and the ellipticity angle ψ – the angle between the major axis of the ellipse and diagonal that circumscribes the ellipse – are expressed as:

$$tan2\theta = \frac{2Re[\chi]}{1 - |\chi|^2}, \tag{2.85}$$

$$sin2\psi = \frac{2Im[\chi]}{1 + |\chi|^2}. \tag{2.86}$$

Ellipticity can also be defined via the coefficient *e* which is the ratio of the minor to the major axis of the polarization ellipse ($e = tan\psi$). A wave is called elliptically polarized if the ellipticity is different from zero. A special case is that of the circularly polarized wave with $|e| = 1$.

[5]This is the equivalent of the fact that the transverse E_x and the longitudinal E_z field amplitudes are in perfect quadrature.

with the plus and the minus sign corresponding respectively to a forward and backward propagating mode. Due to the magnetooptic Faraday effect the effective refractive index of the left- and right-circularly polarized component is different. The *c*-coefficients can be calculated as:

$$c_1 = \frac{E_x(x)}{\sqrt{2}}(1 \pm |\chi|) \qquad c_2 = \frac{E_x(x)}{\sqrt{2}}(1 \mp |\chi|). \tag{2.91}$$

As such, if the polarization factor χ is different from zero, meaning that the polarization of the TM-mode in the top cladding is not linear in the *xz*-plane, the Faraday effect results in a net difference of the effective refractive index of forward and backward propagating light. This net effect is maximized if the light wave is circularly polarized, i.e. $|\chi| = 1$.
In view of this, one expects the magnitude of the polarization factor to appear in the guided mode condition of the magnetooptic waveguide. Indeed, with $\chi = \frac{k_x}{\beta} \equiv \frac{jp}{\beta}$ the TM-mode eigenvalue equation 2.75 for a transparent waveguide can be rewritten as:

$$tan(hd) = \frac{h\left(\bar{q} + \bar{p}\left[1 - \frac{Q}{|\chi|}\right]\right)}{h^2 - \bar{q}\bar{p}\left[1 - \frac{Q}{|\chi|}\right]}. \tag{2.92}$$

This discussion can directly be extended towards slab waveguide structures with an absorbing magnetooptic top cladding. In this case the components of the propagation vector β and k_x have a real and an imaginary part, hence, according to equation 2.87, the polarization factor can be complex. In other words, the transverse and longitudinal electric field components are not necessarily in quadrature. Expression 2.88 obviously still holds and shows that the magnitude of the polarization factor χ can in principle have any value between 0 and infinity. Again the electric field vector of the light wave in the top cladding layer can be decomposed into a left and a right circularly polarized component:

$$\begin{aligned} \mathbf{E}_0(x) &= E_x(x) \begin{pmatrix} 1 \\ 0 \\ \chi \end{pmatrix} \\ &= c_1 \frac{1}{\sqrt{2}} \begin{pmatrix} 1 \\ 0 \\ j \end{pmatrix} + c_2 \frac{1}{\sqrt{2}} \begin{pmatrix} 1 \\ 0 \\ -j \end{pmatrix}, \end{aligned} \tag{2.93}$$

with the *c*-coefficients given by:

$$c_1 = \frac{E_x(x)}{\sqrt{2}}(1 - j\chi) \qquad c_2 = \frac{E_x(x)}{\sqrt{2}}(1 + j\chi). \tag{2.94}$$

In dissipative media the magnetooptic Faraday effect is accompanied by MCD which causes a difference of the absorption of right and left-handed circular polarization. Expression 2.94 shows that again the net magnetooptic effect due to

Faraday/MCD is maximized if the light wave is circularly polarized in the top cladding layer, with $|\chi| = 1$ and $\angle\chi = \frac{\pi}{2}$. An extensive study on how the polarization factor χ is influenced by the materials choice and the dimensions of the slab waveguide will be given in section 2.3.

In the case of dissipative media there is another important contribution to the non-reciprocal absorption shift caused by the effect of magnetore-flectivity at the magnetooptic metal interface. The TM-mode eigenvalue equation 2.75 of the magnetooptic waveguide shows that the non-zero off-diagonal elements in the permittivity tensor of the magnetooptic metal cause a change of the components of the modal wave vector in the different layers of the waveguide. In other words, the modal field profile is modified. As a result, the amount of light that penetrates into the metal changes due to the presence of the magnetization. Since the optical absorption by a metal is directly proportional to the amount of light inside metal, the absorption of a waveguide mode is also modified.

We will now investigate these two magnetooptic effects contribute to the total non-reciprocal loss shift on a three-layer slab waveguide with a magnetooptic metal cladding. It is important to remark that this exercise is purely academic, as both contributions are essentially inseparable and determined by the guided mode condition 2.75 of the magnetooptic waveguide. Solving this equation for a mode traveling in each of both propagation directions directly results in the exact value of the propagation constant, hence to the exact value of the non-reciprocal loss shift, containing both the effect of magnetoreflectivity and MCD. However, it is possible to estimate the influence of both effects separately by using the formulas of ray optics, elaborated in section 2.1.2.1. The absorption of a traveling mode α can be related to the reflection coefficients at the core-substrate r_s and core-metal r_M interfaces by formulating the power decrease of the mode after having traveled one zigzag path in the waveguide core:

$$\begin{aligned} P_B &= P_A \, exp(\alpha \Delta z) \\ &= P_A |r_M|^2 |r_s|^2, \end{aligned} \tag{2.95}$$

hence

$$\alpha = \frac{ln(|r_M|^2 |r_s|^2)}{\Delta_z}, \tag{2.96}$$

with Δz the longitudinal distance between points A and B, as indicated on figure 2.5. For a guided mode in a waveguide containing absorbing media, the magnitude of these reflection coefficients is different from one. Δz can be calculated as:

$$\Delta_z = 2d \, tan(\phi_c) = 2d \frac{\beta}{h}, \tag{2.97}$$

with h and β the transverse and longitudinal component of the wave vector in the core. In the next paragraph it is discussed how equation 2.96 can be used to calculate the non-reciprocal loss shift caused by both the MCD and the magnetoreflectivity.

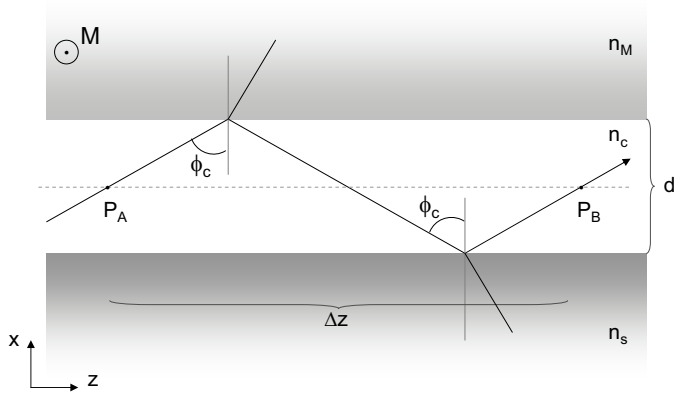

Figure 2.5: Schematic drawing of a slab waveguide, with indication of the symbols used in the theoretical elaboration.

Magnetic circular dichroism The effect of magnetic circular dichroism (MCD) causes a difference of the absorption of right and left circularly polarized light. The contribution of MCD to the total non-reciprocal loss shift can be calculated by initially solving the guided mode condition 2.75 for the waveguide in the demagnetized state ($Q = 0$). This way the components of the propagation vectors h, p, q and β in a standard (non-magnetic) metal-clad waveguide are obtained. Next, the magnetization is switched on. The corresponding reflection coefficient at the magnetooptic metal cladding is expressed by equation 2.59:

$$r_M = \frac{j\bar{p} + h(1 + \frac{Q\beta}{\bar{p}} \frac{n_c^2}{n_M^2})}{j\bar{p} - h(1 + \frac{Q\beta}{\bar{p}} \frac{n_c^2}{n_M^2})}, \tag{2.98}$$

while the reflection coefficient at the substrate follows the standard fresnel formula:

$$r_s = \frac{j\bar{q} + h}{j\bar{q} - h}. \tag{2.99}$$

With the reflection coefficients r_M and r_s the absorption of forward and backward propagating modes can be calculated through equation 2.96. This directly leads to the contribution of magnetic circular dichroism to the non-reciprocal loss shift $\Delta\alpha_{MCD}$.

Magnetoreflectivity For the calculation of the contribution of magnetoreflectivity we start by solving the eigenvalue equation 2.75 of the magnetooptic waveguide – with $Q \neq 0$. This directly directly results in the correct values of the wave vector components in the different layers of the magnetooptic waveguide, that is of the parameters h, p, q and β, different for forward and backward propagation. The wave numbers obviously yield the modal field profile through equations 2.71 and 2.72. The influence of magnetoreflectivity can now be found from the calculated values of p, q and h by considering the waveguide as a standard reciprocal

structure for which the reflection coefficients at the core-substrate interface r_s and the core-metal interface r_M are expressed by the Fresnel formulas:

$$\begin{aligned} r_s &= \frac{j\bar{q}+h}{j\bar{q}-h} \\ r_M &= \frac{j\bar{p}+h}{j\bar{p}-h}. \end{aligned} \tag{2.100}$$

Substitution of equations 2.100 into the expression for the absorption coefficient 2.96 and subtracting the result for forward and backward propagation direction yields the non-reciprocal loss shift generated by the effect of magnetoreflectivity $\Delta\alpha_{MR}$.

Total non-reciprocal loss shift The total non-reciprocal loss shift is the sum of the magnetic circular dichroism and the magnetoreflectivity contribution:

$$\Delta\alpha_{total} = \Delta\alpha_{MCD} + \Delta\alpha_{MR}. \tag{2.101}$$

As an example we simulate the magnetooptic three-layer slab that was also calculated in section 2.1.2.1; a waveguide consisting of an InP substrate (n_{substr} = *3.2* at λ = 1300nm), an InGaAlAs core (n_{core} = *3.57* at λ = 1300nm) and a $Co_{50}Fe_{50}$ metal superstrate ($n_{Co_{50}Fe_{50}}$ = *3.23-4.5j*, $g_{Co_{50}Fe_{50}}$ = *-1.7+1.7j*). In figure 2.6 the evolution of the non-reciprocal loss shifts $\Delta\alpha_{total}$, $\Delta\alpha_{MCD}$ and $\Delta\alpha_{MR}$ with the thickness of the waveguide core is plotted. As a reference, the exact solution, as elaborated earlier in sections 2.1.2.1 and 2.1.2.2, is also depicted. It can clearly be concluded that the sum of the magnetoreflectivity (MR) and the MCD contribution corresponds well to the exact solution. This confirms the validity of the statement that the non-reciprocal loss shift in a metal-clad optical isolator originates from the combined effect of magnetoreflectivity and magnetic circular dichroism.
The results plotted in figure 2.6 show that for this particular waveguide example the two contributions to the magnetooptic effect have opposite signs, which obviously causes the overall non-reciprocal loss shift to be lower than each of the contributing effects. Simulations of different waveguide structures however show that this is not a fundamental rule, but instead that both contributions can have identical signs. For example for a three-layer slab waveguide identical to the one used for figure 2.6 but with a SiO_2 substrate (n_{SiO_2} = *1.45* at λ = 1300nm) both magnetooptic contributions are positive.[6]

2.2 Calculation of non-reciprocal waveguide structures

As extensively discussed in the previous section a three-layer magnetooptic waveguide can easily be calculated either analytically or on the basis of geometric optics. If the number of layers exceeds three, as is the case in a practical amplifying waveguide optical isolator, different simulation algorithms are required for as

[6]However, it might be clear that this not necessarily means that the magnetooptic performance is higher. The impact of the materials choice on the isolator performance is extensively discussed in sections 2.3 and 3.4.5.

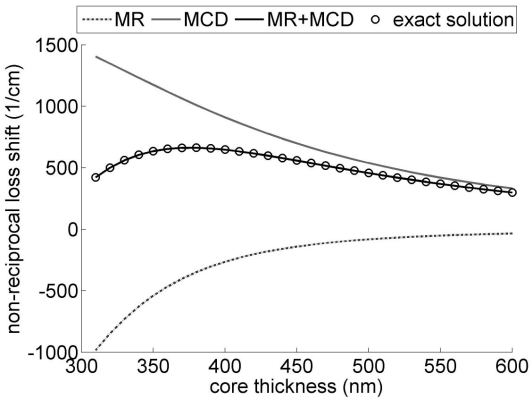

Figure 2.6: Evolution of the non-reciprocal loss shift with the thickness of the core of a three-layer slab. The sum of the magnetoreflectivity (MR) and the magnetic circular dichroism (MCD) contribution is equal to the non-reciprocal loss shift obtained by solving the magnetooptic waveguide.

both the analytical and the ray optics method become too complex. This section deals with the calculation of practical optical isolators. We start by discussing the expression for the non-reciprocal change of the propagation constant on the basis of a first-order perturbation approach. Next, we focus on the issue of a suitable figure-of-merit of the amplifying waveguide optical isolator. Finally, we determine a number of general design rules that optimize the isolator performance.

2.2.1 Perturbation calculation

If for a magnetooptic ferromagnetic metal the magnitude of the off-diagonal elements $\epsilon_0 g$ of the permittivity tensor $\hat{\epsilon}$ is small compared to the magnitude of the diagonal tensor elements $\epsilon_0 \epsilon^0$, perturbation techniques may be used to deduce the TM eigenspectrum – eigenvalues and eigenvectors (modal profiles) – of the magnetized waveguide from the eigenspectrum of the isotropic waveguide. The optical and magnetooptic properties of the ferromagnetic metal compositions used throughout this work are further discussed in section 3.2, but at this point it is important to stress that for all of these compositions the magnitude of g is at least an order of magnitude smaller than that of ϵ^0, hence it is justified to consider the magnetooptic effect as a perturbation.
The derivation of the perturbation formulae has to be done with great care as the unperturbed eigenspectrum is not power orthogonal, due to the metal losses already present in the unperturbed waveguide. As a result the perturbation formulae do not bare any resemblance to those traditionally encountered when calculating non-reciprocal TM phase shift in YIG-based magnetooptic waveguides [5]. In that case, the original modal spectrum can be orthogonalized using the power integral of the modes, as the unperturbed waveguide is lossless. For lossy waveguides instead the orthogonalization of the original modal spectrum is done through the fundamental Lorentz reciprocity theorem. The derivation of the per-

turbation formula for lossy magnetooptic waveguides has been developed by Vanwolleghem [6, 7], and shall not be repeated here. In the same work, the validity of the perturbation approach is numerically proved by showing that a rigorous model and the perturbation formalism achieve the same accuracy for the non-reciprocal Kerr absorption.
In this text we limit ourselves to a summary of the important expressions of the perturbation model, more specifically in the special case of transverse magnetooptic non-reciprocal waveguides (see figure 2.5). The first-order perturbation non-reciprocal TM phase shift is given by:

$$\Delta\beta = -j\omega\epsilon_0 \frac{\int\int g(x,y) E_x^{(0)} E_z^{(0)} dxdy}{\int\int \left[E_x^{(0)} H_y^{(0)} - E_y^{(0)} H_x^{(0)}\right] dxdy}, \tag{2.102}$$

with $E_i^{(0)}$ and $H_i^{(0)}$ (i = x,y,z) the field amplitudes of the unperturbed TM-mode:

$$\begin{aligned} \mathbf{E}^{(0)}(x,z,t) &= [E_x^{(0)}, 0, E_z^{(0)}]\ exp(j\omega t - j\beta z), \\ \mathbf{H}^{(0)}(x,z,t) &= [0, H_y^{(0)}, 0]\ exp(j\omega t - j\beta z). \end{aligned} \tag{2.103}$$

The important formulae for the isolator design that can directly be derived from this expression are the necessary length L_π for a non-reciprocal phase shift π – when designing a non-reciprocal Mach-Zehnder interferometer – and the non-reciprocal absorption difference between modes propagating in opposite directions $\Delta\alpha$ – used in an amplifying waveguide optical isolator, which is the main focus of this work:

$$L_\pi = \frac{\pi}{2|Re[\Delta\beta]|} = \frac{Z_{vac}\lambda}{4} \left| 1/Im \left[\frac{\int\int g(x,y) E_x^{(0)} E_z^{(0)} dxdy}{\int\int \left[E_x^{(0)} H_y^{(0)} - E_y^{(0)} H_x^{(0)}\right] dxdy} \right] \right|. \tag{2.104}$$

and

$$\Delta\alpha = 4Im[\Delta\beta] = -\frac{8\pi}{Z_{vac}\lambda} Re \left[\frac{\int\int g(x,y) E_x^{(0)} E_z^{(0)} dxdy}{\int\int \left[E_x^{(0)} H_y^{(0)} - E_y^{(0)} H_x^{(0)}\right] dxdy} \right]. \tag{2.105}$$

with $Z_{vac} = \sqrt{\mu_0/\epsilon_0}$ the vacuum impedance. In what follows we drop the index *(0)* in the modal field amplitudes.
In the case of a metal-clad slab waveguide the gyrotropy g is zero outside the metal and constant throughout the metal layer and the expression for the non-reciprocal phase shift $\Delta\beta$ can be rewritten as:

$$\Delta\beta = -jg\omega\epsilon_0 \frac{\int_{metal} E_x E_z dx}{\int E_x H_y dx}, \tag{2.106}$$

with E_y and H_x both zero for the pure TM-mode of a slab waveguide. If we now assume that the unperturbed modal profiles have been properly normalized, the

denominator in equation 2.106 equals 2 and the behavior of $\Delta\beta$ is entirely determined by the gyrotropy constant g – an experimentally determinable material property – the wavelength of the light – through $\omega = \frac{2\pi}{\lambda c}$ – and the field integral $\int_{metal} E_x E_z dx$. The latter is obviously influenced by the exact slab layer structure. For a slab waveguide, this field integral can easily be evaluated. Within a homogeneous region, the Maxwell equations yield (equation 2.83):

$$E_z = \frac{-j}{k_0 n_{eff}} \frac{dE_x}{dx}. \tag{2.107}$$

Using this relation, the field integral evaluates to:

$$\begin{aligned} \int_{metal} E_x E_z dx &= \frac{-j}{2k_0 n_{eff}} \int_{metal} \frac{d\left(E_x\right)^2}{dx} dx \\ &= \frac{j}{2k_0 n_{eff}} \left[\left(E_x(x_{i+})\right)^2 - \left(E_x(x_{e-})\right)^2 \right], \end{aligned} \tag{2.108}$$

with x_{i+} and x_{e-} the x coordinates infinitesimally above the magnetooptic metal-semiconductor interface and infinitesimally below the interface between the magnetooptic metal and any top layer (such as gold or air), respectively. The expression for the non-reciprocal loss shift for a metal-clad slab waveguide hence becomes:

$$\Delta\alpha = Im \left[\frac{1}{n_{eff} Z_{vac}} g \left[\left(E_x(x_{i+})\right)^2 - \left(E_x(x_{e-})\right)^2 \right] \right]. \tag{2.109}$$

In a transparent waveguide the transverse E_x field component of a TM-mode has a constant phase angle throughout the structure. This implies that by properly normalizing the modal profiles, E_x can be made purely real. Equation 2.109 learns that the non-reciprocal loss shift $\Delta\alpha$ is in that case entirely determined by the imaginary part of the gyrotropy constant g. In contrast, in the lossy waveguides studied throughout this work the modal field profiles exhibit a non-negligible phase front curvature in the neighborhood of and within the absorbing layer. This follows directly from the differential equation that describes the transverse electric field amplitude E_x:

$$\frac{1}{E_x(x)} \frac{\partial^2 E_x}{\partial x^2} = \beta^2 - k_0^2 \epsilon^2, \tag{2.110}$$

whose right-hand side is a complex constant in case of a waveguide containing dissipative media. This phase front curvature implies that E_x is no longer purely real and according to equation 2.109 both the real and the imaginary part of the gyrotropy influence the value of $\Delta\alpha$. As such, this formula can be rewritten in terms of the complex moduli and complex arguments:

$$\begin{aligned} \Delta\alpha \approx\ & \frac{|g||E_x(x_{i+})|^2}{Z_{vac}|n_{eff}|} \, sin(\angle g + 2\angle E_x(x_{i+})) \\ & - \frac{|g||E_x(x_{e-})|^2}{Z_{vac}|n_{eff}|} \, sin(\angle g + 2\angle E_x(x_{e-})), \end{aligned} \tag{2.111}$$

where the phase angle of the effective index is neglected. In most practical cases the metal layer is sufficiently thick to be optically opaque, causing the second term to be zero:

$$\Delta\alpha = \frac{|g||E_x(x_{i+})|^2}{Z_{vac}|n_{eff}|}\ sin(\angle g + 2\angle E_x(x_{i+})). \tag{2.112}$$

This last form of the non-reciprocal loss shift indicates very clearly that the isolation effect is determined by the interplay of three factors: (1) the amplitude of the gyrotropy $|g|$ has to be as high as possible, (2) the amplitude of the transverse electric field component at the metal interface has to be as high as possible, and (3) the phase angle of this field amplitude and the gyrotropy phase angle $\angle g$ have to be adequately matched to maximize to sine-factor. A more detailed discussion of the optimization of $\Delta\alpha$ is given in section 2.2.3.

Now, remember the guided mode condition of the TM-mode three-layer metal clad waveguide (equation 2.75); the magnetooptic correction to the transverse wave-number $\bar{p}$ depends on the Voigt parameter Q and the polarization factor χ. Therefore, we expect both parameters to appear in the perturbation formula of the non-reciprocal phase shift $\Delta\beta$. Using Maxwell's equations 2.78 the longitudinal electric field amplitude E_z of the waveguide mode in the cladding can be expressed in terms of the magnetic field amplitude H_y:

$$\begin{aligned} E_z &= \chi E_x \\ &= \chi\frac{\beta}{\omega\epsilon_0\epsilon^M}H_y, \end{aligned} \tag{2.113}$$

which, together with $Q = \frac{g}{\epsilon^M}$ allows to write equation 2.106 as:

$$\Delta\beta = -jQ\chi\beta\ \frac{\int_{metal} E_x H_y dx}{\int E_x H_y dx}. \tag{2.114}$$

As such, the non-reciprocal phase shift is proportional to the magnetooptic Voigt parameter Q, the polarization factor χ, the modal propagation constant β, and an overlap integral which expresses the confinement of the guided mode in the metal.

To finalize this section we compare the perturbation-based calculation to the rigorous calculation discussed in the previous section. Consider a three-layer slab consisting of an InP substrate (n_{substr} = *3.2* at λ = 1300nm), an InGaAlAs core (n_{core} = *3.57* at λ = 1300nm) and a $Co_{50}Fe_{50}$ superstrate. The optical and magnetooptic parameters of $Co_{50}Fe_{50}$ have experimentally been determined, as discussed in chapter 3: $n_{Co_{50}Fe_{50}}$ = *3.23-4.5j* and $g_{Co_{50}Fe_{50}}$ =*-1.7+1.7j*. In figure 2.7 the variation of the real (left graph) and imaginary (right figure) part of the effective index of the forward propagating guided mode with the core thickness is plotted, calculated with both techniques. It should be clear that the results of the perturbation-based (solid line) and the rigorous calculation (dotted line) coincide almost perfectly.

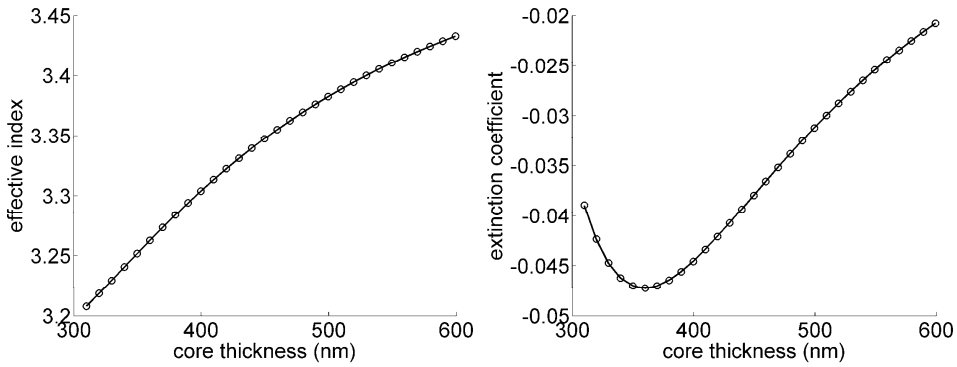

Figure 2.7: Variation of the real (left) and imaginary (right) part of the effective index of the forward propagating guided mode of a non-reciprocal three-layer slab with the core thickness. The results of the perturbation-based (solid line) and the rigorous calculation (dotted line) coincide almost perfectly.

2.2.2 Figure-of-Merit

Before studying the magnetooptic waveguides in detail it is necessary to determine a suitable figure of merit (FoM). The non-reciprocity is a consequence of the interaction of light with the magnetized media at the interface of and in the ferromagnetic metal film. In the largest part of this work we study the non-reciprocal loss shift $\Delta\alpha$ caused by this interaction. Obviously the interaction of light with the absorbing metal also causes a reciprocal loss term, which is the main contribution to the total internal loss α of the component.[7] The most fundamental parameter to evaluate the quality of the magnetooptic interaction can therefore be written as:

$$FoM_{fund} = \frac{\Delta\alpha}{\alpha} \tag{2.115}$$

which we call the isolation-to-loss ratio. As will be elaborated in a next paragraph this FoM is only minimally dependent on the dimensions of the magnetooptic waveguide and is therefore perfectly suited to optimize the non-reciprocal waveguide from a fundamental point of view.
Apart from the interaction of the light with the magnetooptic metal, the performance of a practical metal-clad isolator is determined by the amount of material gain that can be provided by the amplifying waveguide core to overcome the residual loss in the forward propagation loss. A FoM that takes into account the quality of the gain material therefore directly reflects the practical performance of the amplifying waveguide optical isolator. The important physical parameters of the isolator are the current required for forward transparency I_{transp} and the

[7] With α we denote the internal loss of the component in the forward propagation direction, i.e. $\alpha = \alpha_0 - \frac{\Delta\alpha}{2}$, with α_0 the internal loss in the absence of a magnetic field.

device length *L*, both per unit of optical isolation (dB) and per unit of ridge width (μm). A practical FoM – that needs to be minimized – can therefore be written as:

$$FoM_{pract,mn} = L^m \times I^n_{transp} \qquad (m \; and \; n \; positive \; integers) \tag{2.116}$$

The device parameters I_{transp} and L can be written in terms of their more fundamental parameters $\Delta\alpha$ and the transparency current density J_{transp}:

$$L = \frac{1}{10 \; log^{10}(exp(\Delta\alpha))} \tag{2.117}$$

$$I_{transp} = L \times J_{transp} = \frac{1}{10 \; log^{10}(exp(\Delta\alpha))} \times J_{transp}, \tag{2.118}$$

hence,[8] keeping in mind that

$$10 \; log^{10}(exp(A)) = \frac{10}{ln(10)} \; A, \tag{2.119}$$

the FoM reads

$$FoM_{pract,mn} = \frac{J^n_{transp}}{(\frac{10}{ln(10)})^{m+n} \; \Delta\alpha^{m+n}}. \tag{2.120}$$

As is elaborated in the next chapter, the amplifying core of the optical isolator is a multiple quantum well structure. It is well known that for this type of gain material the material gain-current density relation obeys a logarithmic equation:

$$G_{mat} = G_0 \; ln\left(\frac{J}{J_0}\right). \tag{2.121}$$

Now, at forward transparency the material gain G_{mat} equals the modal loss α divided by the optical confinement in the gain material Γ:

$$G_{mat} = \frac{\alpha}{\Gamma}. \tag{2.122}$$

As such, the expression for the practical FoM can be written in terms of $\Delta\alpha$ and α:

$$FoM_{pract,mn} = \frac{J^n_0}{(\frac{10}{ln(10)})^{m+n}} \times \frac{exp(\frac{n \; \alpha}{G_0 \; \Gamma})}{\Delta\alpha^{m+n}}. \tag{2.123}$$

It needs to be remarked that in the rest of this work we will focus only on the cases of m=0,n=1 and m=1,n=1. In other words we recognize that the minimization of the current required for forward transparency is primordial for this component. With n = 1, equation 2.123 shows that a practical FoM depends inverse exponentially – scaled by the confinement factor Γ and the differential gain g_0 – on the forward propagation loss, but linearly (m=0) or quadratically (m=1) on the

[8] If the current density J_{transp} is expressed in $\frac{kA}{cm^2}$ per μm ridge width and the current in mA then another factor of 10$\times$ridge width needs to be added.

non-reciprocal loss shift. This immediately implies that a design point that corresponds to a high value of the forward propagation loss – relative to the value of Γg_0 – is definitely not favorable. This is in contrast to the fundamental optimization parameter – the isolation-to-loss ratio – which is inverse linearly proportional to the forward propagation loss and linearly proportional to the non-reciprocal loss shift.

2.2.3 Theoretical study of the performance of the magnetooptic metal-clad waveguide

As discussed in the previous paragraph the performance of an optical isolator is mainly determined by the non-reciprocal loss shift $\Delta\alpha$ and the total loss in the forward propagation direction α:

$$\alpha = \alpha_0 - \frac{\Delta\alpha}{2}, \tag{2.124}$$

with α_0 the loss in the absence of a magnetic field. We assume here that $\Delta\alpha$ and α_0 have identical signs, which can always be guaranteed by changing the sign of the gyrotropy g, which is nothing more than a switch of the direction of the magnetization $\boldsymbol{M}$. The first-order perturbation formula for the non-reciprocal loss shift $\Delta\alpha$ reads:

$$\Delta\alpha = Re\left[-4\omega\epsilon_0 \frac{\int_{metal} gE_xE_z dx}{\int E_xH_y dx}\right], \tag{2.125}$$

where all electric field amplitudes are those of the unperturbed TM-mode ($\boldsymbol{M}$ = *0*). On the other hand based on the theorem of Poynting or the power theorem, an analytical formula can straightforwardly be derived for the modal absorption α_0 of the fundamental TM-polarized guided mode [8]:

$$\alpha_0 = \frac{\omega}{2} \frac{\int_{metal} \epsilon''(|E_x|^2 + |E_z|^2)dx}{Re[\int E_xH_y^* dx]}, \tag{2.126}$$

with ϵ'' the imaginary part of the dielectrical permittivity constant and H_y^* the complex conjugate of the transverse magnetic field amplitude. The different normalization in both formulas follows from the fact that the non-reciprocal formula 2.125 is calculated starting from the Lorentz reciprocity theorem while the expression for the reciprocal loss is based on the Poynting theorem. As we consider dissipative media in this work – more in particular the magnetooptic material itself – both denominators are essentially different in value. Despite this, the analytical equations 2.125 and 2.126 can be used to determine some fundamental design rules for the metal-clad optical isolator. The rest of this section is dedicated to the calculation and discussion of these rules. In what follows we consider the electric and magnetic fields to be normalized according to the normalization condition $\frac{1}{2}\int\int(\boldsymbol{E}\times\boldsymbol{H})\cdot\boldsymbol{u}_z dS = 1$. This implies that the denominator in equation 2.125 equals 1.

As we want to come to a set of general design rules of a metal-clad optical isolator the isolation-to-loss ratio $\frac{\Delta\alpha}{\alpha}$ is the one performance figure that should

be studied in this section. Indeed, equations 2.125 and 2.126 show that the non-reciprocal loss shift $\Delta\alpha$ and the reciprocal modal loss α_0 are proportional to an overlap integral of the modal field amplitudes in the metal. As such, their values depend heavily on the exact characteristics of the layer structure, like the thickness of the buffer layer between the waveguide core and the metal film. However, by considering the ratio $\frac{\Delta\alpha}{\alpha}$ these overlap integrals are canceled out, resulting in a parameter that is quasi-independent of the exact geometry of the structure. This is not the case for the more practical figure-of-merit (FoM) functions, due to their non-linear dependence on the reciprocal loss and/or the non-reciprocal loss shift. It is important to realize that the design rules derived here remain applicable for the optimization of the isolator towards the practical FoM-functions, although they are not sufficient to come to an optimized structure.

The isolation-to-loss ratio $\frac{\Delta\alpha}{\alpha}$ can, with the aid of formulas 2.124 through 2.126, be written as:

$$\frac{\Delta\alpha}{\alpha} = \frac{-4\omega\epsilon_0\ Re[\int_{metal} gE_xE_z dx]}{\omega\epsilon''_{MO}D\ \int_{metal}(|E_x|^2+|E_z|^2)dx + 2\omega\epsilon_0\ Re[\int_{metal} gE_xE_z dx]}, \tag{2.127}$$

where we assume that only the magnetooptic metal has an absorption different from zero and with $D = \frac{1}{Re[\int E_x H_y^* dx]}$ the inverse of the denominator in equation 2.126. This can directly be rewritten as:

$$\begin{aligned}\frac{\Delta\alpha}{\alpha} &= \frac{-2}{\frac{\epsilon''_{MO}}{2\epsilon_0}\ D\ \frac{\int_{metal}(|E_x|^2+|E_z|^2)dx}{Re[\int_{metal} gE_xE_z dx]} + 1} \\ &= \frac{-2}{\frac{\epsilon''_{MO}}{2\epsilon_0|g|}\ D\ \frac{\int_{metal}(|E_x|^2+|E_z|^2)dx}{\int_{metal}|E_x||E_z|cos(\angle E_x+\angle E_z+\angle g)dx} + 1},\end{aligned} \tag{2.128}$$

which is obviously maximized if the cosine factor is equal to 1. We assume this for a moment and will discuss the relation between the phases of the electric field amplitudes and the gyrotropic constant g later in this section. Furthermore, consider the case of a metal layer that is thick enough for the evanescent tail of the guided mode to have dropped to zero at the end surface of the metal, which corresponds well to the situation in practical isolator devices. In this case the ratio of the integrals appearing in the denominator of equation 2.128 reduce to a ratio of field amplitudes at the metal-semiconductor interface:

$$\frac{\int_{metal}(|E_x|^2+|E_z|^2)dx}{\int_{metal}|E_x||E_z|dx} = \frac{|E_x(x_{i+})|^2+|E_z(x_{i+})|^2}{|E_x(x_{i+})||E_z(x_{i+})|} = \left|\frac{E_x(x_{i+})}{E_z(x_{i+})}\right| + \left|\frac{E_z(x_{i+})}{E_x(x_{i+})}\right|, \tag{2.129}$$

with x_{i+} the x-coordinate at the metal side of the interface. This identity can easily be verified with formula 2.84 which relates the longitudinal and the transverse electric field amplitudes of a TM-mode in the top cladding of a slab waveguide:

$$E_z(x) = \frac{k_{x,M}}{\beta}E_x(x). \tag{2.130}$$

Now, the ratio $\left|\frac{E_z(x_{i+})}{E_x(x_{i+})}\right|$ is exactly the complex modulus of the polarization factor χ in the metal (see formula 2.27). The expression for the isolation-to-loss ratio hence becomes:

$$\frac{\Delta\alpha}{\alpha} = \frac{-2}{\frac{\epsilon''_{MO}}{2\epsilon_0|g|}\ D\ [|\chi| + \frac{1}{|\chi|}] + 1}. \tag{2.131}$$

From this equation it directly follows that the performance of a non-reciprocal device enhances the closer the polarization factor $|\chi|$ approaches unity. This is in total agreement with the discussion of section 2.1.2.3, where it was concluded that the Faraday effect and the magnetic circular dichroism have the largest impact on a metal-clad slab waveguide if the polarization in the magnetooptic material is circular.
The only assumption that has been made to come to formula 2.131 is that the metal film is sufficiently thick. The other parameters that appear in the formula for the isolation-to-loss ratio are the optical and magnetooptic constants of the metal layer and the normalization related factor *D*. The latter is obviously close to one if the waveguide loss is moderate, that is if the overlap of the guided mode with the absorbing metal is not too high. Simulations show that *D* deviates less than 4% from one for a TM-modal loss below 1000cm^{-1}, which actually exceeds the upper limit for a device to be practically viable. In comparison, without current injection the optimized amplifying waveguide isolator has a modal loss of 97cm^{-1}. In the approximation of *D* equal to one, an absolute upper limit on the isolation-to-loss ratio for a specific magnetooptic material can be calculated with equation 2.131; if the structure is designed such that $|\chi|$ is 1 we get:

$$\frac{\Delta\alpha}{\alpha} = \frac{-2}{\frac{\epsilon''_M}{2\epsilon_0|g|}2 + 1} = \frac{-2}{\frac{-2n_M\kappa_M}{|g|} + 1}, \tag{2.132}$$

with n_M and κ_M the real and imaginary part of the refractive index of the magnetooptic metal. This shows that the isolation-to-loss ratio is heavily dependent on both the optical and magnetooptic characteristics of the ferromagnetic metal and increases with increasing value of the ratio $\frac{|g|}{n_M\kappa_M}$. In this work three Co_xFe_{1-x} compositions have been studied: $Co_{90}Fe_{10}$, $Co_{50}Fe_{50}$ and Fe. In chapter 3 the optical and magnetooptic parameters of these materials are given. Formula 2.132 – among other equations – can then be used to evaluate the quality of these metals for application in a metal-clad optical isolator. In section 2.3 the evolution of the polarization factor χ with changing layer structure parameters will be discussed.

In the previous discussion we have assumed that the phase relation between the electric field amplitudes and the gyrotropy constant is optimized for a maximum non-reciprocal loss shift, i.e. *cos(∠E_x + ∠E_z + ∠g) = 1*. This is however not a trivial issue. Let us first remark that only the non-reciprocal loss shift $\Delta\alpha$ depends on this phase information and not the (reciprocal) modal absorption. To study the influence of the phase of the electric field we use the modified formula for $\Delta\alpha$ (equation 2.112):

$$\Delta\alpha = \frac{|g||E_x(x_{i+})|^2}{Z_{vac}|n_{eff}|}\ sin(\angle g + 2\angle E_x(x_{i+})), \tag{2.133}$$

where we only consider the case of sufficiently thick magnetooptic metal layers. It immediately becomes clear that in order to maximize the non-reciprocal loss shift, the argument of the transverse electric field amplitude at the metal-semiconductor interface $E_x(x_{i+})$ must obey the following relationship:

$$\angle E_x(x_{i+}) = \frac{\pi}{4} - \frac{\angle g}{2} + m\frac{\pi}{2}, \tag{2.134}$$

with m an integer. In section 2.3 we will describe how the phase of the transverse electric field amplitude can be modified by varying the composition and dimensions of the waveguide structure. Criterion 2.134 serves to evaluate the magnetooptic performance of these configurations. On the other hand, as is done in chapter 3, relationship 2.134 is another way – together with formula 2.132 – to assess the magnetooptic quality of a material, for a given isolator layer structure.

In conclusion, based on mathematical expressions for the non-reciprocal loss shift and the modal absorption three main design rules could be derived for the metal-clad optical isolator: (1) the ratio of the magnitude of the gyrotropy constant g to the imaginary part of the relative permittivity of the metal must be maximized, (2) the polarization factor χ of the TM-mode in the metal cladding must be as close as possible to 1 and (3) the phase of the transverse electric field amplitude at the metal-semiconductor interface must be matched to the argument of the gyrotropy constant g according to equation 2.134.

2.3 Fundamental design of a non-reciprocal slab waveguide

On the basis of the mathematical design rules derived in the previous section it should be feasible to realize the perfect optical isolator structure. However, the available material systems place certain limits on what can actually be achieved. In this section we want to explore these limits and come to a layer structure that essentially maximizes the performance of a TM-mode isolator based on the magnetooptic Kerr effect. In this discussion we only consider the isolation-to-loss ratio $\frac{\Delta\alpha}{\alpha}$ which describes the fundamental characteristics of the metal-clad isolator. As such, at this point we won't take into account issues that determine a practical component such as the amount of material gain that can be achieved or the actual magnetooptic parameters of the ferromagnetic metal. This will be the subject of chapter 3.

As extensively discussed in paragraph 2.2.3 the isolation-to-loss ratio is determined by three parameters: (1) the ratio of the magnitude of the gyrotropy constant g to the imaginary part of the relative permittivity of the metal, (2) the magnitude of the polarization factor χ in the magnetic material and (3) the phase relation between the transverse electric field amplitude at the metal-semiconductor interface $\angle E_x(x_{i+})$ and the gyrotropy constant g. The first quantity, which depends only on the specific characteristics of the ferromagnetic metal, will be discussed more in detail in section 3.2.

Consider the four-layer slab structure pictured in figure 2.8, with a non-magnetic waveguide core and a uniform cladding layer between the core and the mag-

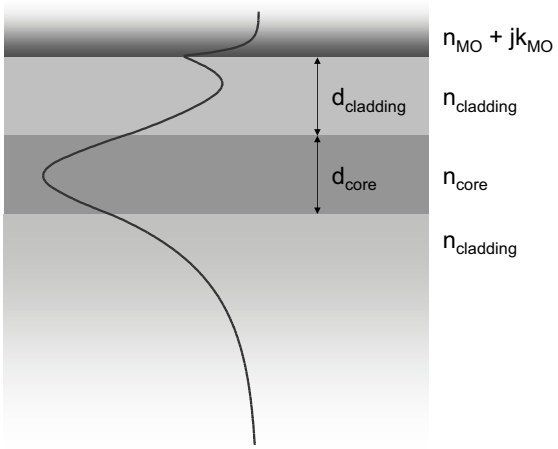

Figure 2.8: Schematic layout of the four-layer slab isolator structure with indication of the different design parameters.

netooptic material. The parameters that determine this structure are the refractive indices of the materials – which is a complex value for the magnetooptic metal – and the thickness of the core and the upper cladding layer. We assume the bottom cladding layer and the magnetooptic material to be sufficiently thick to be optically opaque. In order to limit the degree of asymmetry of the mode in the guiding core we assume the same material for the upper and bottom cladding. Furthermore, we assume that the unperturbed modes are properly normalized according to the normalization condition $\frac{1}{2}\int\int(\boldsymbol{E}\times\boldsymbol{H})\cdot\boldsymbol{u}_z dS = 1$, such that equations 2.131 and 2.133 are valid. Moreover, this normalization unambiguously establishes the phase of the transverse electric field amplitude at the metal interface $\angle E_x(x_{i+})$.

Let us first elaborate on the magnitude of the polarization factor χ which, for the non-reciprocal waveguide should be as close as possible to one. As pointed out in section 2.1.2.3 χ is constant in the top and bottom layer of a slab waveguide and equals:

$$\chi \equiv \frac{E_z}{E_x} = \sqrt{\frac{n_M^2}{n_{eff}^2} - 1} \tag{2.135}$$

with n_M the – possibly complex – refractive index of this cladding material and n_{eff} the effective index of the guided mode. For a transparent waveguide all refractive indices are purely real and $n_{eff} > n_M$ for a guided mode. Expression 2.135 shows that the polarization factor is always smaller than 1 and closer to 1 as the ratio of n_M to n_{eff} is smaller. A transparent magnetooptic slab waveguide can therefore be optimized by choosing a magnetooptic material with a low refractive index and a high index core surrounded by low-contrast cladding layers, so as to maximize the modal effective index. For the (dissipative) magnetooptic metals studied throughout this work the situation is completely different due to

Layer	Refractive index	Thickness
MO metal ($Co_{50}Fe_{50}$)	3.2-4.5j	
Cladding	3.2	500 (upper cladding)
Core	3.57	400

Table 2.1: Layer structure specifications of the four-layer magnetooptic slab structure.

the complex nature of the refractive index of the metal.[9] Mathematically, the magnitude of χ can have any value between 0 and infinity. However, within realistic boundaries of the effective index and the metal indices $|\chi|$ is always higher than 1 and its value decreases with decreasing extinction coefficient of the metal and increasing modal effective index. Other than that, its dependence on the real part of the metal index is somewhat more complicated and is influenced by the modal effective index.

Now, everything is set to start our study on how the four-layer slab waveguide characteristics determine the isolation-to-loss-ratio through $|\chi|$ and $\angle E_x(x_{i+})$. We vary two of the six waveguide parameters and keep the rest fixed at the – realistic – values tabulated in table 2.3. Remember that the magnitude of the polarization factor must be as close as possible to 1. The phase of the transverse electric field amplitude maximizes the non-reciprocal loss shift if it obeys the relationship 2.134. For the magnetooptic medium $Co_{50}Fe_{50}$ has been considered, with a gyrotropy constant g = *-1.7+1.7j* at 1300nm (see chapter 3).
In figure 2.9 the variation of $|\chi|$ and $\angle E_x(x_{i+})$ with the thickness of the upper cladding and the cladding material are plotted. It is clear that the value of both parameters is practically independent of the layer thickness. The polarization factor can be modified only minimally by varying the cladding material with a variation of 7% between n_{clad} = 1 and n_{clad} = 3.4. On the other hand the cladding refractive index largely changes the phase angle of the electric field amplitude, with a variation of more than $\frac{\pi}{2}$ between n_{clad} = 1 and n_{clad} = 3.4. Due to the factor 2 in the sine-function $sin(\angle g + 2\angle E_x(x_{i+}))$, this immediately implies that, whatever the phase of the gyrotropy constant, the sine-factor can be maximized (in absolute value) by properly choosing the cladding material. As an example the evolution of the sine-function for a $Co_{50}Fe_{50}$ covered waveguide is depicted in figure 2.10.
As the materials' choice apparently has a large influence on the device characteristics, we should examine the impact of a modification of both the core and the cladding refractive index. The simulation results are plotted in figure 2.11. As we anticipate that it is especially the refractive index contrast that is of importance for the waveguide characteristics $|\chi|$ and $\angle E_x(x_{i+})$, the refractive index is given as a percentage of the core index. Changing the refractive indices of core and cladding has only a moderate influence on the magnitude of the polarization factor which varies between 2.26 for the refractive index couple (3.0,0.75)[10] and 1.74 for (3.55,3.37). Anyhow it can be decided from the left part of figure 2.11 that the refractive index contrast between the waveguide core and cladding layers must be

[9] Obviously the effective index also has an imaginary part, but it is several orders of magnitude smaller than the real part, hence it is fair to neglect it here.

[10] which is obviously only a mathematical point as a transparent material with a refractive index below 1 does not exist.

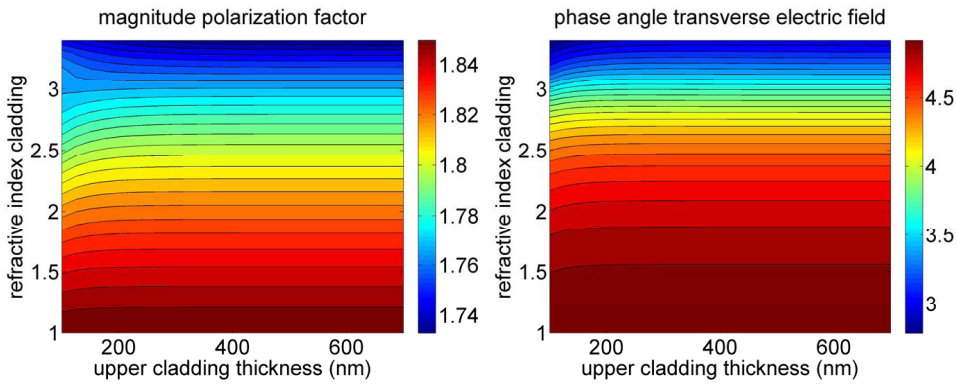

Figure 2.9: Evolution of (left) the magnitude of the polarization factor and (right) the phase angle of the transverse electric field amplitude with refractive index and thickness of the cladding layer of a four-layer magnetooptic slab waveguide.

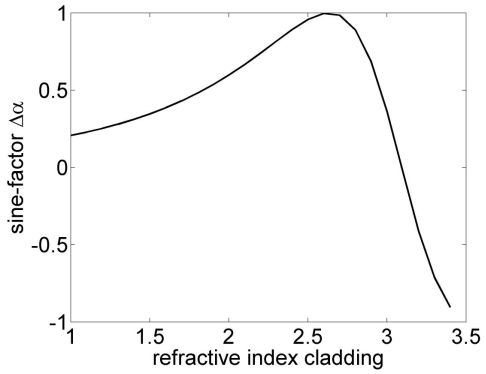

Figure 2.10: Variation of the sine-factor of equation 2.112 with the refractive index the cladding layers of a four-layer magnetooptic slab waveguide, with a $Co_{50}Fe_{50}$ magnetooptic metal. This evolution is independent of the thickness of the upper cladding.

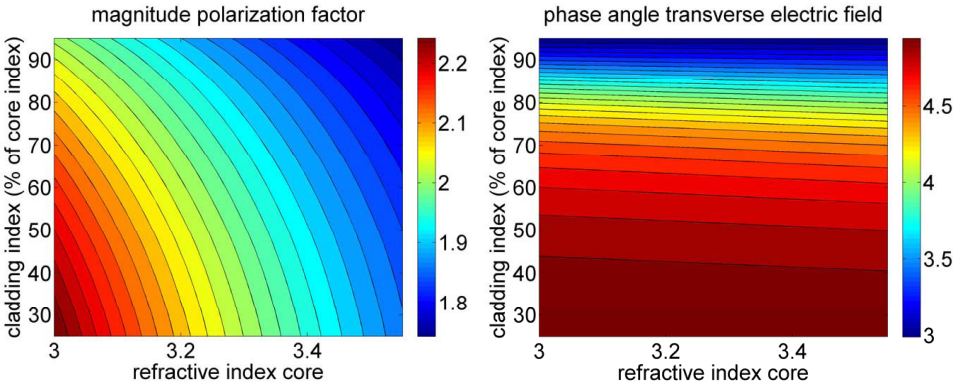

Figure 2.11: Evolution of (left) the magnitude of the polarization factor and (right) the phase angle of the transverse electric field amplitude with refractive indices of the core and cladding layers of a four-layer magnetooptic slab waveguide.

minimized and that the core index must be maximized to obtain a polarization state that is the closest to circular polarization. This observation is obviously in total correspondence to the conclusions made earlier in this section on the basis of equation 2.135. Regarding the phase angle of the transverse electric field amplitude it can easily be concluded from the right plot of figure 2.11 that it remains quasi-constant with variations of the core material. Instead, it is the refractive index contrast between core and cladding that determines the phase front curvature, hence the phase of the non-reciprocal shift of the complex effective index. Again, the desired value of the phase angle of the field depends on the gyration constant g of the chosen ferromagnetic metal.

Another point of interest is the influence of the metal choice, i.e. of the real and imaginary part of the inherently complex refractive index. We vary these parameters between realistic boundaries, that is $n_M \in$ *[0.1,5.0]* and $\kappa_M \in$ *[-2.5,-5.0]*. The result of these calculations is plotted in figure 2.12. As anticipated the magnitude of the polarization factor χ (left graph of figure 2.12) is significantly influenced by the metal choice and is closer to unity for a low absorbing metal. In the largest part of the working space its value decreases slightly with decreasing refractive index of the metal, except in the region of low extinction coefficients where there is an optimum value of n_M. However, it must be remarked that the minimum in $|\chi|$ is shallow and roughly speaking minimizing the refractive index of the metal yields the optimal point. As a matter of fact these rules do not only optimize the magnitude of the polarization factor, but also maximize the ratio $\frac{|g|}{n_M \kappa_M}$ appearing in the expression for the isolation-to-loss ratio (equation 2.132). With respect to the phase of the transverse electric field amplitude at the metal interface, the right plot of figure 2.12 shows that the possible variation by appropriately choosing a metal composition are limited. Compare for example with the change as a function of the cladding material plotted in figure 2.9.

As a last part in this study we look into the change of the thickness of the waveguide core and upper cladding thickness. The graphs, plotted in figure 2.13 in-

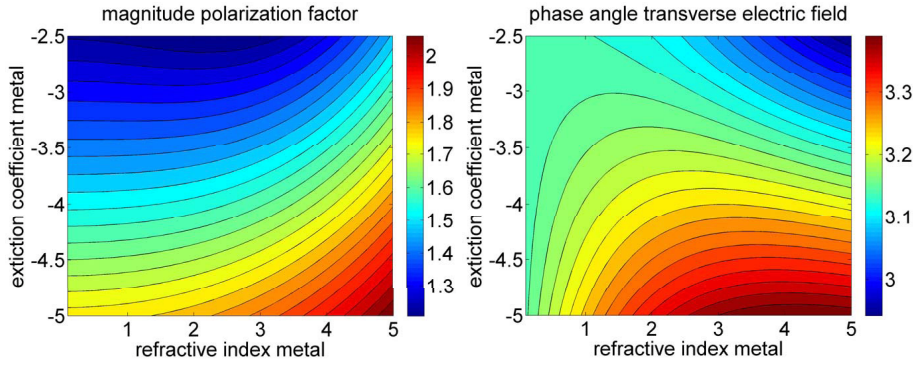

Figure 2.12: Evolution of (left) the magnitude of the polarization factor and (right) the phase angle of the transverse electric field amplitude with the (real part of the) refractive index and the extinction coefficient of the magnetooptic metal on a four-layer slab waveguide.

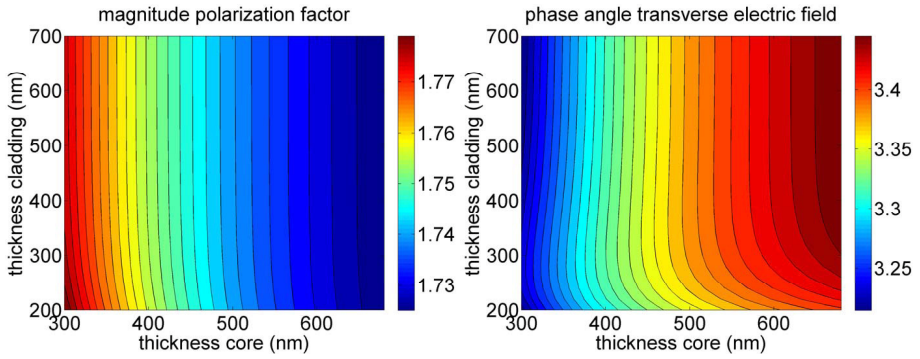

Figure 2.13: Evolution of (left) the magnitude of the polarization factor and (right) the phase angle of the transverse electric field amplitude with thickness of the core and cladding layers of a four-layer magnetooptic slab waveguide, indicating that the isolation-to-loss ratio is only minimally influenced by the exact geometry of the structure.

dicate that the dimensions of the slab waveguide layers have only a minor influence on the values of $|\chi|$ and $\angle E_x(x_{i+})$. This directly implies that the fundamental figure-of-merit (FoM) isolation-to-loss ratio is quasi-independent of these dimensions. It should be stressed that this is not at all valid for the practical FoM-functions.

On the basis of this study we come to the following design procedure for a four-layer slab waveguide optical isolator. First of all, the dimensions of the different layers are unimportant from a fundamental non-reciprocal point of view. Instead it is the materials choice that determine the performance. Start by choosing a ferromagnetic metal with a high degree of gyrotropy $|g|$ and low values of the real n_M and imaginary part κ_M of the refractive index. A good criterion is to maximize the ratio $\frac{|g|}{n_M \kappa_M}$. Next, select a waveguide core material with the highest possible refractive index. Finally, calculate the phase angle of the gyrotropy constant $\angle g$ and choose a cladding material – for the upper and lower cladding layer – for

which the phase angle of the transverse electric field amplitude $\angle E_x(x_{i+})$ obeys the relation:

$$\angle E_x(x_{i+}) = \frac{\pi}{4} - \frac{\angle g}{2} + m\frac{\pi}{2}. \tag{2.136}$$

This can be done with the aid of figure 2.11. With this recipe a non-reciprocal slab waveguide structure can be designed that shows an isolation-to-loss ratio level that approaches the value predicted by formula 2.132:

$$\frac{\Delta\alpha}{\alpha} = \frac{-2}{\frac{-2n_M\kappa_M}{|g|} + 1}. \tag{2.137}$$

So far we have limited ourselves to four-layer slab structures. In more complex devices the number of parameters is obviously larger, but the same conclusions hold with respect to the dependence of the waveguide characteristics $|\chi|$ and $\angle E_x(x_{i+})$ on the core-cladding index contrast and the metal indices. In the next chapter the design of a realistic waveguide isolator – which contains much more layers – is extensively discussed. The case of a three-layer waveguide – with a non-magnetic substrate, a waveguide core and a magnetooptic metal superstrate – is however a different story. Let us first remark that a three-layer metal-clad structure cannot be used as an amplifying waveguide optical isolator, because the modal loss levels are far too high to be compensated by the material gain in the waveguide core. Indeed, with a modal loss of at least 1000cm^{-1} the material gain should be an unrealistically high 5000cm^{-1} if a large confinement of 20% is assumed. Instead these structures should be used as short, absorbing non-reciprocal devices.

With respect to the magnitude of the polarization factor, formula 2.135 remains obviously valid and the case of a three-layer slab is completely equivalent to that of a waveguide with four or more layers. Again, to approach a circular polarization in the magnetooptic cladding layer the effective modal index should be maximal and both the real and the imaginary part of the metal refractive index must be as small as possible. Not so for the phase angle of the transverse electric field amplitude. The essential difference is that the magnetooptic metal is directly neighboring the waveguide core. As seen in the case of a four-layer slab the material choice of the cladding layer between core and metal and its contrast with the core material is the determining parameter for the phase of the electric field at the metal interface. In the absence of such a cladding layer one can expect that the refractive indices of the core layer and the metal play a defining role. This is confirmed with the calculation results of figure 2.14. Simulations have been done analogously as before, varying two parameters of the layer structure while keeping the others fixed on the values tabulated in table 2.3. The left plot of figure 2.14, showing the dependence of the phase angle $\angle E_x(x_{i+})$ on the indices of the magnetooptic metal, proves that the value of the refractive index of the metal influences the phase of the electric field at the metal interface significantly.[11] This is in contrast to the four-layer slab case where the choice of the metal was of minimal influence. The same holds for the material choice of the waveguide core, as can be seen in the right

[11] As opposed to the extinction coefficient.

Layer	Refractive index	Thickness
MO metal ($Co_{50}Fe_{50}$)	3.2-4.5j	
Core	3.57	400
Cladding	3.2	

Table 2.2: Layer structure specifications of the three-layer magnetooptic slab structure.

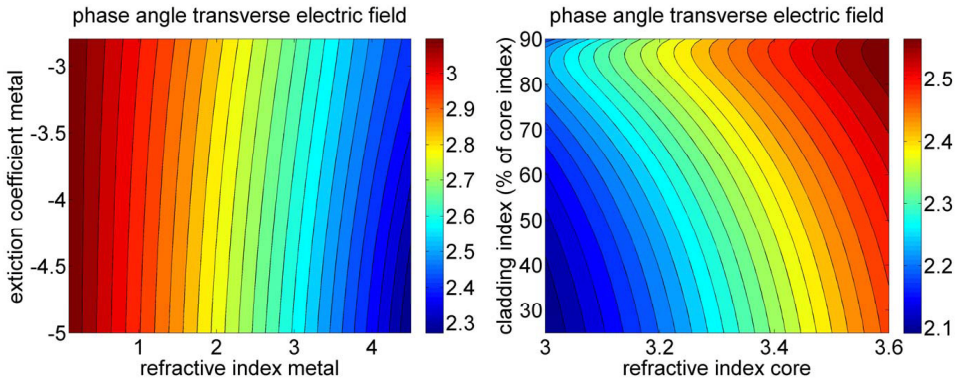

Figure 2.14: Evolution of the phase angle of the transverse electric field amplitude with (left) the (real part of the) refractive index and the extinction coefficient of the magnetooptic metal and (right) the refractive indices of the core and cladding layer on a three-layer slab waveguide.

graph of figure 2.14. The refractive index of the substrate medium is of minor importance. The last parameter that can be varied is the thickness of the waveguide core. While this has almost no influence in a four-layer structure (see figure 2.13), the core thickness is an important design parameter in the three-layer slab case as can be derived from the plot in figure 2.15. Anyhow, from figures 2.14 and 2.15 it can easily be seen that the degree of variation of the phase of the electric field is not nearly as large as in the case of a four-layer slab. In conclusion, designing a three-layer metal-clad non-reciprocal waveguide is mainly a matter of making a good choice for the magnetooptic metal both in terms of the magnitude and the phase of the optical and magnetooptic parameters. The thickness and the material of the waveguide core are the two parameters that allow a certain degree of fitting of the phase angle of the electric field to match the phase condition 2.136.

One additional point that should be mentioned is the fact that in the case of a three-layer metal-clad waveguide the normalization parameter D appearing in the formula of the isolation-to-loss ratio 2.131 can be much lower than 1, thus implying a much higher value for $\frac{\Delta\alpha}{\alpha}$ than predicted by equation 2.132.

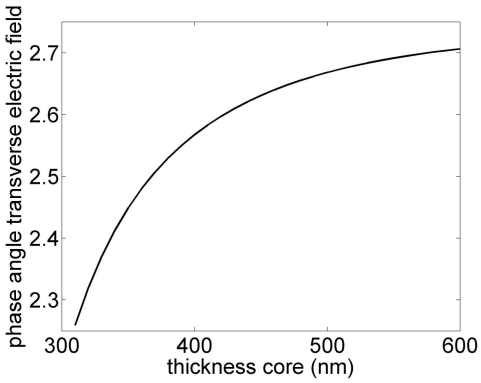

Figure 2.15: Evolution of the phase angle of the transverse electric field amplitude with the waveguide core thickness in a three-layer slab waveguide.

2.4 Magnetic properties of the waveguide isolator

Any magnetooptic device involves the presence of a magnetic field to generate the magnetooptic effect. In this section we highlight some basic principles of magnetism and magnetic materials, on the basis of which the magnetic issues of the waveguide isolator can be understood. For a more thorough elaboration we refer to standard text books of magnetism [9, 10].

2.4.1 Constitutive relations

The material response to a magnetic field is described by a constitutive relation. Applying a magnetic field H causes a change in the magnetic dipole moment p_m. The corresponding macroscopic magnetic dipole density or magnetization $M = np_m$, with n the dipole density, is related to the magnetic field H as:

$$M = \chi_m H \tag{2.138}$$

with χ_m the magnetic susceptibility. The magnetic flux density B is related to M and H trough the magnetic permeability $\mu = \mu_0\mu_r$ with $\mu_0 = 4\pi \times 10^{-7}$ henry/m the permeability of the vacuum:

$$B = \mu_0(H + M) = \mu_0(H + \chi_m H) = \mu_0(1 + \chi_m)H = \mu H \tag{2.139}$$

with $\mu_r = 1 + \chi_m$. The magnetic flux density B is therefore a field that includes both the cause H and the material response M. As such, a ferromagnet – with $\mu_r >> 1$ – represents a low reluctance path for magnetic field lines; they draw in the flux of a nearby field and add to it by their magnetization, as illustrated in figure 2.16. In other words, the B-field in a vacuum is proportional to H but inside a magnetic material ($\mu_r > 1$) there is an additional contribution to B from the sample magnetization.

In magnetism both the SI system and the CGS system are frequently used to express magnetic quantities. Table 2.4.1 lists the SI and CGS units for a number of common quantities and the conversion factors between the two systems.

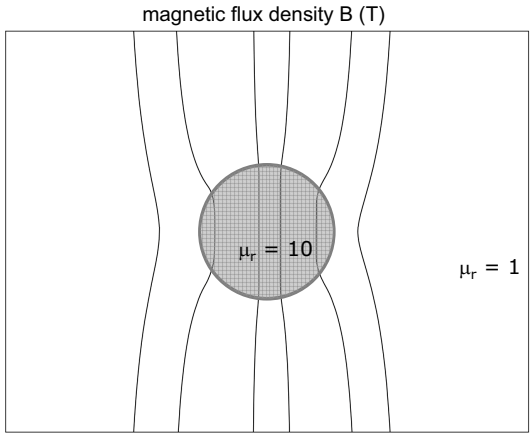

Figure 2.16: Illustration of the magnetic flux B in vacuum and inside a magnetic material ($\mu_r > 1$).

2.4.2 Maxwell equations

The time and space evolution of magnetic fields – and of course also of electrical fields – are described by Maxwell's equations:

$$\begin{array}{ll} \nabla \cdot \mathbf{E} = \frac{\rho}{c} & \nabla \cdot \mathbf{B} = 0 \\ \nabla \times \mathbf{E} = -\frac{\partial \mathbf{B}}{\partial t} & \nabla \times \mathbf{B} = \mu \mathbf{J} + \frac{\mu_0 \epsilon \partial \mathbf{E}}{\partial t} \end{array} \tag{2.140}$$

with ρ and $\boldsymbol{J}$ the charge density and the current density respectively. The magnetic divergence equation $\nabla \cdot \boldsymbol{B} = 0$ expresses that $\boldsymbol{B}$ fields never terminate at a source, while the magnetic curl equation shows that in the presence of a current density these fields may have a curling character. In all applications studied in this work the magnetic fields do not vary in time[12] – or at least very slowly – hence Maxwell's differential equations simplify to:

$$\begin{array}{ll} \nabla \cdot \mathbf{E} = \frac{\rho}{c} & \nabla \cdot \mathbf{B} = 0 \\ \nabla \times \mathbf{E} = 0 & \nabla \times \mathbf{B} = \mu \mathbf{J} \end{array} \tag{2.141}$$

This regime is called magnetoquasistatics, where the 'quasi' stems from the possibility of moving electrical charges or $\boldsymbol{J} \neq 0$.

[12]This obviously doesn't include the magnetic field of the light wave.

Label	SI unit	CGS unit	Conversion factor
B	tesla (T)	gauss (G)	1 T = 10^4 G
H	ampere/m (A/m)	oersted (Oe)	1 A/m = $4\pi/10^3$ Oe
M	ampere/m (A/m)	emu/cm^3	1 A/m = 10^{-3} emu/cm^3
μ	henry/m (H/m)	dimensionless	SI: $\mu_0(1+\chi_m)$ CGS: $1+4\pi\chi_m$

Table 2.3: SI units and CGS units for some magnetic quantities and the conversion factors between the two systems.

The magnetic curl equation originates from Ampère and the physical meaning becomes clear when rewriting the equation in its integral form. Integrating the magnetic curl equation over a surface S and using the Stokes theorem $\int(\nabla \times \mathbf{F}) \cdot \mathbf{dS} = \int \mathbf{F} \cdot \mathbf{dl}$, with l the path enclosing the surface, yields:

$$\oint B \cdot dl = \mu \int J \cdot dS = \mu I. \tag{2.142}$$

Ampère's law therefore states that the normal component of a current density $\boldsymbol{J}$ passing through an area S gives rise to a $\boldsymbol{B}$ field circulating around that area.
Now, for numerical calculations it is useful to introduce the concept of a magnetic potential $\boldsymbol{A}$ defined as:

$$\mathbf{B} = \nabla \times \mathbf{A}. \tag{2.143}$$

Ampère's law in differential form can now be rewritten as:

$$\nabla \times (\mu_0^{-1} \nabla \times \mathbf{A} - \mathbf{M}) = \mathbf{J}. \tag{2.144}$$

In chapter 4 this law will be used to design a micro-electromagnet that can be integrated onto the amplifying waveguide optical isolator. The boundary conditions at the interface between two media with different magnetic properties read:

$$\begin{array}{rcl} (\mathbf{B}_2 - \mathbf{B}_1) \cdot \mathbf{n} & = & 0 \\ \mathbf{n} \times (\mathbf{H}_1 - \mathbf{H}_2) & = & \mathbf{K}, \end{array} \tag{2.145}$$

with $\boldsymbol{n}$ the interface normal vector and $\boldsymbol{K}$ the surface current density at the interface. Across an interface between two layers the normal component of $\boldsymbol{B}$ is always continuous and the tangential component of $\boldsymbol{H}$ is continuous in the absence of transverse surface currents.

2.4.3 Ferromagnetism and magnetization loops

One method to classify magnetic materials is through the way the local atomic moments couple to each other: parallel, anti-parallel or not at all, for respectively ferromagnetic materials, ferri- and anti-ferromagnets and para- and diamagnetic materials. Here we limit ourselves to the class of ferromagnetic materials, as these are the materials studied throughout this work.
Ferromagnetic materials are characterized by a long-range ordening of their atomic moments even in the absence of an external field. This long-range ordening is caused by interatomic electronic exchange forces, creating a molecular field that overcomes the thermal agitation – below a specific temperature called the Curie temperature – essentially aligning all the magnetic moments so that $M \approx np_m$ = M_s, with M_s the saturation magnetization. However, in the absence an external field a ferromagnetic specimen is not necessarily magnetized to its saturation value. This is attributed to the presence of magnetic domains in a (bulk) ferromagnetic specimen. Within a domain all magnetic moments are aligned parallel, but the magnetization in different domains can have different directions such that over the entire sample their vector sum even may vanish. Domains are separated

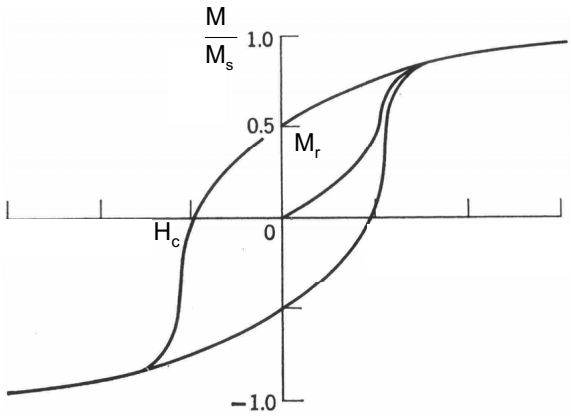

Figure 2.17: A typical example of a magnetic hysteresis loop, with indication of the important parameters.

from each other by domain walls, surfaces over which the orientation of the magnetic moment changes relatively abrupt, within a distance in the order of 10nm to 100nm. The orientation of the magnetization of the domains is such that the magnetostatic energy is minimized.

Now the basic shape of the magnetization *M-H* loops in ferromagnetic materials can easily be understood. A typical example of such a magnetic hysteresis loop is plotted in figure 2.17. Consider a magnetic material in a demagnetized state ($M = 0$ and $H = 0$), for which the magnetization of the magnetic domains are randomly oriented. Application of a weak field produces motion of domain walls so as to expand the volume of those domains having the largest component of M along the applied field H. When most domain wall motion has been completed, often domains remain with non-zero components of magnetization perpendicular to the field direction. At higher magnetic fields domain magnetization is rotated towards the parallel direction in order to minimize the potential energy $-\mu_0 \boldsymbol{M} \cdot \boldsymbol{H}$. This process generally costs more energy as it involves rotating the magnetization away from an 'easy' direction (see section 2.4.4). When the applied field is of sufficient magnitude to complete these two processes (domain wall motion and magnetization rotation) the sample is in a state of magnetic saturation ($M = M_s$). Upon decreasing the magnitude of the applied field, the magnetization rotates back toward its 'easy' directions, generally without hysteresis (rotation is a largely reversible, lossless process). As the applied field decreases further, domain walls start moving back across the sample. In real materials domain walls do not move reversibly. Instead, defects, such as grain boundaries and precipitates, can locally lower the wall energy, effectively pinning of the domain wall motion. This causes an irregular domain wall motion as it jumps abruptly from one local energy minimum to the next, the so-called Barkhausen jumps. At this process, energy is lost, hence domain wall motion is irreversible and lossy. This translates into the opening of the *M-H* loop, i.e it shows hysteresis. The magnetization remaining in the sample when the applied field is zero is called *remanence* M_r. The remanent behavior is extremely important for the isolator application. After all, we want to

avoid the need for an external magnetic field. The remanent behavior is normally expressed in terms of its fraction of the saturation magnetization,[13] the so-called squareness $S = \frac{M_r}{M_s}$. The reverse field needed to restore M to zero is called the *coercive field* H_c. For soft magnetic materials, of which the transition metal alloys Co_xFe_{1-x} studied in this work are an example, the bulk coercive field is small; $H_c < 10Oe$.

2.4.4 Magnetic anisotropy

2.4.4.1 Introduction

Magnetic anisotropy is defined as the preference for the magnetization to be oriented along a particular direction in a sample. It can have its origin in the sample shape (shape or magnetostatic anisotropy), crystal symmetry (magneto-crystalline anisotropy), stress (magneto-elastic anisotropy), and its pre- and/or post-fabrication conditions (field- or texture-induced anisotropy). Depending on the characteristics of a magnetic sample one or the other anisotropy mechanism is dominant. A comprehensive discussion of the phenomenology of magnetic anisotropy, and the influence on the magnetization process can be found in reference [12].
The concept of magnetic anisotropy can be understood using a thermodynamic approach. The stable equilibrium state of a specimen's magnetization corresponds to a minimum of the free energy. The total free energy of a ferromagnetic sample F_T can be written as a sum of several free energy terms:

$$F_T = F_H + F_D + F_K + F_o. \tag{2.146}$$

The first term F_H is the Zeeman energy corresponding to the magnetization in the applied field H,

$$F_H = -\int \mu_0 \mathbf{M} \cdot \mathbf{H} dV, \tag{2.147}$$

which, for a uniform **M** and **H** gives a free energy density of -$\mu_0 \boldsymbol{M} \cdot \boldsymbol{H}$. The second term F_D is the self-energy of the magnetization in its own field which is related to demagnetizing fields and describes the shape anisotropy of the sample (see section 2.4.4.2). The third term F_K denotes the magneto-crystalline anisotropy and is obviously dependent on the crystal state of the material. Other free energy contributions, such as the magnetostrictive energy and the exchange free energy, are assembled here in the last term F_o, as they are of less importance for the magnetic samples considered in this work. The magnetization is said to lie along an easy axis if the total free energy is minimized, in the absence of an external magnetic field ($F_H = 0$).

Magnetic anisotropy essentially determines the shape of the magnetization curves. This can be understood qualitatively as follows. Consider first magnetization rotation as the only possible magnetization re-orientation mechanism. If a sample is completely saturated along a hard axis, the anisotropy causes a gradual rotation of the magnetization towards an easy axis as soon as the applied field

[13] A more correct definition of the squareness, taking into account the coercive field strength thereby expressing the stability of the magnetized state of the sample, can be found in reference [11]

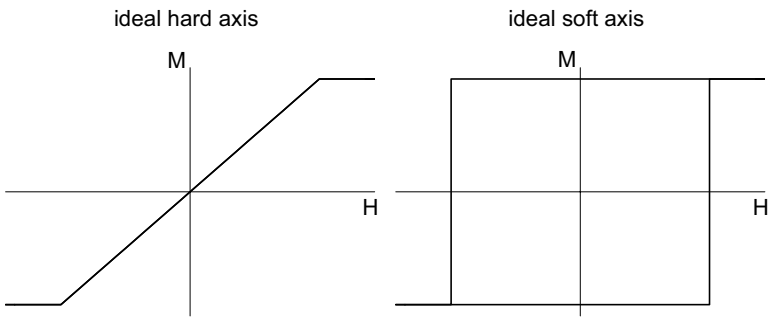

Figure 2.18: Illustration of the magnetization hysteresis along an ideal hard axis (left) and an ideal soft axis (right).

decreases below a certain value (the anisotropy field), for as this decreases the total free energy of the system. This rotation is a completely reversible process. As a result the magnetization curve shows no hysteresis and the coercive field and magnetic remanence are zero, as illustrated in the left part of figure 2.18.
Conversely, if a sample is completely magnetized along an easy direction, a decrease of the magnitude of the field obviously doesn't cause magnetization rotation, as the free energy is already at its minimum. If a magnetic field is applied in the opposite direction, the first term in equation 2.147 causes a torque on the magnetization, which is counteracted by the anisotropy term. The anisotropy barrier is climbed faster than the decrease of the Zeeman energy, hence the magnetization remains perfectly oriented to the original direction. If the field in the opposite direction reaches the anisotropy field, the magnetization switches discontinuously to the direction parallel to the applied field (anti-parallel to the original direction). This process is a purely irreversible magnetization orientation. The ideal magnetization curve along an easy direction therefore has a perfect squareness (S = 1) and the coercive field equals the saturation field or anisotropy field, as shown in figure 2.18. In real magnetic samples however, the coercive forces are considerably lower, as the irreversible magnetization re-orientation is almost always due to domain wall motion (the Barkhausen jumps). It is intuitively clear that the magnetization along a general direction is a combination of reversible rotations and irreversible jumps, yielding a magnetization loop such as the one illustrated in figure 2.17.
This qualitative treatment of the influence of anisotropy on the magnetization loops indicates that in order to have a high magnetic remanence and a large coercive force, two elements desired for the isolator application, there must be an easy axis oriented perpendicular to the waveguide stripes – the magnetization direction corresponding to a TM-mode non-reciprocal loss shift.

2.4.4.2 Demagnetization and shape anisotropy

Consider a specimen of magnetic material and assume that it is magnetized perpendicular to the ends. At the end surfaces uncompensated magnetic poles exist, traditionally characterized by the surface pole density $\sigma = \boldsymbol{M}\cdot\boldsymbol{n}$. These free poles

give rise to a magnetic field on both sides of the surface. Its magnitude in the direct vicinity of the surface can directly be derived from the boundary condition for the magnetic induction at the interface between the sample (medium *i*) and the surrounding vacuum (medium *o*):

$$(\mathbf{B}_o - \mathbf{B}_i) \cdot \mathbf{n} = 0, \tag{2.148}$$

hence, with the magnetization in vacuum obviously equal to zero,

$$(\mathbf{H}_o - \mathbf{H}_i) \cdot \mathbf{n} = M, \tag{2.149}$$

with $\boldsymbol{n}$ the interface normal vector and M the magnitude of the magnetization perpendicular to the sample interface. This shows that even in the absence of an externally applied field, magnetic fields exist inside $H_i = \frac{-M}{2}$ and outside $H_o = \frac{M}{2}$ the sample oriented perpendicular to the sample end. If an external field H_{ext} is applied, its magnitude adds to H_o and H_i:

$$H_o = H_{ext} + \frac{M}{2} \qquad H_i = H_{ext} - \frac{M}{2}. \tag{2.150}$$

In other words, the internal magnetic field in the sample is equal to the applied field reduced by half the amount of magnetization normal to the surface. Note that if the sample is thin in the direction of M there are contributions to the internal field of $\frac{-M}{2}$ from each surface. The field from the surface poles is called the *demagnetizing* field H_d with for this specific sample $H_d = \frac{-M}{2}$ (in the direct vicinity of the surface).
For an arbitrarily shaped sample, the demagnetizing field is described by a demagnetization factor N:

$$H_d = -NM, \qquad 0 \leq N \leq 1. \tag{2.151}$$

In general, N is a tensor function of the sample shape and a function of the position in the specimen (except for ellipsoids).
The existence of demagnetizing fields and their large dependence on the sample shape is one of the sources of magnetic anisotropy in a sample, the so-called shape anisotropy. The magnitude of this shape anisotropy is related to the distribution of demagnetization factors in the sample. Consider the special case of a very thin magnetic sheet, with length l, width w and thickness t (see figure 2.19). If the thickness is at least an order of magnitude smaller than the other dimensions the field can be considered as uniform along this direction. Furthermore, for aspect ratios of l to w that are not too extreme, it is a fairly good approximation to take the field in the specimen due to the end poles independent of the coordinate along the direction in which these poles lie. The following coordinate-independent demagnetization factors can be derived:

$$\begin{aligned} \text{magnetization along length: } N_l &\approx \frac{2t}{\pi l}\sqrt{\frac{2w}{l}} \\ \text{magnetization along width: } N_w &\approx \frac{2t}{\pi w}\sqrt{\frac{2l}{w}}. \end{aligned} \tag{2.152}$$

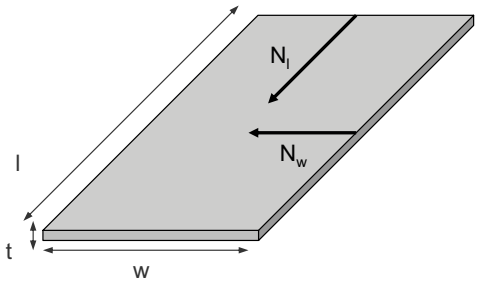

Figure 2.19: Demagnetization factors of a rectangular thin ferromagnetic film.

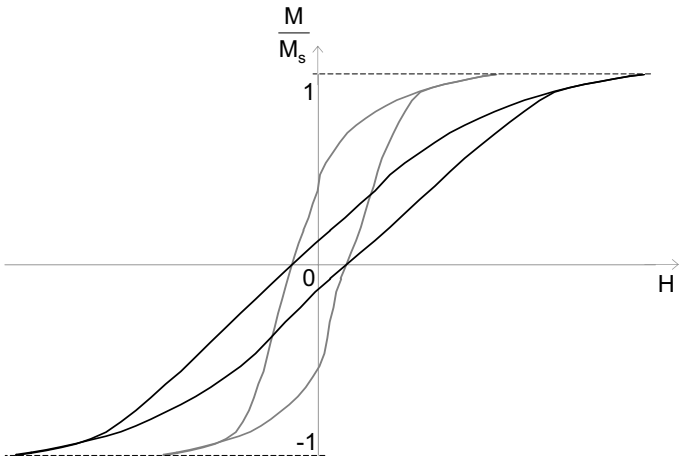

Figure 2.20: Illustration of the shearing of the observed magnetization curve when taking into account the effect of sample size; the mechanism of demagnetization transforms the grey line (= intrinsic M-H_i *loop) to the black line (= observed* M-H_{ext} *loop). Both curves are identical in the case of infinite dimensions.*

As an example, we consider a sheet with the typical dimensions of the ferromagnetic metal contact of the waveguide optical isolator: t = 50nm, w = 10μm, l = 1000μm. The corresponding demagnetization factors are $N_w \approx 4.5\ 10^{-2}$ and $N_l \approx 4.5\ 10^{-6}$. In other words, the demagnetization field along the width is four orders of magnitude stronger than along the length. This favors a magnetization along the length of the sheet.

The effect of demagnetization has a direct influence on the observed magnetic hysteresis loop. To comprehend this it is important to realize that the *observed M-H_{ext}* loop shows the response of the sample – the magnetization – to the internal field H_i in the specimen as a function of the externally applied magnetic field H_{ext}. In the absence of demagnetizing effects – a sample with infinite dimensions – the internal field H_i is equal to the applied field H_{ext}. If the sample has a finite size, demagnetization reduces the internal field and the corresponding magnetization by a value proportional to the magnetization, as is expressed by equation 2.151. The result is a shearing of the *M-H_{ext}* loop. The easiest way to understand this is by comparing the intrinsic hysteresis curve (*M-H_i* loop) to the observed *M-H_{ext}* loop, respectively the grey and black curve in figure 2.20. Both loops are identical in a sample with infinite dimensions. From equation 2.151 it follows that vertical lines of constant internal field $H_i = C_H$ in the *M-H_i* loop transform to tilted lines in the *M-H_{ext}* loop, described by $M = \frac{1}{N}(H_{ext}\text{-}C_H)$. In other words, the vertical lines are sheared over an angle *tan* $\alpha = N$. The main effect of shape anisotropy is thus a reduction of the magnetization at a given applied field. This implies a reduction of the magnetic remanence, as clearly illustrated in figure 2.20. The mechanism of shape anisotropy in principle doesn't change the value of the coercive field. For the metal stripe with dimensions t = 50nm, w = 2μm, l = 1000μm, the hysteresis is sheared over $\alpha = 27°$ for magnetization along the width. In the longitudinal direction the shear angle is negligible.

In the polycrystalline ferromagnetic films that form the magnetic element in the amplifying waveguide optical isolator, shape anisotropy is the dominant anisotropy mechanism. Indeed, the magneto-crystalline anisotropy has little influence due to the random distribution of the easy direction among the grains. On the other hand, with a ridge width of a few micrometer and a device length of several millimeters, the metal stripe intrinsically has a very large shape anisotropy. If this anisotropy is not compensated the lateral direction, which is the required magnetization direction for the TM-mode isolator, is a hard axis with respect to the soft axis along the longitudinal direction. This inherently lowers the magnetic squareness, which prohibits isolator operation under remanent conditions.
One way to overcome the parasitic anisotropy is to induce an uniaxial, in-plane (lateral) magneto-crystalline anisotropy by depositing the magnetic material under applied magnetic field bias [13]. The mechanism is supposedly the influence of the texture during the growth. This technique has been used in all the fabricated devices. Alternating gradient force magnetometer (AGFM) measurements on $Co_{90}Fe_{10}$ metal stripes show that the field-biased deposition can reduce the shape anisotropy significantly. In fact, it is possible to obtain a lateral squareness higher than 0.9 on a stripe of several millimeters long and only 50μm wide [14]. Below a width of 50μm the shape anisotropy remains dominant which drastically reduces the magnetic squareness. One solution for this issue is to integrate an elec-

tromagnet onto the isolator. A theoretical and experimental study of this concept is given in section 4.4.

2.5 Conclusion

In this chapter we have extensively studied non-reciprocal phenomena. We have started from the constitutive relations that establish the response of a medium to a light wave and have showed that the presence of a magnetic field introduces an anti-symmetric contribution to the permittivity tensor of the material. At reflection of light off a transversely magnetized substance the reflection and transmission coefficients undergo a non-reciprocal change if the light is TM-polarized, while the TE-wave remains unaffected. With the aid of a geometric optics approach it has been elaborated how this change in reflection causes a non-reciprocal modification of the propagation constant of a TM-polarized mode in a three-layer metal-clad slab waveguide. Furthermore, it has been proven that the non-reciprocal phenomena in such a metal-clad waveguide can be traced back to the magnetooptic Faraday effect and magnetic circular dichroism, combined with the effect of magnetoreflectivity. This yields the first design criterion for the TM-mode non-reciprocal device: for the non-reciprocity to be maximal the polarization state of the light in the magnetooptic substance must be circular.

For the extension towards more complicated waveguide structures first-order perturbation calculation – where the off-diagonal elements in the permittivity tensor are considered as a small perturbation – results in a formula for the non-reciprocal phase shift, expressed as the product of the gyrotropy constant with an overlap integral of the unperturbed electric field amplitudes in the magnetooptic substance. Elaboration of this expression shows that the non-reciprocal loss shift – the imaginary part of the non-reciprocal phase shift – is proportional to a sine-factor relating the phase angle of the gyrotropy to the phase of the electric field amplitude at interface of the magnetooptic metal. A second design criterion is therefore that both phases match such that the sine-factor equals one, or is as close as possible to one.

We have established a number of figure-of-merit (FoM) functions specifically for the amplifying waveguide optical isolator and distinguish a fundamental FoM, the ratio of the non-reciprocal loss shift to the loss in the forward propagation direction, and practical FoM-functions, which express the amount of current required for transparency and the length of the optical isolator. The first one is quasi-independent of the dimensions of the isolator layer structure, but instead is only influenced by more fundamental parameters such as the materials' choice – hence the designation as a fundamental FoM. With the aid of an analytical expression for the unperturbed modal loss, it has been shown that the fundamental FoM is indeed only determined by the two design criteria mentioned earlier, together with the requirement that the ratio of the magnitude of the gyrotropy constant g to the imaginary part of the relative permittivity of the metal is maximal.

On the basis of these three rules it is possible to optimize the choice of materials of the non-reciprocal device.[14] The thickness of the layers is then merely determined by the gain-current relation of the amplifying material and the choice of practical FoM-function, as is extensively discussed in chapter 3.

[14] This optimization is obviously only from a purely magnetooptic point of view. In a real amplifier-based device the quality of the amplifying region (current injection, strain, emission wavelength) imposes a number of restrictions upon the choice of materials of the layer stack.

Next we have investigated how the layer structure characteristics change the phase of the transverse electric field amplitude at the metal-semiconductor interface and the polarization state in the metal. It was shown that a circular polarization can be approached by maximizing the effective index of the guided mode while minimizing the refractive index and extinction ratio of the metal. With respect to the phase angle of the modal fields it is especially the refractive index of the material(s) between waveguide core and magnetooptic metal that is the modifying factor. More in particular, whatever value of the phase angle of the gyrotropy constant, a cladding material can be found that fulfills the phase requirement, hence maximizes the imaginary part of the non-reciprocal phase shift.

As a last point in this chapter we have reviewed some basic concepts of magnetism and have indicated that shape anisotropy places important restrictions on the dimensions of the magnetooptic metal contact.

Bibliography

[1] A. K. Zvezdin, and V. A. Kotov, *chapter 5* in "Modern Magnetooptics and Magnetooptical Materials." Institute of Physics Publishing, Philadelphia, USA (1997).

[2] L. Onsager, "Reciprocal relations in irreversible processes." *Phys. Rev.,* 37, pp. 405-426 (1931).

[3] M. Schubert, T. Hofmann, and C.M. Herzinger "Generalize far-infrared magneto-optic ellipsometry for semiconductor layer structure: determination of free-carrier effective-mass, mobility, and concentration parameters in n-type GaAs." *J. Opt. Soc. Am. A,* 20(2), pp. 347-356 (2003).

[4] V. Zayets, and K. Ando, "Isolation effect in ferromagnetic-metal/semiconductor hybrid optical waveguide." *Appl. Phys. Lett.* 86, pp.261105261107 (2005).

[5] A.F. Popkov, M. Fehndrich, M. Lohmeyer, and H. Dötsch, "Non-reciprocal TE-mode phase shift by domain walls in magnetooptic rib waveguides." *Appl. Phys. Lett.,* 72, pp.2508-2510 (1998).

[6] M. Vanwolleghem, "Een geintegreerde InP-gebaseerde optische golfgeleiderisolator op basis van ferromagnetische CoFe-contacten, An integrated InP-based Optical Waveguide Isolator Using Ferromagnetic CoFe Contacts." *Ph.D. thesis,* ISBN , 90-8578-013-6, Ghent University, Belgium (2005).

[7] K. Postava, M. Vanwolleghem, D. Van Thourhout, R. Baets, S. Visnovsky, P. Beauvillain, and J. Pistora, "Modeling of a novel InP-based monolithically integrated magneto-optical waveguide isolator." *J. Opt. Soc. Am. B,* 22, pp.261-273 (2005).

[8] T.D. Visser, H. Blok, B. Demeulenaere, and D. Lenstra, "Confinement factors and gain in optical amplifiers." *J. Quant. Electr.,* 33, pp. 1763-1766 (1997).

[9] A.H. Morrish, "The Physical Principles of Magnetism." (John Wiley & Sons inc., 1965).

[10] R. C. O'Handley, *Modern Magnetic Materials : Principles and Applications,* (Wiley-Interscience, New York, USA, 2000).

[11] R. C. O'Handley, §17.3 in *Modern Magnetic Materials : Principles and Applications,* (Wiley-Interscience, New York, USA, 2000).

[12] R. C. O'Handley, chapters 6 and 9 in *Modern Magnetic Materials : Principles and Applications,* (Wiley-Interscience, New York, USA, 2000).

[13] Th.G.S.M. Rijks, R.F.O. Reneerkens, R. Coehoorn, J.C.S. Kools, M.F. Gillies, J.N. Chapman, and W.J.M. de Jonge, "Switching field interval of the sensitive magnetic layer in exchange-biased spin valves." *J. Appl. Phys.,* 82(7), pp. 3442-3451 (1997).

[14] M. Vanwolleghem, §4.1.2 in "Een geintegreerde InP-gebaseerde optische golfgeleiderisolator op basis van ferromagnetische CoFe-contacten, An integrated InP-based Optical Waveguide Isolator Using Ferromagnetic CoFe Contacts." *Ph.D. thesis,* ISBN , 90-8578-013-6, Ghent University, Belgium (2005).

3

Design of the amplifying waveguide isolator

IN this chapter the design of a TM-mode amplifying waveguide optical isolator will be discussed. As pointed out in chapter 1, the concept has been proposed by Nakano [1] and Ando [2]. The device is essentially a semiconductor optical amplifier (SOA) with a ferromagnetic metal film magnetized along the lateral direction. The magnetooptic Kerr effect in the metal causes a non-reciprocal difference of the complex effective index of the TM-guided mode. In the simplest configuration the ferromagnetic film also serves as the electrical contact for the underlying SOA.

We start our discussion with the individual building blocks of the isolator. The main issues to be elaborated are the development of the TM-selective gain material, the choice of the ferromagnetic metal on the basis of its optical and magnetooptic properties and the optimization of the electrical injection in the SOA. The theoretical and experimental study of these aspects are given in the first part of this chapter.

On the basis of these studies, the different building blocks can be assembled to one non-reciprocal device. In the second part of this chapter we elaborate in detail the design of this isolator. The fabrication and subsequent characterization will be presented in chapter 4.

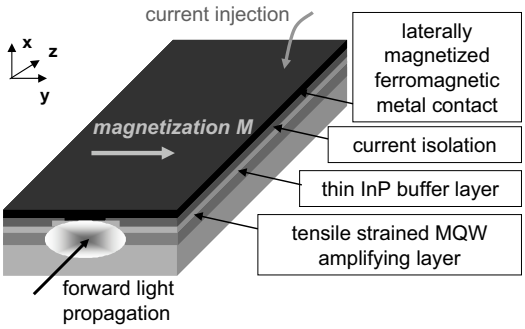

Figure 3.1: Schematic layout of the TM-mode amplifying waveguide optical isolator.

3.1 TM-selective gain material: tensile strained quantum wells

Chapter 2 has shown that a (passive) optical waveguide with a magnetooptic metal cladding magnetized along the lateral direction has an internal modal loss that is different for both propagation directions of the light and that this non-reciprocity is the result of the interaction of the optical mode with the magnetic field in the metal. This is however not sufficient to talk about an optical isolator, which is a device that is optically transparent in one direction while showing loss in the opposite propagation direction. The solution is to include optical gain to compensate for the absorption in the metal film and other sources of loss. As will be discussed later in this chapter the modal loss that needs to be compensated is in the order of 100cm^{-1}. With a modal confinement between 10% and 20% in the amplifying material this is equivalent to material gain levels around 1000cm^{-1}. Such high gain can only be achieved with a multiple quantum well (MQW) waveguide core. What is equally important is the fact that the gain must be TM-polarization selective, as the magnetooptic effect in the isolator configuration illustrated in figure 3.1 and studied throughout this work, only affects TM-light and is zero for TE-polarization. TE light therefore only adds to the noise of the signal and might lead to gain saturation, this way reducing the performance of the isolator. Polarization selective gain can be realized by building in strain in the MQW.
In this section we shortly review the principles behind strained multiple quantum wells and discuss the development of the gain region for the TM-mode waveguide isolator.

3.1.1 Strained quantum wells: a short review

3.1.1.1 Introduction

In order to understand the effect of introducing strain in the active layers we start from the expression of the gain *G* as a function of the photon energy *E* [3]:

$$G(E) = \frac{e^2 h}{2Ec\epsilon_0 m_0^2} \frac{n_g}{n^2} |M_T|^2 \rho_{red}(E)(f_c - f_v), \tag{3.1}$$

where *e* is the electron charge, *h* is Plank's constant, n_g is the group velocity, *n* is the refractive index of the crystal, *c* is the speed of light in free space, ϵ_0 is the vacuum permittivity, m_0 the electron mass, $|M_T|^2$ is the transition matrix element, ρ_{red} the reduced density of states, and f_c and f_v the electron and hole Fermi functions. In the case of bulk semiconductors ρ_{red} is calculated as:

$$\rho_{red}(E) = 4\pi \left(\frac{2m_r}{h^2}\right)^{\frac{3}{2}} \sqrt{E - E_g}, \tag{3.2}$$

with E_g the bandgap energy and m_r the reduced effective mass:

$$m_r = \left(\frac{1}{m_c} + \frac{1}{m_v}\right)^{-1}, \tag{3.3}$$

where m_c and m_v are the effective masses of an electron and a hole respectively. From the gain function 3.1 and using the concept of quasi-Fermi levels E_{fc} and E_{fv} the requirement for optical gain (G > 0) at an energy $E = h\nu$ is:

$$E_{fc} - E_{fv} > E > E_g, \tag{3.4}$$

that is the quasi-Fermi level separation must be wider than the bandgap energy. It can be shown that the requirements for optimum gain performance – minimal transparency current density and maximal differential gain – are a small effective mass and a symmetric band structure with $m_c = m_v$. Bulk III-V semiconductors are characterized by a conduction band with a small effective mass m_c, a degenerate valence band at the zone center with heavy effective mass at the bandgap E_g, and a spin split-off valence band at energy $E_g + \Delta_{so}$. In other words, bulk III-V semiconductors do not fulfill these optimum gain requirements. Furthermore, at long wavelengths the complex valence subband structure facilitates substantial non-radiative recombinations through Auger processes and intervalence band absorption [4].

3.1.1.2 Quantum well active structures

A logical continuation in the efforts striving for improved performance of long wavelength semiconductor lasers was the trend to shrink structures to smaller dimensions. For layer thicknesses in the order of the De Broglie wavelength of confined carriers ($\lambda \approx h/p \approx$ 200-300Å, *p* = momentum) the kinetic energy for motion normal to the direction of the interfaces (z-direction) becomes quantized into discrete energy levels. Every quantum number corresponds to one conduction band and three valence band levels, the light hole (lh), the heavy hole (hh) and the split-off (so) band. A typical energy scheme of a quantum well is depicted in figure 3.2. Due to the quantization of the kinetic energy, the density of states is modified from the three dimensional case (equation 3.2) to [3]:

$$\rho_{red} = \frac{4\pi m_{i,\|}}{h^2} \frac{1}{d_z}, \tag{3.5}$$

where d_z is the well thickness and $m_{i,\|}$ the effective mass for the *i*-level parallel to the quantum well (QW) interface. This shows that in a QW the density of states is

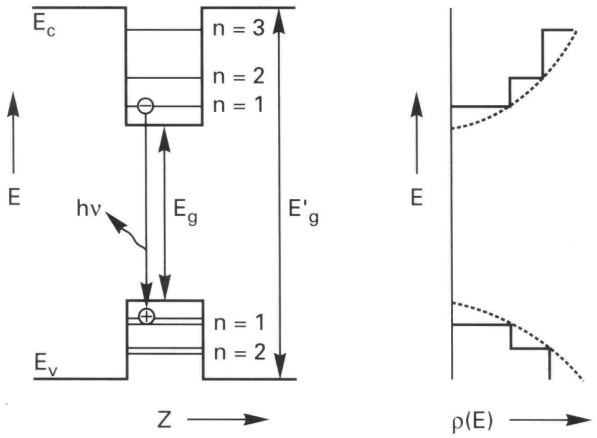

Figure 3.2: Energy scheme (left) and density of states (right) for a quantum well of e.g. InGaAsP embedded in InP. Due to the confinement, for motion normal to the interfaces, the kinetic energy of carriers is quantized into discrete energy levels. The density of states for non-quantized carriers is shown by the dashed curves, the quantization changes them to the solid step-like curves.

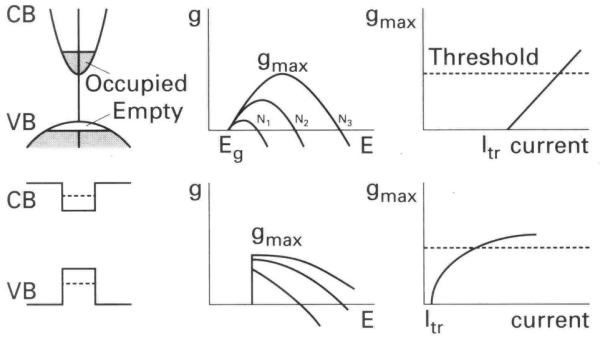

Figure 3.3: Schematics of band filling, gain formation under increased injection, and gain-current characteristics for semiconductor lasers with bulk (top) and quantum well (bottom) active layers (CB = conduction band, VB = valence band).

independent of the carrier energy and is determined by the effective mass in the QW plane (x-y plane). A direct result of the modified band structure is a change of the gain spectrum and the gain-current relation, as is illustrated in figure 3.3. For bulk active layers the spectral gain bandwidth increases with carrier density and above transparency the peak gain is linearly proportional to the injection current. In contrast, the step-like density of states in quantum well active layers causes a steep onset of the gain at the bandgap energy. Plotted against the injection current the gain becomes positive for smaller values of the injection current compared to bulk active layers. At high injection currents the gain shows a tendency to saturate, which is expressed by a logarithmic gain-current relation [5, 6, 7]:

$$G = \frac{J_{tr}}{\eta_i}\beta ln\frac{J\eta_i}{J_{tr}}, \tag{3.6}$$

where *J* and J_{tr} are the injection and the transparency current density respectively, η_i is the internal quantum efficiency, and β is the differential gain.
Near transparency the differential gain in a quantum well structure is enhanced with respect to a bulk active layer. This increase can be attributed to a modification of the transition matrix element $|M_T|$. The transition matrix element is a measure for the strength of stimulated electron transitions in a given material. In zinc blende bulk semiconductors the transition matrix element is isotropic, meaning that the gain does not depend on the optical polarization – the angle between the electron wave vector ***k*** and the optical field vector ***E***. This is no longer the case for quantum well structures. We distinguish two polarization states, with either the electric field (TE) or the magnetic field (TM) lying in the quantum well xy-plane. The corresponding transition strengths are different for heavy holes and light holes [8]:

$$\begin{aligned}
|M_{hh}^{TE}|^2 &= \frac{3+3cos^2\theta}{4}O_{e,hh}M_{b,hh}^2 \\
|M_{lh}^{TE}|^2 &= \frac{5-3cos^2\theta}{4}O_{e,lh}M_{b,lh}^2 \\
|M_{hh}^{TM}|^2 &= \frac{3-3cos^2\theta}{2}O_{e,hh}M_{b,hh}^2 \\
|M_{lh}^{TM}|^2 &= \frac{1+3cos^2\theta}{2}O_{e,lh}M_{b,lh}^2,
\end{aligned} \tag{3.7}$$

where $M_{b,j}$ is the isotropic bulk transition matrix element, and $O_{i,j}$ the overlap integral of the two quantum well envelope wave functions with a value between 0 and 1. θ is the angle of the electron **k** vector with the k_z direction and is equal to zero at the zone center Γ.
In unstrained quantum wells the lh-hh degeneracy is lifted due to a difference in effective mass of the subbands, with the hh-levels getting on top. If we consider the limit where there is no overlap between the conduction band and the lh-valence band Bloch wave function ($O_{e,lh}$ = *0*), then the overlap $O_{e,hh}$ of the electron-heavy hole transition equals 1. From expression 3.7 it can be deduced that at the band edge (Γ point, *cos* θ = *1*) only the TE-gain is different from zero and the corresponding transition strength equals 1.5 times that in bulk material. This proves that the use of quantum wells enhances the optical gain. In reality, the hh-lh splitting is small in unstrained quantum wells, leading to hh-lh band mixing. This introduces electron-light hole transitions, reducing the overall transition matrix element.
Later in this section we will discuss the influence of strain on the hh-lh splitting, but it can already be remarked from the transition matrix 3.7 that if the light-hole transitions are favored – that is if the lh-levels form the valence band maximum – TM-polarized gain is dominant with the transition matrix element at the band edge $|M_{lh}^{TM}|^2 = 2M_{b,lh}^2$ against $|M_{lh}^{TE}|^2 = 0.5M_{b,lh}^2$ for TE-polarization.

We have mentioned earlier that the gain performance of an active structure rises with increasing symmetry of the electron and hole effective mass. To conclude this paragraph on unstrained quantum wells, we prove this statement for quantum well active material. The modal gain per quantum well from the lowest energy subband transition can be derived as [9]:

$$G_{max} \sim \frac{m_c m_v}{m_c + m_v}. \tag{3.8}$$

Furthermore, for a nearly symmetric band structure, the transparency carrier density per quantum well can be expressed as $N_{tr} \sim \sqrt{m_c m_v}$ [10]. Consequently, the maximal differential gain at transparency is given by:

$$\frac{dG}{dN} = \frac{G_{max}}{N_{tr}} \sim \frac{\sqrt{m_c m_v}}{m_c + m_v}. \tag{3.9}$$

From these expressions it can be seen that the transparency carrier density reduces and the differential gain increases with decreasing hole effective mass. For equal electron and hole effective masses the differential gain is maximal.

3.1.1.3 Strained quantum wells

The conclusion of the previous paragraph on quantum well material is that a maximal polarization-selective gain can be obtained by increasing the hh-lh subband splitting and equalizing the electron and hole effective masses. Reshaping of the band structure to obtain a higher symmetry between the valence band and the conduction band by growing active material lattice-mismatched to the substrate has been proposed in the mid-80's [10, 11, 12]. For sufficiently thin layers below the critical thickness [13], the resulting biaxial in-plane strain causes tetragonal deformation of the cubic symmetry of the crystal lattice, modifying the valence subband structure but hardly affecting the conduction band. For growth on (001) substrates, a simple strain tensor ϵ is obtained with the only non-vanishing components given by:

$$\epsilon_{xx} = \epsilon_{yy} = \epsilon_{\parallel} = \frac{a_s - a_e}{a_e}, \tag{3.10}$$

and

$$\epsilon_{zz} = \epsilon_{\perp} = -2\frac{C_{12}}{C_{11}}\epsilon_{\parallel}, \tag{3.11}$$

where x and y are taken in the growth plane and z perpendicular to the growth plane. a_s and a_e are the relaxed lattice parameters of the substrate and the epitaxial layer respectively, and C_{ij} are components of the elastic stiffness tensor. For $a_e > a_s$, that is $\epsilon_{\parallel} < 0$, the epitaxial layer is under biaxial compressive strain, while for $a_s > a_e$ the strain is tensile. The total strain can be decomposed in a purely hydrostatic component:

$$\epsilon_{hy} = \frac{\Delta V}{V} = \epsilon_{xx} + \epsilon_{yy} + \epsilon_{zz} = 2\epsilon_{\parallel} + \epsilon_{\perp}, \tag{3.12}$$

and a purely axial component:

$$\epsilon_{ax} = \epsilon_{zz} - \epsilon_{xx} = \epsilon_{\perp} - \epsilon_{\parallel}. \tag{3.13}$$

The hydrostatic strain component shifts the conduction band by the energy:

$$\delta E_c(x,y) = a_c \epsilon_{hy}. \tag{3.14}$$

The valence bands are modified as:

$$\begin{aligned} \delta E_{hh}(x,y) &= -P_\epsilon - Q_\epsilon \\ \delta E_{lh}(x,y) &= -P_\epsilon + Q_\epsilon, \end{aligned} \tag{3.15}$$

where

$$\begin{aligned} P_\epsilon &= -a_v \epsilon_{hy} \\ Q_\epsilon &= b\epsilon_{ax}. \end{aligned} \tag{3.16}$$

a_c and a_v are the conduction-band and valence-band hydrostatic deformation potentials and b is the valence-band shear deformation potential. For the InGaAsP and InAlGaAs material systems a_v is positive while a_c and b are negative, and the ratio $\frac{C_{12}}{C_{11}}$ is in the order of 0.5 [14]. These expressions show that the hydrostatic strain component affects the bandgap. The most important effect for semiconductor lasers and amplifiers however arises from the axial component which affects the splitting between the heavy-hole and light-hole valence subband. Remember that the quantum size effect lifts the degeneracy of the valence subbands at the band edge, causing the hh-band to form the valence band maximum in unstrained quantum well active layers. In the case of compressive strain ($\epsilon_\parallel < 0$), Q_ϵ is negative which enhances this hh-lh splitting largely. This eliminates the band-mixing, which results in a reduction of the effective mass in the in-plane direction. For tensile strain, Q_ϵ is positive, hence the lh-levels are lifted with respect to the hh-states. In bulk material, this brings the lh-levels on top of the valence band, again causing a reduction of the in-plane valence band effective mass. In quantum wells the quantum confinement is counteracting this strain-induced valence band modification, which may result in an asymmetric bulk-like band structure with even an indirect valence band maximum [4]. Therefore, sufficiently high levels of tensile strain must be built-in to elevate the lh-level to the top of the valence band. This implies that relatively thick wells need to be used for a defect-free tensile strained quantum well structure.
The principle of strain induced band structure engineering is schematically depicted in figure 3.4, for a bulk active layer. Figure 3.5 shows three examples of the in-plane energy dispersions for the valence subbands in the quantum wells grown under 1.6% tensile strain (left), lattice matched (middle) and 1.2% compressive strain (right) in the $In_xGa_{1-x}As$/InGaAsP material system, clearly illustrating the strain-induced increase of the hh-lh splitting and the large reduction of the effective mass in the compressive strain case. An example of the evolution of the band structure with the amount of built-in strain is given in figure 3.6. Varying the Ga

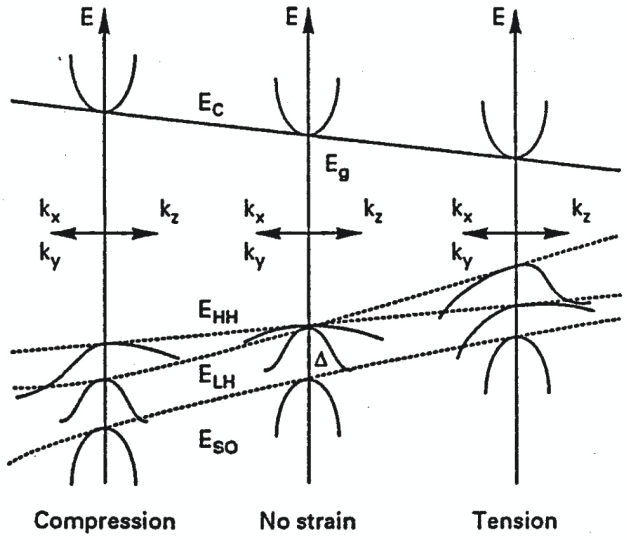

Figure 3.4: Schematic representation of the (bulk) band dispersion of a strained III-V semiconductor under compression, lattice matching, and tension.

content of $In_{1-x}Ga_xAs_{0.7}P_{0.3}$ quantum well material, grown on an InP substrate, results in compressively (x $<$ 0.32) or tensile strained (x $>$ 0.32) gain material, with the hh-levels or the lh-levels at the top of the valence band, respectively. For very high strain levels, the conduction band offset ΔE_c – the difference between the conduction band positions of the well and the adjacent layer – becomes negative, due to the difference in the hydrostatic deformation potentials [14]). In these so-called type II quantum wells, the electrons are confined to the barrier or separate confinement heterostructure layers, whereas the holes remain confined to the wells.

In conclusion, band structure reshaping by building in strain, either compressive or tensile strain, in a quantum well active layer structure lowers the in-plane valence band effective mass, hence increases the symmetry between the valence band and the conduction band. This largely enhances the gain performance of the structure. Furthermore, strain can increase the splitting between the heavy-hole and light-hole subbands and as such enables for polarization-selective gain; TE-gain for compressively strained structures and TM-polarized gain favored for active layers with (a large enough) built-in tensile strain. The latter is exactly what we want to obtain for the TM-mode amplifying waveguide optical isolator. In the next section we will discuss the tensile strained multiple quantum well structures developed for this specific application.

We end this section with the remark that the decrease of the effective mass of the valence band in strained-layer quantum wells is expected to enhance the performance of active structures further by reducing optical and carrier loss mechanisms such as the non-radiative Auger recombination and the intervalence band absorption. This is attributed to the fact that the carriers are confined to smaller

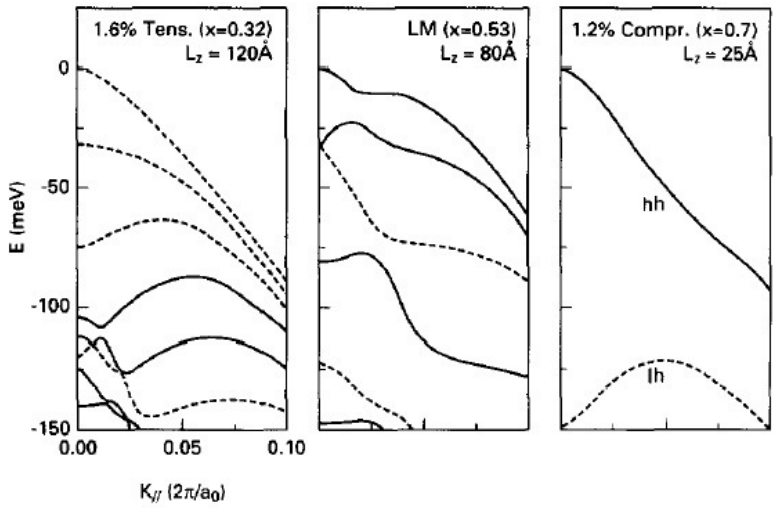

Figure 3.5: Calculated band structure of 1.6% tensile-strained (x = 0.32), lattice-matched (x = 0.53), and 1.2% compressively strained (x = 0.7) $In_xGa_{1-x}As/InGaAsP$ in the left, middle, and right figure, respectively. The well width L_z is chosen for emission at 1500nm wavelength. The solid and dashed lines denote the hh and lh subbands, respectively [4].

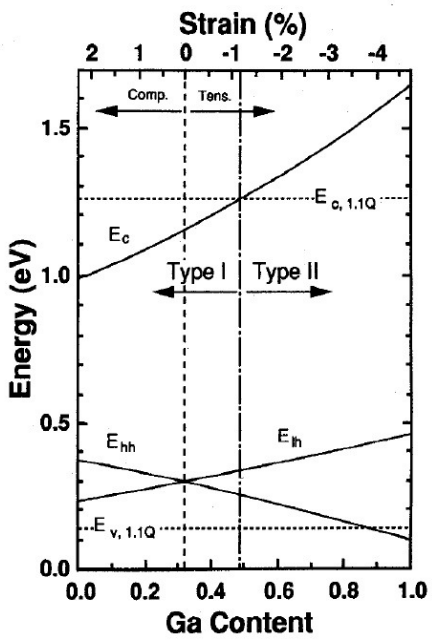

Figure 3.6: Calculated conduction and valence band diagram for $In_{1-x}Ga_xAs_{0.7}P_{0.3}$/InP quantum well material with varying Ga content [17].

values of the **k**-vector, causing a large reduction in the number of transitions involved in Auger recombination and intervalence band absorption [4].

3.1.2 Gain material for the TM-mode isolator

The development of tensile strained multiple quantum well (MQW) gain material at 1300nm wavelength has been described earlier by Vanwolleghem [15], both from a theoretical and an experimental point of view. Tensile strained MQW structures in $In_{1-x}Ga_xAs_yP_{1-y}$ and $In_{1-x-y}Ga_xAl_yAs$ material systems have been investigated experimentally, with measurements of the differential gain and the external quantum efficiency as a function of the applied strain and the number of quantum wells. We will not repeat this work here, but instead give a summary of the main results. Especially the experimental gain-current density relations of the different quantum well structures are of interest here, since they serve as important input in the simulations of the amplifying waveguide optical isolator.

The most common III-V semiconductor material system for light emission in the telecom wavelength window (1310nm - 1550nm) is $In_{1-x}Ga_xAs_yP_{1-y}$-InP. The InGaAsP strained quantum wells have been grown by gas source molecular beam epitaxy (GSMBE) under standard growth conditions. By optimizing the (compressive) strain compensation in the barrier layers up to fifteen 12nm-thick QWs with a tensile strain of -1.1% can be stacked. X-ray diffraction, room-temperature photoluminescence measurements and transmission electron microscopy observation indicate good structural properties of these heterostructures [16]. The gain performance of the quantum well active layers can straightforwardly be evaluated through laser measurements. Broad-area lasers have been fabricated with an amplifying core comprising -1.1% tensile strained InGaAsP quantum wells emitting at 1310nm confined by +0.3% compressively strained barriers (λ_g = 1060nm) and enclosed within two undoped lattice-matched InGaAsP separate confinement heterostructure (SCH) layers (λ_g = 1030nm). The number of wells varies up to 15 (3, 6, 9, 12, 15). TM-polarized lasing has been observed on all samples. The threshold current density was found to be minimal for 6 QWs and equal to 0.8kA/cm^2, measured on 600μm $\times$ 50μm broad area lasers. The T_0 characteristic temperature[1] is 75K in the range of 20°C - 80°C. With these numbers the tensile strained MQW material has a performance comparable to standard compressively strained InGaAsP/InP 1300nm TE-lasers [17, 18, 19]. Based on the evaluation of the threshold current density and the external quantum efficiency as a function of the cavity length an estimation of the internal optical loss can be made [3], and the gain-current density relationship can be deduced. This last expression is plotted in figure 3.7 for 3 QWs and 6 QWs, with indication of the fitted logarithmic relationship (equation 3.6). It can easily be seen that the differential gain and the transparency current both increase when shifting from 3 to 6 wells, which is as can be expected due to the increased confinement of the optical mode in the ac-

[1] The threshold current density of a laser obeys the following phenomenological relation:

$$J_{th} = J_0 exp\left(\frac{T}{T_0}\right). \tag{3.17}$$

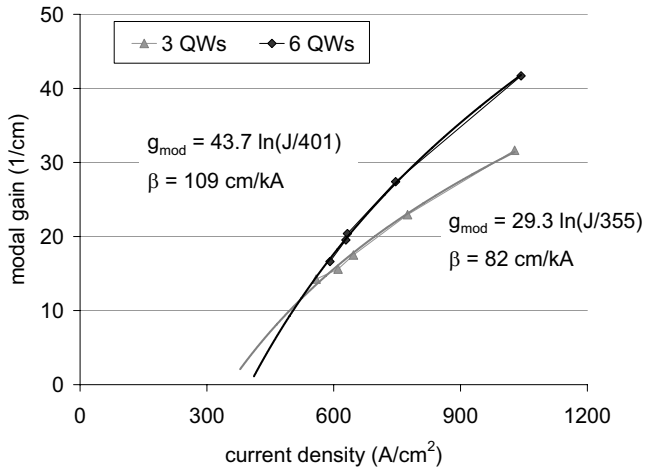

Figure 3.7: Modal gain-current relationship obtained via threshold measurements of broad area lasers with different lengths for the 3QW and 6QW samples (at room temperature).

tive layers [20]. At quantum well numbers higher than six, the total threshold current density increases [16], hence the gain performance reduces.

While these demonstrated gain levels are promising and, as is discussed in chapter 4, have allowed for the first demonstration of the concept of the TM-mode amplifying waveguide optical isolator, a substantial improvement is required to obtain optical transparency for realistic injection current values. Therefore, we have shifted our attention from the conventional $In_{1-x}Ga_xAs_yP_{1-y}$ QW active material system to the $In_{1-x-y}Al_yGa_xAs$ system. The latter material system has been reported to provide superior gain performance and reduced temperature sensitivity [21, 22]. This can be attributed to a better electron and hole confinement in the wells as a result of increased band offsets and a more favorable band-offset ratio. The difference between the bandgap of the barriers and the bandgap of the wells ΔE_g is divided between the conduction and the valence bands, denoted as the conduction band offset ΔE_c and the valence band offset ΔE_v respectively.[2] The ratio $\frac{\Delta E_c}{\Delta E_v}$, termed the band-offset ratio, has a characteristic intrinsic value for a particular well-barrier system. In quantum well structures, carrier leakage through the barrier layer is one important factor limiting the performance, especially at high current density or high temperature. Due to the difference in effective mass, the electron, with its lighter effective mass, requires a tighter confinement than the hole. Hence, the requirement $\Delta E_c > \Delta E_v$ enhances the active layer performance. In addition, the value of the valence band offset ΔE_v should not be too high, to allow for the heavier holes to equally occupy all the QWs [22], especially for an active region containing a large number of wells. The conventional InGaAsP-InP QW material system has a small band-offset ratio of about 0.67 or a conduction band offset of E_c = *0.4* E_g. In contrast, the band-offset ratio of the

[2]The bandgap energy obviously varies for the different transitions between the discrete energy levels in the quantum confined layers, i.e. electron-heavy hole (c-hh) or electron-light hole (c-lh) transitions.

InAlGaAs-InP QW system is much larger with $\frac{\Delta E_c}{\Delta E_v} = 2.57$ or $E_c = 0.72E_g$, which results in a better electron confinement and an equal hole filling in the QWs. We remark that these values of the band offsets are calculated with respect to InP barriers and are average numbers. The band offset can be modified to some extent by varying the alloy composition [14].
The high band-offset ratio has potentially another important implication for the gain performance of InAlGaAs QWs. Due to the low valence band offset it is very likely that the heavy-hole valence band offset between well and barrier becomes negative and the heavy holes are located in the barrier. The result of this mechanism – called type II behavior – is that the negative influence of hh-carriers on the lh-band curvature at the band edge can be completely eliminated, resulting in a large decrease of the in-plane effective mass of the light holes. As explained earlier, this enhances the differential gain and lowers the transparency current density. Type II band line-up for the heavy holes cannot be induced in the InGaAsP QW system for realistic strain values.
Apart from a more favorable band offset ratio, the $In_{1-x-y}Al_yGa_xAs$ quaternary alloy system has the advantage over $In_{1-x}Ga_xAs_yP_{1-y}$ of a higher flexibility to control the properties of the heterostructure. Indeed, if we assume the notation $(Al_zGa_{1-z})_uIn_{1-u}As$, the amount of strain is mainly determined by the number u – the indium mole fraction – while the bandgap wavelength can be adjusted by varying the Al/Ga ratio, described by z. This is due to the fact that the lattice constant of GaAs and AlAs differ only by 0.12%. Figure 3.8 shows the strain and bandgap energy versus the gallium (x) and arsenic (y) mole fraction for the $In_{1-x}Ga_xAs_yP_{1-y}$ material system (left) and versus the gallium (x) and aluminium (y) mole fraction for $In_{1-x-y}Al_yGa_xAs$ (right) [14]. In the top graphs the contours of constant strain and bandgap energy are plotted, while the lines in the bottom figures are contours of constant x and y values. In these figures the bandgap with the smallest energy is presented (i.e. c-hh for compressive strain, c-lh for tensile strain) and the bandgap shift due to strain effects is taken into account. The strain is calculated with respect to InP and negative values of strain are tensile. These plots clearly illustrate the fact that in the Al-based system the strain and bandgap energy can be controlled separately through the Al/Ga ratio, respectively the In mole fraction.
A third advantage of the $In_{1-x-y}Al_yGa_xAs$ active system is from a pure technological point of view. The fact that the Al-based system contains only one group V element (As) facilitates to obtain abrupt QW interfaces. In the $In_{1-x}Ga_xAs_yP_{1-y}$ system As-P exchanges are often observed, which can cause undulations of the QWs interfaces [16].
In conclusion, despite the fact that the aluminium element is more difficult to handle, shifting from $In_{1-x}Ga_xAs_yP_{1-y}$ to the $In_{1-x-y}Al_yGa_xAs$ material system holds the promise of the large improvement of the active region performance required to realize a TM-mode amplifying waveguide optical isolator.

Our co-workers at Alcatel-Thales III-V Lab have developed tensile strained InAlGaAs-InP MQW active structures, emitting around a wavelength of 1300nm [23]. The material has been grown by metal-organic vapor phase epitaxy (MOVPE). The quality of the fabricated structures has been checked and confirmed through high resolution X-ray diffraction, and the absence of degradation has been ob-

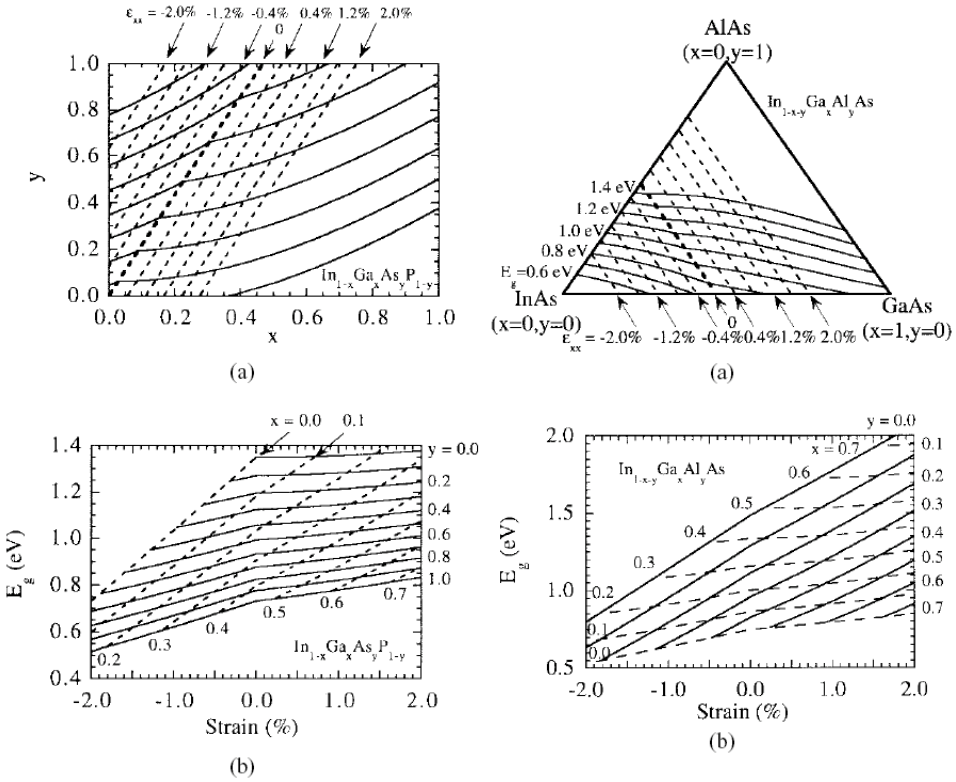

Figure 3.8: Strain and bandgap energy versus Ga (x) *and As* (y) *mole fraction for the $In_{1-x}Ga_xAs_yP_{1-y}$ material system (left) and versus the Ga* (x) *and Al* (y) *mole fraction for $In_{1-x-y}Al_yGa_xAs$ (right). In graphs (a) contours of constant strain and bandgap energy are plotted while in (b) the lines are contours of constant* x *and* y *values.*

served even at very high strain values of -1.65% [23]. The QW tensile strain has been varied between -0.72% and -1.65%, partially compensated by the fixed +0.64% compressive strain in the barrier layers. The optical performance has again been evaluated by measurements on fabricated broad area lasers. The active region consists of six 10nm-thick, undoped $In_{1-x-y}Al_yGa_xAs$ tensile strained wells surrounded by seven 20nm-thick $In_{0.62}Al_{0.30}Ga_{0.08}As$ barriers. Lattice-matched InAlGaAs and InGaAsP layers of 40nm thickness serve as separate confinement heterostructure layers (SCH) above and below the MQW active region, respectively. This asymmetric choice of SCH layer material might enhance the carrier injection in the active region. Indeed, the high conduction band offset of InAlGaAs on InP and the high valence band offset of InGaAsP on InP increase the barrier height for electrons and holes respectively, resulting in a better carrier confinement in the MQW region sandwiched between both SCH layers. Experiments show that the improvement with respect to symmetric InGaAsP SCH layers is negligible, but that with two InAlGaAs SCH layers the performance decreases significantly [24].

Photoluminescence measurements have indicated that the first electron-light hole (c1-lh1) and the first electron-heavy hole (c1-hh1) transitions are present, with a wavelength separation that obviously increases with strain. The c1-lh1 transition becomes dominant at a tensile strain of -0.3%. Furthermore, tensile strain higher than -0.77% results in a type II band line-up for heavy holes.
Broad area lasers, with a stripe width of 100μm, with different cavity lengths have been cleaved and the threshold current density and the external quantum efficiency have been recorded at various controlled temperatures. For the higher strain-valued lasers a characteristic temperature T_0 of 80K has been found, which illustrates the decrease of the temperature sensitivity with respect to the InGaAsP QW system where a T_0 of 75K has been found. The experimental threshold and efficiency data combined with the logarithmic gain model of equation 3.6 yield a room temperature transparency current density of 350A/cm^2, i.e. 58.3A/cm^2 per well, a value which is quasi-independent of the amount of strain.[3] Remember that for the 6QWs InGaAsP-InP broad area lasers a transparency current density of 400A/cm^2 has been extracted. The evolution of the differential gain β with tensile strain is plotted in figure 3.9. Increasing the strain clearly enhances the differential gain, with a doubling when moving from -0.72% to -1.65%. This improvement can only be explained by an increase of the c1-lh1 transition strength as a function of strain, as was theoretically predicted in section 3.1.1. The differential gain of 253cm/kA is an increase by more than a factor 2 compared to the 6QWs InGaAsP active structure. Whereas in figure 3.9 the differential gain seems to 'saturate' at high strain values, it should not immediately be concluded from this one series of measurements that the upper limit performance has been reached. Variation of the number of quantum wells is one possible way to further optimize the tensile strained InAlGaAs QW active material.
In summary, tensile strained multiple quantum wells have successfully been developed in the InAlGaAs-InP material system. Experimental results on broad area lasers confirm the theoretically predicted enhanced performance with respect to InGaAsP QW active material. The Al-based system outperforms the traditional P-based system, with a higher differential gain, reduced transparency and threshold current densities and an increased internal efficiency.[4] Furthermore, an extensive strain study on InAlGaAs QWs has confirmed that the TM differential gain increases largely as a function of the amount of tensile strain.

We conclude this section on QW gain material with the following remark regarding the gain-current density relation used during the isolator simulations. Not one but two subsequent runs of the InAlGaAs tensile strained active material have been completed. All results mentioned so far are from the second (more optimized) run. However, at the time of designing the isolator demonstrators only the first run was fabricated and characterized. The corresponding relationship between gain and current density is plotted in figure 3.10, measured on broad area lasers with six 10nm-thick -1.25% tensile strained $In_{1-x-y}Al_yGa_xAs$ wells, sur-

[3] This value is the total transparency current density J_0 instead of the radiative transparency current density J_{tr} appearing in equation 3.6, which are related as: $J_0 = \frac{J_{tr}}{\eta_i}$, with η_i the internal quantum efficiency.

[4] The last two parameters have not been discussed here. In references [16, 23, 15] the experimental results are given that validate this statement.

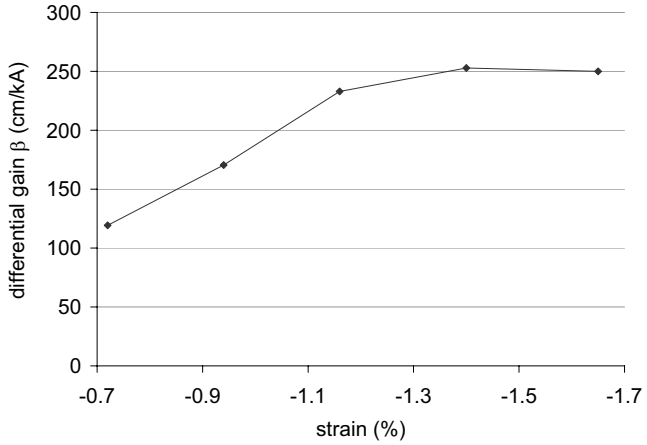

Figure 3.9: Evolution of the gain performance of the 1300nm InAlGaAs material system as a function of the tensile strain, measured on 6QWs broad area lasers. An increase of the strain from -0.72% to -1.65% results in a doubling of the differential gain.

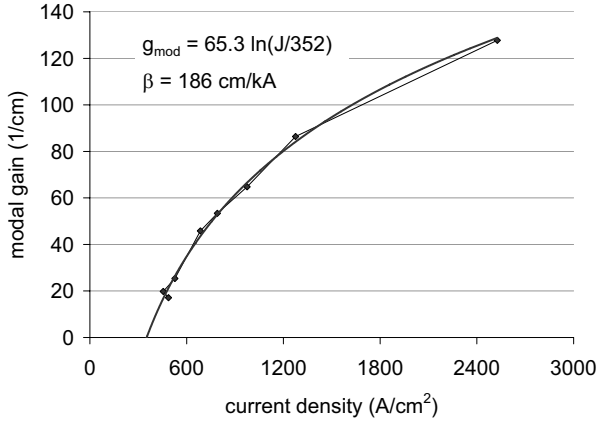

Figure 3.10: Modal gain-current relationship of 6QWs -1.25% tensile strained InAlGaAs-InP active material (first run) obtained via threshold measurements of broad area lasers with different lengths (at room temperature).

rounded by 20.8nm-thick +0.6% compressively strained barriers. The differential gain of 186cm/kA clearly is lower than the value of an equally strained structure of the second run, given in figure 3.9. We believe this is mainly due to an overestimate of the internal loss when using threshold current density and external quantum efficiency data measured on very short cavity lasers (down to 95μm). In any case, the possibly underestimated gain-current density relationship of figure 3.10 has been used in the calculations. Combining this with the calculated value of the TM modal confinement in the 6 quantum wells ($\Gamma_{TM,6QWs}$ = *0.14*) yields

the following expression for the fundamental QW material gain G_{mat} (in units of $1/\text{cm}$) in terms of the total injected current density J_{tot} (expressed in kA/cm^2):

$$G_{mat} = \frac{65.3}{\Gamma_{6QW}^{TM}} ln\left(\frac{6}{N_w}\frac{J_{tot}}{0.352}\right) = 466 ln\left(\frac{6}{N_w}\frac{J_{tot}}{0.352}\right), \tag{3.18}$$

with N_w the number of wells in the MQW core. This equation obviously assumes that the injection and the internal quantum efficiency are independent of the number of wells, and that the carrier concentration is uniformly distributed over the wells, which is a safe assumption for a number of wells not much exceeding ten. This experimentally determined gain-current relationship has been used as input for the isolator design calculations.

3.2 Ferromagnetic metal choice

Ferromagnetic metals, with their high optical absorption at telecom wavelengths, have only recently been considered for magnetooptic devices operating in the infrared spectral range. Instead, this class of materials has been studied for decades in the area of magnetooptic recording with visible wavelengths as the region of intrest. As a consequence, very little is known about the magnetooptic properties of ferromagnetic metals at telecom wavelengths, except for an old Russian research initiative [25, 26]. In addition, for magnetooptic recording the Kerr rotation Φ_K (defined in equation 2.34) is the important parameter, whereas for the isolator application the Kerr ellipticity angle:

$$\Psi_K = Re\left(\frac{Qn}{n^2-1}\right), \tag{3.19}$$

is equally important, but far less tabulated in literature. Therefore, to enable accurate design of the waveguide isolator, the only valid option was to characterize these materials ourselves. These experiments have been done in collaboration with IEF [27]. For the selection of candidate materials we must rely on the tabulated values of the Kerr rotation Φ_K at visible wavelengths. Based on this data the Co_xFe_{1-x} alloy system turns out to be the most promising. In table 3.2 the magnetooptic Kerr rotation of some Co_xFe_{1-x} compositions is given, as measured by Bushow [28]. These numbers suggest that the equiatomic $Co_{50}Fe_{50}$ is magnetooptically the strongest. Experiments discussed later in this section indicate that $Co_{50}Fe_{50}$ is indeed the preferred alloy for the InP-based waveguide optical isolator.

3.2.1 Experimental extraction of the permittivity tensor elements of ferromagnetic metals

The elements of the permittivity tensor of a magnetooptic material depend on the magnetization $\boldsymbol{M}$ as:

$$\epsilon_{ik} = \epsilon_{ik}^0 - j e_{ikl} a_{lq} M_q + \delta_{iklm} M_l M_m, \tag{3.20}$$

Alloy	Φ_K (deg) $\lambda = 633$ nm	Φ_K (deg) $\lambda = 830$ nm
Fe	–0.41	–0.53
$Fe_{75}Co_{25}$	–0.42	–0.46
$Fe_{50}Co_{50}$	–0.51	–0.60
$Fe_{25}Co_{75}$	–0.48	–0.58
Co	–0.30	–0.36

Table 3.1: The polar Kerr rotations (at normal incidence) at two wavelengths for a few members of the Co_xFe_{1-x} alloy system [28].

where e_{ikl} is the antisymmetric 3D-order pseudotensor (the Levi-Civita tensor). The first term of the right-hand side is the zeroth-order permittivity tensor including optical anisotropy, a_{lq} is the gyrotropy tensor defining the gyration vector $g_l = a_{lq}M_q$, and the third term includes the fourth-order tensor δ_{iklm} which describes the quadratic magnetic optical anisotropy. The polar tensors ϵ^0_{ik}, a_{lq} and δ_{iklm} are defined by the crystallographic symmetry [29]. In this work we only consider sputtered polycrystalline ferromagnets which can be considered as optically isotropic with negligible magnetic optical anisotropy. In this case a material is described by two complex constants: the dielectric permittivity constant ϵ^0 and the magnetooptic Voigt parameter Q. The latter is related to the magnitude of the gyration vector $\boldsymbol{g}$ as $Q = \frac{g}{\epsilon^0}$. As such, the optical and magnetooptic characterization of these magnetooptic materials comes down to the measurement of two complex parameters. These values can be obtained through (generalized) ellipsometry.
The idea behind ellipsometry is the extraction of the optical properties of a stack of materials through the measurement of the change of the polarization state undergone at reflection off this stack by an incident light beam of a known specific polarization state, and with a known wavelength and incidence angle. In the case of optically isotropic materials this change, characterized by the rotation angle of the polarization ellipse Ψ and the phase difference Δ between *s* and *p* waves after reflection, relates to the Fresnel coefficients as:

$$tan\Psi\ exp(j\Delta) = \frac{r_p}{r_s}. \tag{3.21}$$

Numerical fitting of the obtained data to an optical model yields accurate values of the optical constants and thicknesses of the layer stack. If the stack contains a magnetooptic layer – in which case the technique is called generalized ellipsometry – the reflectivity matrix is a 2×2 complex matrix:

$$\mathbf{R} = \begin{pmatrix} r_{ss} & r_{ps} \\ r_{sp} & r_{pp} \end{pmatrix}, \tag{3.22}$$

and the observed phase shift now represents the combined effects of reflection and magnetooptic rotation. A multitude of methods exist to separate the two effects [30, 31]. Our co-workers at IEF have performed the (magneto-)optic characterization of the ferromagnetic metals using a technique of photoelastic modulated

Composition	n	κ	g′	g″
$Co_{90}Fe_{10}$	4.65±0.1	4.82±0.03	-1.7±0.2	-1.05±0.1
$Co_{50}Fe_{50}$	3.2±0.08	4.5±0.04	-1.7±0.2	-1.7±0.1
Fe	3.82±0.27	3.5±0.05	-1.4±0.3	-0.75±0.17

Table 3.2: Extracted values of the optical and magnetooptic parameters for three Co_xFe_{1-x} compositions at 1310nm.

ellipsometry. For a detailed description of the measurement setup, the experiments and the numerical fitting procedure we refer to their work [27, 15]. The complex refractive index *n-jκ* and the gyrotropy constant *g = g′-jg″* of three alloys of the Co_xFe_{1-x} system have been determined experimentally and the results are given in table 3.2.1. The main uncertainty on the magnetooptic data stems from the uncertainty on the values of the refractive index. In the next section we evaluate the magnetooptic quality of these three compositions and deduce which is the preferred material for the amplifying waveguide optical isolator.
Important issue to interpret the experimental data is the sign convention that is used for the optical and magnetooptic constants. With both ϵ and g complex quantities it has to be decided whether to take a positive or a negative imaginary part. A second sign choice is whether to use a plus or a minus sign for the off-diagonal element ϵ_{xy}. Atkinson [32] argued on the basis of the casuality principle that a logical sign scheme exists. If we assume the time dependence of the electromagnetic fields to be described by *exp(+jωt)* this scheme reads:

$$\begin{aligned} \epsilon^0 &= \epsilon'^0 - j\epsilon''^0 = (n - j\kappa)^2, \\ g &= g' - jg'', \\ \hat{\epsilon} &= \epsilon_0 \begin{pmatrix} \epsilon^0 & +jg & 0 \\ -jg & \epsilon^0 & 0 \\ 0 & 0 & \epsilon^0 \end{pmatrix}. \end{aligned} \tag{3.23}$$

The sign of the other magnetooptic off-diagonal elements ϵ_{yz} and ϵ_{xz} obviously follow from that of ϵ_{xy} through antisymmetric cyclic permutation of the Levi-Civita tensor.

3.2.2 Discussion of the ferromagnetic materials

From the experimental metal properties tabulated in table 3.2.1 the following reflections can be made about the quality of the tested Co_xFe_{1-x} alloys. Based on the magnitude of the gyrotropy constant $|g|$ it can be concluded that the equiatomic composition $Co_{50}Fe_{50}$ is magnetooptically the strongest among the three examined alloys, next is the Co-rich material and pure iron (Fe) seems to be the weakest. However, this does not at all ensure that the same 'sequence' holds for the application of these materials in a waveguide optical isolator. Indeed, as has been proven in chapter 2 (see equation 2.114) the non-reciprocal phase shift $\Delta\beta$ is proportional to the Voigt parameter $Q = \frac{g}{\epsilon^0}$ rather than to the gyrotropy constant g alone. In addition, specifically for the amplifying waveguide optical isolator the

Composition	$\frac{g}{\epsilon^0}$	$\frac{\lvert g\rvert}{n\kappa}$	$\frac{\Delta\alpha}{\alpha}\Big\vert_{max}$ (%)
$Co_{90}Fe_{10}$	-0.0220 -0.0387j	0.088	9.2
$Co_{50}Fe_{50}$	-0.0344 -0.0710j	0.167	18.2
Fe	-0.0324 -0.0495j	0.119	12.6

Table 3.3: Magnetooptic performance parameters for three Co_xFe_{1-x} alloys. The last column gives the upper limit of the isolation-to-loss ratio, calculated according to equation 3.24.

isolation-to-loss ratio is determined by the ratio $\frac{|g|}{n\kappa}$ of the magnetooptic metal. Remember from chapter 2 that a fundamental limit on this figure-of-merit (FoM) function is expressed by:

$$\frac{\Delta\alpha}{\alpha}\bigg|_{max} = \frac{-2}{\frac{-2n\kappa}{|g|}+1}. \tag{3.24}$$

The third column of table 3.2.2 gives the values of $\frac{|g|}{n\kappa}$ for the three ferromagnetic alloys, and in the last column the corresponding upper limit on the isolation-to-loss ratio is tabulated. Based on the numbers in table 3.2.2 it can again be concluded that $Co_{50}Fe_{50}$ is the preferred metal alloy. Furthermore, despite a much lower magnitude of the gyrotropy constant a non-reciprocal device with an iron film as the source of the non-reciprocity performs potentially better than one with the Co-rich alloy. Potentially, as there are two other important issues that should be taken into account when making the ferromagnetic metal choice for the waveguide isolator; the phase relation between the gyrotropy and the modal electric field amplitude and the polarization of the TM mode in the metal layer, both of which depend heavily on the optical and/or magnetooptic parameters of the metal. We shall now discuss these, starting with the phase relation.
Equation 2.112 for the non-reciprocal loss shift $\Delta\alpha$ expresses that $\Delta\alpha$ depends sinusoidally on the phase angle of the gyrotropy constant $\angle g$ and the phase angle of the transverse electric field amplitude of the unperturbed TM guided mode at the metal interface $\angle E_x^{(0)}(x_{i+})$ as:

$$\Delta\alpha = \frac{|g||E_x^{(0)}(x_{i+})|^2}{Z_{vac}|n_{eff}|}\ sin(\angle g + 2\angle E_x^{(0)}(x_{i+})), \tag{3.25}$$

with Z_{vac} the vacuum impedance and n_{eff} the effective index of the unperturbed guided mode. To maximize $\Delta\alpha$ the phase angle of g must therefore obey the condition:

$$\angle g = \frac{\pi}{2} - 2\angle E_x^{(0)}(x_{i+}) + m\pi. \tag{3.26}$$

Now, as elaborated in chapter 2 the phase of the transverse electric field amplitude can be altered by changing the cladding material, but remains quasi-constant when changing the thickness of the cladding. Furthermore, the optical constants of the metal alloy also have a (moderate) influence on the value of $\angle E_x^{(0)}(x_{i+})$. To evaluate the intrinsic quality of the three Co_xFe_{1-x} alloys with respect to this

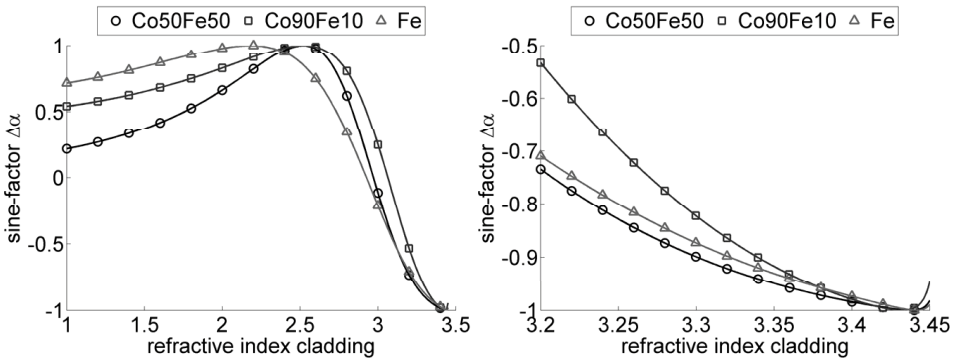

Figure 3.11: Evolution of $sin(\angle g + 2\angle E_x^{(0)}(x_{i+}))$ [equation (3.25)] with the refractive index of the cladding layer of a four-layer magnetooptic slab waveguide. The different graphs correspond to a different Co_xFe_{1-x} alloy as the top layer. The right graph is a detailed view for InP-related cladding layers.

phase condition, a four-layer slab waveguide has been simulated with each of the three metals as a top layer. The waveguide core is a 300nm passive InAlGaAs layer ($n_{InAlGaAs}$ = *3.5*).[5] The refractive index of the substrate and the buffer material is being altered between 1.0 (air) and the core index and the corresponding change of the sine factor of equation 3.25 is being monitored. The thickness of the buffer layer between the core and the metal is practically arbitrary for these simulations and is fixed at 500nm. The simulation results are plotted in figure 3.11, with on the right a detailed view for InP and InP-related cladding materials ($n_{InP,1300nm}$ = 3.2). It can be seen that for all three alloys the variation of the sine factor is similar, with a maximum of one at intermediate cladding indices, passing through zero around n_{clad} = *3.0* and evolving towards another maximum (in absolute value) at a low contrast between core and cladding. Zooming in on the index range relevant for InP-based devices (right graph) shows that the three alloys have a perfect phase match at the same index value close to the core index of 3.5. This refractive index value can be tuned to some extent by changing the core index and thickness.[6] The main difference between the alloys is the width of the maximum; Fe and $Co_{50}Fe_{50}$ have a much broader maximum than the Co-rich metal. For an actual device, for which the cladding index cannot simply be chosen arbitrarily due to the requirement of lattice-matching, this is obviously an advantage. In any case, from figure 3.11 it can be concluded that an InP cladding is for none of the examined materials the best option. Instead a higher index material should be chosen. In the next section, we will discuss how the addition of a ohmic contact layer enhances the performance by optimizing the phase relation between gyrotropy and electrical field.

[5]This can be considered as a suitable one-layer equivalent of the 9 well InAlGaAs MQW region used as the core of the actual amplifying waveguide optical isolator.

[6]However, it must be remarked that specifically for the amplifying waveguide optical isolator the composition and the thickness of the MQW active core region have been optimized for maximal gain performance, hence should not be considered as variable.

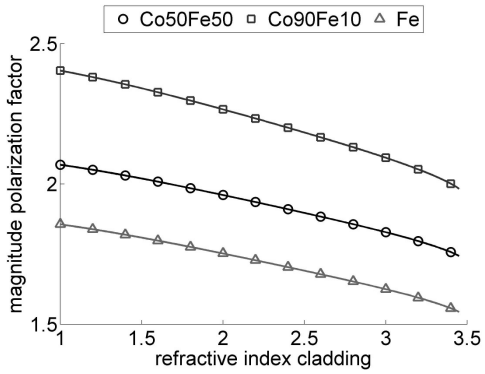

Figure 3.12: Evolution of the magnitude of the polarization factor $|\chi|$ with the refractive index of the cladding layer of a four-layer magnetooptic slab waveguide. The different graphs correspond to a different Co_xFe_{1-x} alloy as the top layer.

On the lower index side the variation is slow and there is a very large difference between the three alloys, with Fe as the best performing material. This is an important observation in view of the realization of a high index-contrast isolator. One could for example think of a (passive) non-reciprocal component based on a silicon-on-insulator (SOI) waveguide covered with a ferromagnetic metal film. This idea is elaborated in chapter 6.

The second issue to be discussed is the polarization of the TM guided mode in the metal cladding. Remember from chapter 2 that this polarization, described by the ratio of the longitudinal electric field component E_z to the transverse field component E_x denoted as χ and constant in the top and bottom cladding of a slab waveguide, must be as close as possible to a circular polarization, which implies that the magnitude of χ must approach one. In section 2.3 it has been derived that $|\chi|$ is entirely determined by the complex refractive index of the metal and the modal effective index. As such, we expect the polarization factor to differ significantly for the three Co_xFe_{1-x} alloys. Indeed, identical simulations as the ones used to evaluate the phase relation result in the plots of figure 3.12 describing the evolution of $|\chi|$ with the buffer material index for a four-layer slab with a Co_xFe_{1-x} alloy as the top layer. It needs no explanation that pure iron is by far the preferred material from a polarization point of view, followed by $Co_{50}Fe_{50}$. The slight decrease of $|\chi|$ as a function of the cladding index is entirely due to a corresponding rise of the modal effective index. The aspect of modal polarization in the metal hence additionally favors Fe with respect to $Co_{90}Fe_{10}$ – apart from the higher value of $\frac{|g|}{n\kappa}$.

So far we have only examined the quality of the ferromagnetic metal alloys from a rather fundamental approach. The implications of the metal choice on the practical performance of an amplifying waveguide isolator will be highlighted later in this chapter when we treat the entire design of the isolator layer structure (section 3.4). However, it shouldn't come as a surprise that the general trends observed here are repeated in the practical figure-of-merit functions. We can therefore consider this study of Co_xFe_{1-x}-alloys as finalized. In conclusion, the opti-

cal and magnetooptic parameters of three Co_xFe_{1-x} compositions have been experimentally extracted. Specifically for structures with a low index contrast the equiatomic $Co_{50}Fe_{50}$ alloy is by far the best option, both from a purely magnetooptic point of view, i.e. highest *Q*-value, as for application in an optical isolator, i.e. highest $\frac{|g|}{n\kappa}$-value.[7] Moreover, it has been proven that looking solely at the off-diagonal magnetooptic perturbation to the permittivity tensor, described by g, doesn't necessarily lead to the correct conclusion about the quality of a material for a non-reciprocal device. Instead the diagonal permittivity elements – the optical parameters of the material – play an equally important role. As such Fe would be preferred over $Co_{90}Fe_{10}$, despite the much lower magnitude of the gyrotropy constant |g|. A third point that determines the suitability of a ferromagnetic metal is its interaction with the guided mode, which is reflected by the modal polarization in the metal and phase relation between the electric field amplitude and the gyrotropy.

Apart from Co_xFe_{1-x}-alloys, manganese-based compounds have been investigated as the source of the non-reciprocal phase shift, more specifically MnAs and MnSb. The optical and magnetooptic parameters of MnSb have been determined experimentally using the ellipsometer described earlier. Despite a significant uncertainty on the extracted values,[8] these measurements show that both the real and imaginary part of the gyrotropy constant of MnSb are only a few percent of the corresponding values of $Co_{50}Fe_{50}$, at 1300nm wavelength. For MnAs, we rely on experiments done by Amemiya [33]. With a gyrotropy g constant at 1300nm equal to -0.1+1.2j [34], it can be concluded that also MnAs does not at all outperform the equiatomic $Co_{50}Fe_{50}$.

3.3 Magnetooptic metal contact optimization

The simplest amplifying waveguide optical isolator configuration operating for TM-polarized light is illustrated in figure 3.1. In this scheme the magnetooptic metal not only acts as the source of the non-reciprocal effect, but also serves as the electrical contact for the underlying semiconductor optical amplifier. Consequently one of the issues that needs to be treated is the development of an ohmic contact for application in the amplifying waveguide optical isolator. In this section we will discuss why this is not a trivial task and show that a compromise is to be made between good electrical behavior and good (magneto)-optical performance.

The physical parameter that describes the quality of a metal-semiconductor contact is the contact resistivity ρ_c, defined as:

$$\rho_c = \left[\frac{\partial J}{\partial V}\right]^{-1}_{V=0} = \frac{kT}{qJ_s} \tag{3.27}$$

with J the current density and V the voltage across the contact, J_s the saturation current of the metal-semiconductor contact, k the Boltzmann constant, T the temperature and q the electron charge. If the contact resistivity is low (order

[7] Despite its less favorable polarization factor compared to pure iron.
[8] Probably related to the oxidation of the capping layer

Layer	Material	Thickness (nm)
Metallization	Au	100
MO metal	$Co_{50}Fe_{50}$	50
Contact	$In_{0.54}Ga_{0.46}As$	variable
Contact	$In_{0.81}Ga_{0.19}As_{0.41}P_{0.59}$	variable
Cladding	InP	400
SCH	$In_{0.86}Ga_{0.14}As_{0.32}P_{0.68}$	0
Barrier	InAlGaAs (λ_g = 1100nm, +0.62% strain)	20
Well	InAlGaAs (λ_g = 1288nm, -1.6% strain)	10 x 9
Barrier	InAlGaAs (λ_g = 1100nm, +0.62% strain)	20 x 9
SCH	$In_{0.86}Ga_{0.14}As_{0.32}P_{0.68}$	0
Cladding	InP	1000
Substrate	InP	

Table 3.4: Details of the isolator layer structure used in the simulations for the magnetooptic metal contact optimization.

$10^{-5}\Omega cm^2$) – or equivalent the saturation current high – implying that the contacted device is not substantially influenced by the metal-semiconductor contact, the contact is said to be ohmic. The saturation current increases with diminishing barrier height between metal and semiconductor and with increasing dopant levels of the semiconductor layer in contact with the metal. The latter is due to the increase of the tunneling current contribution to the saturation current. Due to pinning of the Fermi level in III-V semiconductors [35], the barrier height and consequently the contact resistivity are quasi independent of the work function of the metal, hence the unusual choice of the contact metal – a ferromagnetic metal – is not expected to deteriorate the contact quality. Furthermore, as one can expect that the p-barrier height is about one third of the bandgap energy [36], a semiconductor contact material with a small bandgap is preferable for an ohmic electrical contact. The material lattice-matched to InP with the lowest bandgap is $In_{0.53}Ga_{0.47}As$, hence the standard electrical contact of an amplifying device is composed of a highly doped $In_{0.53}Ga_{0.47}As$ layer (100nm to 150nm thick) between the cladding and the metal. For the amplifying waveguide isolator the situation is more complicated. As the isolator performance is determined by the overlap of the guided mode with the ferromagnetic metal, it is essential that the semiconductor contact structure absorbs as little as possible. After all, any absorption in the contact layers enhances the overall modal loss of the device without contributing to the non-reciprocal loss shift. Therefore, with the complex refractive index of $In_{0.53}Ga_{0.47}As$ *n-jk* = 3.6-j0.207 [37] at 1300nm wavelength, a standard contact is not suitable for the isolator. Instead we propose a contact scheme consisting of an $In_{0.81}Ga_{0.19}As_{0.41}P_{0.59}$ layer topped with a (thin) $In_{0.53}Ga_{0.47}As$ layer, both heavily doped. The absorption of $In_{0.81}Ga_{0.19}As_{0.41}P_{0.59}$ at 1300nm is low compared to $In_{0.53}Ga_{0.47}As$: *n-jk* = 3.37-j0.0027 [37] [38], including the free carrier absorption due to the high doping (N = 2x$10^{19}cm^{-3}$). In the remainder of this section we will discuss what the thickness of these layers must be to obtain an ohmic contact for the amplifying waveguide isolator.

The influence of the contact scheme on the (magneto)-optical performance is determined through simulation of an isolator benchmark example with a variety of $In_{0.53}Ga_{0.47}As$ and $In_{0.81}Ga_{0.19}As_{0.41}P_{0.59}$ layer thicknesses. The layer structure, tabulated in table 3.3, consists of a tensile strained InAlGaAs-InP multiple quantum well region with 9 wells and a 400nm-thick InP buffer layer separating this core from the contact structure. The ferromagnetic metal is a 50nm $Co_{50}Fe_{50}$ film. As we want to calculate the influence of the contact scheme on the isolator independently of its specific layer structure, the relevant figure of merit (FoM) here is the isolation-to-loss ratio $\frac{\Delta\alpha}{\alpha}$. We simulate the InAlGaAs quantum wells as passive waveguide layers, i.e. $k_{QW} = 0$.[9]
The modal loss obviously increases monotonously with increasing thickness of the absorbing $In_{0.53}Ga_{0.47}As$ layer. The non-reciprocal loss shift $\Delta\alpha$ is calculated with the perturbation formula derived in chapter 2:

$$\Delta\alpha = \frac{|g||E_x^{(0)}(x_{i+})|^2}{Z_{vac}|n_{eff}|}\ sin(\angle g + 2\angle E_x^{(0)}(x_{i+})). \tag{3.28}$$

with Z_{vac} the vacuum impedance, $E_x^{(0)}(x_{i+})$ the transverse electric field amplitude at the semiconductor-metal interface and n_{eff} the effective index of the TM-guided mode of the waveguide device. With the complex argument of g for $Co_{50}Fe_{50}$ equal to $\frac{-\pi}{4}$, $\Delta\alpha$ is maximal if the complex argument of $E_x^{(0)}(x_{i+})$ equals $\frac{3\pi}{8}+p\frac{\pi}{2}$, with p an integer. In figure 3.13 the absolute value of $sin(\angle g+2\angle E_x^{(0)}(x_{i+}))$ (equation (3.28)) is plotted as a function of the two contact layer thicknesses. Variation of these layers clearly allows for tuning of the phase of the transverse electric field component $E_x^{(0)}(x_{i+})$. With every thickness of the absorbing layer below 80nm corresponds a quasi-transparent layer thickness that maximizes the sine factor and consequently the non-reciprocal loss shift $\Delta\alpha$. For absorbing layer thickness values of a few tens of nanometers – the range important for the amplifying waveguide isolator – there is a broad maximum around InGaAsP-layer thicknesses in the order of 150 to 200nm. Maximizing $\Delta\alpha$ is therefore a matter of choosing the quasi-transparent contact layer 'thick enough'.
It is now straightforward to understand the evolution of the isolation-to-loss ratio with variation of the contact layer thicknesses, as plotted in figure 3.14. The isolation-to-loss ratio is maximized by minimizing the absorbing layer and by choosing a thickness combination that maximizes the sine factor of equation 3.28. As such, a 'thick', quaternary contact gives the highest (magneto)-optical performance.

As explained before the electrical quality of the metal-semiconductor contact increases with decreasing bandgap energy of the semiconductor in contact with the metal. Hence, from electrical point of view a quaternary contact might not be preferred. The contact resistivity of five contact schemes with different values of the absorbing ternary and quasi-transparent quaternary layer thickness has been tested (table 3.3): a ternary InGaAs sample (T), used as a reference, two quaternary InGaAsP structures (Q1 and Q2) and two hybrid schemes (H1 and H2) with a 'thick' quaternary layer topped with a 'thin' ternary layer.

[9] The validity of this approach is confirmed in section 3.4.1.

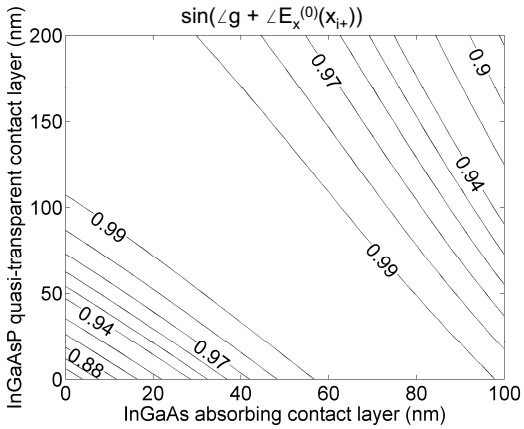

Figure 3.13: Evolution of $sin(\angle g + 2\angle E_x^{(0)}(x_{i+}))$ [equation (3.28)] with variation of the InGaAs absorbing and InGaAsP quasi-transparent layer thickness.

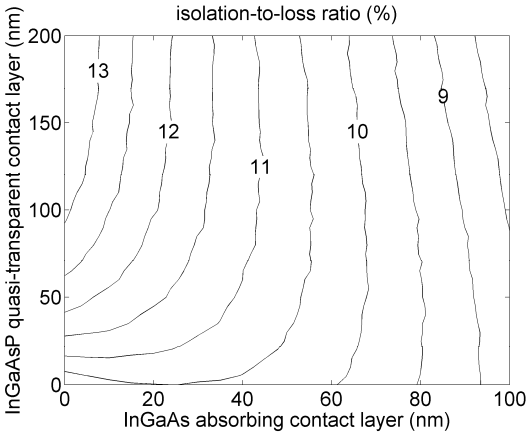

Figure 3.14: Evolution of the isolation-to-loss ratio (in %) with variation of the InGaAs absorbing and InGaAsP quasi-transparent layer thickness.

Label	Composition	Thickness (nm)
T	$In_{0.53}Ga_{0.47}As$	100
H1	$In_{0.81}Ga_{0.19}As_{0.41}P_{0.59}$ / $In_{0.53}Ga_{0.47}As$	100 / 15
H2	$In_{0.81}Ga_{0.19}As_{0.41}P_{0.59}$ / $In_{0.53}Ga_{0.47}As$	100 / 5
Q1	$In_{0.81}Ga_{0.19}As_{0.41}P_{0.59}$	100
Q2	$In_{0.81}Ga_{0.19}As_{0.41}P_{0.59}$	50

Table 3.5: Specifications of the studied contact schemes

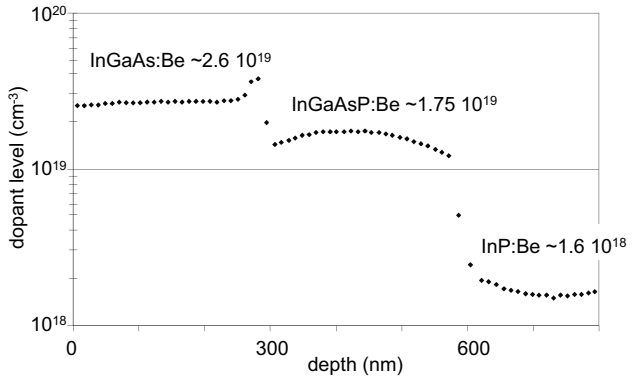

Figure 3.15: Electrochemical capacitance-voltage (ECV) profile of a hybrid contact comprising ternary and quaternary layers. For an accurate measurement of the p-type dopant level, layers of 300nm thickness have been grown.

For the extraction of the electrical quality of the five contact structures, cross-bridge Kelvin resistors (CBKR) have been fabricated. Among all types of test structures the CBKR provides the best compromise between ease of extraction and sensitivity to parasitic current crowding effects, at least when aided with 2D numerical simulations [39]. In a 2D model of the test structure, the voltage (V) distribution is described by the relation:

$$\nabla_t^2 V = \frac{V\ R_s}{\rho_c} \tag{3.29}$$

with R_s the sheet resistance of the semiconductor layer. Solving this boundary value problem with a MATLAB algorithm enables very accurate extraction of the contact resistivity. Our numeric tool takes into account the influence of possible processing imperfections such as misalignment of the lithography mask and underetching of the semiconductor mesa.

Be p^{++}-doped $In_{0.81}Ga_{0.19}As_{0.41}P_{0.59}$ (N_{Be} = 2×10^{19}cm^{-3}) and $In_{0.53}Ga_{0.47}As$ (N_{Be} = 3×10^{19}cm^{-3}) layers have been grown using gas source molecular beam epitaxy (GSMBE) on an InP substrate. Whereas such high dopant levels are standard for $In_{0.53}Ga_{0.47}As$, this is not the case for $In_{0.81}Ga_{0.19}As_{0.41}P_{0.59}$. The high dopant concentration could be achieved by growing the quaternary material at

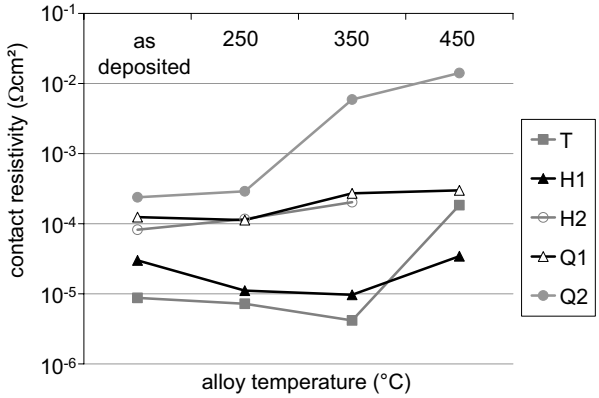

Figure 3.16: Extracted contact resistivity for different rapid thermal processing temperatures, for all five contact structures under study.

low temperature (T_s = 460°C). A 50nm thick $Co_{90}Fe_{10}$ MO metal layer[10] was sputtered and topped with a Ti/Au protective bilayer (40nm/150nm). Rapid thermal processing (RTP), which is known to improve the contact quality [40], was carried out at 250°C, 350°C and 450°C, in a forming gas (N2:H2) atmosphere (duration: 30 seconds).
The experimental verification of the high concentration dopant profile of the ternary and quaternary contact layers is given in figure 3.15. The carrier concentration profile has been measured with the electrochemical capacitance-voltage (ECV) technique [41]. The characterization sample is a three layer stack comprising a (Be-doped) InP layer, a 300nm quaternary Be-doped $In_{0.81}Ga_{0.19}As_{0.41}P_{0.59}$ layer and a 300nm ternary Be-doped $In_{0.53}Ga_{0.47}As$ layer.
The values of the contact resistivity obtained via resistance measurements and subsequent fittings to the mathematical model are plotted in figure 3.16. As anticipated a quaternary contact (Q1 and Q2) has a contact resistivity beyond the acceptable value of $10^{-5}\Omega cm^2$. The quality of a standard electrical contact (T scheme) can however well be approached by topping a 100nm $In_{0.81}Ga_{0.19}As_{0.41}P_{0.59}$ layer with a 15nm $In_{0.53}Ga_{0.47}As$ layer (H1 scheme) and performing RTP at 350°C ($\rho_{c,H1}$ = $10^{-5}\Omega cm^2$).
In table 3.3 the calculated values of the isolation-to-loss ratio for the five contact schemes are given. This shows that the (magneto-)optical performance of the H1 scheme is 39% better than that of the standard ternary contact. As we want to estimate the implications of using the hybrid contact scheme on the practical performance of the isolator, the InP cladding thickness has been optimized for each of the five contact schemes, with minimal transparency current as the FoM-function (see section 3.4 for the optimization procedure). The gain-current density relation of equation 3.18 has been used for the 9QWs InAlGaAs active region. The

[10] At the time of the electrical contact resistivity measurements, $Co_{90}Fe_{10}$ was the only ferromagnetic alloy that had been studied, and $Co_{50}Fe_{50}$ was not yet identified as an alternative. However, as mentioned earlier, the electrical contact quality varies minimally with the metal choice due to Fermi-level pinning, hence we can safely assume that the experimental results are valid for the other Co_xFe_{1-x}-alloys.

Label	Isolation-to loss-ratio (%)	Transparency current (mA/dB)	Length (μm/dB)
T	8.8	9.42	327
H1	12.2	6.76	238
H2	12.8	6.50	225
Q1	13.1	6.38	218
Q2	12.2	6.88	239

Table 3.6: Isolator performance for the five contact schemes.

corresponding forward transparency current and the device length, both per unit (dB) of optical isolation are tabulated in table 3.3 (with 2μm ridge width). It can be concluded that an isolator with the hybrid H1 contact scheme performs more than 37% better than with the standard contact T and less than 10% worse than with the best (magneto)-optical scheme Q1 (neglecting the electrical quality).

This completes the study of an ohmic electrical contact for the optical isolator. Our findings can be summarized as follows. A standard ternary electrical contact leads to unacceptably high losses in a TM-mode amplifying waveguide optical isolator, hence the development of a suitable contact scheme is highly important. From (magneto)-optical point of view a quasi-transparent quaternary contact is preferred, but this does not result in an ohmic contact. By appropriately combining ternary and quaternary layers, we have designed a contact scheme with an electrical quality similar to a standard contact with only a minimal decrease in (magneto)-optical performance.

3.4 Optimization of the amplifying waveguide optical isolator

In the previous sections three main building blocks of the amplifying waveguide optical isolator have been studied and optimized: the TM-gain performance of the amplifying core, the choice of the magnetooptic ferromagnetic metal and the optical, magnetooptic and electrical behavior of the metal-semiconductor contact. The remaining degrees of freedom for the isolator optimization are the thicknesses of both separate confinement heterostructure (SCH) layers that surround the amplifying core and of the superstrate layer between the guiding region and the contact structure. As mentioned earlier the composition of the SCH guiding layers – $In_{0.86}Ga_{0.14}As_{0.32}P_{0.68}$ – has been optimized for an efficient carrier injection hence has not been modified in the design of the amplifying waveguide optical isolator. The composition of the superstrate layer can be considered as variable and the impact of this material choice is discussed in this section. Initially we start with the structure summarized in table 3.4, with an InP cladding layer between the guiding core and the magnetooptic metal. The isolator optimization study has been done in collaboration with Vanwolleghem [42].

Layer	Material	Thickness (nm)
Metallization	Au n=0.403-8.25j	100
MO metal	Co_xFe_{1-x} (x = 90, 50, 0) n,g → table 3.2.1	50
Contact	$In_{0.54}Ga_{0.46}As$ n=3.6-0.2j	15
Contact	$In_{0.81}Ga_{0.19}As_{0.41}P_{0.59}$ n=3.37	100
Cladding	InP n=3.203	variable
SCH	$In_{0.86}Ga_{0.14}As_{0.32}P_{0.68}$ n=3.34	variable
Barrier	InAlGaAs (λ_g = 1100nm, +0.6% strain) n=3.46	20
Well	InAlGaAs (λ_g = 1288nm, -1.25% strain) n=3.57+jk k = $0.00482\ln\left(\frac{6}{9}\frac{J_{tot}[A/cm^2]}{352}\right)$	10 x 9
Barrier	InAlGaAs (λ_g = 1100nm, +0.62% strain) n=3.46	20 x 9
SCH	$In_{0.86}Ga_{0.14}As_{0.32}P_{0.68}$ n=3.34	variable
Substrate	InP n=3.3203	

Table 3.7: Details of the 9QWs tensile strained InAlGaAs-InP multiple quantum well isolator layer structure.

3.4.1 Optimization method and waveguide model

In this section all simulations have been done with a slab waveguide solver – hence 2D effects are neglected – extended with the first-order perturbation algorithm to calculate the non-reciprocal effects. As it is the purpose of this section to design a practical optical isolator a corresponding figure of merit (FoM) must be chosen. As elaborated in section 2.2.2 the general formula of this FoM reads:

$$FoM_{pract,mn} = \frac{J_{transp}^{n}}{(\frac{10}{ln(10)})^{m+n}\ \Delta\alpha^{m+n}} \tag{3.30}$$

.

with $\Delta\alpha$ the non-reciprocal loss shift and J_{transp} the current density required for transparency of the forward propagating mode. Here we will only consider the cases of m=0,n=1 and m=1,n=1. In the first case the FoM equals the total current required for transparency in the forward propagation direction, per decibel of isolation and per micrometer of ridge width. The second case minimizes the product of the current times the length of the non-reciprocal device, again per decibel of isolation and per micrometer of ridge width. Which FoM is suitable depends on the specific requirements of the design. If a minimization of the power consumption is utterly important the first FoM is obviously the preferred one. The second FoM on the other hand results in a trade-off between low current injection and a short device. In what follows we discuss the implications of the actual choice of the FoM function. The experimental values of the optical and magnetooptic parameters of the Co_xFe_{1-x} compositions (tabulated in table 3.2.1) and the experimental relation between the material gain and the total injected current density (equation 3.18):

$$G_{mat}[1/cm] = 466ln\left(\frac{6}{9}\frac{J_{tot}[kA/cm^2]}{0.352}\right) \tag{3.31}$$

are used as input for the optimization calculations.
The transparency current density J_{transp} is found by inverting relation 3.31, where the required material gain G_{mat} is related to the imaginary part of the refractive index in the quantum wells k_{QW} at forward transparency as:

$$G_{mat}[1/cm] = \frac{4\pi}{\lambda[\mu m]}10^4 k_{QW}. \tag{3.32}$$

The calculation of k_{QW} takes a considerable amount of calculation time, which makes the optimization process slow. A much faster method would be to model the amplifying waveguide optical isolator as a passive metal-clad lossy TM-waveguide. The required modal gain for transparency then obviously equals the modal loss in the forward propagation direction:

$$G_{mod}^{TM}(J_{transp}) = \alpha_{mod} = \alpha_0 - \frac{\Delta\alpha}{2}. \tag{3.33}$$

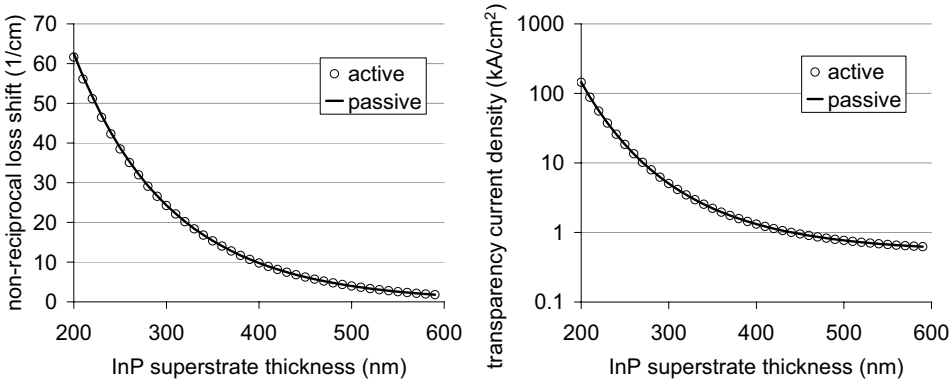

Figure 3.17: Confirmation of the validity of the model that approximates the slab SOA-isolator as a passive lossy waveguide. (left) The non-reciprocal loss shift $\Delta\alpha$ and (right) the forward transparency current J_{transp} are quasi-identical with the active ($\mathrm{k}_{QW} \neq 0$) and the passive perturbation ($\mathrm{k}_{QW} = 0$) waveguide model.

with α_0 the modal loss of the unperturbed TM mode. Furthermore, the TM modal gain is related to the material gain in the quantum wells by:

$$G_{mod}^{TM}(J) = \sum_i \Gamma_i^{TM} G_{mat,i}(J), \tag{3.34}$$

where

$$\Gamma_i^{TM} = Re\left[\frac{\int_{QW_i} n_{QW_i}((E_x^{(0)})^2 - (E_z^{(0)})^2)dx}{Z_{vac}\int E_x^{(0)} H_y^{(0)} dx}\right], \tag{3.35}$$

with $E_x^{(0)}$, $H_y^{(0)}$ and $E_z^{(0)}$ the field components of the unperturbed TM-mode [43]. If we assume a homogeneous carrier injection in the quantum wells, which is a valid assumption if the number of wells is not too large, then a global multiple quantum well TM confinement factor can be defined as $\Gamma^{TM} = \sum_i \Gamma_i^{TM}$. The required material gain can then easily be derived to be:

$$G_{mat}^{TM}(J_{transp}) = \frac{\alpha_0 - \frac{\Delta\alpha}{2}}{\Gamma^{TM}}. \tag{3.36}$$

Together with the gain-current density relationship 3.31 this yields the transparency current density. The validity of the passive waveguide model is examined in figure 3.17. The non-reciprocal loss shift (left graph) and the forward transparency current density (right graph) are plotted for a range of InP superstrate thicknesses, calculated both on an active ($k_{QW} \neq 0$) and a passive ($k_{QW} = 0$) waveguide isolator. The fact that both graphs coincide (almost) perfectly confirms the accuracy of the passive perturbation model.

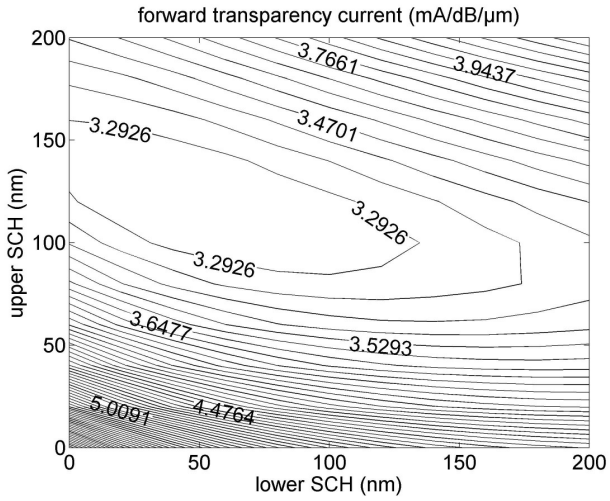

Figure 3.18: Forward transparency current for a scan of the two-dimensional SCH parameter space for a $Co_{50}Fe_{50}$ amplifying waveguide optical isolator; the InP superstrate is kept constant at 300nm.

3.4.2 Calculations

On the basis of this waveguide model the device structure of table 3.4 has been optimized. This three-dimensional non-linear optimization problem can be tackled with a conjugated gradient minimization algorithm, as the FoM functions have a sufficiently smooth dependence on the three optimization parameters, without other local extremes. A typical scan of the SCH parameter space is depicted in figure 3.18. The forward transparency current (expressed in $\mathrm{mA}/\mu\mathrm{m}/\mathrm{dB}$ of isolation) is plotted for the layer structure of table 3.4 with $Co_{50}Fe_{50}$ as the ferromagnetic contact layer for an InP superstrate layer thickness of 300nm. This example illustrates the smoothness of the FoM function and the existence of a single optimum for each value of the InP superstrate thickness.

Each of the FoM-functions has been minimized in the SCH parameter space – with t_{InP} constant – for a range of superstrate thickness values. This has been repeated for the three ferromagnetic metal alloys considered in this work. The outcome of the calculations is plotted in figure 3.19, the transparency current on the left and the length-current product on the right. The minimum in each of these plots thus corresponds to the absolute minimum of the FoM throughout the entire 3D parameter space, and as such represent the optimum design for that particular choice of FoM and Co_xFe_{1-x} composition. These are indicated with arrows. Figure 3.20 plots the device length and transparency current, both per decibel of optical isolation, corresponding to the points in figure 3.19. The arrows correspond to the absolute minima of the two FoM functions. In table 3.4.2 the results of the optimization calculations are tabulated: the dimensions of the three design parameters and the corresponding isolator performance figures for both FoM functions and the three ferromagnetic metal compositions.

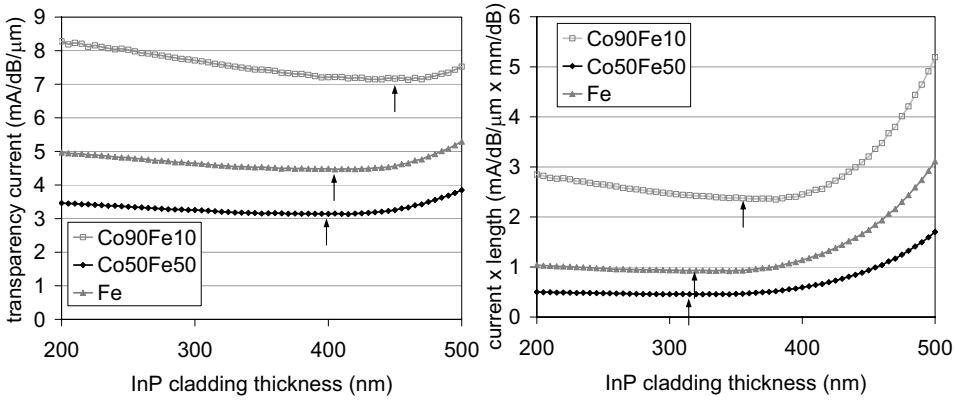

Figure 3.19: Variation as a function of the InP superstrate thickness of the optimum values of the two considered FoM-functions – (left) I*, (right)* I×L *– minimized within each* (t_{SCHu},t_{SCHl})*-plane. The arrows indicate the absolute minima.*

One other layer whose thickness might be varied is the quaternary InGaAsP contact layer. Remember from section 3.3 that this layer must be thick enough to maximize the magnetooptic effect. Figure 3.14 indicates that for a 15nm InGaAs absorbing layer a thickness of 100nm is actually just too small to achieve the maximum in the isolation-to-loss ratio. Consequently, an increase of the InGaAsP layer might result in the enhancement of the isolator performance. The optimization calculations have therefore been repeated with the thickness of the quaternary contact layer as an additional design parameter. The results are plotted in figure 3.21 for the $Co_{50}Fe_{50}$ composition. For each of the InP superstrate thickness values the FoM functions have been minimized in the 3D parameters space ($t_{InGaAsP}$,t_{uSCH},t_{lSCH}). To guarantee the electrical quality of the contact a minimal value of 100nm has been set for the thickness of the quaternary contact layer. The curves for a fixed InGaAsP layer of 100nm are added as a reference. The possible improvement of the *I*-FoM-function is limited to 2.3%.

3.4.3 Discussion of the simulation results

The results of the optimization reveal several important characteristics of the amplifying waveguide optical isolator. In this section, we discuss the attainable practical performance of the device and its design tolerance.
Looking at the FoM-functions plotted in figure 3.19, it can be seen that, starting from a thick InP buffer layer of 500nm, the performance can be improved, irrespective of the choice of the FoM-function, by placing the metal closer to the guiding core (and simultaneously adjusting the thicknesses of the SCH layers). Continuing to decrease t_{InP} below a certain optimal thickness, causes the FoM-function to increase again. In order to understand this trend we rewrite the FoM-expression 3.30 in terms of the forward modal loss that needs to be compensated. With the

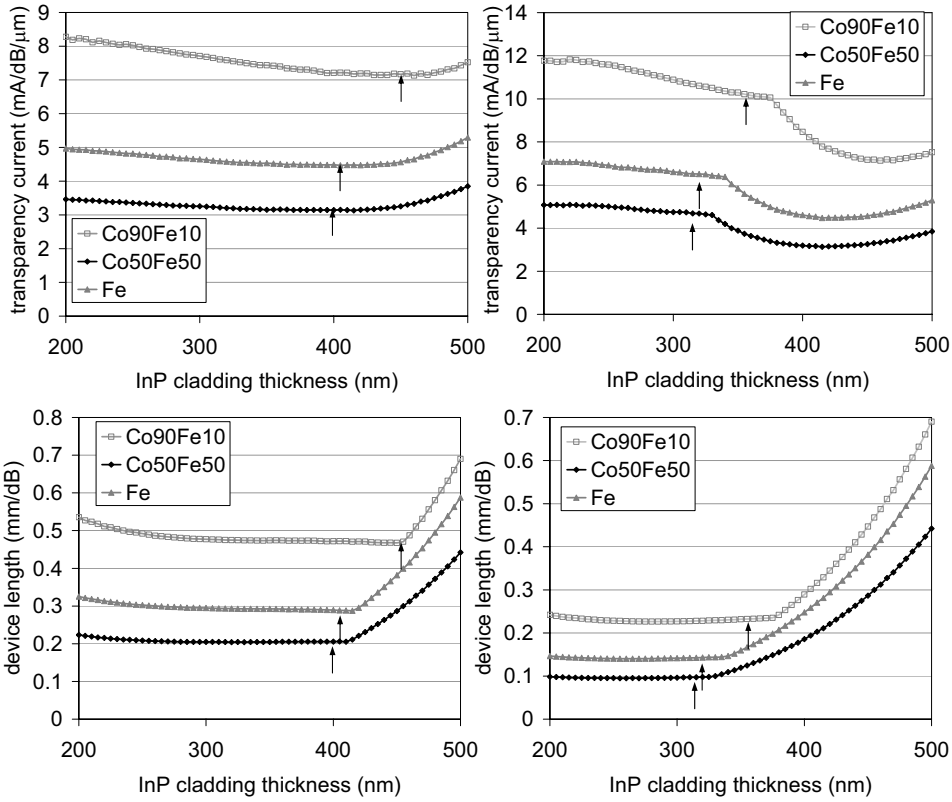

Figure 3.20: Transparency current [mA/μm/dB] (top graph) and isolator length [mm/dB] (bottom graphs) corresponding to the design points of figure 3.19; (left) I-*FoM, (right)* L×I-*FoM.*

FoM I

	t_{InP} (nm)	t_{SCHl} (nm)	t_{SCHu} (nm)	I (mA/μm/dB)	L (mm/dB)
$Co_{90}Fe_{10}$	450	0	5	7.15	0.47
$Co_{50}Fe_{50}$	400	4	11	3.14	0.20
Fe	405	6.5	10	4.47	0.29

FoM $L{\times}I$

	t_{InP} (nm)	t_{SCHl} (nm)	t_{SCHu} (nm)	I (mA/μm/dB)	L (mm/dB)
$Co_{90}Fe_{10}$	360	4	15.5	10.16	0.23
$Co_{50}Fe_{50}$	320	3.5	7.5	4.68	0.10
Fe	325	4.5	12.5	6.50	0.14

Table 3.8: Results of the optimization of the Co_xFe_{1-x} InAlGaAs amplifying waveguide optical isolator.

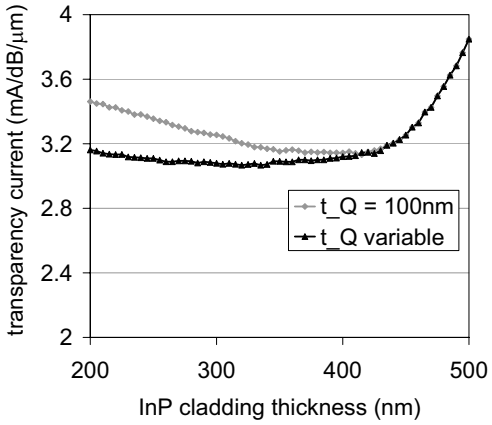

Figure 3.21: Variation of the forward transparency current with the thickness of the InP cladding for optimized points in the 2D (t_{SCHu},t_{SCHl})-parameter plane (grey curve) and the 3D (t_Q,t_{SCHu},t_{SCHl})-parameter plane (black curve).

aid of the logarithmic gain-current density relation of the quantum well active material:

$$G_{mat} = G_0 \; ln\left(\frac{J}{J_0}\right), \tag{3.37}$$

and keeping in mind that at the transparency point the forward loss α is related to the material gain as $\alpha = \Gamma G_{mat}$, the expression for the practical FoM-function becomes:

$$FoM_{pract,mn} = \frac{J_0^n}{(\frac{10}{ln(10)})^{m+n}} \times \frac{exp(\frac{n\,\alpha}{G_0\,\Gamma})}{\Delta\alpha^{m+n}}. \tag{3.38}$$

Both the non-reciprocal loss shift $\Delta\alpha$ and the modal loss α decrease as a function of t_{InP} as a consequence of the lower overlap of the guided mode with the metal layer, but their ratio $\frac{\Delta\alpha}{\alpha}$ – the isolation-to-loss ratio – remains quasi-constant throughout the entire parameter space (t_{InP},t_{uSCH},t_{lSCH}). The general shape of the FoM-plots of figure 3.19 can now readily be explained. Consider a structure with a thick InP buffer layer, for which $\Delta\alpha$ and α are small. Keeping in mind that the *I*-FoM (m=0,n=1) depends inverse linearly on $\Delta\alpha$ and exponentially on α, it is clear that if the InP thickness is reduced the dominator in formula 3.30 increases more rapidly than the numerator. This leads to a reduction of the current required for transparency. Below a critical thickness the exponential in the numerator becomes dominant, which results in an increase of the transparency current.
For the $L{\times}I$-FoM (m=1,n=1) the situation is equivalent, but this time the FoM-function is inverse quadratically dependent on the non-reciprocal loss shift due to the explicit inclusion of the device length, which is inversely proportional to $\Delta\alpha$. Consequently, the denominator of equation 3.30 remains the dominant factor for t_{InP}-values that are below the point of optimal current. Physically, this means that the increase of the transparency current can be compensated by a reduction

of the device length. But also in this case, below some optimal InP thickness, the required current increases faster than the device length decreases.
Table 3.4.2 illustrates that the use of the $L\times I$-FoM leads to an optimal design point with a shorter device length than with the I-FoM. This obviously comes at the price of a higher transparency current. However, the numbers in this table show that the relative increase of the current is lower than the relative decrease in device length. For example, for $Co_{50}Fe_{50}$, the current increases by approximately 33%, while the length decreases by 50%. Whether one or the other FoM-function is preferred above the other depends on the specific situation; if device dimensions are the dominant issue minimization of $L\times I$ is the way to do, if minimal power consumption is the most important the transparency current I should be optimized. In any case, the calculations indicate that the best obtainable performance for a 25dB waveguide isolator with the layer structure of table 3.4, is either a device of 5mm-length consuming 78.5mA (per micrometer ridge width) or a device of 2.5mm length consuming 117mA of current (per micrometer ridge width).[11]

We have already stressed several times the importance of phase matching between the gyrotropy constant g and the transverse electric field amplitude at the magnetooptic metal interface $E_x^{(0)}(x_{i+})$, described by the sine-factor in the expression of the non-reciprocal loss shift:

$$\Delta\alpha = \frac{|g||E_x^0(x_{i+})|^2}{Z_{vac}|n_{neff}|}\ sin(\angle g + 2\angle E_x^{(0)}(x_{m+})). \tag{3.39}$$

It is worth calculating this sine-factor for the optimized InAlGaAs MQW isolator structure, to establish a possible route towards further optimization. Keeping in mind the conclusions of section 2.3 it should not come as a surprise that its value fluctuates minimally throughout the 3D (t_{InP},t_{uSCH},t_{lSCH})-parameter space. The main variation occurs for a thickening of the upper SCH layer compared to the – lower refractive index – InP buffer layer, for as this causes a change of the core-cladding contrast. In any case, for the six optimized designs tabulated in table 3.4.2 the sine-factor has a value that exceeds 0.98 and even 0.99 for $Co_{50}Fe_{50}$ and Fe, hence the virtual improvement by adjusting the phase of the electric field is negligible. Note that it is actually the improvement of the phase matching that causes the performance enhancement if the thickness of the quaternary InGaAsP contact layer is truly optimized (figure 3.21).

With respect to the choice of Co_xFe_{1-x} alloy, the optimization calculations entirely confirm the observations made earlier in section 3.2; irrespective of the FoM-function, the equiatomic composition $Co_{50}Fe_{50}$ easily outperforms pure Fe and the Co-rich alloy. Fe, despite its much lower magnitude of the gyrotropy constant results in a much higher isolator performance than $Co_{90}Fe_{10}$. In the rest of this section we will solely discuss device structures with $Co_{50}Fe_{50}$ as this is obviously the metal that should be used in a practical situation.

[11] All these numbers are the result of one-dimensional slab waveguide calculations. As will be pointed out in section 3.5, two-dimensional (2D) effects occurring for realistic ridge widths have a significant influence on the isolator performance. The phrase 'per micrometer ridge width' should therefore be approached with caution. In chapter 4, when calculating the theoretical performance of the actually fabricated devices, the 2D effects will be taken into account.

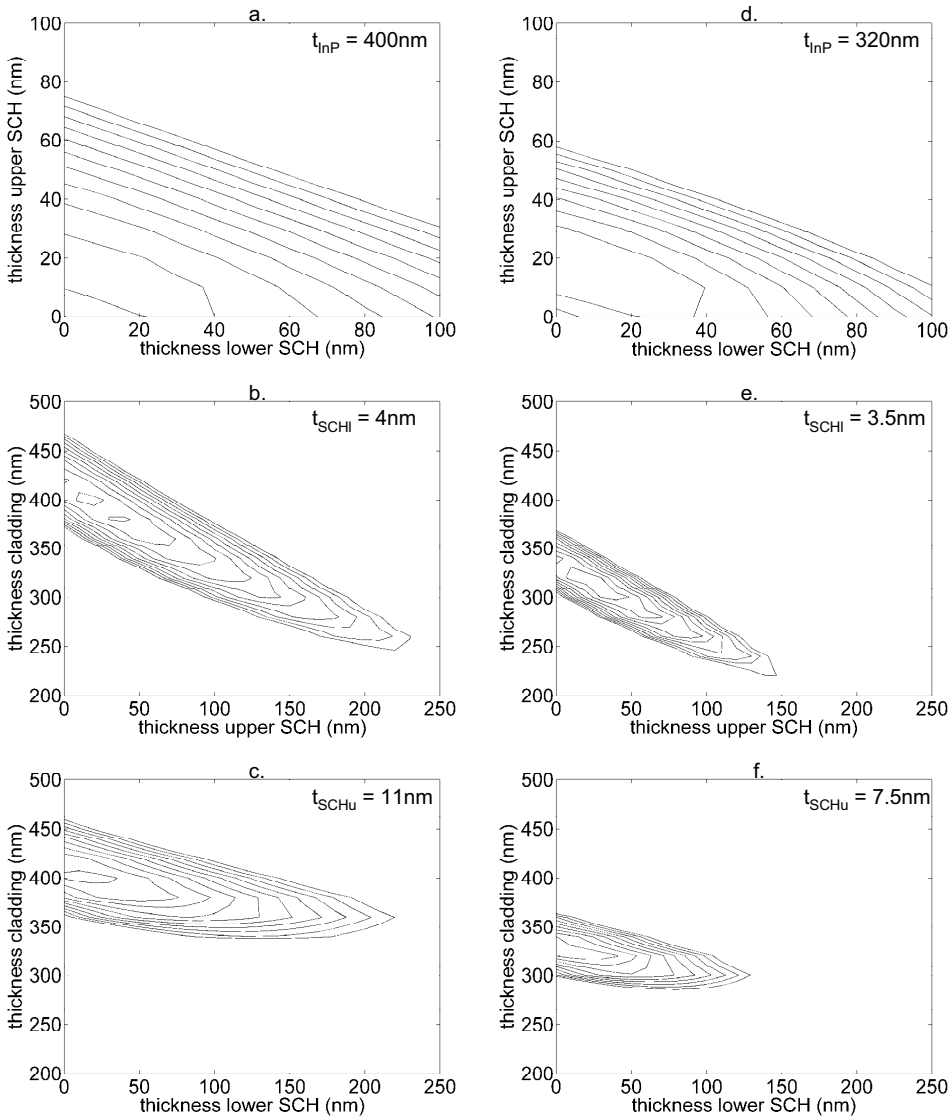

Figure 3.22: Equi-FoM contours for the $Co_{50}Fe_{50}$ InAlGaAs waveguide isolator in the neighborhood of the optimum design point. The outer contour represents an increase of 10% of the absolute minimum value; the spacing of the contours is 1%. Subplots (a) (b), and (c) are for the I*-FoM function and for the optimum thickness of, respectively, (a) InP layer, (b) lower SCH layer, and (c) upper guiding layer. The same applies for the subplots (d)-(f) but for the* L×I*-FoM.*

3.4.4 Tolerance study

3.4.4.1 Layer thickness

An important aspect of the isolator design is the tolerance of the predicted performance with respect to the layer structure variables. To get a clear idea of the different tolerances, the two merit functions are evaluated in the neighborhood of the optimum design points for the equiatomic alloy. This is depicted in figure 3.22. The FoM-function is contour plotted as a function of two of the three thickness parameters – t_{InP}, t_{SCHl} and t_{SCHu} – with the third one fixed at its optimum value (see table 3.4.2). Each subsequent contour corresponds to an increase of 1% of the minimum of the considered FoM-function; the outer contour represents a deviation of 10% from the optimum.
The top plots (figures 3.22a. and 3.22d.) teach us that the optimally designed device is robust with respect to SCH layer thickness variations. At the optimum InP buffer thickness, this guiding layers can take any value between 0nm and 50nm without causing an increase of more than 10% of the FoM-function. It is however a different story for an InP thickness away from the optimum, as can be derived from the middle graphs of figure 3.22. These contour plots show that the thickness of the InP superstrate layer t_{InP} and the upper SCH layer t_{SCHu} are strongly correlated. In fact, within a 10% margin of the FoM minimum, the design points in the (t_{InP},t_{SCHu})-plane obey the relationship $t_{InP} + t_{SCHu} = constant$. On the other hand, the bottom contour plots of figure 3.22 (c. and f.) clearly illustrate that the device has only a minimal dependence on the thickness of the lower SCH layer, with contours that are almost horizontally oriented. This is the direct consequence of the fact that the non-reciprocal waveguide is intrinsically asymmetric and of the plasmonic amplitude enhancement of a TM mode at the interface between a strongly absorbing metal and a dielectric [44], illustrated by the plots of the modal electrical field profile in figure 3.23. As a result of these phenomena, the lower SCH has a minimal influence on the balance between the confinement in the active region and the confinement in the magnetooptic metal. In other words, the isolator performance is primarily controlled by the thicknesses of the layers between the guiding core and the magnetooptic metal.

3.4.4.2 Metal indices

A second issue to be studied is the tolerance of the isolator performance with respect to uncertainties on the metal indices. While standard ellipsometry easily achieves accuracies on the complex refractive index of just a few percent, the gyrotropy constant g can only be determined with an accuracy of 10% or worse (see table 3.2.1).
It can be checked that uncertainties on the optical constants of the metal of this order of magnitude do not influence the device performance by more than a few percent. If we therefore safely assume that the optical indices are correct, the influ-

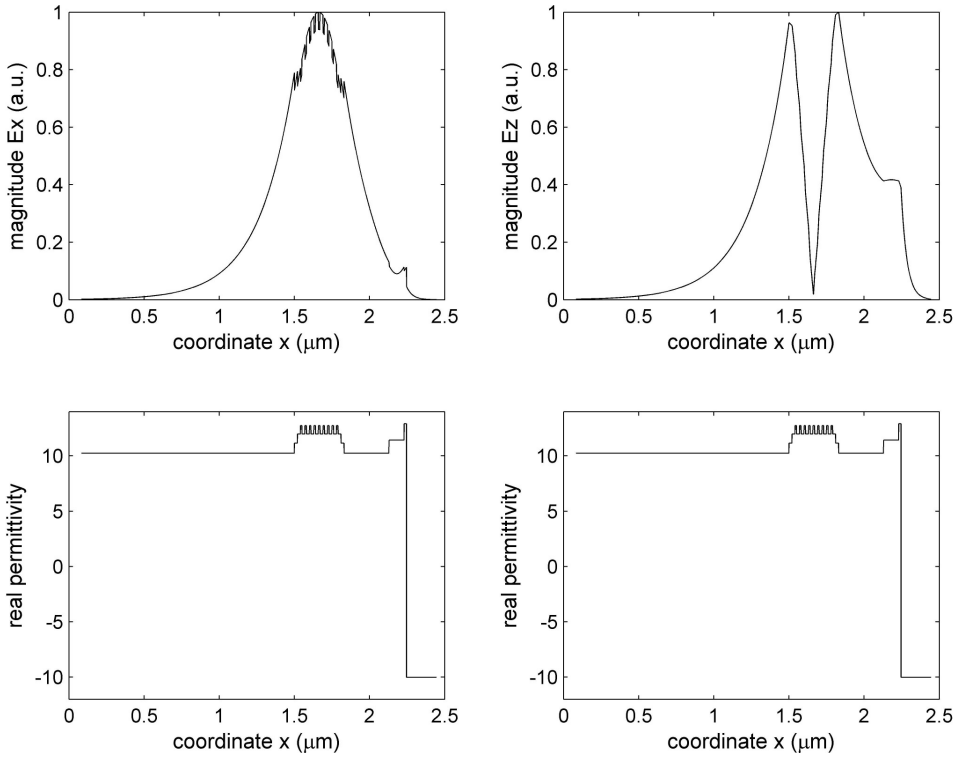

Figure 3.23: Plots of the amplitude of the transverse E_x *(left) and longitudinal* E_z *(right) electric field amplitude of the TM guided mode of the metal-clad waveguide isolator, illustrating the asymmetric modal profile and the plasmonic amplitude enhancement at the metal-dielectric interface. The bottom plots show the corresponding profile of the real part of the permittivity constant.*

ence of variations in the value of the magnetooptic constant can easily be studied in our perturbation model since the perturbation integral:

$$\Delta\alpha = -\frac{8\pi}{Z_{vac}\lambda} Re\left[\frac{\int\int gE_x^{(0)}E_z^{(0)}dS}{\int\int\left[E_x^{(0)}H_y^{(0)} - E_y^{(0)}H_x^{(0)}\right]dS}\right]. \tag{3.40}$$

does not have to be re-evaluated. Indeed, as we consider the magnetooptic perturbation to be constant throughout the metal, g can be pulled out of the integral and the non-reciprocal absorption shift $\Delta\alpha$ can be written as:

$$\Delta\alpha = Re[gA], \tag{3.41}$$

with

$$A = -\frac{8\pi}{Z_{vac}\lambda}\left[\frac{\int\int E_x^{(0)}E_z^{(0)}dS}{\int\int\left[E_x^{(0)}H_y^{(0)} - E_y^{(0)}H_x^{(0)}\right]dS}\right], \tag{3.42}$$

or, in terms of the real and imaginary parts of $g = g' - jg''$:

$$\Delta\alpha = g'Re[A] + g''Im[A]. \tag{3.43}$$

The uncertainty on the non-reciprocal loss shift can directly be calculated from the uncertainties on g' and g'', using the well-known relationship for the propagation of (uncorrelated) errors over a sum:

$$x = au + bu \Rightarrow \sigma_x^2 = a^2\sigma_u^2 + b^2\sigma_v^2, \tag{3.44}$$

with σ_i the uncertainty on parameter *i*. If we consider that the structure is optimized such that both terms in equation 3.43 have the same sign, it follows that the relative uncertainty on $\Delta\alpha$, $\sigma_{\Delta\alpha}/\Delta\alpha$, is never higher than the highest relative uncertainty on either g' or g''. Furthermore, the uncertainty on the non-reciprocal loss shift results in an uncertainty on the other device performance figures I and L, which are inverse linearly related to $\Delta\alpha$. These uncertainties can be derived via the relationship:

$$x = au^{\pm b} \Rightarrow \frac{\sigma_x}{x} = b\frac{\sigma_u}{u}. \tag{3.45}$$

The relative uncertainty on I and L is therefore equal to that on $\Delta\alpha$.

In conclusion, the highest relative uncertainty on the real or imaginary part of the gyrotropy g gives an absolute upper limit on the relative uncertainty on the device performance.

3.4.4.3 Operation wavelength

A final tolerance aspect that needs to be studied is the wavelength sensitivity. Contrary to waveguide isolator configurations that employ the non-reciprocal phase shift in transparent garnet media, the amplifying waveguide optical isolator concept is not based on any interference effect, hence it can be expected that

the device is intrinsically broadband. The two main parameters that determine the wavelength dependence are the gain spectrum of the multiple quantum well core and the wavelength dispersion of the optical and magnetooptic constants of the ferromagnetic metal. For a standard multiple quantum well (MQW) semiconductor optical amplifier (SOA) the gain spectrum is traditionally not much wider than 20-30nm. As it is safe to assume that the optical nor the magnetooptic indices of the Co_xFe_{1-x} alloys will vary importantly over such an interval, it can be expected that the bandwidth of the MQW gain limits the bandwidth of the isolator. The wavelength dependence of the device has been studied experimentally and the measurements confirm this theory, as is discussed in chapter 4.
Here we want to explore whether the waveguide structure itself adds to the wavelength dependence. Assume a spectrally homogenous gain – described by the empirical relationship 3.31 – and zero dispersion of the permittivity of all materials of the isolator over a 30nm wide wavelength window centralized around 1300nm, and recalculate for each wavelength the two practical FoM-functions with their corresponding optimized layer structure at 1300nm. Within this spectral window I and $L{\times}I$ vary by less than 4%. This shows that the optimization calculation is very robust with respect to the wavelength.
With the wavelength λ appearing in the formula for the non-reciprocal loss shift $\Delta\alpha$ (equation 3.40), this parameter itself depends stronger on the operation wavelength, but the effect is partially canceled out due to the similar wavelength dependence of the modal loss α. In fact, the isolation-to-loss ratio is quasi-independent of the wavelength (if the material dispersion is neglected).

3.4.5 Influence of the cladding material

Earlier, in section 2.3, we have pointed out the large influence of the choice of the cladding material on the non-reciprocal loss shift $\Delta\alpha$. The main cause for this is the major dependence of the phase of the transverse electric field amplitude at the metal interface on the refractive index of the adjoining cladding layers. Furthermore, as the reciprocal modal absorption is independent of the phase of the electric field, the isolation-to-loss ratio $\frac{\Delta\alpha}{\alpha}$ – the fundamental FoM-function – is also highly dependent on the refractive index of the cladding layer between the core and the magnetooptic metal.
On the other hand, the isolation-to-loss ratio $\frac{\Delta\alpha}{\alpha}$ is quasi-independent of the dimensions of the superstrate layer between the core and the metal due to its linear dependence on both the non-reciprocal loss shift $\Delta\alpha$ and the modal loss α. This can clearly be seen on figure 3.24. In this graph the variation of the isolation-to-loss ratio is plotted with the refractive index of the cladding material – where the substrate and the superstrate material are the same – and with the thickness of the superstrate layer between guiding core and magnetooptic metal. The simulated layer structure consists of the InAlGaAs 9QW stack sandwiched between two cladding layers. The thickness of the SCH layers is fixed at 0nm. Directly on top of the superstrate is a 50nm $Co_{50}Fe_{50}$ film, hence the electrical contact structure is left out, in order to really investigate the influence of the cladding material.

In the rest of this section we look into the influence of the cladding material on the practical figures of merit $\mathrm{FoM}_{pract,mn}$. After all, the situation differs from

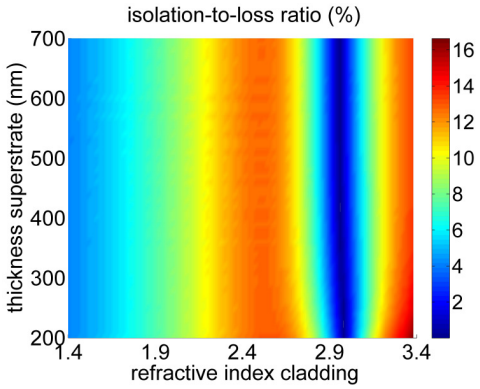

Figure 3.24: Variation of the isolation-to-loss ratio $\frac{\Delta\alpha}{\alpha}$ with the refractive index of the cladding material (superstrate and substrate) and with the thickness of the superstrate layer between the guiding core and the magnetooptic metal.

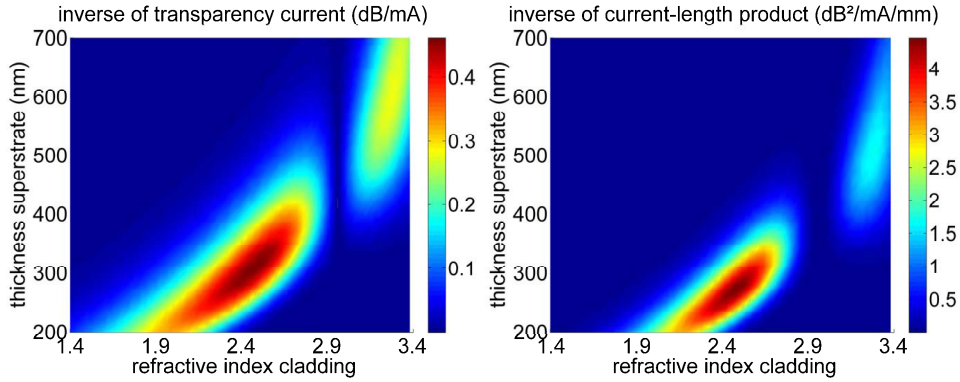

Figure 3.25: Variation of the inverse of the practical FoM functions with the refractive index of the cladding material (superstrate and substrate) and with the thickness of the superstrate layer between the guiding core and the magnetooptic metal – (left) the inverse of the transparency current and (right) the inverse of the current-length product both per dB of optical isolation and per micrometer of ridge width.

the $\frac{\Delta\alpha}{\alpha}$-case; the FoM$_{pract,mn}$-functions depend exponentially on the modal loss α and inverse linearly (I-FoM$_{pract,01}$) or quadratically ($L{\times}I$-FoM$_{pract,11}$) on the non-reciprocal loss shift $\Delta\alpha$. In addition, these FoM-functions are also strongly influenced by the confinement Γ of the guided mode in the amplifying waveguide core:

$$FoM_{pract,mn} = \frac{J_0^n}{(\frac{10}{ln(10)})^{m+n}} \times \frac{exp(\frac{n}{g_0}\frac{\alpha}{\Gamma})}{\Delta\alpha^{m+n}}. \tag{3.46}$$

As such it can be expected that the thickness of the cladding layer does have an important impact on the value of these practical FoM functions, apart from the

material choice of the cladding material. In figure 3.25 the variation of (the inverse of) both practical FoM functions (left graph I, right graph $L{\times}I$) with the refractive index of the cladding material and with the thickness of the superstrate layer is plotted, for the waveguide layer structure described above. These plots clearly show the presence of two local optima for both practical FoM-functions. The first local optimum is for cladding indices in the neighborhood of 3.3 for a total cladding thickness of 600nm and 500nm for respectively the I-FoM and the $L{\times}I$-FoM. This is obviously the optimum discussed in the previous paragraphs. However, there is another –global – optimum, which corresponds to a refractive index of the cladding of approximately 2.45 for a thickness of 300nm (I-FoM) and 250nm ($I{\times}L$-FoM). The important observation is that the device performance at this last point is remarkably higher than at the previously known local optimum; the transparency current decreases by 38% (accompanied by a length reduction) and the current-length product reduces by 62%. This improvement can be attributed to a larger confinement Γ in the waveguide core for the lower index cladding, reducing the transparency current density according to equation 3.46. While this clearly opens up a way towards device improvement, the practical realization of this idea is not an easy task. While materials can be found with a refractive index around 2.45 at 1300nm wavelength, these are electrical insulators. An important issue that needs to be solved is therefore how to achieve current injection in the amplifying MQW core. Although we will not elaborate this idea more in detail, it serves as the perfect example of the subtlety of the interaction between the different parameters of an amplifying waveguide isolator.

3.5 Simulation of a two-dimensional magnetooptic cross-section

So far the non-reciprocal waveguide has always been assumed to be a one-dimensional (1D) slab layer structure. This is obviously only a first order approximation of the ridge waveguide structure that the device actually is. Figure 3.26 illustrates the cross-section of a ridge waveguide isolator. For the study of the physical principles of the magnetooptic waveguide the 1D approximation proves to be accurate enough. However, the calculation of the actual theoretical performance figures requires the inclusion of the effects of the two-dimensionality (2D) of the ridge waveguide structure. To this end, the 2D perturbation formula 2.102 has been implemented in the commercial full 2D optical mode solver FIMMWAVE [45]. The algorithm, written in a PYTHON [46] programming environment, defines the 2D cross-section of the unperturbed waveguide structure in FIMMWAVE and commands the mode solver to calculate the corresponding guided modes. The resulting field profiles of the unperturbed TM-mode, E_i and H_i (i = x,y,z), are imported in PYTHON and the TM phase shift is calculated according to equation 2.102.
The integrals are calculated numerically used a 2D extension of the Simpon's rule [47]. Consider the function $F = f(x,y)$ over the rectangle $R = [(x,y): x_b \leqslant x \leqslant x_e, y_b \leqslant y \leqslant y_e]$. The interval $[x_b, x_e]$ is subdivided into $2m$ subintervals $[x_{i-1}, x_i]_{i=1}^{2m}$ of equal width $h = \frac{x_e - x_b}{2m}$ by using the equally spaced sample points $x_i = x_0 + ih$ for $i = 0,1,...,2m$ and with $x_0 = x_b$ and $x_{2m} = x_e$. Analogously for the y-coordinate

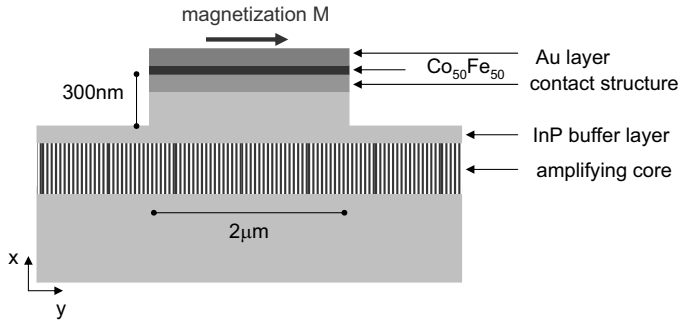

Figure 3.26: Schematic layout of a ridge waveguide optical isolator.

where the interval $[y_b, y_e]$ is subdivided into *2n* subintervals $[y_{j-1}, y_j]_{j=1}^{2n}$ of equal width $k = \frac{y_e - y_b}{2n}$ by using the equally spaced sample points $y_i = y_0 + jk$ for *j = 0, 1, ..., 2n* and with $y_0 = y_b$ and $y_{2n} = y_e$. The 2D Simpson's rule reads:

$$\int\int f(x,y)dA = \int_{x1}^{x2}\int_{y1}^{y2} f(x,y)dxdy = S2D(f,h,k) + O(h^4) + O(k^4), \quad (3.47)$$

where

$$\begin{aligned} S2D(f,h,k) \quad = \quad & \frac{1}{9}hk\Bigg[f(x_b,y_b) + f(x_b,y_e) + f(x_e,y_b) + f(x_e,y_e) \\ & +4\sum_{j=1}^{n} f(x_b,y_{2j-1}) + 2\sum_{j=1}^{n-1} f(x_b,y_{2j}) \\ & +4\sum_{j=1}^{n} f(x_e,y_{2j-1}) + 2\sum_{j=1}^{n-1} f(x_e,y_{2j}) \\ & +4\sum_{i=1}^{m} f(x_{2i-1},y_b) + 2\sum_{i=1}^{m-1} f(x_{2i},y_b) \\ & +4\sum_{i=1}^{m} f(x_{2i-1},y_e) + 2\sum_{i=1}^{m-1} f(x_{2i},x_e) \\ & +16\sum_{j=1}^{n}\left(\sum_{i=1}^{m} f(x_{2i-1},y_{2j-1})\right) \\ & +8\sum_{j=1}^{n-1}\left(\sum_{i=1}^{m} f(x_{2i-1},y_{2j})\right) + 8\sum_{j=1}^{n}\left(\sum_{i=1}^{m-1} f(x_{2i},y_{2j-1})\right) \\ & +4\sum_{j=1}^{n-1}\left(\sum_{i=1}^{m-1} f(x_{2i},y_{2j})\right)\Bigg]. \end{aligned} \quad (3.48)$$

Layer	Material	Refractive index	Thickness (nm)
Metallization	Au	0.403-8.25j	100
MO metal	$Co_{50}Fe_{50}$	3.23-4.5j	50
Contact	$In_{0.54}Ga_{0.46}As$	3.6-0.2j	15
Contact	$In_{0.81}Ga_{0.19}As_{0.41}P_{0.59}$	3.37	100
Cladding	InP	3.2	400
SCH	$In_{0.86}Ga_{0.14}As_{0.32}P_{0.68}$	3.34	20
Barrier	InAlGaAs (λ_g = 1100nm)	3.46	20
Well	InAlGaAs (λ_g = 1288nm)	3.57	10 x 9
Barrier	InAlGaAs (λ_g = 1100nm)	3.46	20 x 9
Cladding	InP	3.2	3000

Table 3.9: Details of the isolator layer structure used for the study of 2D effects. The refractive indices are tabulated for a wavelength of 1300nm and are taken from [48]. The index of $Co_{50}Fe_{50}$ has been determined experimentally (see section 3.2). The quantum wells are simulated as passive layers (k_QW = 0.0*).*

The influence of the 2D structure on the device performance has been investigated through the simulation of a benchmark isolator example. The layer structure is tabulated in table 3.5. The etch depth is set at 300nm, for which a 2μm ridge waveguide is monomodal for TM polarization. Just as in section 3.4 the quantum wells have been simulated as passive layers (k_{QW} = *0.0*) and the modal loss caused by the absorbing contact layer and the metal films has been calculated. In figure 3.27 the variation of the non-reciprocal absorption shift $\Delta\alpha$ (left) and the reciprocal modal loss α_0 (right) with the ridge width are plotted. As a reference the results of the 1D slab calculation are included. As a 1D slab structure is essentially the limit of a ridge waveguide structure with infinite ridge width the 2D simulation results should converge towards the slab performance figures, which, according to figure 3.27, is indeed the case. These graphs show that a decrease of the ridge width results in a decrease of both the non-reciprocal loss shift and the reciprocal modal loss. This is due to the corresponding decrease of the confinement of the guided mode in the absorbing regions of the waveguide. The decrease in the losses is such that the fundamental figure of merit - function, the isolation-to-loss ratio $\frac{\Delta\alpha}{\alpha} = \frac{\Delta\alpha}{\alpha_0 - \Delta\alpha/2}$, remains quasi-constant, as is illustrated in figure 3.28. The practical figure of merit functions defined in section 2.2.2 however, depend non-linearly on the two loss values hence are significantly different in a 2D narrow ridge waveguide (order 2μm width) from the 1D slab case. The quantitative impact depends on the specific isolator structure and will therefore be discussed for each of the isolator designs in chapter 4.

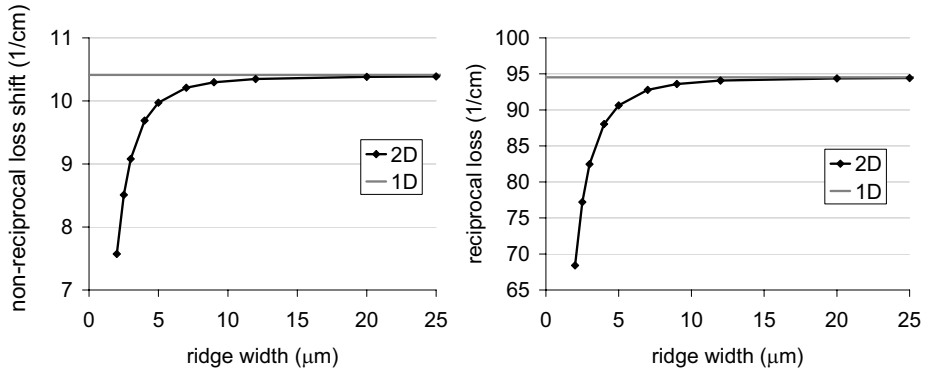

Figure 3.27: Dependence of (left) the non-reciprocal loss shift and (right) the reciprocal modal loss on the ridge width of the shallowly etched amplifying waveguide optical isolator. For large widths both quantities converge towards the values obtained from slab waveguide calculations.

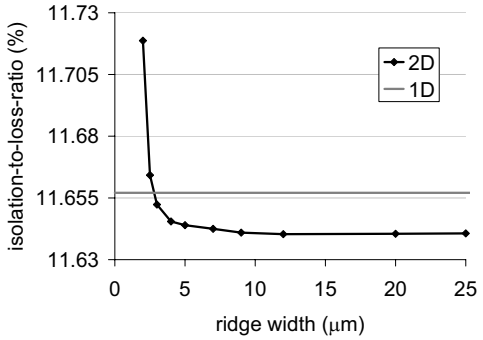

Figure 3.28: Illustration of the marginal dependence of the isolation-to-loss-ratio on the ridge width of the shallowly etched amplifying waveguide optical isolator.

3.6 Conclusion

At the end of this chapter we have obtained a completely optimized TM-mode amplifying waveguide optical isolator, the result of an extensive theoretical and experimental study of the main building blocks of this component. Very high quality TM-selective gain material has been developed. Tensile strained multiple quantum well structures, both in the traditional InGaAsP-InP system and in the improved InAlGaAs-InP system, have been demonstrated and characterized, including a strain study of the gain performance. For the issue of the ferromagnetic metal choice, the transition metal alloy system Co_xFe_{1-x} has been characterized at 1300nm wavelength with respect to its optical and magnetooptic properties. Based on the non-reciprocity study of chapter 2 it could be established that the equiatomic $Co_{50}Fe_{50}$ compound is by far the preferred choice for an InP-based isolator employing the non-reciprocal loss shift. Furthermore, an ohmic electrical contact has been developed that has only a minimal influence on the isolator performance. The solution is to use a hybrid InGaAs/InGaAsP highly p-doped contact scheme. Assembling all these elements into one device forms the basic layer structure of the optimized isolator. Using slab waveguide isolator simulations based on the perturbation-based algorithm, we have studied the influence of the thickness of the cladding layers (buffer and SCH) on the device performance, ultimately leading to two optimized designs, corresponding to two practical figure-of-merit functions. To finalize this chapter we have studied the simulation of the actual two-dimensional cross-section of the amplifying waveguide optical isolator. Calculations show that 2D effects occurring for realistic ridge widths have a significant influence on the device performance.
The next chapter is devoted to the experimental study of the amplifying waveguide isolator. As we will follow a chronological approach in this discussion, devices with less optimized choices for the different building blocks will be treated (InGaAsP instead of InAlGaAs, $Co_{90}Fe_{10}$ instead of $Co_{50}Fe_{50}$,...). The material properties listed before will serve as the input to calculate the theoretical performance figures of these isolator demonstrators.

Bibliography

[1] M. Takenaka, and Y. Nakano, "Proposal of a novel semiconductor optical waveguide isolator." *Proc. of 11th International Conference on Indium Phosphide and Related Materials (Davos, Switzerland* pp. 298292 (1999).

[2] W. Zaets, and K. Ando, "Optical waveguide isolator based on nonreciprocal loss/gain of amplifier covered by ferromagnetic layer." *IEEE Photon. Technol. Lett.* 11, pp.10121014 (1999).

[3] G.P. Agrawal, and N.K. Dutta "Long wavelength semiconductor laser devices." *John Wiley,* (1980).

[4] P.A. Thijs, L.F. Tiemeijer, J.J.M. Binsma, and T. van Drongen, "Progress in Long-Wavelength Strained-Layer InGaAs(P) Quantum-Well Seminconductor Lasers and Amplifiers" *IEEE J. Quant. Electron.,* 30(2), pp. 477-499 (1994).

[5] Y. Arakawa, and A. Yariv "Quantum Well Lasers - Gain, Spectra, Dynamics" *IEEE J. Quant. Electron.,* 22(9), pp. 1887-1899 (1986).

[6] T.A. DeTemple, and C.M. Herzinger, "On the semiconductor laser logarithmic gain-current density relation." *IEEE J. Quantum Electron.,* vol. 29(5), pp. 1246-1252 (1993).

[7] J.E.A. Whiteaway, G.H.B. Thompson, P.D. Greene, and R.W. Glew, "Logarithmic gain/current-density characteristic of InGaAs/InGaAlAs/InP multi-quantum-well separate-confinement-heterostructure lasers." *Electron. Lett.,* vol. 27(4), pp 340-342 (1991).

[8] J. Piprek, "Semiconductor Optoelectronic Devices. Introduction to Physics and Simulation." *Academic Press - Elsevier Science,* pp. 89–90 (2003).

[9] K.J. Vahala, and C.E. Zah. "Effect of doping on the optical gain and the spontaneous noice enhancements factor in quantum well amplifiers and lasers studied by simple analytical expressions." *Appl. Phys. Lett.,* 52, pp. 1945-1947 (1988).

[10] E. Yablonovitch, and E.O. Kane, "Band structure engineering of semiconductor lasers for optical communications." *J. Lightwave Technol.,* 6(8), pp. 1292-1299 (1988).

[11] A.R. Adams, "Band structure engineering for low threshold high efficiency semiconductor lasers." *Electron. Lett.,* 22, pp. 249-250 (1986).

[12] E. Yablonovitch, and E.O. Kane, "Reduction of the lasing threshold current density by lowering the valence band effective mass." *J. Lightwave Technol.,* 4, pp. 504-506 (1986); see also "Correction." *J. Lightwave Technol.,* 4, pp. 961 (1986).

[13] J.W. Matthews, and A.E. Blakeslee, "Defects in epitaxial multilayers." *J. Crystal Growth,* 27, pp. 118-125 (1974).

[14] J. Minch, S.H. Park, T. Keating, and S.L. Chuang, "Theory and experiment of $In_{1-x}Ga_xAs_yP_{1-y}$ and $In_{1-x-y}Ga_xAl_yAs$ long-wavelength strained quantum-well lasers." *J. Quant. Electron.,* 35(5), pp. 771-782 (1999).

[15] M. Vanwolleghem, "Een geintegreerde InP-gebaseerde optische golfgeleiderisolator op basis van ferromagnetische CoFe-contacten, An integrated InP-based Optical Waveguide Isolator Using Ferromagnetic CoFe Contacts." *Ph.D. thesis,* ISBN , 90-8578-013-6, Ghent University, Belgium (2005).

[16] F. Lelarge, B. Dagens, C. Cuisin, O. Le Gouezigou, G. Patriarche, W. Van Parys, M. Vanwolleghem, R. Baets, and J.L. Gentner, "GSMBE growth of GaInAsP/InP 1.3μm-TM-lasers for monolithic integration with optical waveguide isolator." *J. Crystal Growth,* 278, p.709-713 (2005).

[17] N. Yokouchi, N. Yamanaka, N. Iwai, Y. Nakahira, and A. Kasukawa, "Tensile-strained GaInAsP-InP quantum-well lasers emitting at 1.3μm." *J. Quant. Electron.,* 32(12), pp. 2148-2155 (1996).

[18] P.J.A. Thijs, J.J.M. Binsma, L.F. Tiemeijer, and T. Van Dongen, "Submilliamp threshold current (0.62 mA at 0°C) and high output power (220 mW) 1.5μm tensile strained InGaAs single quantum well lasers." *Electron. Lett.,* 28, pp. 829-830 (1992).

[19] H. Sugiura, M. Itoh, N. Yamamoto, M. Ogasawara, K. Kishi, and Y. Kondo, "Metalorganic molecular beam epitaxy of 1.3μm wavelength tensile-strained InGaAsP multi-quantum-well lasers" *Appl. Phys. Lett.,* 68, pp. 3213 (1996).

[20] P.W.A. Mc Ilroy, A. Kurobe, and Y. Uematsu, "Analysis and Application of Theoretical Gain Curves to the Design of Multi-Quantum-Well Lasers." *J. Quant. Electron.,* 21(12), pp. 1985-1963 (1985).

[21] C.E. Zah, R. Bhat, B.N. Pathak, F. Favire, W. Lin, M.C. Wang, N.C. Andreadakis, D.M. Hwang, M.A. Koza, T.P. Lee, Z. Wang, D. Darby, D. Flanders, and J.J. Hsieh, "High-Performance Uncooled 1.3μm $Al_xGa_yIn_{1-x-y}As/InP$ Strained-Layer Quantum-Well Lasers for Subscriber Loop Applications." *IEEE J. Quant. Electon.*, 30, pp. 511-523 (1994).

[22] J.C.L.Yong, J.M. Rorison, and I.H. White, "1.3μm Quantum-Well InGaAsP, AlGaInAs, adn InGaAsN Laser Material Gain: A Theoretical Study." *IEEE J. Quant. Electron.,* 38, pp. 1553-1564 (2002).

[23] J. Decobert, N. Lagay, C. Cuisin, B. Dagens, B. Thedrez, and F. Laruelle, "MOVPE Growth of AlGaInAs-InP Highly Tensile Strained MQWs for 1.3μm Low-Threshold Lasers." *J. Crystal Growth,* 272, pp.542-548 (2004).

[24] M. Vanwolleghem, p. 4-41 in "Een geintegreerde InP-gebaseerde optische golfgeleiderisolator op basis van ferromagnetische CoFe-contacten, An integrated InP-based Optical Waveguide Isolator Using Ferromagnetic CoFe Contacts." *Ph.D. thesis,* ISBN , 90-8578-013-6, Ghent University, Belgium (2005).

[25] G. S. Krinchik, and V. A. Artemjev, "Magneto-optic Properties of Nickel, Iron, and Cobalt." *J. Appl. Phys.,* 39(2), pp. 1276-1278 (1968).

[26] G. S. Krinchik, and V. A. Artemjev, "Magneto-optical properties of Ni, Co, and Fe in the ultraviolet visible, and infrared parts of the spectrum." *Sov. Phys.-JETP,* 26(6), pp. 1080-1085 (1968).

[27] A. Lesuffleur, M. Vanwolleghem, P. Gogol, B. Bartenlian, P. Beauvillain, J. Harmle, L. Lagae, J. Pistora, K. Postava, S. Visnovsky, and R. Wirix- Speetjens, "Magneto-optical parameters of $Co_{90}Fe_{10}$ and $Co_{50}Fe_{50}$ ferromagnetic thin films for 1.3μm integrated isolator." *J. Magn. Magn. Mater.* 305, pp.284-290 (2006).

[28] K. H. J. Buschow, P. G. van Engen, and R. Jongebreur, "Magneto-optical properties of metallic ferromagnetic materials." *J. Magn. Magn. Mater.,* 38(1), pp. 1-22 (1983).

[29] A. K. Zvezdin, and V. A. Kotov, *chapter 2* in "Modern Magnetooptics and Magnetooptical Materials." Institute of Physics Publishing, Philadelphia, USA (1997).

[30] G.J. Sprokel, "Photoelastic modulated ellipsometry on magnetooptic multilayer films" *Appl. Opt.,* 25(22), pp. 4017-4022 (1986).

[31] A. Berger, and M. R. Pufall, "Generalized magneto-optical ellipsometry." *Appl. Phys. Lett.,* 71(7), pp. 965–967 (1997).

[32] R. Atkinson, and P. H. Lissberger, "Sign conventions in magneto-optical calculations and measurements." *Appl. Opt.,* 31(28), pp. 6076–6081 (1992).

[33] T. Amemiya, H. Shimizu, Y. Nalano, P.N. Hai, M. Yokoyama, and M. Tanaka, "Semiconductor waveguide optical isolator based on nonreciprocal loss induced by ferromagnetic MnAs." *Appl. Phys. Lett.,* 89, pp.021104 (2006).

[34] T. Amemiya, *private communication,* November 2006.

[35] S. Kurtin, T.C. McGill, and C.A. Mead, "Fundamental Transition in Electronic Nature of Solids." *Phys. Rev. Lett.* 22, pp.1433-1436 (1969).

[36] C.A. Mead, and W.G. Spitzer, "Fermi-Level Position at Metal-Semiconductor Interfaces." *Phys. Rev.* 134, pp.A713-A716 (1964).

[37] B. Jensen, "Handbook of Optical Constants of Solids II." *E.D. Palik ed.*, pp.125-149 (Academic Press, 1991).

[38] A. Sneh and C.R. Doerr, "Integrated Optical Circuits and Components." *E.J. Murphy ed.*, pp.164 (Marcel Dekker inc., 1999).

[39] W.M. Loh, S.E. Swirhun, T.A. Schreyer, R.M. Swanson, and K.C. Saraswat, "Modeling and measurement of Contact Resistances." *IEEE Trans. on Electron. Devices* 34, pp.512-523 (1987).

[40] A. Katz, P.M. Thomas, S.N.G. Chu, W.C. Dautremont-Smith, R.G. Sobers, and S.G. Napholtz, "Pt/Ti Ohmic contact to p++-InGaAsP (1.3μm) formed by rapid thermal processing." *J. Appl. Phys.*, 67, pp.884-889 (1990).

[41] P. Blood "Capacitance-voltage profiling and the characterisation of III-V semiconductors using electrolyte barriers." *Semiconductor Science and Technology*, 1, pp. 7-27 (1986).

[42] M. Vanwolleghem, W. Van Parys, P. Gogol, P. Beauvillain, and R. Baets, "Design and optimization of a monolithically integratable InP-based optical waveguide isolator." *J. Opt. Soc. Am. B*, 24(1), pp.94-105 (2007).

[43] T. D. Visser, B. Demeulenaere, J. Haes, D. Lenstra, R. Baets, and H. Blok, "Confinement and modal gain in dielectric waveguides." *J. Lightwave Technol.*, 14, pp. 885887 (1996).

[44] H. Raether, "Surface Plasmonson Smooth and Rough Surfaces and on Gratings." *Vol. III of Springer Tracts in Modern Physics, Springer-Verlag*, (1988).

[45] http://www.photond.com/products/fimmwave/fimmwave2.htm

[46] http://www.python.org/

[47] J.D. Mathews, "2D Integration using the Trapezoidal and Simpson Rules." http://math.fullerton.edu/mathews/n2003/SimpsonsRule2DMod.html

[48] B. Jensen, in *Handbook of Optical Constants of Solids II*, E. D. Palik, ed., chapter 6 "Calculation of the refractive index of compound semiconductors below the band gap", pp. 125–149, Academic Press (1991).

4

Characterization of the amplifying waveguide isolator

IN the previous chapter the optimization of the main building blocks of the waveguide optical isolator and the actual design of this component have been addressed. Here, we elaborate on the experimental work that has been carried out. We start by explaining the fabrication of the shallowly etched ridge waveguide isolators and by highlighting the characterization methods and experimental set-up. Next, a chronological overview is given of the different non-reciprocal structures that have been developed. Starting point is the first experimental verification of the isolator concept. We show how subsequent improvements have resulted in a progressive increase of the performance. The final result is the demonstration of a transparent monolithically integratable waveguide isolator with a performance that is more than 80 times better than that of the first non-reciprocal device.
In the last main section of this chapter we focus on the realization of an amplifying waveguide optical isolator with an integrated electromagnet, which addresses the issue of low magnetic remanence of these isolator structures.

4.1 Fabrication of ridge waveguide isolators

One of the main advantages of the TM-mode amplifying waveguide optical isolator scheme is the ease of fabrication. As the device basically is a semiconductor optical amplifier (SOA) with a sputtered metal contact, standard SOA/laser fabrication can be used and we can profit from the extensive know-how on this processing. The only additional processing step is the deposition of the ferromagnetic metal film. The initial processing sequence is summarized below. A more detailed description is given in appendix A.
The deposition of the ferromagnetic film is done in a custom-made magnetron sputtering system. The deposited Co_xFe_{1-x} film is polycrystalline with a grain size of some tens of nanometers. During sputtering of the ferromagnetic metal, a magnetic field of 100Oe is being applied oriented perpendicular to the waveguide stripes. This is done to induce in-plane magnetocrystalline anisotropy in the polycrystalline ferromagnetic layer [1] to counteract the shape anisotropy caused by the high aspect ratio of the ferromagnetic strip (see section 2.4.4.2).

1. etching of the ridge waveguides
2. spinning of the current isolation layer + etching of the current injection windows
3. metallization via a lift-off process (30μm wide metal stripes: 50nm Co_xFe_{1-x} + 40nm Ti + 150nm Au)
4. additional steps: electro-plating, substrate thinning and back contact deposition

The specific configuration of the amplifying waveguide isolator however adds a difficulty to the fabrication of the devices. Because the cladding thickness between the core and the metal is thin, the etch depth of the ridge waveguides is inherently small. In other words, the aspect ratio of the ridge – the ratio of the ridge height to the width – is low compared to that of standard ridge lasers or SOAs. This places very stringent requirements on the alignment of the photo-resist mask that defines the window in the current isolation layer. Misalignment of the mask causes the plasma etched window to be partially located next to the ridge. In the case of a very shallowly etched ridge, the chances are high that the thin current isolation layer (polyimide or benzocyclobutene (BCB)) is completely removed, causing deposition of (ferromagnetic) metal next to the ridge. This is obviously highly unwanted as it leads to an increase of the internal loss of the device. Of course with a high aspect ratio ridge misalignment of the lithography mask also causes a misaligned window, but with a negligible impact on the device due to the thick isolation layer. Figure 4.1 illustrates the difference in impact of mask misalignment between waveguide ridges with high and low aspect ratios.
To overcome these inaccuracies a number of modifications to the fabrication process have been tested. For the second run[1] of non-reciprocal devices it has been decided to make the current isolation window substantially smaller than the ridge

[1] which we call the first run of the second-generation (see section 4.3.2)

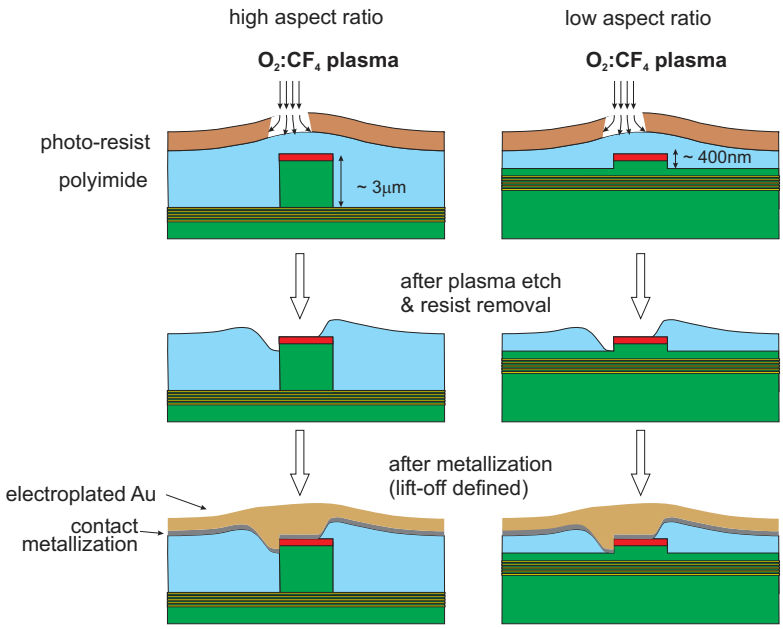

Figure 4.1: Illustration of the effects of a misalignment of the isolation mask on high and low aspect ratio ridges. A misalignment might lead to part of the contact window opening up next to the ridge, which for a low aspect ratio ridge can have dramatic consequences (after [2]).

width. This largely reduces the impact of mask misalignment. A big disadvantage of the partial coverage of the ridge with ferromagnetic metal is the fact that the strength of the non-reciprocity is only a fraction – the covered width divided by the total ridge width – of the maximum value.
A second possibility to improve the isolator fabrication is to use the ferromagnetic metal strip as the etch mask for the ridge waveguide definition. First, ferromagnetic metal strips with a width equal to the required waveguide ridge width are deposited onto unprocessed wafer material. Subsequent etching of this material creates ridge waveguides that are automatically completely covered with the ferromagnetic metal. This processing scheme is illustrated in figure 4.2. The ferromagnetic metal film is covered with a protective Ti/Au bilayer before etching. A second metallization step is required to define the electrical contact pads. For more details on this fabrication method we refer to appendix A.
The modified processing sequence has been applied for the fabrication of all non-reciprocal devices since the third run[2]. In figure 4.3 scanning electron microscope (SEM) images of cross-sections of such components are shown. Clearly, complete covering of the waveguide ridge with metal has successfully been obtained and the actual ridge width is in good agreement with the design value. Close inspection of the metal stack on top of the waveguide ridge reveals a minor residual fabrication error, i.e. an imperfection of the lift-off step. The consequences are a

[2]which we call the second run of the second-generation (see section 4.3.3)

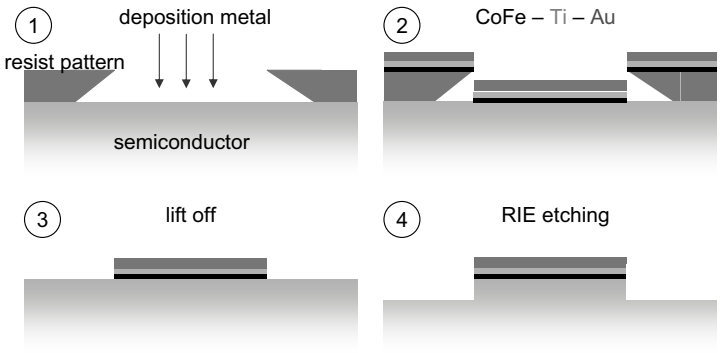

Figure 4.2: Modified processing sequence of the optical isolator, using the ferromagnetic metal as an etch mask for the ridge waveguide definition.

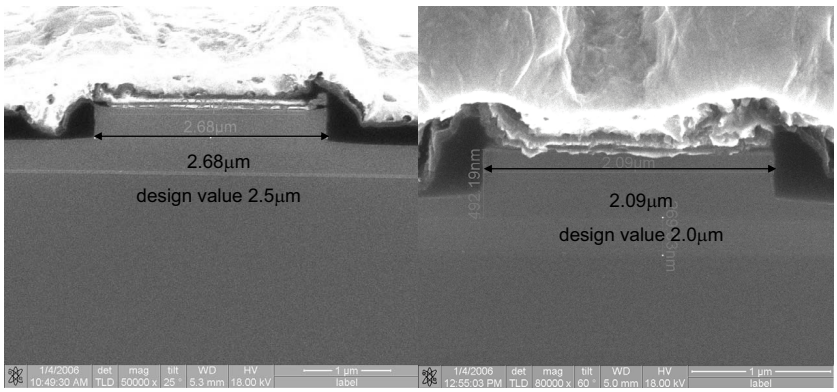

Figure 4.3: Scanning electron microscope images of the cross-section of the non-reciprocal devices of the third generation, fabricated with the modified processing scheme.

slight increase of the ridge width and the fact that the metal film is not in contact with the semiconductor at the (lateral) edges. Note that the rough 'cut' of the metal layers on the right part of figure 4.3 results from the cleaving of the waveguide facets.

We end this section on the fabrication of ridge waveguide isolators with the following remark on the thickness of the Co_xFe_{1-x} layer. In all practical devices the Co_xFe_{1-x} film has been limited to a thickness of 50nm. This limit is imposed by technological constraints. At higher thickness values tension in the film detaches the metal from the semiconductor during cooling after sputter deposition. It can however be proven that at 50nm the Co_xFe_{1-x} film is close to being optically opaque. Nevertheless, for certain applications (see section 4.4) it is preferable to have a thicker Co_xFe_{1-x} layer. One solution could be to deposit the metal in several subsequent steps.

4.2 Characterization of optical isolators

In this section an overview is given of the characterization methods and tools that have been used for the experimental determination of the performance of the fabricated devices.

4.2.1 Characterization methods

The basic specifications of the stand-alone optical isolator that need to be characterized are the optical isolation ratio (in dB/cm) or the isolation (in dB) and the bias current needed to achieve transparency in the forward propagation direction. Depending on the quality of the device a number of extraction techniques are available and have been applied during this work. In this section these methods will be discussed.

4.2.1.1 Non-reciprocal amplified spontaneous emission

In case the internal loss of the isolator waveguides is very high it is not possible to get close to the transparency point with realistic bias currents. This implies that it is not possible to evaluate the transmission of light through the device. However, the performance of the non-reciprocal device[3] can also be characterized on the basis of the emitted amplified spontaneous emission (ASE), both qualitatively and quantitatively. An extensive study of this is given in reference [2], hence we will limit ourselves to summarizing the outlines here.
TM-polarized spontaneous emitted light generated in the amplifying waveguide interacts with the magnetized metal contact and experiences a non-reciprocal loss shift. The strength and the sign of this shift are determined by the off-diagonal elements of the permittivity tensor of the metal $\epsilon_{ij}(\boldsymbol{M})$ which scale linearly with the magnetization vector $\boldsymbol{M}$, as thoroughly discussed in section 2.1.1.2. The detected output power therefore also scales with $\boldsymbol{M}$. This implies that if the ferromagnetic

[3]One can only use the term 'optical isolator' once transparency in one propagation direction is achieved.

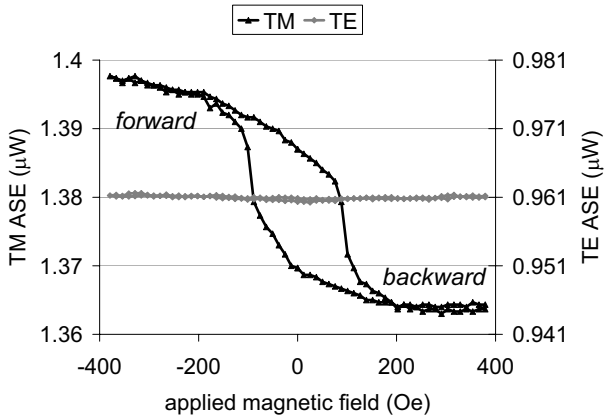

Figure 4.4: First qualitative demonstration of the optical isolator concept; TM-power is proportional to the magnetization, while TE-light remains unaffected by the magnetic field. First-generation $Co_{90}Fe_{10}$/InGaAsP device (3QW, t_{InP} = 250nm, L = 800μm, w = 2.5μm, J = 5kA/cm^2) [3].

film is looped through its magnetic hysteresis loop – through variation of an externally applied magnetic field – this hysteresis should be reflected in the measured optical intensity. At the same time, as there is no magnetooptic Kerr effect for TE-polarization in this configuration, the response of TE-ASE on a variation of the external magnetic field should be zero. This guarantees the absence of magnetic effects in the mechanical parts of the experimental set-up. Observation of the hysteresis shape for TM-polarization is therefore an unambiguous qualitative proof of the presence of the magnetooptic Kerr effect. A measurement example is illustrated in figure 4.4. As a matter of fact this was the first ever observation of the desired non-reciprocal effect on the novel isolator configuration, demonstrated by Vanwolleghem [2, 3].

In addition, as the TM-ASE hysteresis loop is the direct translation of the magnetic hysteresis loop of the magnetic metal strip, its properties such as coercitivity and the magnetic squareness are identical, hence it is straightforward to estimate the magnetic quality of the ferromagnetic film.

Detection of the emitted amplified spontaneous emission not only results in a qualitative proof of the non-reciprocal effect, but can also be used to extract quantitative information. This can be understood from figure 4.5, on which the TM ASE hysteresis loops are plotted for a range of bias current density values. Increasing the current obviously increases the global intensity of emitted light, but also the magnitude of the non-reciprocal effect increase. This is the manifestation of the enhanced contribution of ASE generated deeper inside the device, as the current injection increases. Because this light has traveled a longer distance through the device the observed non-reciprocity is higher. As such, several measurement points are available for the same effect. The important quantity is the so-called ASE ratio, that is the the ratio of the output power at magnetic saturation in both lateral directions. Measurement of this ASE ratio as a function of the injected current and on devices with different lengths, combined with fitting to

a suitable theoretical ASE model, allows for qualitative extraction of the strength of the non-reciprocal effect. Additional information that follows from this fitting is the value of the gain parameters G_0 and J_0 of the logarithmic relation between modal gain and the injected current.
The ASE-based method has been used during the first research steps towards an amplifying waveguide optical isolator.

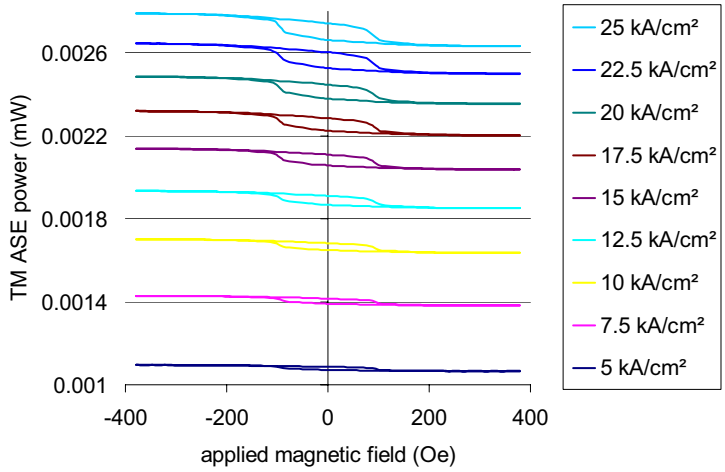

Figure 4.5: TM ASE hysteresis measurements on the same device as in figure 4.4 for varying injection current densities [4].

4.2.1.2 Non-reciprocal lasing

The ASE-based characterization method is laborious and requires fitting to a theoretical model. An easier method is therefore desirable. If the pump current is high enough the device approaches optical transparency. In an as-cleaved optical isolator optical feedback comes into play and the device essentially becomes a Fabry-Pérot cavity with an internal loss that depends on the propagation direction of the light. At sufficiently high currents there can be on-set of lasing. In this above-threshold regime the non-reciprocal loss shift $\Delta\alpha$ and the isolation ratio IR are described by the expressions:

$$\begin{aligned} \Delta\alpha[1/mm] &= \frac{2}{L[mm]} ln(\rho) \\ IR[dB/mm] &= \frac{10}{ln(10)} \frac{2}{L[mm]} ln(\rho) \end{aligned} \tag{4.1}$$

with only the cavity length L and the ratio of the forward to the backward emitted power ρ as required parameters. The proof of these formulas is given in appendix B. As this method of non-reciprocal lasing requires nothing but a measurement of the output power of a (non-reciprocal) laser for two different directions of an

externally applied magnetic field, it is a fast and robust way of characterizing the most basic property of an optical isolator, i.e. the optical isolation ratio.
Furthermore from the experimental value of the threshold current I_{thresh} an estimate of the forward transparency current $I_{transp,fw}$ of the device can be made:

$$I_{transp,fw} = dLJ_0 exp\Big[ln\Big(\frac{I_{thresh}}{dLJ_0}\Big) + \frac{\Delta\alpha}{2\Gamma A} - \frac{1}{\Gamma AL} ln\Big(\frac{1}{R}\Big)\Big] \tag{4.2}$$

with d the width of the waveguide ridge,[4] L the cavity length, A and J_0 the parameters of the gain relation of the quantum well material, Γ the confinement of the optical mode in the quantum wells and R the facet reflectivity. This expression is elaborated in appendix B. Anyhow, the threshold current is an upper limit of the transparency current and is in long cavity devices not so different from the actual value.

4.2.1.3 Transmission measurement

The non-reciprocal laser technique described in the previous paragraph is a handy tool for fast characterization of an amplifying waveguide optical isolator. However, an optical isolator is a device used in transmission, hence should be evaluated as such. A stand-alone isolator is tested by coupling TM-polarized light from an external laser to the waveguide and measuring the output signal while electrically biasing the device. This signal consists of the transmitted laser light and the generated amplified spontaneous emission (ASE). The broadband ASE contributes to the noise on the signal and is expected to decrease the optical signal to noise ratio (OSNR). The optical isolation is by definition the difference in transmitted power between forward and backward direction:

$$Iso[dB] = P_{fw}[dB] - P_{bw}[dB]. \tag{4.3}$$

With a large contribution of the ASE to the total signal it is necessary to look at the spectral picture of the emitted power for a correct determination of the optical isolation. After all the difference between forward and backward ASE-power is lower than the difference on the transmitted light.

4.2.2 Characterization setup

Characterization of the amplifying waveguide optical isolator comes down to the detection of light emitted by or transmitted through the amplifier-based waveguide device, under the application of a magnetic field. As such, the measurement setup basically is a SOA setup extended with an electromagnet. This is illustrated in figure 4.6. The heart of the setup is the photonic chip mounted on a sample holder. The device is cleaved and possibly provided with anti-reflection coatings on the waveguide facets. The electrical pumping of the SOA is done via probe needles placed on the front and back contact of the active component. The temperature of the chip is controlled and stabilized with a thermoelectric cooler (TEC). A

[4] Actually d is the effective width of the ridge waveguide, taking into account the lateral current spreading.

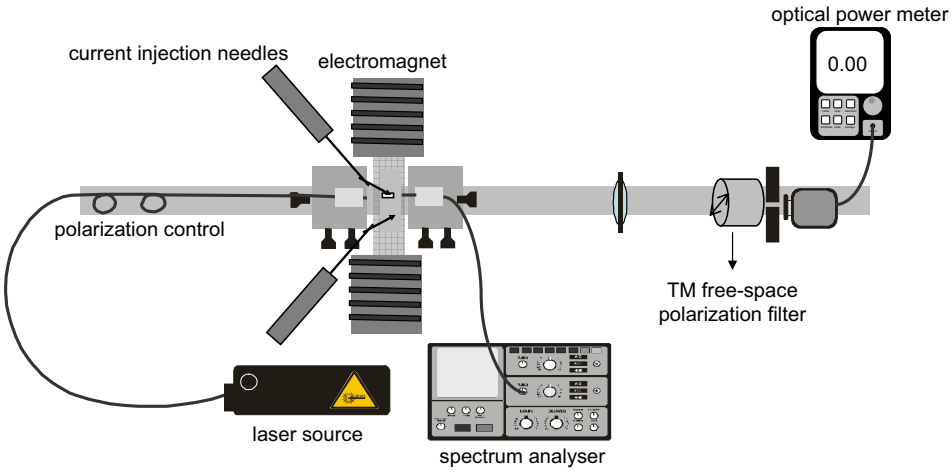

Figure 4.6: Schematic illustration of the isolator characterization setup.

(tunable) laser input signal is coupled to the device via a lensed fiber. The output light can be captured either with a free-space detector or a spectrum analyzer. In principle the output intensities at both facets need to be compared. This however requires that the coupling efficiencies between chip and detector are identical at both sides, which is extremely difficult to realize. The fact that the magnetooptic effect is symmetric with respect to the zero-magnetization state provides a solution. An equivalent experiment is to compare the output intensities at one facet for magnetization in both lateral directions ($\boldsymbol{M}$ = +M and $\boldsymbol{M}$ = -M). As it is the ratio of both intensities that contains the useful information, the requirement for the identical coupling is eliminated.
For a more detailed description of the measurement setups we refer to appendix C.

4.3 Experimental results

In this section we give a detailed and chronological overview of the measurement results. As an introduction and for the sake of completeness we shortly summarize the work described earlier in the PhD of Vanwolleghem [2], that is, the first demonstration of the isolator principle and the first iteration in the optimization. We also evaluate the shortcomings of these devices and describe opportunities for improvement. Next, we continue with two subsequent optimization steps.

4.3.1 First demonstration - generation I

At the time of developing a device for the first demonstration of the amplifying waveguide optical isolator concept, choices had to be made on the materials used in this device. For the amplifying core, it was decided to develop TM-selective

Label	t_{InP} (nm)	t_{SCH_l} (nm)	t_{SCH_u} (nm)	$\Delta\alpha$ (dB/mm)	g_{QW} (cm^{-1})
3QWs	450	120	100	1.9 - 2.8	3000
3QWn	300	150	150	3.0 - 5.0	5000
3QWr	250	155	170	4.0 - 6.0	6000
6QW	300	100	50	4.0 - 5.5	3000
9QW	300	50	50	3.5 - 5.5	1700

*Table 4.1: Overview of the specifications and the theoretically predicted performance of the first-generation isolator demonstrator designs. The two values for the non-reciprocal loss shift correspond to the lower (*Q = 0.02+0.02j*) respectively upper limit (*Q = 0.03+0.03j*) on* Q*.*

multiple quantum well (MQW) material in the common InGaAsP-InP material system. For the magnetooptic metal the $Co_{90}Fe_{10}$ compound was chosen, a choice which was merely based on previous expertise with deposition of this material. The ohmic metal-semiconductor contact structure as described in chapter 3 was already developed, although it was unknown at that time what the influence of this contact structure would be on the magnetooptic performance of the isolator. Instead, the optimization aimed for a low contact resistivity combined with minimal extra absorption. As elaborated in chapter 3 the design of the isolator layer structure includes the determination of the thickness values of the separate confinement heterostructure layers (SCH) surrounding the MQW section and of the InP cladding layer between the active core and the contact structure. The design of the first isolator demonstrator was seriously complicated due to the fact that important simulation parameters such as the optical and magnetooptic parameters of $Co_{90}Fe_{10}$ were unknown at that time. Instead, a not too optimistic value of the MO constant Q of $Co_{90}Fe_{10}$ and the refractive index of pure Cobalt (Co) were used.[5] The outcome of these simulations was a set of five designs, given in table 4.1, each of which have been fabricated and subsequently characterized. g_{QW} is the TM material QW gain needed for transparency in the forward propagation direction. In table 4.2 the layer structure of the first-generation non-reciprocal devices is given.

The first ever verification of the amplifying waveguide optical isolator concept was done on these fabricated devices, by measuring the TM- and TE-ASE response to looping the magnetic contact through its entire hysteresis loop, as was illustrated before in figure 4.4. With respect to quantitative characterization of the first generation non-reciprocal devices it needs to be noticed that the levels of material gain required for forward transparency are too high to achieve transparency. The ASE-based characterization method was therefore the only possible way of extracting the device performance. As explained before, measuring the emitted non-reciprocal ASE on devices with different lengths at various bias current levels enables for the determination of the non-reciprocal loss and the modal gain characteristics of the devices. The experimental values are tabulated in table 4.3. The last column shows the theoretical non-reciprocal loss shift, calculated afterwards with the experimental optical and magnetooptic constants of $Co_{90}Fe_{10}$.

[5]The estimated upper and lower limit for Q are 0.03+0.03j respectively 0.02+0.02j. The subsequently extracted value equals 0.022+0.039j

Layer	Composition	Refractive index	Thickness (nm)
MO metal	$Co_{90}Fe_{10}$	$3.29 - 5.54j$ $Q = (0.02, 0.03)$ $+(0.02, 0.03)j$	50
Contact layer	$In_{0.54}Ga_{0.46}As$ $N_{Be} = 3 \times 10^{19}$ cm^{-3}	$3.6 - 0.2j$	15
Contact layer	$In_{0.81}Ga_{0.19}As_{0.41}P_{0.59}$ $N_{Be} = 2 \times 10^{19}$ cm^{-3}	3.37	100
Cladding	InP	3.203	table 4.1
Upper SCH	$In_{0.9}Ga_{0.1}As_{0.21}P_{0.79}$	3.28	table 4.1
Barrier ($\times 4 - 10$)	$In_{0.93}Ga_{0.07}As_{0.22}P_{0.78}$ $\epsilon = +0.3\%$	3.29	22
Well ($\times 3 - 9$)	$In_{0.48}Ga_{0.52}As_{0.78}P_{0.22}$ $\epsilon = -1.1$ %	$3.34 - kj$	12
Lower SCH	$In_{0.9}Ga_{0.1}As_{0.21}P_{0.79}$	3.28	table 4.1
Substrate	InP	3.203	

Table 4.2: Slab layer structure of the first-generation InGaAsP isolator demonstrator. The refractive index values are taken from [5]. For the optical constants of the magnetooptic layer the values of pure Co have been used [6]. The uncertainty in the magnetooptic Voigt parameter Q of $Co_{90}Fe_{10}$ is reflected by the variation considered in the real and imaginary parts of Q. These have been obtained by considering a 50% uncertainty on both real and imaginary parts of the constant for pure Co (found in [7]). ϵ is the amount of built-in strain in the wells and the barriers ($\epsilon > 0$ compressive strain, $\epsilon < 0$ tensile strain). k *is determined by the current injection in the amplifying region.*

Label	A (1/mm)	B (1/mm)	A ln(J)-B (1/mm) (for $J = 20$kA/cm^2)	$\Delta\alpha_{meas}$ (dB/mm)	$\Delta\alpha_{sim}$ (dB/mm)
3QWn	4.0	42.0	-30.0	4.4	7.6
3QWr	4.5	21.0	-7.5	2.0	9.3
6QW	8.4	52	-26.8	6.5	8.7

Table 4.3: Experimental performance of the first-generation non-reciprocal devices. In the last column the reassessed theoretical non-reciprocal loss shift, calculated using the known optical and magnetooptic properties of $Co_{90}Fe_{10}$.

While there clearly is a discrepancy between the experimental values and those predicted by theory, the difference is not an order of magnitude. These results can therefore be considered as a very good start in the development of an optical isolator.

4.3.2 Improved non-reciprocal devices - generation II: first run

4.3.2.1 Description

One way to increase the performance of the amplifying waveguide optical isolator is to improve the quality of the amplifying core material, as this lowers the current

Label	t_{InP} (nm)	t_{SCH_l} (nm)	t_{SCH_u} (nm)	$\Delta\alpha$ (dB/mm)	J_{tr} (kA/cm^2)
O	345	0	15	4.7	4.87
R1	295	0	15	7.41	16.9
R2	280	0	15	8.5	28.2

Table 4.4: Design values of the 3 second-generation 9QW InAlGaAs $Co_{90}Fe_{10}$ demonstrators.

required for forward transparency. At the time of designing the second-generation of non-reciprocal devices tensile strained InAlGaAs-InP MQW material had been demonstrated and the corresponding gain-current relationship had been experimentally determined. On top of that the entire permittivity tensor of $Co_{90}Fe_{10}$ had been extracted. This extra input enabled much more accurate simulation of the isolator layer structure compared to the first-generation devices. The specifications and theoretical performance of the 3 second-generation non-reciprocal devices are tabulated in table 4.4. All details on the layer structure can be found in table 4.5. The calculations that have led to these values are extensively described by Vanwolleghem [2], hence shall not be repeated here. However, in view of further development of the isolator it is worth formulating the following comments. The 'O' design is the result of optimization with the following figure-of-merit (FoM):

Layer	Composition	Refractive index	Thickness (nm)
MO metal	$Co_{90}Fe_{10}$	$4.65 - 4.82j$ Q=0.022+0.039j	50
Contact layer	$In_{0.54}Ga_{0.46}As$ $N_{Be} = 3 \times 10^{19}$ cm^{-3}	$3.6 - 0.2j$	15
Contact layer	$In_{0.81}Ga_{0.19}As_{0.41}P_{0.59}$ $N_{Be} = 2 \times 10^{19}$ cm^{-3}	3.37	100
Cladding	InP	3.203	table 4.4
Upper SCH	$In_{0.86}Ga_{0.14}As_{0.31}P_{0.69}$	3.34	table 4.4
Barrier ($\times$10)	$In_{0.93}Ga_{0.07}As_{0.22}P_{0.78}$ $\epsilon = +0.6\%$	3.29	20
Well ($\times$9)	$In_{0.34}Al_{0.14}Ga_{0.52}As$ $\epsilon = -1.25$ %	$3.57 - kj$	10
Lower SCH	$In_{0.86}Ga_{0.14}As_{0.31}P_{0.69}$	3.34	table 4.4
Substrate	InP	3.203	

Table 4.5: Slab layer structure of the second-generation InAlGaAs isolator demonstrator. The refractive index values are taken from [5] and the optical and magnetooptic constants of $Co_{90}Fe_{10}$ follow from experimental characterization (table 3.2.1). The extinction coefficient of the wells k *is related to the current density through the experimental relation 3.18.*

$$FoM_{gII} = \frac{\Delta\alpha^2}{J_{transp}}, \tag{4.4}$$

which means that the product of the length and the transparency current has been minimized, as elaborated in chapter 2. The 2 other designs, 'R1' and 'R2', do not

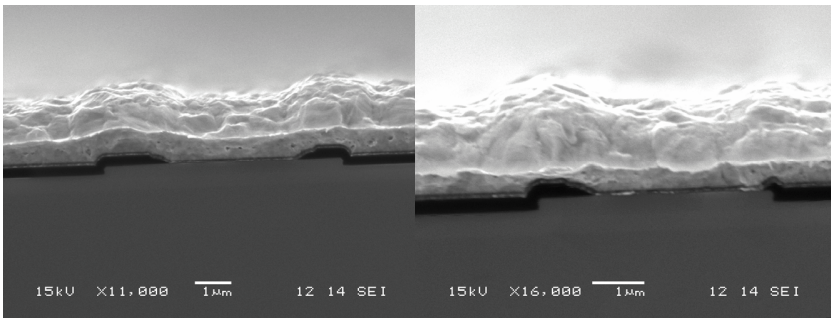

Figure 4.7: Scanning electron microscope images of the cross-section of the first run of the second generation non-reciprocal devices.

maximize this or any other practical FoM but have been found by decreasing the InP cladding thickness starting from the 'O'-point. The non-reciprocal loss shift and the reciprocal absorption increase accordingly. As such the purpose of the R1 and R2 designs was to demonstrate very high non-reciprocity with more or less realistic transparency current values.

Another route towards improvement is to find a ferromagnetic metal with improved optical and magnetooptic properties, resulting in lower optical loss and/or higher non-reciprocity. As reported by Zvezdin [8] the equi-atomic $Co_{50}Fe_{50}$ compound shows a higher value of the Kerr rotation in the visible wavelength range. As the dispersion of magnetooptic effects can be substantial, this increase cannot be directly interpolated to the infrared wavelength range and it is therefore not at all certain that the equi-atomic alloy has a higher Kerr rotation at 1300nm wavelength. Furthermore, not only the Kerr rotation but also the Kerr ellipticity plays an important role in the metal-clad isolator. Still, it was decided to fabricate a number of second-generation isolators with a $Co_{50}Fe_{50}$ film as the source of the magnetooptic effect. It was only later that experimental determination of all elements of the permittivity tensor, as described in chapter 3, confirmed that the material properties of $Co_{50}Fe_{50}$ are much better for use in the isolator scheme.

The second-generation devices have been fabricated as described in section 4.1, with wide waveguide ridges that are only partially covered with the ferromagnetic contact. Electron microscope images of two of these devices are depicted in figure 4.7.

4.3.2.2 Characterization

The fabricated non-reci-procal devices have been characterized using the non-reciprocal lasing technique described earlier. Table 4.6 gives an overview of some observed trends. The most important result is that a high non-reciprocal loss shift of 3.47dB/mm has been observed – on a $Co_{90}Fe_{10}$ device – which is an improvement by 75% compared to the first-generation. With respect to the ferromagnetic metal choice, we remark that a real comparison between $Co_{90}Fe_{10}$ and $Co_{50}Fe_{50}$ devices was not possible due to processing imperfections. However, as indicated in the bottom part of table 4.6, first measurements on $Co_{50}Fe_{50}$ devices indicate

Family		$\Delta\alpha$ (dB/mm)
$Co_{90}Fe_{10}$, 7μm	O	1.95
	R1	1.52
	R2	3.26
$Co_{90}Fe_{10}$, R1	5μm	3.47
	7μm	1.52
	9μm	1.09
R2, 5μm	$Co_{90}Fe_{10}$	1.95
	$Co_{50}Fe_{50}$	2.82

Table 4.6: Experimental non-reciprocal loss shift values obtained on the isolators of the first run of the second-generation.

that a shift towards the equi-atomic Co_xFe_{1-x} compound leads to an improvement of at least 45% in terms of the isolation ratio (in dB/mm).

The specific fabrication method of the second-generation devices has some important effects on their performance. First of all, the non-reciprocal components are only partially covered with ferromagnetic metal, which reduces the non-reciprocal loss shift largely. On top of that the ridge waveguides are wide, hence bimodal or even multimodal. Multimodality is in itself obviously unwanted for the optical isolator as the light of the (integrated) laser diode might couple to the different guided modes of the isolator. Even more important is the fact that the non-reciprocal loss shift of a higher order mode is smaller than that of the fundamental mode. The reason for this is that the lateral confinement of higher order light in the ridge is lower, hence there is less overlap with the ferromagnetic metal.

4.3.3 Generation II: second run

4.3.3.1 Description

As explained in section 4.1 an improved fabrication method has been developed to overcome the problems of partial coverage and misalignment of the ferromagnetic metal encountered with the standard laser processing. The improved processing procedure, based on the use of the contact metal as the etch mask should result in the accurate fabrication of narrow, hence monomodal, waveguide isolators. Furthermore, the ferromagnetic metal parameter extraction (table 3.2.1) and the first-run isolator experiments (table 4.6) have indicated that the $Co_{50}Fe_{50}$ composition is essentially better suited for the waveguide isolator than $Co_{90}Fe_{10}$.
As we were convinced that the second-generation layer structure had not been exploited to its limits, we decided to do a second processing run on the same wafer material, using the modified processing sequence and with $Co_{50}Fe_{50}$ metal contacts. To have an idea of the theoretical performance non-reciprocal slab waveguide simulations with this structure have been performed.[6] The description and theoretical performance of the second-run layer structure are given in table 4.7. Comparison with the values in table 4.4 shows that, even though the layer

[6]Remember that the layer structure design has been carried out for the $Co_{90}Fe_{10}$ alloy.

Label	t_{InP} (nm)	t_{SCH_l} (nm)	t_{SCH_u} (nm)	$\Delta\alpha$ (dB/mm)	J_{tr} (kA/cm^2)
O	345	0	15	7.55	2.34
R1	295	0	15	11.9	4.94
R2	280	0	15	13.62	7.65

Table 4.7: Design values of the 3 second-generation 9QW InAlGaAs $Co_{50}Fe_{50}$ demonstrators.

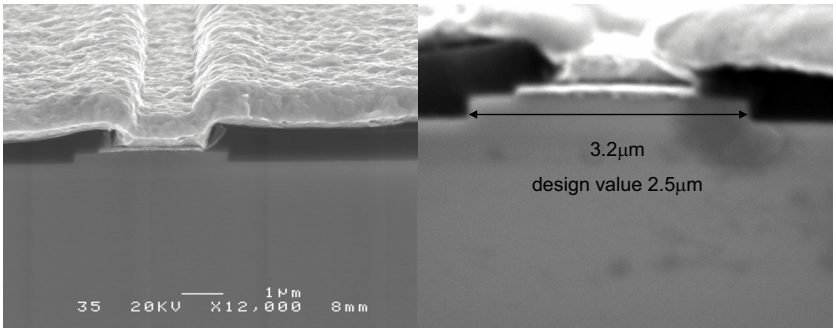

Figure 4.8: Scanning electron microscope images of the cross-section of the second run of the second generation non-reciprocal devices. Bad directionality of Ti deposition causes fabrication inaccuracies.

structure is not optimized for $Co_{50}Fe_{50}$, the performance of the second-generation waveguide isolators is substantially improved when using $Co_{50}Fe_{50}$ as the magnetooptic metal contact, with a non-reciprocal loss shift that is 60% higher and a transparency current density of less than half the value of the $Co_{90}Fe_{10}$ case.

As indicated in the SEM images of figure 4.8 the fabrication is however not perfect, with again ridge waveguides that are substantially wider than designed, i.e. 3.7μm instead of 2.5μm. This fabrication error can be explained from bad directionality of the sputtering of at least one of the metal layers, causing metal to be deposited underneath the photo-resist, as illustrated in figure 4.9. Here, the Ti film has caused the imperfection. As such, the side part of the ridge is only covered with Ti and not with the ferromagnetic $Co_{50}Fe_{50}$, which increases the loss without contributing to the magnetooptic effect. Due to these fabrication errors the ridge waveguides support two guiding modes instead of being monomodal, which would have been the case with a 2.5μm wide stripe. The calculated optical and magnetooptic parameters of the guided modes are given in table 4.8 for the R2 design.[7] These values have been obtained through simulations with a 2D mode solver extended with the perturbation-based algorithm for magnetooptic waveguide calculation (see section 3.5). The exact cross-section (ridge width, etch depth and partial coverage with ferromagnetic metal), derived from SEM images of the fabricated devices, served as input for these simulations. The extinction coefficients have been calculated with the multiple quantum well core considered as a passive, transparent stack. In other words, only the absorption in the metal layers and the ternary contact layer have been accounted for. As anticipated, the

[7] As it was the goal at this stage of the research to demonstrate as high as possible non-reciprocity almost all experiments on the second run components have been done on the R2 layer structure.

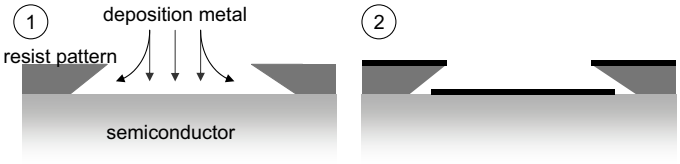

Figure 4.9: Illustration of increased metal film width due to bad directionality of metal deposition or sputtering.

Mode	n	k	$\Delta\alpha$ (dB/mm)	J_{tr} (kA/cm^2)
0	3.317	0.0025	10.59	11.2
1	3.312	0.0014	4.66	10.0

Table 4.8: Calculated properties of the two guided modes of a 3.7μm wide ridge waveguide with layer structure R2. A 2.5μm wide metal contact is positioned central on the waveguide.

non-reciprocal loss shift on the first order mode is much lower than that on the fundamental mode due to the lower overlap of the first with the ferromagnetic metal. However, the low lateral confinement of the odd first order mode within the pumped guiding region – 9.7% against 16.9% for the zeroth order mode – enhances the required bias current density, making the required current injection almost the same for both guided modes despite the much higher extinction coefficient of the fundamental mode.

4.3.3.2 Characterization

We start this section with the characterization of the actual modal structure of the fabricated non-reciprocal devices. This is done by measuring the far-field pattern of the emitted ASE – or the laser signal if above threshold. A free-space detector is rotated in y-z plane – coordinate system as indicated in figure 4.10 – at a fixed transverse (x-axis) position at the center of the output beam, while the distance between the detector and the output facet is kept constant. The detected power as a function of the rotation angle gives the angular pattern of the light intensity. Figure 4.11 shows the evolution of this far-field pattern with increasing current injection. The threshold current I_{th} equals 230mA and the magnetization is set to zero, as we focus on the performance of the waveguide device as a normal Fabry-Pérot laser. These graphs show that the output signal is a complicated mixture of two lateral guided modes, where both the fundamental and the first order mode have an important contribution.

With the non-reciprocal lasing technique the optical isolation ratio of the non-reciprocal structures has been determined. Devices with a length of 490μm have been electrically pumped and the output power has been detected on a free-space detector for magnetic saturation in either lateral direction. A measurement example performed on a device of type R2 (table 4.7), is shown in figure 4.12. The output power versus current – the so-called LI-curve – is drawn in the left part of the figure. The corresponding power ratio evolution is shown on the right. The ratio above threshold equals 1.6, which on a 490μm long device, corresponds to

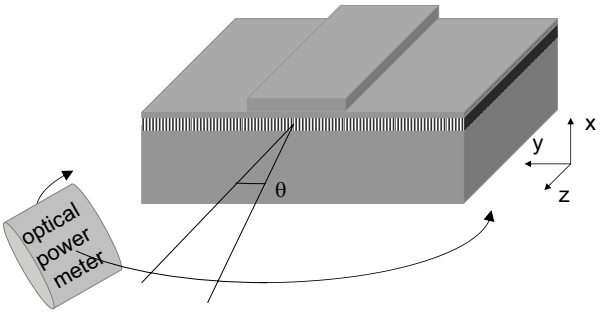

Figure 4.10: Schematic illustration of the setup used to measure the far-field pattern.

an optical isolation ratio of 8.33dB/mm according to formula 4.1.
As elaborated in section 4.2.1.2 is it possible to make a fairly accurate estimate of the forward transparency current from the experimental threshold current, using equation 4.2. The experimental threshold current equals 210mA. The calculated value of the optical confinement factor is 0.15, calculated with a 2D optical mode solver. The gain parameters can be found in section 3.1 and the facet reflectivity for the fundamental TM mode equals 0.28. The corresponding value for the forward transparency current is 166mA.
This result is a major improvement with respect to the first run of devices with a 2.4 times higher isolation ratio. However, comparing this to the theoretical value of 10.6dB/mm shows that there still is a discrepancy by a factor 1.27. It is straightforward that this is mainly due to the bimodality of the ridge waveguide. It is however possible to filter out the first order mode to a certain extent by measuring the optical output power with a monomode lensed fiber instead of a free-space detector. It can be expected that the power ratio increases significantly. The corresponding experimental result is presented in figure 4.13, with on the left graph the LI-curves for forward and backward propagation and on the right the corresponding power ratio. For comparison the ratio detected with a free-space detector is also given. The experimental power ratio measured with a lensed fiber equals 1.82, which corresponds to an optical isolation ratio of 10.6dB/mm. This is another significant improvement and compared to the first run the performance is three times better. In addition, this experimental result is in perfect correspondence to the theoretical performance.

As the second-generation non-reciprocal devices of the second run can easily be brought to lasing it should be possible to characterize them with a transmission experiment. TM-polarized incident light from an external cavity tunable laser (6dBm output power) is coupled to the waveguide, with the wavelength set close to that of the peak gain of the active material. The output signal is picked up with a single mode lensed fiber and detected with a spectrum analyzer at a resolution bandwidth of 0.5nm. The cleaved waveguide facets are uncoated and the length equals 380μm. Figure 4.14 shows the experimental nonreciprocal loss shift for an incident wavelength of 1290nm. The bias current is 175mA and is pulsed (pulse width 0.1μs, duty cycle 10%) to avoid heating due to the imperfect mounting of

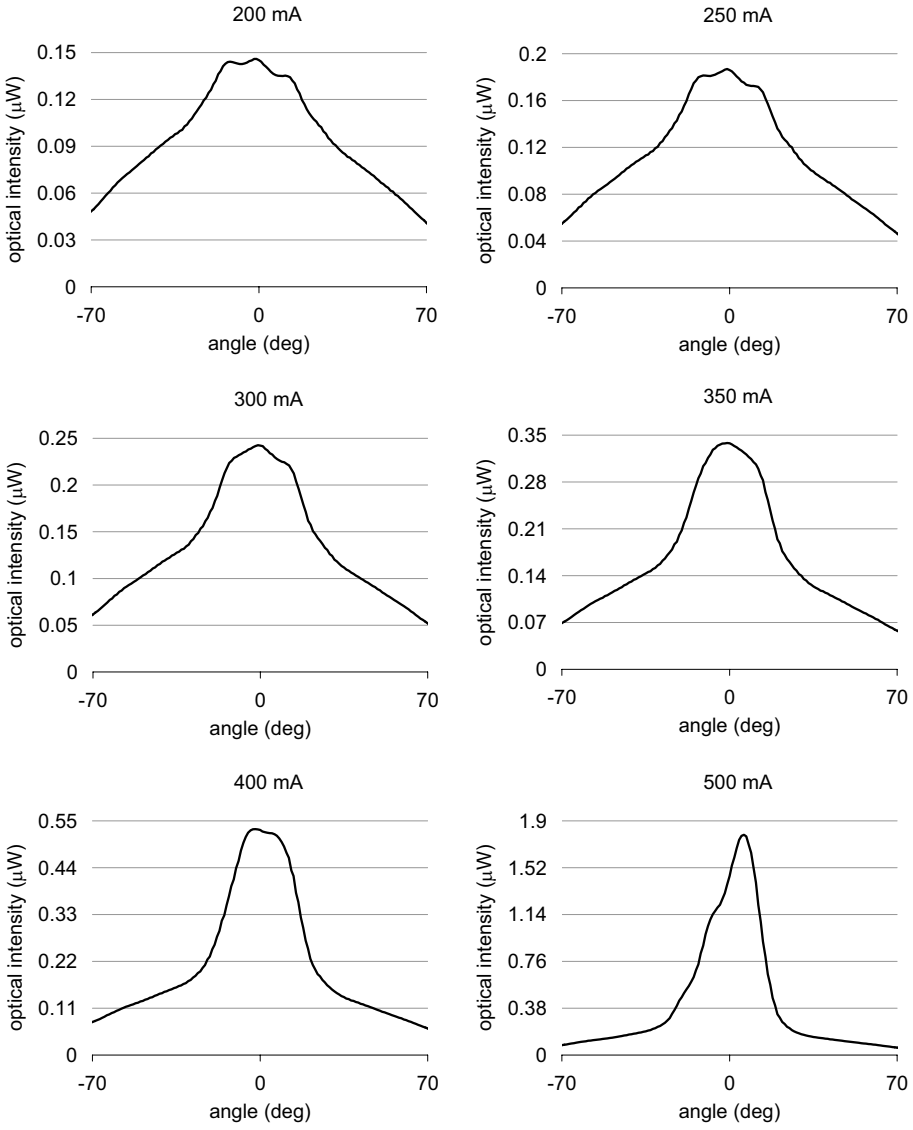

Figure 4.11: Evolution of the far-field pattern with injected bias current of the second-generation second-run devices (I_{th} = 230mA, w = 3.7μm).

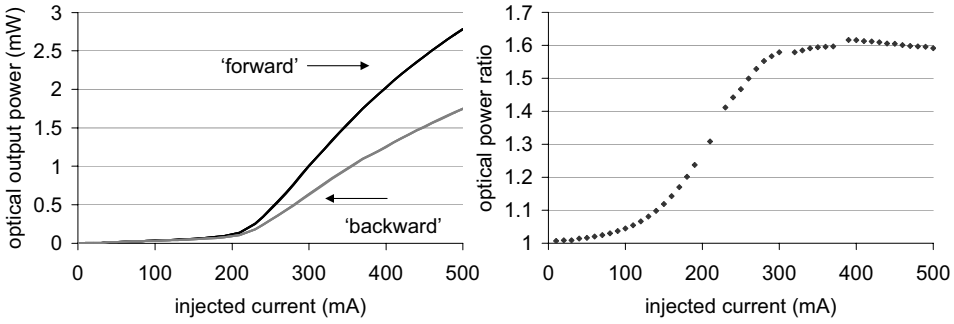

Figure 4.12: Non-reciprocal lasing experiment on devices of the second-generation second-run, measured with a free-space detector. The left picture shows the evolution of the output power with increasing bias current for forward and backward propagation. The right graph gives the corresponding power ratio. The ratio of 1.6 corresponds to an optical isolation ratio of 8.33dB/mm.

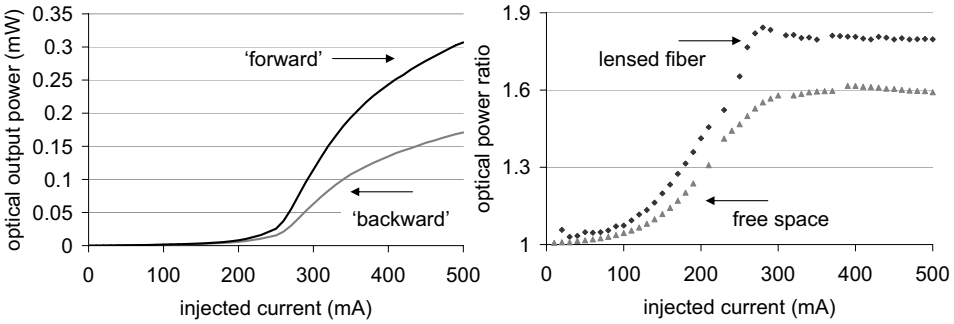

Figure 4.13: Non-reciprocal lasing experiment on devices of the second-generation second-run, measured with a monomode lensed fiber. The left picture shows the evolution of the output power with increasing bias current for forward and backward propagation. The right graph gives the corresponding power ratio and that measured with a free space detector for comparison. The ratio of 1.82 corresponds to an optical isolation ratio of 10.6dB/mm.

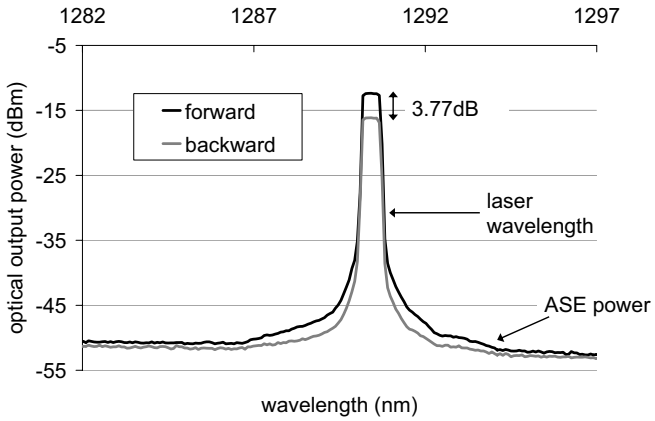

Figure 4.14: Transmission experiment on a 380μm long non-reciprocal device of the second-generation second-run. The spectrum of the output signal is plotted at saturation magnetization in both lateral directions. 3.77dB of isolation is equivalent to an isolation ratio of 9.9dB/mm.

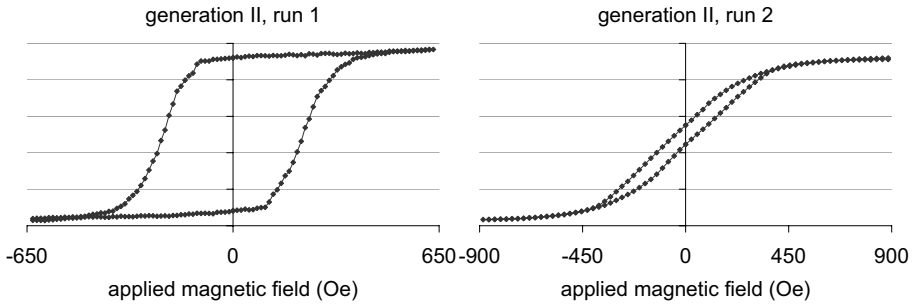

Figure 4.15: Comparison of the magnetic properties of the ferromagnetic metal strip of the first and second run of second-generation non-reciprocal devices. The output power is measured while looping the metal through its hysteresis loop.

the devices. The difference in power level between the 'forward' and 'backward' signal equals 3.77dB which, for a length of 380μm, is equivalent to an isolation ratio of 9.9dB/mm. This is in fairly good agreement with the experimental value obtained via the non-reciprocal lasing technique.

An intrinsic consequence of the fabrication method that uses the contact metal as the etch mask is that the width of the ferromagnetic strip is very small, in the order of 2μm. In other words, the aspect ratio of this strip – the ratio of the length to the width, is very high. As pointed out in section 2.4 this directly implies that the effect of shape anisotropy is huge, making the lateral direction a hard axis. In other words, the magnetic remanence is minimal. The impact of the high aspect ratio on the magnetic properties can be visualized with the ASE-hysteresis curves of the non-reciprocal devices. In figure 4.15 such graphs are plotted for the first (left) and the second (right) run of the second-generation demonstrators, measured on components with a length of 500μm. For the first run, standard laser processing has

been used, leading to 30μm wide CoFe contacts. The squareness of the magnetic contact – the ratio of the remanent magnetization to the saturation magnetization – is clearly close to 1. As a consequence these 'isolators' operate without application of an external magnetic field. With the adapted fabrication method the measured squareness is below 0.1. As such, operating the non-reciprocal device without application of an external magnetic field is not an option as this implies a poor performance of less than 10% of the potential isolating effect.
A number of solutions have been identified to enhance the remanent isolation performance. The possibility that is the easiest to implement is to replace the gold of the second metallization by the ferromagnetic metal. This way the effective width of the contact is much larger, if no cracks occur in this metal film. The first run of the second generation shows that this is possible if special care is taken of the planarization. Prerequisite for this solution is that the CoFe stripes defining the ridge waveguides aren't covered with a protective Ti/Au bilayer before etching. This might cause problems if the ferromagnetic film itself is etched away during the ridge waveguide definition.
A second solution is to integrate a magnet, either a permanent magnet or an electromagnet, in the vicinity of the isolator contact. In section 4.4 the development of an amplifying waveguide optical isolator with an integrated electromagnet is extensively discussed.
Another possibility is to use other magnetic materials with high magnetocrystalline anisotropy to balance the shape anisotropy. However, no such material has been identified with high magnetooptic parameters.
The remanence properties of the isolator could also be improved by adding an antiferromagnetic layer in between the ferromagnetic film and the Ti/Au contact. Through a phenomenon called exchange bias [9], the antiferromagnet shifts the hysteresis loop to higher fields, such that at zero magnetic field, the magnetic stripe is still magnetized. Since exchange bias is a surface effect where the shift scales with the inverse thickness of the ferromagnetic layer, the ferromagnetic layer needs to be very thin, i.e. less than 10 nm. A dramatic consequence is that the optical mode feels the presence of the antiferromagnetic layer, hence the non-reciprocity of the optical waveguide decreases.
In the frame of this work only the second possibility has been examined experimentally.

4.3.3.3 Conclusion generation II: second run

The extensive characterization of the second-generation optical isolators has made clear that, while the demonstrated levels of non-reciprocity are very high, the corresponding transparency current is about an order of magnitude above the acceptable value for a practical device. With no obvious improvements at the gain material side nor in the choice of the ferromagnetic metal, the remaining option was to reconsider the design procedure of the isolator layer structure. This has resulted in a third generation of optical isolator devices, as will be described in the next section. Furthermore, as the importance of lateral monomodality of the waveguide isolators had been clearly demonstrated, further perfection of the fabrication method was necessary.

4.3.4 Generation III

4.3.4.1 Description

The design of the second generation of amplifying waveguide optical isolators has two important shortcomings; first of all the layer structure was not at all optimized for the equi-atomic $Co_{50}Fe_{50}$, but instead for $Co_{90}Fe_{10}$ of which it has been shown that it is not the best choice for the isolator. Secondly, the R2 design, on which the best measurement results have been realized, focussed on achieving an as high as possible isolation ratio with a realistic forward transparency current. This approach does not necessarily minimize any of the practical figures of merit described in section 2.2.2. This is illustrated in figure 4.16 where the transparency current (in mA/dB), the product of the length times the transparency current (in mm/dB x mA/dB) and the isolation ratio (in dB/mm) are plotted for a variation of the InP cladding thickness on a benchmark optical isolator structure. The ferromagnetic metal is $Co_{50}Fe_{50}$, the thickness of the SCH layers is kept constant at 0nm and the ridge width is fixed at 2μm. The performance of the second-generation R2 design is indicated. The corresponding current-length product is 14% higher than the minimal value and the transparency current is even 121% higher than in the optimized case.
While maximizing the isolation ratio was appropriate in the first stages of the development of the optical isolator, the final goal is to maximize the practical performance, i.e. to minimize a parameter such as the transparency current or the device length. As it is our primary target to demonstrate a transparent amplifying waveguide optical isolator, we have to consider the minimization of the forward transparency current as the design criterion for the third-generation layer structure. It is obvious that for the third generation devices the $Co_{50}Fe_{50}$ alloy is used and that the amplifying core is a tensile strained multiple quantum well InAlGaAs-InP structure. With respect to the previous devices the built-in tensile strain is higher, -1.6% instead of -1.25%, which should result in a higher differential gain, as demonstrated in section 3.1. Just as in the previous designs the thickness of the SCH-layers and of the top cladding layer are the parameters that can be varied to optimize the figure of merit. In addition, for the third generation of isolators it has been examined whether a variation of the transparent quaternary contact layer thickness could deliver an improvement of the device performance. A conjugated gradient minimization algorithm has been used to find the optimized combination of thickness values. This has resulted in the two designs tabulated in table 4.9, with design D4P the one with an optimized contact thickness and D3P the design with the 15nm/100nm contact bilayer. The waveguide core has been assumed to be passive, an approach which has been validated in section 3.4.1. The current injection required for forward transparency has been calculated as:

$$I_{transp}[mA] = J_{transp}Lw = 5.28Lw\ exp\left(\frac{-\alpha_{fw}[cm^{-1}]}{466\Gamma}\right), \tag{4.5}$$

with w and L the waveguide ridge width (in μm) and the length (in mm) respectively and Γ the confinement of the guided mode in the quantum wells. In this equation the experimental gain-current relation of the -1.25% tensile strained material has been used as a best guess of the -1.6% strain gain parameters. The third-

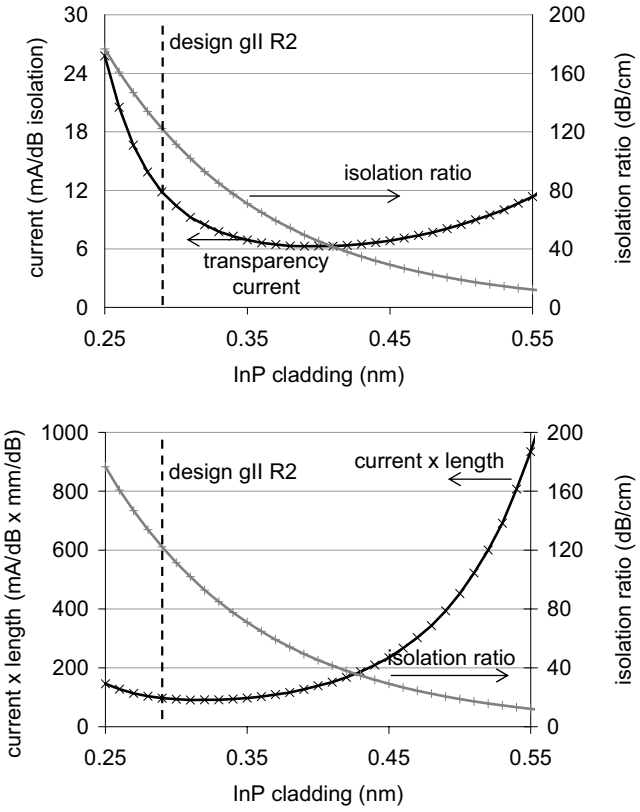

Figure 4.16: Simulation of a benchmark optical isolator structure illustrating that the optimized design according to a practical figure of merit does not necessarily correspond to a high isolation ratio; at the top the minimization of the transparency current is plotted, below the minimization of the current-length product.

generation values of table 4.9 are the result of 1D slab waveguide calculations. As pointed out earlier, the lateral variation of the ridge waveguide structure has a non-negligible influence on the isolator performance, hence a magnetooptic perturbation calculation of the actual isolator cross-section is required. As this 2D calculation is extremely slow, a global optimization is however not appropriate. Instead we have used the slab results as a starting point and have investigated with the 2D-tool how the isolator performance parameters change for a variation of the thickness of the InP superstrate layer. A realistic ridge width of 2μm is considered and an etch depth of 300nm, for which the waveguide is laterally monomodal in TM-polarization. In table 4.10 the results of this 2D optimization process are summarized for both isolator designs D4P and D3P; the optimized thickness values of the InP cladding together with the corresponding theoretical performance of a $Co_{50}Fe_{50}$ amplifying waveguide isolator are tabulated. It can be seen that the optimized operation point of the 2D calculations is at a somewhat lower cladding thickness. This follows from the fact that in the actual 2D situation the modal confinement in the metal is lower, which implies a decrease of

Layer	Material	D4P (nm)	D3P (nm)
MO metal	$Co_{50}Fe_{50}$	50	50
Contact	$In_{0.54}Ga_{0.46}As$	15	15
Contact	$In_{0.81}Ga_{0.19}As_{0.41}P_{0.59}$	170	100
Cladding	InP	335	400
SCH	$In_{0.86}Ga_{0.14}As_{0.32}P_{0.68}$	33.5	11
Barrier	InAlGaAs (λ_g = 1100nm, +0.62% strain)	20	20
Well	InAlGaAs (λ_g = 1288nm, -1.6% strain)	10 x 9	10 x 9
Barrier	InAlGaAs (λ_g = 1100nm, +0.62% strain)	20 x 9	20 x 9
SCH	$In_{0.86}Ga_{0.14}As_{0.32}P_{0.68}$	13.5	4
Cladding	InP	1000	1000
Substrate	InP		

Table 4.9: One dimensional design values of the third-generation 9QW InAlGaAs $Co_{50}Fe_{50}$ demonstrators, for two different designs labeled D4P and D3P. In the D4P-calculations 4 parameters have been varied: both SCH layers the InP cladding and the quaternary contact layer, while for the D3P design only the first three have been modified.

	D4P 1D	D4P 2D	D3P 1D	D3P 2D
t_{InP} (nm)	335	310	400	375
Transparency current (mA/dB)	6.14	8.04	6.28	8.07
Length (mm/dB)	0.21	0.23	0.2	0.22

Table 4.10: Theoretical specifications for the third generation InAlGaAs $Co_{50}Fe_{50}$ demonstrators following the 1D and 2D optimizations, together with the corresponding calculated isolator performance. The ridge width is set at 2μm.

both the non-reciprocal loss shift $\Delta\alpha$ and the reciprocal loss α_0. Keeping in mind that the transparency current depends linearly on $\Delta\alpha$ and inversely proportional to the exponential of α_0, it can be deduced that the minimum in transparency current indeed shifts to smaller cladding thickness values. Furthermore, the minimal transparency current is significantly higher when accounting for 2D effects. This can directly be attributed to the lower confinement of the optical mode in the amplifying part of the multiple quantum well core; 16% instead of 19.5% with the slab calculations. Finally, the reduction of the value of $\Delta\alpha$ causes about 10% increase of the length of the isolator in the realistic 2D situation.

With a slight modification of the Ti deposition method the inaccuracies encountered in the previous devices could be avoided, resulting in a good fabrication quality of the third-generation demonstrators. Shallowly etched ridge waveguide isolators with a width of 2.0μm are illustrated in figure 4.17. Measurements have confirmed the lateral monomodality of these devices. Closer inspection under the scanning electron microscope (SEM) however reveals an inaccuracy in the fabrication that has an important impact on the isolator performance. On the SEM images the multiple quantum well stack and the metal layer structure can clearly be distinguished. As such the total thickness of the cladding layers can accurately be measured, which gives an indication about the accuracy of the metal organic

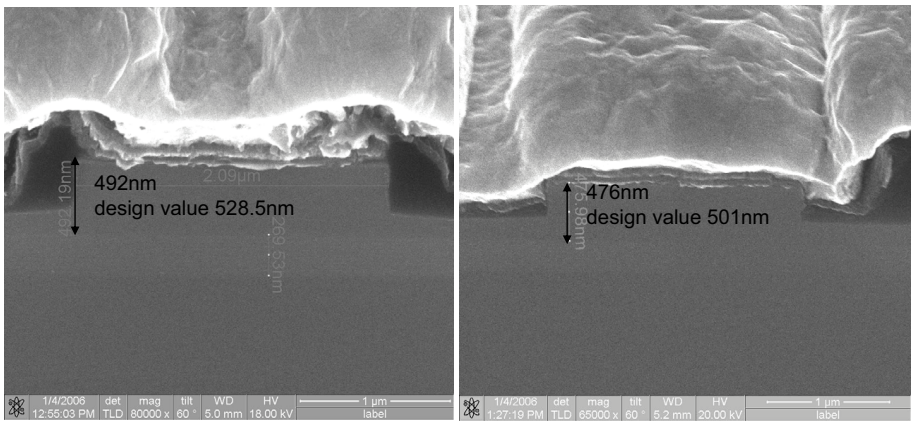

Figure 4.17: Electron microscope images of a cross-section of the third generation amplifying waveguide isolators, with indication of the measured total layer thickness between the guiding core and the metal; the left picture is design D4P and the right image is design D3P.

	D4P design	D4P actual	D3P design	D3P actual
$t_{clad\ total}$ (nm)	528.5	492	501	476
Isolation (dB)	4.35	6.5	4.58	6.0
Current (mA)	35	57	37	51

Table 4.11: Calculated performance of a third generation isolator with the optimal ('design') and the actual ('actual') dimensions of the layer structure, for a length of 1mm.

vapor phase epitaxy (MOVPE) growing process. For the D4P design, the measured thickness equals 492nm, as can be seen on the left image of figure 4.17, while the design value is 528.5nm. In the case of the D3P design the actual thickness is 476nm and the optimized value is 501nm. These deviations have a significant influence on the isolator performance; the magnetooptic metal is closer to the guiding core, hence both the non-reciprocal and the reciprocal loss are higher and consequently the figure of merit – in this case the forward transparency current – deviates to a certain extent from its minimal value. Assuming it is the InP thickness that is smaller than the theoretical optimum, the impact of this fabrication error can be modeled. In table 4.11 the optical isolation (dB) and the transparency current (mA) of a 1mm long optical isolator are tabulated, both for the design point and for the actual structure. As anticipated, both the optical isolation and the forward transparency current, the figure of merit of the isolator, increase significantly.

4.3.4.2 Characterization

The basic performance figures for the amplifying waveguide optical isolator are obviously the optical isolation and the amount of current required for transparency in the forward propagation direction. The latter is equivalent to the inser-

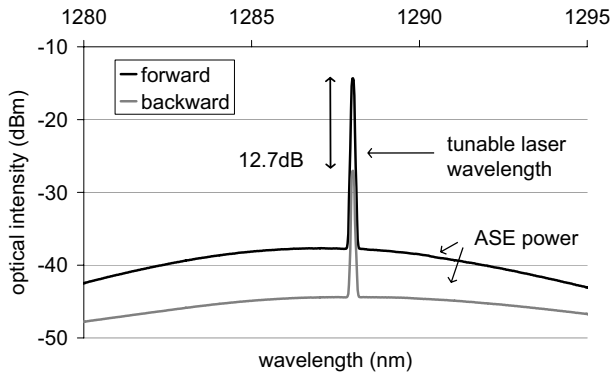

Figure 4.18: Transmission experiment on a 2.1mm long AR-coated isolator of the third generation. The spectrum of the output signal is plotted at saturation magnetization in both lateral directions, showing 12.7dB optical isolation; measured with 160mA bias current and the fiber-to-chip losses are 4 to 5 dB per facet. With the total insertion loss lower than the coupling losses this is the first demonstration of a transparent amplifying waveguide optical isolator.

tion loss of the device at a certain bias current level. Apart from these parameters it is important to study some other aspects of the component such as the spectral dependence and the influence of the bias current on the optical isolation. All of this will be done in this section.

Optical isolation and insertion loss Consider a $Co_{50}Fe_{50}$ optical isolator with a D3P layer structure. The length equals 2.1mm and the ridge width 2μm. The cleaved facets have been covered with a four-layer broadband anti-reflection coating. Figure 4.18 plots the results of a transmission experiment on this component. TM-polarized laser light from an external cavity tunable laser (output power -10dBm) is coupled in the device through a lensed fiber and the output signal is picked up with an identical lensed fiber and evaluated on a spectrum analyzer (resolution bandwidth 0.1nm). The laser wavelength is fixed at 1288nm. The injected current equals 160mA. The difference in optical intensity at the laser wavelength between forward and backward propagating signals – the optical isolation – amounts up to 12.7dB. The total insertion loss in the forward direction – the internal losses combined with the fiber-to-chip coupling losses – equals 4.6dB, while the fiber-to-chip coupling loss is measured to be 4 to 5 dB per facet. As such, this result proves on-chip amplification at the bias current of 160mA. The experiment depicted in figure 4.18 is the first – and so far only – worldwide demonstration of a transparent monolithically integratable waveguide optical isolator.
The actual transparency point was found to be at 155mA of current injection, at which an optical isolation of 13.0dB has been measured. Comparing these experimental results with the theoretical values (12.6dB and 107mA)[8] shows that the correspondence on the optical isolation is very good, but that the actual bias current level required for transparency is 49% higher than the theoretically predicted

[8] 2.1 times the values tabulated in the last column of table 4.11

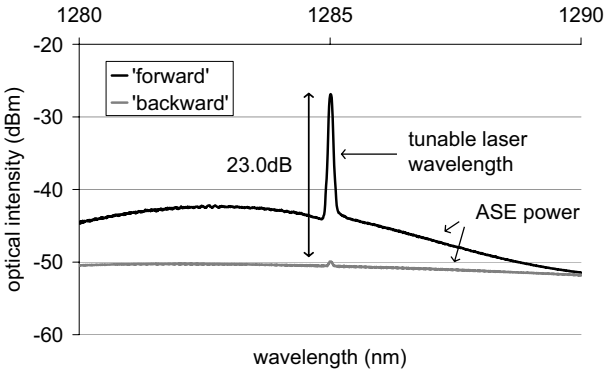

Figure 4.19: Transmission experiment on a 4.5mm long isolator of the third generation with as-cleaved facets. A record optical isolation of 23.0dB has been demonstrated at a pulsed bias current (duty cycle 10%) of 500mA.

value. This indicates that either the internal loss of the waveguide is higher than calculated or that the current injection is less efficient or a combination of both. This issue is further examined in the next paragraph.
For a practical optical isolator an isolation level of at least 20dB would be required. On the basis of table 4.11, a device with a length of 3.1mm can be expected to show this level of performance. As it was our primary goal to demonstrate an optical isolation of at least 20dB, measurements have been done on a 4.5mm long device. The facets are left uncoated and the layer structure is of design type D4P.[9] The outcome of a transmission experiment on this component is plotted in figure 4.19. The isolator is biased in pulsed regime (duty cycle 10%, pulse width 0.1μs) to avoid heating.[10] The experimental optical isolation amounts up to 23dB, which is by far the highest value ever obtained on this configuration of waveguide isolator. In comparison, Shimizu has demonstrated a TE-polarization isolator with 10.3dB of optical isolation [10]. With respect to the insertion loss, we need to remark that the waveguide facets are uncoated, hence a contribution of the Fresnel losses equal to 3dB has to be added to the fiber-chip coupling losses (4 to 5 dB per facet) to obtain the total coupling loss. With a forward intensity of -27dBm and a laser input power of -10dBm, the on-chip loss at 500mA current injection can therefore be estimated at 5dB. Clearly, the D4P devices operate worse than what can be expected from the calculations, although it is not clear why. Because of the good performance of the D3P isolators (figure 4.18) it was however decided not to spend more time on this discrepancy. The result plotted in figure 4.19 should therefore only be considered as the demonstration of a very high optical isolation of 23dB.

Transparency current While the experimental level of optical isolation corresponds well to the calculated value, the measured forward transparency current

[9] We experienced that the D3P design components perform significantly better than the D4P devices, but due to a lack of material the latter had to be used for the 4.5mm long isolators.

[10] The current is injected through a single probe needle with consequently a very high current density at the injection point.

is significantly higher. In this section we will investigate the origin of this discrepancy. First of all the inspection of the cross-section of the ridge waveguides shows that there are no major inaccuracies in the fabrication, hence the increased transparency current doesn't originate from fabrication errors.

A significant underestimate of the actual transparency current comes from the fact that in the design calculations it has been assumed that every injected carrier contributes to the signal amplification, while an amount of carriers actually recombines spontaneously or non-radiatively (Schockley-Read-Hall and Auger recombination). In the next paragraph we will develop a rate equations model of the SOA-based isolator that includes spontaneous and non-radiative recombination.

A second contribution comes from a deviation of the current injection efficiency in the device. For the design of the isolator layer structures a gain-current relationship has been used that was obtained from measurements on 6 quantum well broad area lasers. The waveguide isolators differ however from these test lasers in two ways. First of all the number of quantum wells is higher – 9 instead of 6. Remember that we have modified the extracted gain-current relationship for this under the assumption that the injection and internal quantum efficiency are independent of the number of wells. If this assumption is however not entirely correct the actual efficiency factor η_{inj} is lower than anticipated. Secondly, the isolator devices are shallowly etched 2μm wide ridge waveguides instead of broad area components. It is well known that shallowly etched ridge waveguide active devices suffer from leakage current phenomena due to the lateral carrier diffusion. As a direct result the actual injection efficiency is significantly lower than assumed in the design of the layer structure.

In addition there might be an increase of the internal loss of the isolator. This can be the result of imperfections of the fabricated device – for example deviations of the cladding layers thicknesses – or due to uncertainties on material parameters, especially the optical constant of the ferromagnetic metal. One particular contribution to the loss that we have looked into is that of the intervalence band absorption (IVBA) in the highly p-doped contact layers,[11] which can be approximated as a linear function of the dopant concentration p_i [11]:

$$\alpha_{IVBA,i} = k_p p_i, \tag{4.6}$$

with i = InGaAs or InGaAsP and k_p the IVBA coefficient, which is material and wavelength dependent. In p-doped InP and related materials this IVBA coefficient equals $k_p = 13{\times}10^{-18} cm^2$ [12]. The refractive indices of the contact layers have been corrected for IVBA and the waveguide isolator performance has been recalculated. However, the impact of these extra loss terms on the overall internal loss appears to be negligible compared to the very high absorption in the ferromagnetic metal.

A last issue that we want to address here is that of longitudinally inhomogeneous current injection. In all calculations regarding the required bias current for forward transparency it has assumed that the current injection in the SOA is longitudinally homogeneous. In other words, current injected through a needle is

[11] These material dependent loss terms are not included in the experimental gain-current relationship 3.18. After all, this equation has been derived from measurements on lasers, on which the modal overlap with the contact layers is negligible.

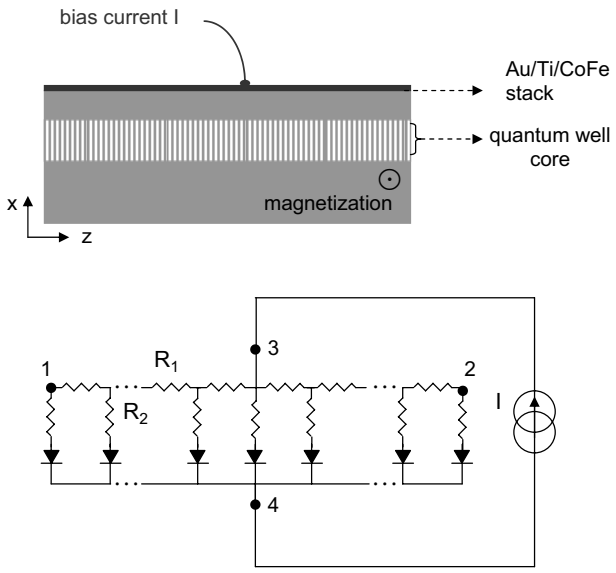

Figure 4.20: Schematic longitudinal view of the amplifying waveguide isolator and its equivalent electrical network. The resistance values R_1 and R_2 are related to R_{Au} and R_{SOA}. The distributed diode symbols the pn-heterojunction.

presumed to distribute homogeneously along the (electro-plated) gold strip before crossing the barrier between the metal and the semiconductor. For this scenario to be the case the electrical resistance of the gold stripe should be low compared to the resistance of the metal-semiconductor contact of the SOA. In the opposite case of longitudinally inhomogeneous current injection, the overall gain in the waveguide at a certain bias current level can seriously be decreased. This originates from the sublinear (logarithmic) relation between material gain and bias current; gain saturation at positions with high injection current densities results in a lower value of the total gain. This phenomenon can be modeled with the equivalent electrical network of the amplifying waveguide isolator illustrated in figure 4.20. The resistances R_1 and R_2 are related to two resistance values that can experimentally be determined, i.e the resistance of the gold strip R_{Au}, measured between node 1 and 2 on figure 4.20, and the total resistance of the isolator R_{SOA}, measured between node 3 and 4. The electrical network can be solved with the aid of the current and voltage laws of Kirchoff. Fitting to the experimental values of R_{Au} and R_{SOA} results in the correct values of R_1 and R_2. The outcome is a longitudinal profile of the current injected in the quantum well region. With the help of the experimental gain-current relation, this directly leads to the longitudinal modal gain profile along the device. Figure 4.21 shows two examples. The longitudinal current flowing through the distributed diode and the resulting gain profile corresponding to resistance values equal to R_{Au} = 0.3Ω and R_{SOA} = 3.0Ω (top) and R_{Au} = 30.0Ω and R_{SOA} = 3.0Ω (bottom) have been plotted. The total bias current is 150mA and the length is 2mm, both of which are realistic values for the amplifying waveguide optical isolator of the third generation. The gain-current density

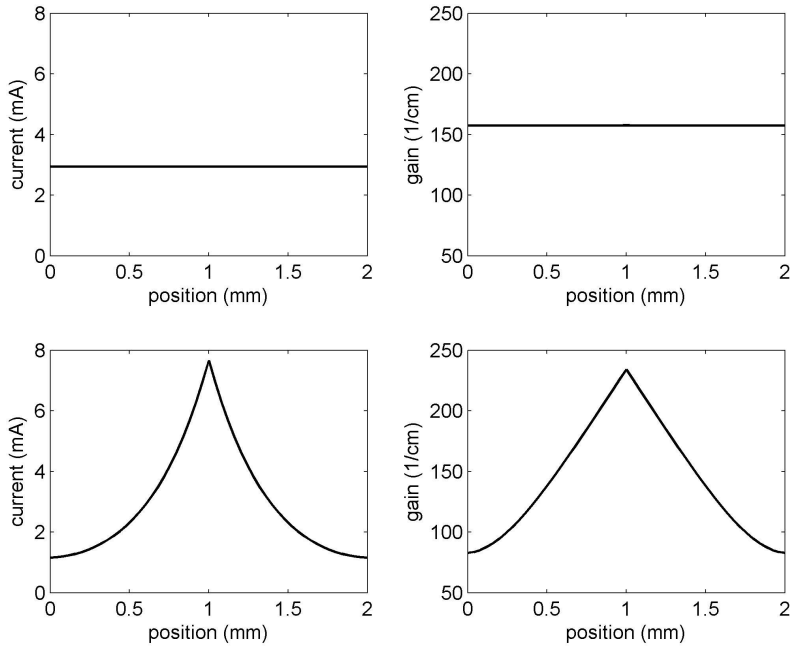

Figure 4.21: Two examples of the longitudinal current and gain profile for R_{Au} *= 0.3Ω and* R_{SOA} *= 3.0Ω (top) and* R_{Au} *= 30.0Ω and* R_{SOA} *= 3.0Ω (bottom).*

relation of the quantum well region is the one described by equation 3.18 and the modal confinement in the quantum wells equals 0.16. In the first case the current is indeed quasi-homogeneously distributed, while this is not at all the case when the resistance of the gold stripe exceeds that of the current injection in the diode. Integrating the gain over the entire device length shows the impact of inhomogeneous current injection on the total gain. In figure 4.22 the evolution of the total gain with increasing injected current is plotted in both the homogeneous (R_{Au} = 0.3Ω, R_{SOA} = 3.0Ω) and the inhomogeneous case (R_{Au} = 30.0Ω, R_{SOA} = 3.0Ω) for an internal loss of 117cm^{-1}. The required current to overcome this internal loss increases with 18mA, almost 20%, as a consequence of inhomogeneous current injection.

To assess whether this effect is significant in the fabricated devices, we have measured the actual values of R_{SOA} and R_{Au}. While R_{SOA} is consistently in the order of 3Ω, the observed value of R_{Au} is not at all a linear function of the distance between the two measurement points on the gold contact, but instead is randomly distributed between 3 and 15Ω. As such, the degree of inhomogeneity cannot readily be estimated. However, the following experiment shows that this effect is not at all negligible. In figure 4.23 the output power of a 2mm-long AR-coated third-generation isolator device is plotted as a function of the position of the current injection probe needle on the top gold contact. For position 0 the needle is the nearest to the output facet at which the intensity is detected, for position L the furthest. The injection current is fixed at 160mA. The detected ASE-power varies largely with the needle position, which gives clear evidence of the presence of

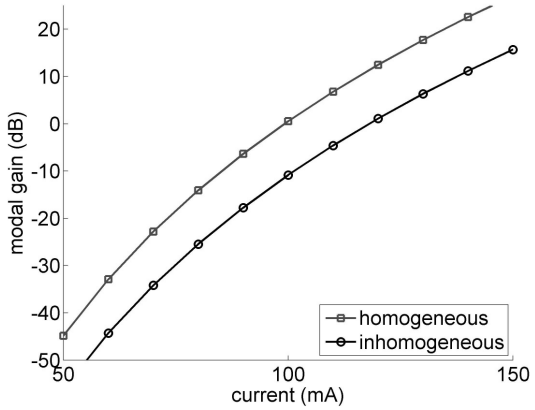

Figure 4.22: Evolution of the total gain with injected current; illustration of the decrease of the modal gain due to inhomogeneous current injection. The homogeneous case corresponds to R_{Au} *= 0.3Ω and* R_{SOA} *= 3.0Ω, the inhomogeneous graph to* R_{Au} *= 30.0Ω and* R_{SOA} *= 3.0Ω.*

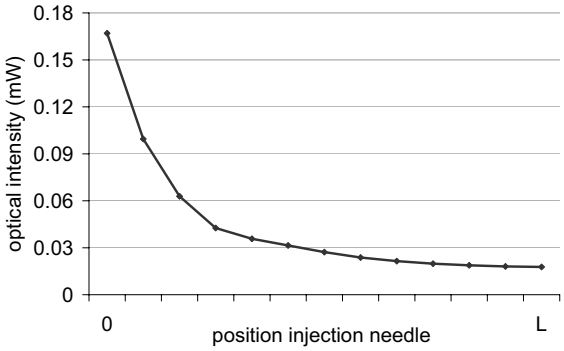

Figure 4.23: Evolution of the emitted optical power of an AR-coated isolator waveguide with position of the current injection needle.

longitudinal inhomogeneity of the current injection. This, together with the large variation in the observed R_{Au} value suggests that the top gold contact is not at all a smooth low resistivity film, but instead consists of a series of gold islands linked through high resistance paths. To estimate the impact of the inhomogeneous current distribution on this structure, an effective resistance should be determined. To this purpose the experiment depicted in figure 4.23 has been repeated for a number of current values. Furthermore a simple ASE model has been assumed that relates the optical intensity to the gain:

$$P = \int_0^L exp(Gx)dx, \tag{4.7}$$

where G is the modal gain:

$$G = \Gamma g\left(J, \frac{R_2}{R_1}, x_{needle}\right) - \alpha, \tag{4.8}$$

with the material gain g depending on the current density J, the position of the probe needle x_{needle} and $\frac{R_2}{R_1}$ the ratio of the resistances R_2 and R_1 of the equivalent electrical network (figure 4.20).[12] Fitting this model to the experimental data with $\frac{R_2}{R_1}$ as the variable parameter results in an effective resistance value R_{Au} for the top contact, provided R_{SOA} is known (= 3Ω). The extracted effective resistance R_{Au} equals 12Ω. The corresponding effect of the inhomogeneous current injection on the transparency current is a minimal increase of 2mA if the 2mm device is electrically pumped at the center of the waveguide. If on the other hand the current is injected at one of the facets (position *0* or *L*), the required value rises by no less than 65mA.
At least as important is the non-uniformity of the longitudinal gain profile introduced by the injection inhomogeneities, especially in a transmission experiment, as it modifies importantly the signal amplification and the emitted ASE. In the next paragraph a mathematical model of the isolator will be developed. To account for the effect of injection inhomogeneities, the calculation of the longitudinal current profile has been implemented in this model. The position of the injection needle is considered as a variable parameter and the experimental resistance values R_{Au} = 12Ω and R_{SOA} = 3Ω are used.

The problem of inhomogeneous current injection can obviously be reduced by contacting the device through a multiple of wire bonds. Another possible solution might be to anneal the gold contact to smoothen the film. This however should be done with care, as annealing at elevated temperatures can deteriorate the ohmic contact quality.

Injection current dependence The optical isolation of a light wave transmitted through an isolator device is expressed as:

$$Iso[dB] = P_{fw}[dB] - P_{bw}[dB] = 10log^{10}\left(\frac{P_{fw}[mW]}{P_{bw}[mW]}\right). \tag{4.9}$$

Under the assumption of the absence of gain saturation and amplified spontaneous emission and of a uniform gain profile this can be rewritten as:

$$Iso[dB] = 10log^{10}\left(\frac{P_{in}exp(G_{fw}L)}{P_{in}exp(G_{bw}L)}\right), \tag{4.10}$$

with P_{in} the intensity of the input signal, L the length and G_{fw} and G_{bw} the modal gain in the forward and backward propagation direction respectively:

$$G_{fw} = \Gamma G_{mat} - \alpha_0 + \frac{\Delta\alpha}{2} \qquad G_{bw} = \Gamma G_{mat} - \alpha_0 - \frac{\Delta\alpha}{2}, \tag{4.11}$$

[12] It can indeed be proven that it is $\frac{R_2}{R_1}$ that determines the level of inhomogeneity.

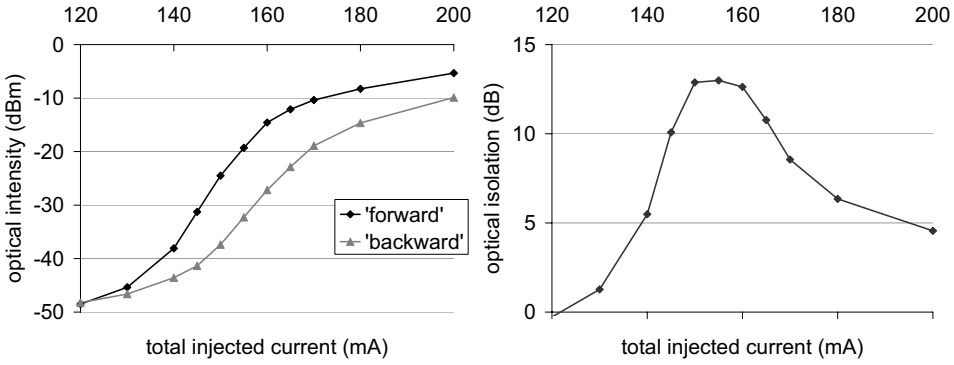

Figure 4.24: Experimental study of the variation of the optical isolation with total injected current. (left) Optical intensity of forward (+M$_{sat}$) and backward (-M$_{sat}$) propagating light and (right) the corresponding optical isolation as a function of the total injection current in the isolator component. The optical isolator is a 2.1mm long third-generation device with specifications as tabulated in table 4.9.

with G_{mat} the material gain in the quantum wells, Γ the modal confinement in the multiple quantum well region, α_0 the modal loss in the absence of a magnetic field and $\Delta\alpha$ the non-reciprocal loss shift. The optical isolation of the transmitted signal hence becomes:

$$Iso[dB] = 10log^{10}\big(exp(\Delta\alpha L)\big). \tag{4.12}$$

According to this expression the optical isolation is independent of the amount of current injected in the device. The reality however is a lot more complex, as is illustrated by the experimental result shown in figure 4.24. The measurements have been performed on D3P devices (see table 4.11) with a length of 2.1mm and with the cleaved facets covered with a four-layer broadband anti-reflection coating. On the left graph the evolution of the optical intensity of a transmitted signal traveling in forward (+M_{sat}) and backward (-M_{sat}) direction with the total injected current is plotted. TM-polarized input light (-10dBm power) from an external cavity tunable laser has been used and the output signal has been evaluated on a spectrum analyzer (resolution bandwidth 0.1nm). The measurement points in figure 4.24 correspond to the power measured at the lasing wavelength of 1288nm. The right plot of figure 4.24 depicts the corresponding optical isolation *Iso* as a function of the injected current. This value clearly remains not at all constant, indicating that gain saturation and the presence of spontaneous emission do have a non-negligible influence on the isolator performance.

To understand the experimentally observed evolution of the optical isolation with the injected current the amplifying waveguide isolator has been modeled with a one-dimensional longitudinal multi-section single mode Finite Difference Time Domain (FDTD) SOA model based on traveling wave field equations and longitudinal carrier density equations [14]. This model assumes perfect anti-reflection

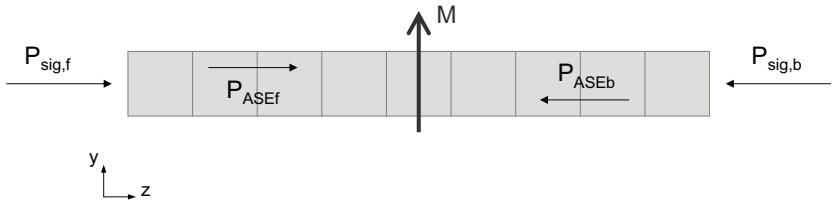

Figure 4.25: Schematic layout of the multi-section SOA-isolator with indication of the optical powers as used in the FDTD SOA-model and of the (fixed) magnetization M.

coatings at the waveguide facets such that feedback can be neglected. The following set of equations has been used:

$$\begin{aligned}
\frac{\partial N(z,t)}{\partial t} &= \frac{I(t)\eta_{inj}}{qwdL} - AN(z,t) - BN^2(z,t) - CN^3(z,t) \\
&\quad - \frac{G(z,t)}{h\nu_{sig}wd}[P_{sig,i}(z,t) + P_{ASEf}(z,t) + P_{ASEb}(z,t)] \qquad (4.13)\\
\frac{dP_{sig,i}(z,t)}{dz} &= (G(z,t) - \alpha_{int,i})P_{sig,i}(z,t) \qquad i = f,b \qquad (4.14)\\
\frac{dP_{ASEf}(z,t)}{dz} &= (G(z,t) - \alpha_{int,f})P_{ASEf}(z,t) \\
&\quad + \frac{1}{2}h\nu_{sig}\beta_{sp}BN^2(z,t)wd \qquad (4.15)\\
-\frac{dP_{ASEb}(z,t)}{dz} &= (G(z,t) - \alpha_{int,b})P_{ASEb}(z,t) \\
&\quad + \frac{1}{2}h\nu_{sig}\beta_{sp}BN^2(z,t)wd, \qquad (4.16)
\end{aligned}$$

with

$$G(z,t) = \frac{\Gamma g_0 ln\left(\frac{N(z,t)}{N_0}\right)}{1 + \frac{P_{tot}(z,t)}{P_{sat}}}. \qquad (4.17)$$

N is the carrier density, *I* the total injected current, η_{inj} the current injection efficiency, $P_{sig,i}$, P_{ASEf} and P_{ASEb} the optical power of respectively the signal and the forward and backward traveling amplified spontaneous emission (ASE) and *G* the modal gain. $P_{tot}(z,t)$ equals the total optical power at the longitudinal position *z* at the moment *t*. Figure 4.25 shows the convention made here for these optical powers, with an indication of the (fixed) direction of the magnetization *M*. $\alpha_{int,i}$ is the internal loss in the forward (i=f) or the backward (i=b) direction:

$$\alpha_{int,f} = \alpha_0 - \frac{\Delta\alpha}{2} \qquad \alpha_{int,b} = \alpha_0 + \frac{\Delta\alpha}{2}. \qquad (4.18)$$

The description of the other symbols is given in table 4.3.4.2. The recombination constants *A*, *B* and *C* are material properties and are not exactly known for the

Symbol	Description	Value
A	Schockley-Read-Hall recombination constant	10^8 s^{-1}
B	Radiative recombination constant	10^{-10} cm^3s^{-1}
C	Auger recombination constant	10^{-29} cm^6s^{-1}
β_{sp}	Spontaneous emission coupling coefficient	fitted
P_{sat}	Saturation power	fitted
g_0	Differential gain coefficient	fitted
α_0	Internal loss	fitted
$\Delta\alpha$	Non-reciprocal loss shift	fitted
Γ	Confinement factor	0.16
N_0	Transparency carrier density	1.4×10^{18} cm^{-3}
η_{inj}	Current injection efficiency	fitted
w	Active layer width	2 μm
d	Active layer thickness	9×10 nm
L	Device length	2100 μm
ν_{sig}	Signal frequency	232.7 $\times$ THz
q	Electric charge per electron	1.60218×10^{-19} C
h	Planck's constant	6.62607×10^{-34} Js

Table 4.12: Physical parameters of the SOA-based isolator and their values used in the isolator model.

waveguide isolator. Values from literature have been taken as best guesses [15]. By numerically solving equations 4.13 through 4.17 the response of the SOA-isolator to an input signal – propagating through the device in either the forward or the backward direction – can be obtained. To account for the longitudinal variation of the carrier density the SOA is segmented into a number of small sections, with a length of 10μm. The carrier density in each section is considered to be constant. This multi-section model enables to take into account the effects of longitudinal spatial hole burning (LSHB) and of inhomogeneous current injection. Even though semiconductor optical amplifiers do not have a strong lasing mode, LSHB can still be induced by intense ASE that propagates in the active layers as well as by the injection of an optical signal [16]. To account for the presence of injection inhomogeneities the mathematical model developed earlier in this section has been implemented in the isolator rate equations. Consequently, the injection current density *J* depends on the longitudinal position, i.e. *J = J(z)*.
The parameters of the logarithmic gain-carrier relationship (equation 4.17), N_0 and g_0 have been deduced from the experimental gain current density relation obtained on 6QWs broad area lasers:

$$G_{mat} = G_0 \, ln\left(\frac{J}{J_0}\right) = 466 \, ln\left(\frac{J_{tot}}{0.528}\right). \tag{4.19}$$

If we assume perfect injection efficiency of the broad area lasers, the current density and the carrier density are related as:

$$\begin{aligned} J &= (AN + BN^2 + CN^3)qd \\ J_0 &= (AN_0 + BN_0^2 + CN_0^3)qd, \end{aligned} \tag{4.20}$$

which transforms equation 4.19 into a gain-carrier density relation. Fitting to the logarithmic expression:

$$g = g_0 \; ln\left(\frac{N}{N_0}\right), \tag{4.21}$$

directly results in a value for the differential gain coefficient g_0. This value is obviously highly dependent on the *A*, *B* and *C* coefficients, which are not exactly known. Therefore, the obtained value is considered as a starting point and a correction factor has been added to the model, the value of which follows from fitting to the experimental data. The effects of gain saturation are included in the gain calculation via the saturation power P_{sat}, which equals the total optical power at which the gain is reduced to half the value in the absence of light.

To simulate the injection current dependence of the amplifying waveguide optical isolator the steady state regime of the SOA model is applicable, in which the carrier density equation 4.13 reduces to:

$$\begin{aligned} 0 &= \frac{I\eta_{inj}}{qwdL} - AN(z) - BN^2(z) - CN^3(z) \\ &\quad -\frac{G(z)}{h\nu_{sig}wd}[P_{sig,i}(z) + P_{ASEf}(z) + P_{ASEb}(z)]. \end{aligned} \tag{4.22}$$

The total optical output power – the sum of $P_{sig,i}$, P_{ASEf} and P_{ASEb} at the output facet – is calculated for a range of current injection values, both for a signal injected in the forward $P_{sig,f}$ and in the backward $P_{sig,b}$ direction[13]. With an appropriate choice of the model parameters the experimental graphs of figure 4.24 should be reproduced. The Nelder-Mead simplex algorithm [17] has been applied to solve this multi-dimensional non-linear problem. The cost function that has been minimized is the sum of the square of the deviations between the experimental points – plotted in figure 4.24 (left) – and their corresponding theoretical values. The quantities that have been fitted are the spontaneous emission coupling coefficient β_{sp}, the saturation power P_{sat}, the injection efficiency η_{inj}, the correction factor to the differential gain and the position of the current injection needle, just as the internal loss α_0 in the absence of a magnetic field and the non-reciprocal loss shift $\Delta\alpha$. Their optimized values are given in table 4.3.4.2. Remark that the differential gain g_0 is of the same order as the values reported in literature [18]. Furthermore, the internal loss α_0 and the non-reciprocal loss shift $\Delta\alpha$ are close to the design characteristics, and only the current injection efficiency η_{inj} appears to be much smaller than anticipated. The calculated emitted power as a function of the injected current corresponding to these isolator parameters is plotted in the left image of figure 4.26 both for forward and backward modal propagation. The

[13] At the right facet in the forward and the left facet in the backward case as indicated in figure 4.25

Symbol	Value
β_{sp}	1.6×10^{-5}
P_{sat}	-2 dBm
g_0	2050 cm^{-1}
α_0	132 cm^{-1}
$\Delta\alpha$	15 cm^{-1}
η_{inj}	0.274
x_{needle}	0.57L

Table 4.13: Fitted values of the SOA-based isolator parameters.

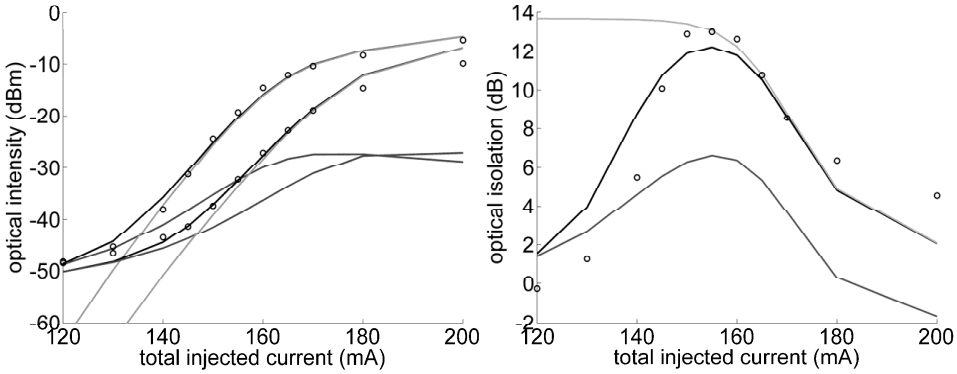

Figure 4.26: Theoretical evolution of the emitted power (left) and the corresponding optical isolation (right) with injection current. The light grey curve corresponds to the transmitted signal, the dark grey graph to the forward ASE and the sum of both is plotted in black. The black circles are the experimental data points.

light grey curve is the signal intensity, in dark grey the ASE power at the signal wavelength is plotted and the black graph is the sum of both. The black circles are the experimental data points. Clearly, there is a good correspondence between the theoretical model and the experimental data. The difference between forward and backward intensities – the optical isolation – is depicted in the right part of figure 4.26, with the same color code.
The optical isolation on the transmitted signal remains constant for low current values and gradually decreases at high injection. This phenomenon can be attributed to gain saturation; at a certain current value the optical power of the guided mode is higher in the forward propagation direction, causing a higher degree of gain saturation than for backward propagation. Equation 4.12 becomes:

$$Iso[dB] = 10log^{10}\big(exp((\Delta\alpha + \Gamma(G_{mat,f} - G_{mat,b}))L)\big), \tag{4.23}$$

with $G_{mat,f}$ and $G_{mat,b}$ the material gain in forward and backward direction and where $G_{mat,f} < G_{mat,b}$. As such, the isolation decreases. The non-reciprocal effect on the ASE-power is low at low pump current and increases with the electrical injection. This evolution originates from the fact that with higher current the

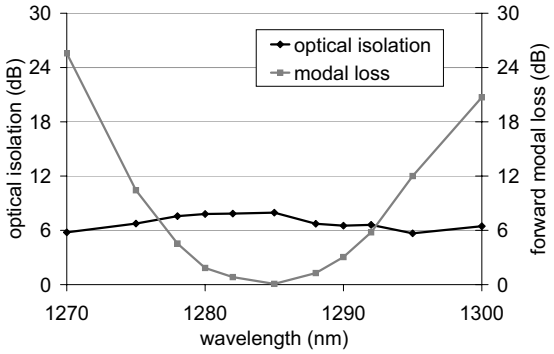

Figure 4.27: Spectral dependence of the optical isolation and forward modal loss of the waveguide isolator; measured with 200mA bias current.

ASE-power contains light from further down the waveguide which has traveled a longer distance, hence has experienced a stronger non-reciprocal effect. At high pump values also the ASE gets saturated. Combining both signals results in the black curve of figure 4.26, which clearly reproduces the observed trend.
In conclusion, the observed optical isolation of an amplifying waveguide optical isolator is largely dependent on the current injection. In the low pump region the presence of spontaneous emission reduces the isolation, while at high current values gain saturation has a annihilating influence. Around the forward transparency point – here at 155mA – both effects are small and the optical isolation goes through a maximum.

Spectral behavior One of the advantages of the amplifying waveguide isolator concept over the interferometer based isolator schemes is the fact that this approach is in principal spectrally broadband due to the absence of interfering signals. In order to examine the wavelength dependence, we have repeated the above described transmission experiment for different values of the tunable laser wavelength. Measurements have been done on 2.3mm D4P isolators with anti-reflection coated facets. The bias current is kept constant at a value of 200mA to ensure optical transparency at the central wavelength of 1285nm. As is illustrated in figure 4.27 the optical isolation varies by less than 2.5dB over a wavelength range of 30nm, while the forward modal loss varies by more than 25dB, making this the dominant influence on the spectral behavior. The wavelength dependence of the loss is obviously mainly related to the gain spectrum of the quantum well material. The intrinsic material dispersion of the ferromagnetic metal is believed to be the main cause of the variation of the optical isolation. Simulations shows that there is a small additional contribution due to the spectral variation of the modal electric field.
In conclusion, the wavelength dependence of the amplifying waveguide optical isolator is predominantly determined by the gain spectrum of the multiple quantum well material, which causes an increase of the modal loss away from the gain peak wavelength (at a certain current injection level).

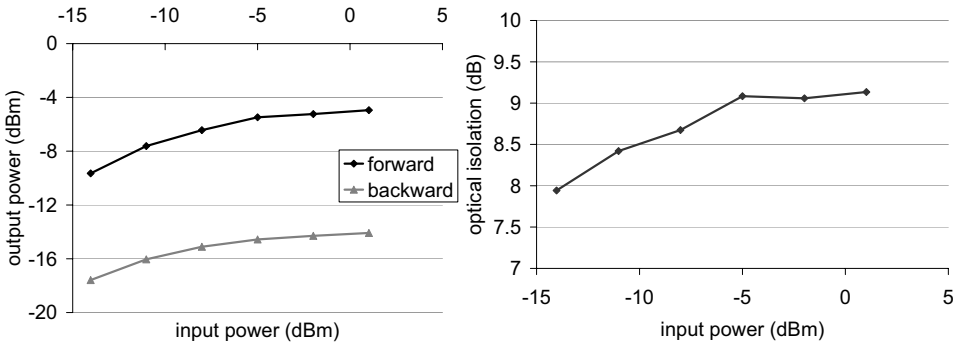

Figure 4.28: (left) Relation between the power of the injected signal and the emitted signal, both corrected for fiber-chip coupling losses; the bias current is set at 160mA. (right) The resulting evolution of the optical isolation with input power.

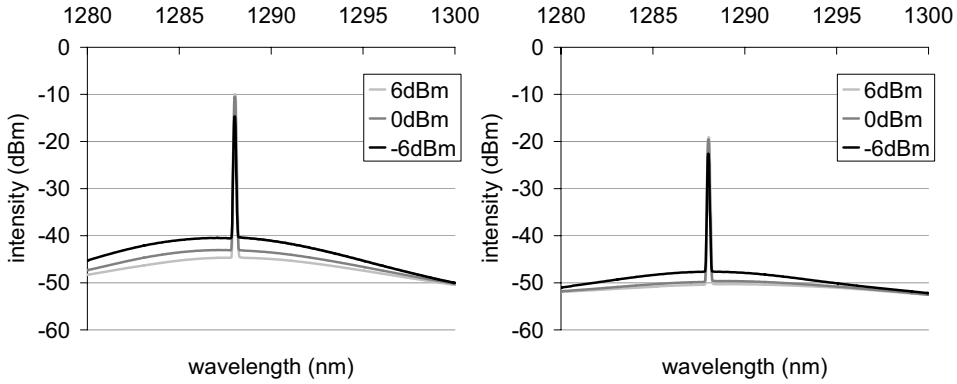

Figure 4.29: Spectra of the emitted light of a third generation waveguide isolator for three different intensities of the laser signal, for (left) forward propagation and (right) backward propagation. The injected current is fixed at 160mA.

Input power saturation If the power inside an amplifying device is high the amplifier saturates. This can be attributed to the fact that in the case of high optical power the stimulated recombination rate is high, causing the excited state concentration to decrease. Therefore, the gain G drops and the output power saturates. This relation can be expressed as:

$$G = \frac{G_{P=0}}{1 + \frac{P}{P_{sat}}} \tag{4.24}$$

and is characterized by the saturation power P_{sat}, defined as the power at which the gain reduces to half the value in the absence of light. Gain saturation occurs at high values of the injection current because the optical power increases largely with propagation through the device. Likewise, gain saturates at elevated power

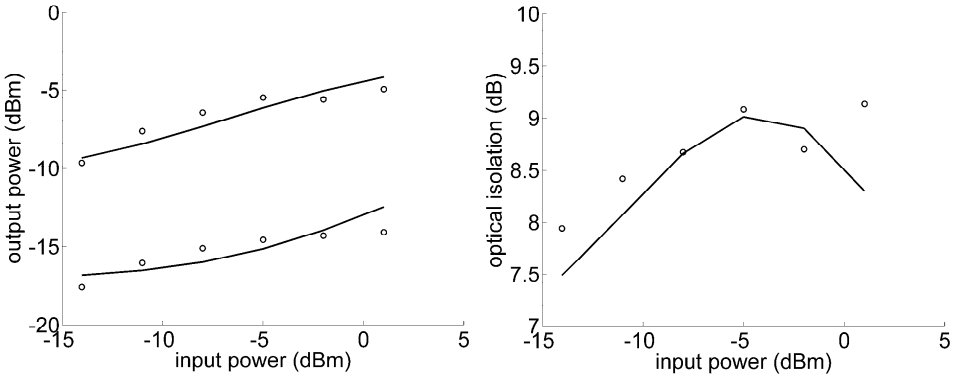

Figure 4.30: Calculated evolution of the emitted optical power with input signal intensity and the corresponding optical isolation. The circles represent the experimental data points.

of the input signal. In this paragraph we investigate the impact of input power saturation on the operation of the amplifying waveguide optical isolator. Remember from a previous paragraph that gain saturation causes the degradation of the optical isolation at high current injection levels.
The input power saturation of the isolator has been studied experimentally by performing a non-reciprocal transmission experiment for a series of signal powers. The test device is 2.1mm long with a D3P design[14] and with anti-reflection coatings deposited on the waveguide facets. The current injection is kept fixed at 160mA which is the transparency current for a tunable laser power of -10dBm. The experimental results are illustrated in figure 4.28. The left plot shows the relation between the power of the injected signal and the intensity of the light emitted at the signal wavelength. All values have been corrected for fiber-to-chip coupling losses, equal to 5dB per facet. Gain saturation clearly has an influence, causing the output power to saturate. The most important question is whether the input power saturation also modifies the optical isolation – the difference between the signal intensity in forward and backward direction. The observed trend is plotted in the right part of figure 4.28. The level of optical isolation appears to rise with increasing input power. This evolution is counter-intuitive, because in the forward direction the power is higher, hence, according to equation 4.24, gain saturation is expected to have a larger influence. However, inspection of the emitted spectra at different input powers clarifies the mechanism behind this rising trend. In figure 4.29 the observed emission spectra for forward (left) and backward (right) propagating light and for three different input powers are given. The important thing to notice is that the ASE power decreases severely with increasing input power. As elaborated earlier, the presence of spontaneous emission reduces the optical isolation, hence as the input power increases so does the observed optical isolation.

[14]This device is nominally identical to the one used in the previous experiments but is not exactly that one.

Obviously this trend should be reproducible with the rate equations model of the waveguide isolator. The model has been evaluated for different signal powers and with a fixed injection current of 160mA. Identical values for the SOA parameters have been used (see tables 4.3.4.2 and 4.3.4.2), except for the position of the probe needle which has been considered as a variable parameter. Accurate fitting to the experimental data points has been obtained, as is illustrated in figure 4.30. The only modification with respect to earlier calculations is that the current is injected closer to the output facet, $x_{needle} = 0.29L$ instead of $x_{needle} = 0.57L$.

Reliability study In order to make an estimate of the robustness of the fabricated amplifying waveguide optical isolators two reliability related issues have been examined experimentally. First of all, it is imperative that the performance of the isolator doesn't degrade as a result of the temperature elevation during the laser diode module packaging. The corresponding temperature step is assessed at 300°C during 5 minutes. The performance of an 'as-fabricated' and a – nominally identical – 'packaged' device have been compared using the non-reciprocal lasing characterization technique.[15] The corresponding LI-graphs and power ratio curves are plotted in figure 4.31, showing that there is only a minor difference between both cases. In fact the optical isolation seems to improve slightly. It is not clear whether the measured difference originates from fabrication variations or whether there is an actual improvement. Anyhow, the bottomline is that the influence of the exposure to packaging conditions is minimal.

Another point that has been examined is the influence of the operation temperature on the isolator performance. All experimental results described so far have been performed with the environment temperature kept constant at 20°C by means of a thermo-electric cooler on the sample holder. In a practical situation, cooling the device means an extra cost, hence is highly unwanted. In order to estimate the performance of such an uncooled isolator, non-reciprocal lasing measurements have been done with the environment temperature fixed at 80°C. A comparison between 20°C and 80°C is given in figure 4.32. The LI-graphs on the left clearly show that the temperature influences the gain performance of the quantum well region; the threshold current I_{th} increases from 40mA to 142mA, and the external quantum efficiency η_d decreases to some extent. This is the normal behavior of gain material, for which the temperature evolution of the threshold current and the external quantum efficiency are described by the phenomenological relations:

$$I_{th} = I_{th,0} exp\left(\frac{T}{T_0}\right) \qquad \eta_d = \eta_{d,0} exp\left(\frac{-T}{T_1}\right) \tag{4.25}$$

with T_0 and T_1 the corresponding characteristic temperatures. The right part of figure 4.32 compares the optical power ratio between forward and backward propagating light at both environment temperatures. The value in the above threshold regime is identical, which is a clear proof that the optical isolation doesn't change with the operation temperature, at least up to 80°C. In conclusion, the temperature dependence of the amplifying waveguide optical isolator is solely determined by

[15] Ideally the performance of the same device before and after exposure to the packaging conditions should be compared. The permanent mounting on the characterization setup prohibits this, so nominally identical devices have been used.

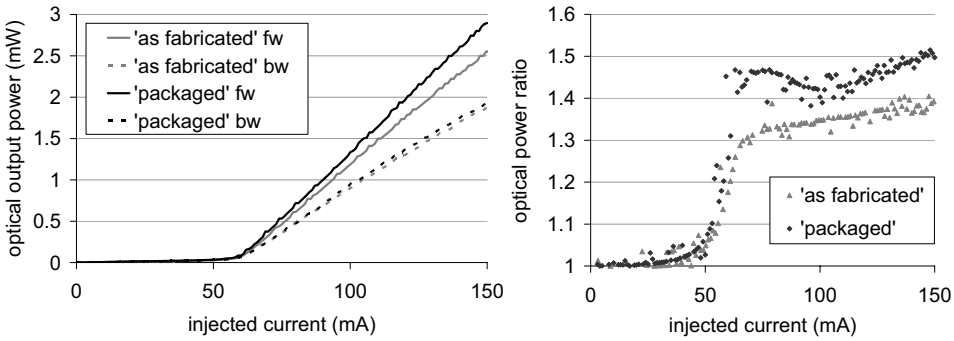

Figure 4.31: Non-reciprocal lasing experiment on optical isolators exposed to packaging conditions, showing that the influence on the isolator performance is minimal.

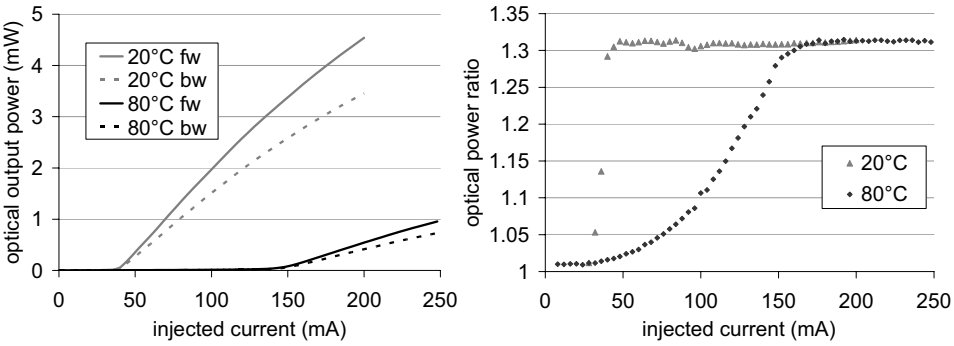

Figure 4.32: Non-reciprocal lasing experiment on optical isolators at operation temperature of 20°C and 80°C.

the temperature dependence of the gain material, meaning that only the insertion loss is influenced but not the optical isolation.

Dynamic measurements Another important aspect of the amplifying waveguide optical isolator is its response to a dynamic input signal. After all, as indicated in the introductory chapter, active devices need to be protected against optical feedback at data rates of 2.5Gbit/s and more. The isolator itself is operated statically, i.e. its injection current remains constant over time. In this paragraph we make a qualitative study of the transmission of a modulated signal.
For these experiments the non-reciprocal measurement setup has been extended with a 10Gbit/s optical modulator generating non-return-to-zero (NRZ) signals, an optical receiver and a digital sampling oscilloscope to visualize the results. Qualitative investigation of the response of the component to a dynamic signal can be done by the inspection of the eye-diagram measured at the isolator output and comparing it to the one generated by the input signal. The device under test is a 2.3mm-long AR-coated D4P waveguide with a transparency injection current

of 210mA and an optical isolation of 9.35dB. Due to the high fiber-to-chip losses on the setup[16] – 17dB in total for the two waveguide facets – the actual output power of the isolator is close to the lower limit of the optical receiver. Therefore, to approach the same receiver sensitivity for the reference measurement the input signal has been attenuated by 17dB before being coupled to the receiver. The experimental results are shown in figure 4.33 with on left the input signal and on the right the eye diagram for the same signal after being transmitted through the optical isolator. We clearly observe an open eye pattern, which shows that the developed waveguide isolator is compatible with modulation speeds at least up to 10Gbit/s.
The addition of noise to the signal originates from the amplified spontaneous emission intrinsic to a semiconductor optical amplifier based component.

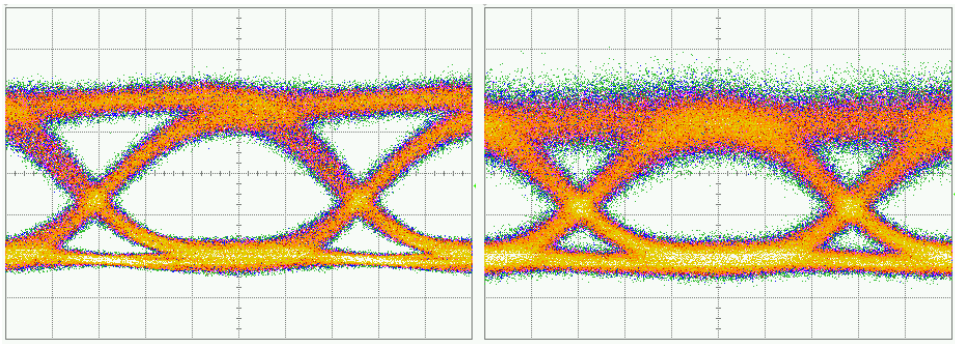

Figure 4.33: Measured eye diagrams of a 10Gbits/s NRZ signal before (left) and after (right) transmission through a 2.3mm-long isolator which is electrically pumped to forward transparency (210mA).

4.3.4.3 Variation of the ferromagnetic metal: CoFe:B

Even if the theoretical performance of $Co_{50}Fe_{50}$ isolators could be achieved, its transparency current is at least a factor 3 too high to be suitable for practical applications. The most obvious way to enhance the performance is to find a ferromagnetic material with either a stronger magnetooptic response or a lower optical absorption, or a combination of both. Promising candidates are the amorphous CoFe-based alloys. These materials, of which CoFeB, FeSi and CoMg are some examples, are known to have a lower electrical conductivity than their pure metallic counterparts, hence possibly a lower optical absorption. If this reduction exceeds the possible decrease of the magnetooptic strength, amorphous CoFe-alloys could enhance the performance of the amplifying waveguide optical isolator. With $Co_{50}Fe_{50}$ the best performing ferromagnetic metal composition so far,

[16] These measurements have been done in the framework of a collaboration with the research group of Nakano [19] at Tokyo University. The specificities of the corresponding setup are described in appendix C.

it is fair to assume that the chemical formula of the amorphous alloy should not deviate too much from $Co_{50}Fe_{50}$.

The material at our disposal for magnetron sputter deposition is $Co_{40}Fe_{40}B_{20}$. Non-reciprocal ridge waveguides with a 50nm $Co_{40}Fe_{40}B_{20}$-film as the top contact have been fabricated on epitaxial wafer material with a third-generation isolator layer structure (see table 4.9, design D3P). The characterization has been done with the method of non-reciprocal lasing. The extracted isolation ratio (see equation 4.1) equals 1.61dB/mm, which, compared to the 6.32dB/mm obtained from a similar experiment on a $Co_{50}Fe_{50}$-isolator, is a reduction by almost a factor 4. The forward transparency current reduces by shifting from $Co_{50}Fe_{50}$ to $Co_{40}Fe_{40}B_{20}$, but only in the order of 20%. The conclusion is that the isolator performance has diminished.

We believe that the large reduction of the optical isolation strength is mainly attributed to the intrinsically lower magnetooptic strength of the B-substituted alloy; Buschow [20] has reported that the addition of boron to pure cobalt reduces the Kerr rotation at 633nm, while for Fe_xB_{1-x}-alloys the Kerr rotation goes through a maximum for x = 0.8 and reduces almost to zero for x = 0.4.[17] Additionally, it should be kept in mind that the layer structure is not optimized for the B-substituted material. A change of the complex optical and magnetooptic constants can influence the phase matching between the modal electric field and the gyrotropy constant importantly – as extensively discussed in chapter 2 – hence the intrinsic quality of $Co_{40}Fe_{40}B_{20}$ for the isolator application might be larger.

Anyhow, in view of the huge reduction of the isolation-to-loss ratio, it is fair to conclude that even with an optimized layer structure the use of amorphous $Co_{40}Fe_{40}B_{20}$ would not lead to a structural improvement of the isolator performance with respect to $Co_{50}Fe_{50}$.

4.3.4.4 Conclusion generation III

The third generation of non-reciprocal waveguide devices has brought us a large enhancement of the demonstrated performance. Compared to the second generation the building blocks of the component have not been modified – the device is a $Co_{50}Fe_{50}$-covered InAlGaAs multiple quantum well structure. Instead, the improvement is entirely attributed to the shift towards a waveguide design that optimizes the practical performance of the device. The result is the first demonstration of a transparent monolithically integratable optical isolator. Furthermore, the experimental performance of 13.0dB isolation in a 2.1mm long isolator with 155mA of current required for forward transparency is the highest level of operation ever obtained on this type of device. The correspondence between the measured and the theoretically predicted values is good, especially for the optical isolation.

Apart from the optical isolation and the transparency current a multitude of parameters have been investigated, both experimentally and mathematically. It should not come as a surprise that the amplifying heart of the isolator implies that the isolator suffers from the typical phenomena encountered in a semiconductor optical

[17] Although the magnetooptic properties at 1300nm are not necessarily the same as those in the visible wavelength range.

Optical isolation	13dB
Transparency current	155mA
Injection current range	150mA - 160mA †
Central wavelength	1288nm
Wavelength range	$>$ 30nm
Operating temperature	15°C - 80°C ‡
Data rate compatibility	$\geq$ 10Gbit/s

† Outside this injection current range the optical isolation decreases significantly due to the influence of ASE.

‡ Outside this temperature range the device has not been tested.

Table 4.14: Experimental characteristics of 2mm-long third-generation amplifying waveguide optical isolators. The wavelength and temperature interval correspond to ranges in which the optical isolation doesn't change significantly. In these ranges the gain performance varies however importantly.

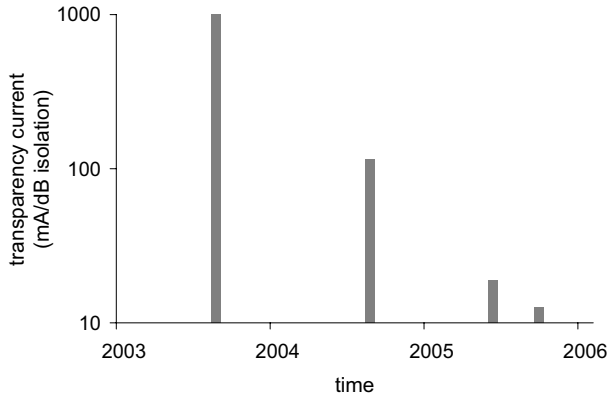

Figure 4.34: Evolution of the demonstrated level of forward transparency current with time.

amplifier such as gain saturation, the degradation of the optical signal-to-noise ratio, the performance decrease with temperature and a limited spectral width. The optical isolation itself is less sensitive with respect to the operation wavelength and the temperature. However, the presence of spontaneous emission has a high impact on the observed optical isolation. The experimental characteristics of the third-generation amplifying waveguide optical isolators are summarized in table 4.14.

At the end of this section it is worth reviewing the evolution in demonstrated performance of the non-reciprocal device since the first demonstration. From the experimental results of the previous generations the interpolated values of the forward transparency current, which we consider the figure of merit to be minimized, can be calculated. The evolution of this parameter is plotted in figure 4.34, illustrating that five years of research on this type of component have resulted in an improvement of the performance by more than a factor 80.
The demonstrated performance is however at least a factor of 6 too low to be suit-

able for practical applications – 50mA of current injection in a 25dB-isolating device can be considered the practical upper limit. The extensive research performed on the third generation of TM-mode optical isolators has indicated that there is no direct route towards further major improvement of this component. Only a better control of the thickness of the waveguide layers could lower the transparency current to a certain extent. The most straightforward increase of performance would be realized by identifying a magnetooptic material with better material properties or the development of a higher gain multiple quantum well material. From the discussion in chapter 3 it should however be clear that the current choices are already best-in-class and no alternatives have been identified so far. One other solution would be to shift from a shallowly etched ridge waveguide isolator towards a buried heterostructure. With an intrinsically much higher lateral contrast between the core and the cladding, the modal confinement in the amplifying core increases, which lowers the material gain required for transparency. Furthermore, the core width of a buried structure is much lower, which further reduces the transparency current. The development of such a buried isolator will be described in chapter 5.

4.4 Integrated electromagnet

4.4.1 Gold stripe electromagnet

4.4.1.1 Introduction

In an earlier paragraph we have discussed the difficulty to obtain a high value of the magnetic squareness of the ferromagnetic metal stripe due to the high aspect ratio of this stripe. One solution is to integrate a magnet – either a permanent magnet or an electromagnet – in the vicinity of the ferromagnetic contact. This section is devoted to the development of an electromagnet integrated with an amplifying waveguide optical isolator.
The cross-section of the isolator with an integrated electromagnet is schematically depicted in figure 4.35. The electromagnet is a gold stripe oriented along the longitudinal z-direction, galvanically isolated from the isolator contact pad. A longitudinal current flowing through the electromagnet induces a magnetic field that points laterally at the isolator contact – parallel to the ferromagnetic metal surface and perpendicular to the light propagation direction. The direction of the magnetic field obviously reverses when the current flow direction is reversed.
Apart from being a solution for the magnetization difficulties, such an integrated electromagnet is interesting as it enables to generate a magnetic field with an arbitrary field direction. This can for example be used to create the radially oriented magnetic field needed in a ring resonator based isolator, as will be discussed in chapter 6. Finally, we remark that in the configuration of an amplifying waveguide optical isolator with an integrated electromagnet the internal loss of a semiconductor optical amplifier can be modified in a non-reciprocal and dynamical way.

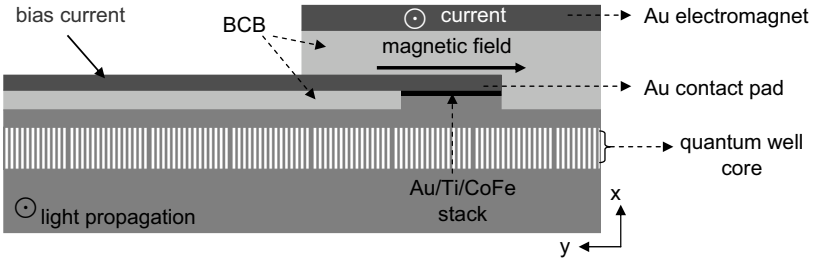

Figure 4.35: Schematic cross-section of the amplifying waveguide isolator with integrated electromagnet.

4.4.1.2 Magnetic design

The parameter that determines the performance of the integrated electromagnet is the amount of current required to realize magnetic saturation of the ferromagnetic metal contact. The suitable figure of merit for the electromagnet is therefore the magnitude of the lateral magnetic field per unity of current flow (in Oe/mA). The design parameters are the width and the thickness of the gold film, the distance separating the gold stripe and the ferromagnetic metal contact and the lateral variation of the magnetic field.
Simulations comprise solving the Biot-Savart law at a certain distance to a current carrying strip. Consider the situation sketched in figure 4.36; an infinitely thin plate with a width d and an infinite longitudinal length (z-axis) carries a current I along the longitudinal z-direction. The angles ϕ and θ determine the projection of the vector $\boldsymbol{r}$ onto the xy- and xz-plane respectively. The magnetic induction $d\boldsymbol{B}$ (in Tesla T) at a point p induced by the current element $I\boldsymbol{dl}$ at a distance $\mathbf{r}$ from p reads:

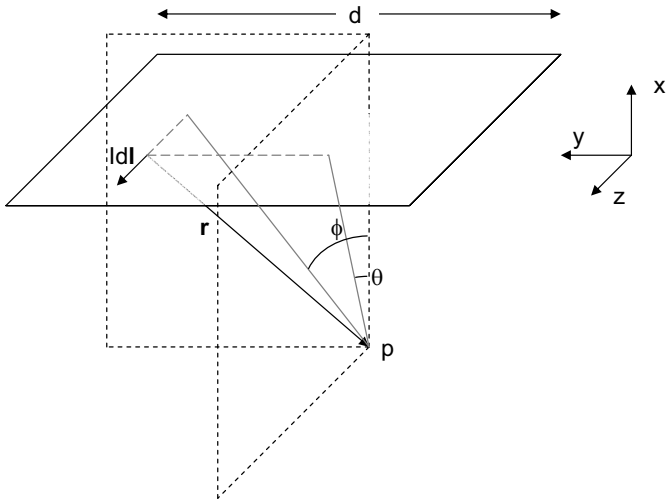

Figure 4.36: Schematic drawing of the configuration considered in the magnetic field simulations.

$$d\mathbf{B} = \frac{\mu_0 \mu_r I}{4\pi} \frac{\mathbf{dl} \times \mathbf{r}}{r^3}, \tag{4.26}$$

with μ_0 the magnetic permeability of the vacuum. Integration over all the current elements of the strip yields the total field $\boldsymbol{B}$ in point p. This field can be decomposed into a transverse (x-direction) and a lateral (y-direction) component:

$$\begin{aligned} B_x &= \frac{\mu_0 I}{4\pi} \int_{-\frac{\pi}{2}}^{\frac{\pi}{2}} \int_{\phi_{min}}^{\phi_{max}} \frac{-tan\phi\ sec^2\phi\ sec^2\theta}{(1+tan^2\phi+tan^2\theta)^{\frac{3}{2}}} d\phi d\theta \\ B_y &= \frac{\mu_0 I}{4\pi} \int_{-\frac{\pi}{2}}^{\frac{\pi}{2}} \int_{\phi_{min}}^{\phi_{max}} \frac{sec^2\phi\ sec^2\theta}{(1+tan^2\phi+tan^2\theta)^{\frac{3}{2}}} d\phi d\theta, \end{aligned} \tag{4.27}$$

with ϕ_{max} and ϕ_{min} determined by the exact location of point p and by the width d of the current carrying strip. The integration limits for the angle θ are $\frac{\pi}{2}$ and -$\frac{\pi}{2}$ due to the infinity of the strip in the longitudinal z-direction. The magnetic field $\boldsymbol{H}$ (in Oe) at point p can easily be found by multiplying the B_x and B_y values (in tesla) by 10^4 (see table 2.4.1). Repeating the calculation for a range of points p yields the plots illustrated in figure 4.37, showing the lateral (y-direction) variation of both magnetic field components at a realistic distance (x-direction) of 1μm from the current strip, for a strip width of 5μm. The magnetic field is expressed in Oe per milliampere of current flowing through the strip. Remember that for the TM-mode isolator a lateral magnetic field is required in the vicinity of the ferromagnetic metal contact. Graph 4.37 indicates that for a symmetrically positioned, 2μm wide isolator contact the variation of the lateral magnetic field strength is less than 5%, even for a narrow current strip of 5μm. Keeping in mind that the electrical field strength of the fundamental guided mode is low at the lateral edges of the metal film, this means that the influence of the lateral variation of the magnetic field on the generated magnetooptic effect can be neglected. In what follows we therefore consider the magnetooptic film to be a point, symmetrically positioned in the y-direction with respect to the current carrying strip.

All of this immediately leads to the design of the integrated electromagnet, which is nothing but a current carrying (gold) strip. In figure 4.38 the lateral magnetic field strength is plotted for a variation of the width of the electromagnet and of the distance between the electromagnet and the magnetooptic metal film. The generated magnetic field is quasi-independent of the distance to the electromagnet for gold strip widths of several micrometers. This is an advantage for the fabrication because the use of a thick separation layer between the isolator contact and the electromagnet reduces the risk of short-circuiting both metal layers. The optimal parameters of the electromagnet are a width of 5μm positioned at a distance of 1μm from the surface of the magnetooptic metal contact. For this configuration a lateral magnetic field of 1Oe per milliampere of current injection is generated. For the first generation of isolators with an integrated electromagnet restrictions on the available contact lithography masks prohibited to have an electromagnet width below 30μm. The generated magnetic field is therefore limited to 0.2Oe/mA – a factor of 5 below the optimized value – which must however be suitable for a proof-of-principle experiment.

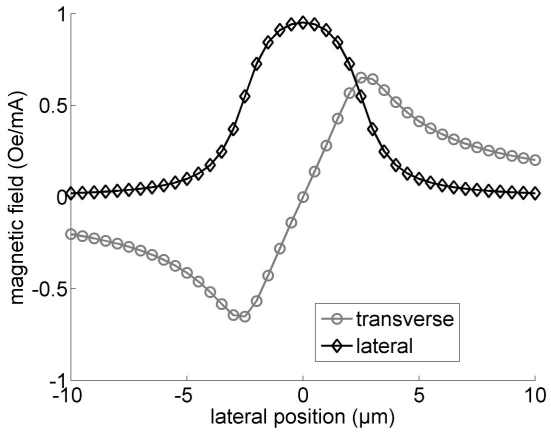

Figure 4.37: Variation of the transverse (x-direction, grey) and lateral (y-direction, black) field component with lateral position at a transverse distance of 1µm from the current strip.

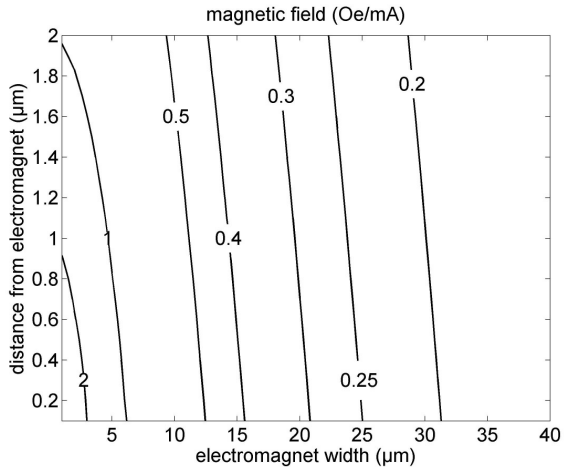

Figure 4.38: Simulation of the lateral magnetic field (y-direction) as a function of the width of the electromagnet gold strip and the distance (x-direction) from the electromagnet, expressed in Oe per milliampere of current injection.

In this simple calculation the influence of the film thickness on the magnetic field profile has not been taken into account. However, as long as the film thickness is much lower than the lateral film width, it has no significant influence on the magnetic field. One argument that justifies an increase of the gold film thickness is that the thicker the film is, the lower its electrical resistance, hence the lower the heat dissipation in the electromagnet.

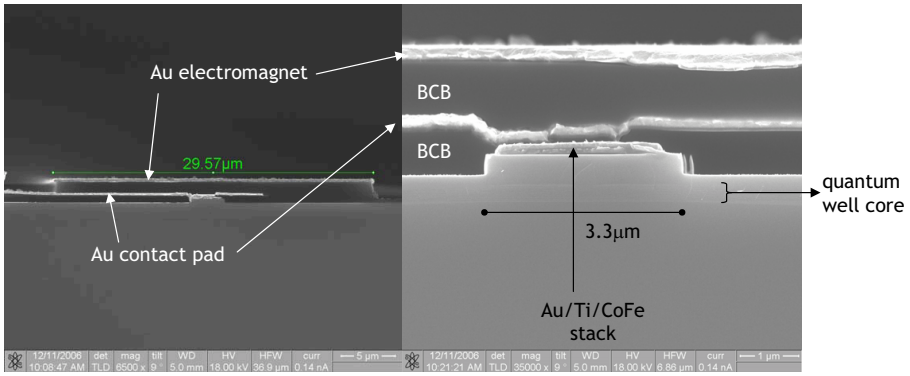

Figure 4.39: Scanning electron microscope images of the cross-section of the amplifying waveguide optical isolator with integrated electromagnet, illustrating the successful fabrication.

4.4.1.3 Experimental results

Based on the design considerations of the previous paragraph and within the limitations of the available lithography masks a first generation of optical isolators with an integrated electromagnet has been fabricated. For the isolator fabrication itself the optimized procedure – as elaborated in section 4.1 – has been followed except for the fact that the second metallization layer has been deposited asymmetrically with respect to the waveguide ridge, in correspondence to figure 4.35. The current isolation layer used in this processing is benzocyclobutene (BCB), known for its excellent planarization properties. On top of the isolator bias contact a 30μm wide and 215nm thick gold stripe has been deposited, serving as the electromagnet. Both metal stripes are separated by a 1μm thick BCB layer. Isolators with a length of 1.3mm have been cleaved and mounted on the dedicated setup for characterization. The quality of the fabrication can be assessed through electron microscope images of a cross-section of the optical isolator (figure 4.39). The left image of figure 4.39 shows good agreement between design and fabrication. When zooming in on the ridge waveguide (right image of figure 4.39) it can be seen that the definition of the ridge is not perfect, with a ridge width that is slightly wider than designed and with some roughness present at the side of the ridge. These inaccuracies will obviously influence the performance of the waveguide isolator, but should not change the operation of the integrated electromagnet.

For the characterization of the optical isolator with an integrated electromagnet the non-reciprocal lasing technique explained earlier in this chapter has been used. To be able to evaluate the performance of the integrated electromagnet, the amplifying waveguide isolator was initially characterized with an external electromagnet. The laser threshold current equals 103mA and the lasing wavelength is 1288nm. In figure 4.40 the emitted power is plotted as a function of the externally applied magnetic field for a bias current of 140mA – well above threshold – on a 1.3mm-long isolator. The corresponding maximal isolation, at saturation magnetization, is 6.2dB. This graph shows that the remanent isolation – at zero

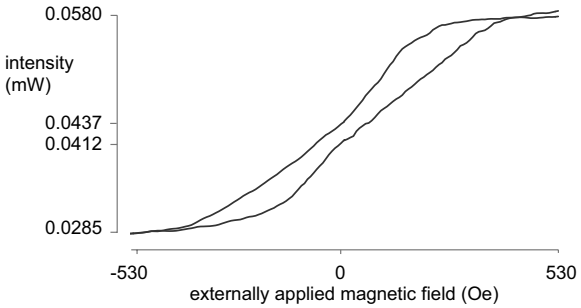

Figure 4.40: Optical power emitted by the isolator as a function of the externally applied magnetic field at a bias current of 140mA (= above threshold).

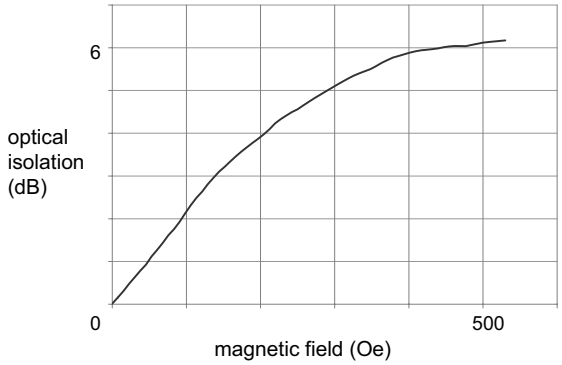

Figure 4.41: Optical isolation of the fabricated 1.3mm long devices as a function of the magnetic field strength.

magnetic field – is only 8.5% of the maximum value. Furthermore, it becomes clear that the saturation magnetic field amounts up to 530Oe. Based on the theoretical calculations plotted in figure 4.38 it can directly be derived that for the fabricated integrated electromagnets a very high current of 2650mA would in theory be required to obtain magnetic saturation of the magnetooptic metal film. With the aid of the non-reciprocal lasing formula (equation 4.1) the optical isolation of the fabricated isolator devices can be related to the strength of the magnetic field, as plotted in figure 4.41.

Next, the integrated electromagnet has been characterized by applying current to the gold strip while electrically pumping the isolator above threshold. To avoid heating, the electromagnet is driven with a pulsed current (500mA, pulse width 0.3μs, duty cycle 3%). The chip temperature is controlled with a thermoelectric cooler at a value of 20°C. The isolator bias current is continuous wave (CW) and fixed at a value of 140mA. The output signal is evaluated on a digital sampling oscilloscope, as is illustrated in the left graph of figure 4.42, with indication of the on-set and off-set of the electromagnet current pulse. The black and grey lines correspond to an electromagnet current flow in opposite longitudinal directions, generating a magnetic field oriented in opposite lateral directions. The intensities

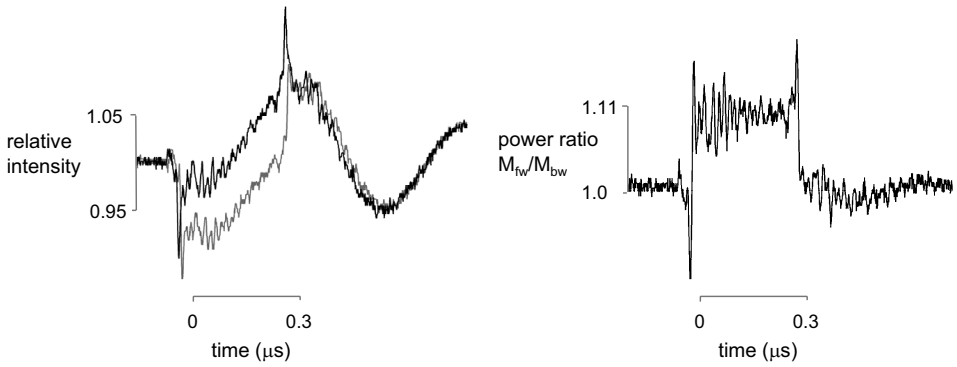

Figure 4.42: Proof-of-principle experiment of an isolator with an integrated electromagnet; (left) the response of the optical isolator to an electromagnet current pulse (500mA, pulse width 0.3μs). The black and grey lines correspond to opposite longitudinal current flow directions. The isolator is electrically pumped with 140mA of current (= above threshold). (right) The corresponding ratio of the intensity at 'forward' to that at 'backward' current injection

are normalized to compensate for variations in the fiber-to-chip coupling. At the on-set of the current pulse the emitted power rapidly increases or decreases, depending on the current flow direction. This is a clear proof of the on-set of the non-reciprocal loss shift. After the off-set of the pulse, the emitted power quickly becomes identical again in both cases, followed by an oscillation of the intensity which we believe is the recovery from heating of the device. The fact that this recovery is identical for both current injection directions is another indication that the observed splitting of the output power is only due to the magnetic field generated by the current flow in the electromagnet. This experiment is the first demonstration of an amplifying waveguide optical isolator with an integrated electromagnet.

As clearly illustrated in the right graph of figure 4.42 the ratio of the intensity at 'forward' to that at 'backward' current injection remains constant during the pulse and equals 1.11, which for an isolator of 1.3mm length corresponds to an isolation of 0.91dB, as can be calculated from formula 4.1. This isolation is 15% of what has been observed at saturation magnetization with an externally applied magnetic field. From figure 4.41 it can be derived that the lateral magnetic field that has actually been generated in our experiment equals 46Oe or 0.092Oe/mA, which is a factor of 2.2 lower than the theoretical value. With a projected current injection of 5760mA to achieve magnetic saturation, the level of performance is two orders of magnitude away from practical application. Decreasing the width of the gold strip would increase the generated magnetic field significantly. Still, at a minimal value for the electromagnet width of 5μm 530mA is required for magnetic saturation, and that is the most optimistic – theoretical – value. Therefore other methods to improve the device need to be explored.

So far we have only looked into the maximization of the current-induced magnetic field. However, what really matters for our application is the internal mag-

netic field inside the (magnetic) metal contact, and the magnetization, which is the material response to this field. As extensively discussed in section 2.4.4.2, surface effects in samples with finite dimensions introduce demagnetizing fields which counteract the externally applied field inside the sample. As a result the total internal magnetic field is smaller than the applied (or current-induced) magnetic field, which in turn reduces the magnetization. Now, as discussed in chapter 2 below saturation the non-reciprocal loss shift varies linearly with the magnetization, i.e. $\boldsymbol{g} = a\boldsymbol{M}$. In other words, if demagnetization effects can be reduced or even avoided, the electromagnet current required to generate a certain optical isolation level would decrease.
A solution is to increase the width of the ferromagnetic metal contact to a value that is a multitude of the original width. As the strength of the demagnetizing field decreases with distance from the sample edge, the magnetization in the center (in the lateral direction) of the metal contact is enhanced. This is obviously the only region of importance of the metal contact, as the optical mode overlaps locally with the metal. For example, increasing the Co_xFe_{1-x} contact width from 2μm to 20μm multiplies the magnitude of the lateral magnetization at the center by a factor 10. Simulations have been done with a 30μm wide electromagnet metal strip. Disadvantage of this approach is that, in order to ensure that the current-induced field is oriented along the lateral direction, the width of the current-carrying (gold) strip must be larger than the width of the ferromagnetic metal contact, which limits the reduction of the electromagnet current. While this is in theory an elegant solution to improve the quality of the integrated electromagnet, the flatness of the metal film has to be extremely good to avoid 'edges' and the associated demagnetizing fields, especially locally at the ridge waveguide. As illustrated on the microscope images of the first generation non-reciprocal devices, this is not at all an easy task. We will not investigate this option further, but instead focus on another, more practical idea, which is the subject of section 4.4.2

4.4.2 Current injection along ferromagnetic metal

4.4.2.1 Experimental observation

Most of the fabricated isolator devices with an integrated electromagnet perform at a level comparable to the one illustrated in figure 4.42, except for one component which operates notably better. The experimental result is plotted in figure 4.43. The measurement procedure is the same as before and the isolator bias current is set at 140mA. The ratio of the intensity at 'forward' to that at 'backward' current injection equals 1.64, which for an isolator of 1.3mm length corresponds to an isolation of 4.3dB, or 70% of the value at saturated magnetization. In other words, this device operates a factor 4.7 better than its nominally identical neighboring components. In an attempt to validate this anomalous result we repeated the measurements for different values of the electromagnet current injection. In figure 4.44 the corresponding evolution of the optical isolation with injected (pulsed) current is plotted (bottom axis). For comparison the optical isolation as a function of the strength of an (externally applied) magnetic field is also drawn (top axis). The fact that it is possible to match both graphs perfectly is a clear argument that the observed result is valid, hence that on this particular device a much higher

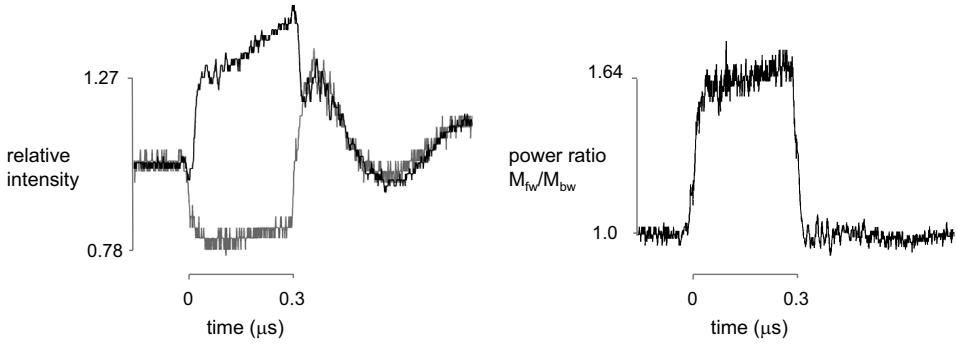

Figure 4.43: (left) (Relative) intensity emitted by the (best performing) optical isolator at a bias current of 140mA (= above threshold) and (right) corresponding ratio of the intensity at 'forward' to that at 'backward' current injection

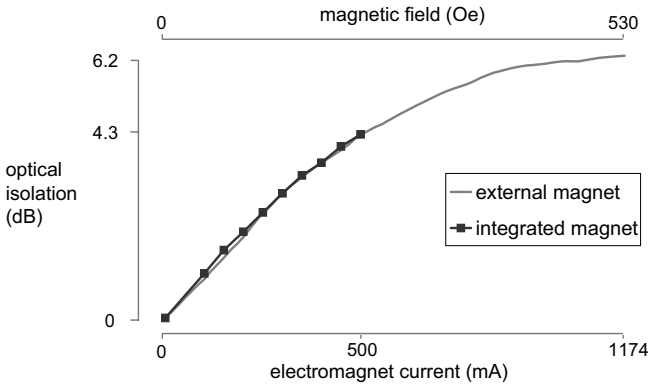

Figure 4.44: Evolution of the optical isolation with injection current in the electromagnet and with externally applied magnetic field.

local magnetic field is created as a result of the current injection. Figure 4.44 also indicates that with a current injection of 500mA the achieved magnetic field is just below half the value needed to saturate the ferromagnetic film. This is equivalent to an externally applied magnetic field of 225Oe or 0.45Oe/mA. Comparison of this value to the outcome of the theoretical calculations (figure 4.38) learns that the operation of this particular device must be fundamentally deviating from the one considered in the simulations.

4.4.2.2 Principle of operation

Consider the limiting case of an integrated electromagnet with no current isolation layer (t_{BCB} = 0). In other words, there is only one metal strip both for the electrical pumping of the isolator and for the generation of a magnetic field. At first sight, keeping in mind the simulation results plotted in figure 4.38, this configuration does not perform significantly better than the case of separated metal

strips. The only obvious advantage is that the fabrication is simpler with two processing steps less to be executed. However, calculations done with Comsol Multiphysics [21] show that there is a large increase of the magnetization induced in the ferromagnetic $Co_{50}Fe_{50}$ film compared to the case of an isolated electromagnet. To understand this, think of a two-layer stack with one magnetic ($\mu_r >> 1$) and one non-magnetic ($\mu_r = 1$) material. Assume infinite dimensions in one direction, which we refer to as the longitudinal direction, a width of several micrometers and a thickness of 100nm. This is a good approximation of the isolator-electromagnet configuration. Now, assume first that both layers are galvanically isolated and that a longitudinal current is flowing through the upper, non-magnetic material. Obviously, this is the equivalent of the 'normal' electromagnet case. The current flow induces a primarily lateral oriented magnetic field in the magnetic strip, which is counteracted to some extent by demagnetizing fields caused by magnetic surface charges. In reality, both metal layers are however not electrically isolated and the longitudinal current will also flow through the magnetic layer. The current distribution depends on the difference in electrical resistivity of the films. As the electrical properties vary largely with deposition quality and film thickness, it is not possible to quantify exactly what fraction of the current flows through the magnetic $Co_{50}Fe_{50}$ layer. However, with the volume resistivities of gold and $Co_{50}Fe_{50}$ of the same order of magnitude – $\rho_{Au} = 2.2 \times 10^{-8}\Omega m$ [22], $\rho_{Co_{50}Fe_{50}} = 7 \times 10^{-8}\Omega m$ [23] (both at 20°C) – it can be concluded that a non-negligible current will flow through the $Co_{50}Fe_{50}$ contact film. This current obviously also induces a magnetic field, inside and outside the magnetic layer.

To understand how this extra field – the so-called self-field[18] – contributes to the total internal magnetic field and the corresponding magnetization, consider the situation in which current is only flowing through the magnetic strip, along the longitudinal z-direction. In addition, assume for a moment that the magnetic permeability of the layer is 1, i.e. that the magnetization is zero, which avoids the presence of demagnetizing fields. It is well known that the magnetic field in a current-carrying thin sheet, of which the metal contact film is an example, is mainly oriented along the longest direction (in this case the lateral y-direction), except at the sheet ends. This lateral field component is quasi-constant in the lateral y-direction and varies linearly along the shortest, transverse x-direction, going through zero at the center of the sheet – again except for positions close to the sheet ends. This is visualized in figure 4.45 where the lateral magnetic field component is depicted for a homogenous current injection of 100mA in a 50nm thick and 2μm wide strip, which are the actual dimensions of the isolator metal contact. Notice the different scale of abscise and ordinate.

Now, if the relative permeability equals its real value, $\mu_{r,CoFe} \approx 5000$, it is expected that demagnetizing fields modify the internal magnetic field inside the sample. This is indeed the case, but the influence is marginal compared to the decrease in a sample placed in a uniform applied magnetic field. This can intuitively be understood by comparing the magnetic surface charges in both situations. On the left drawing of figure 4.46, the magnetization inside a sample placed inside a uniform magnetic field – such as the one induced by the integrated electromagnet

[18] In magnetoresistive read heads this self-field plays an important role, as it reduces the magnetoresistive response [24].

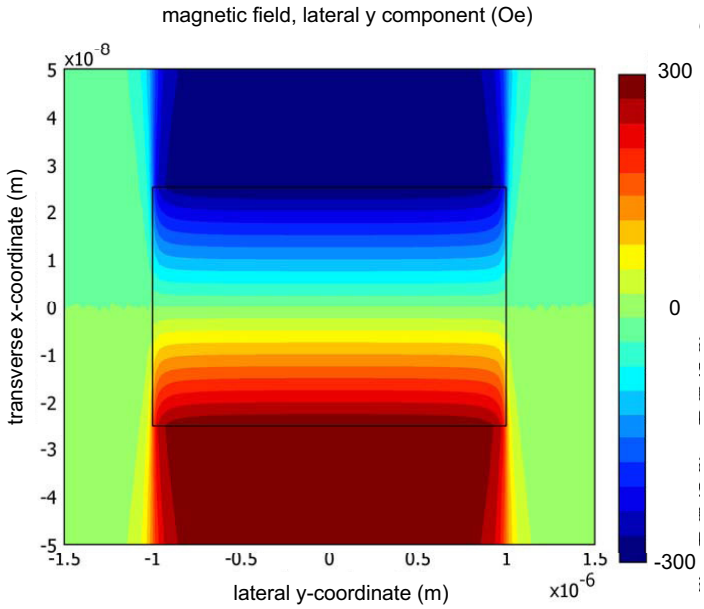

Figure 4.45: Filled contour plot of the lateral magnetic field component induced by current flowing through a thin sheet. The scale of abscise and ordinate are different. Calculations have been done with Comsol Multiphysics [21].

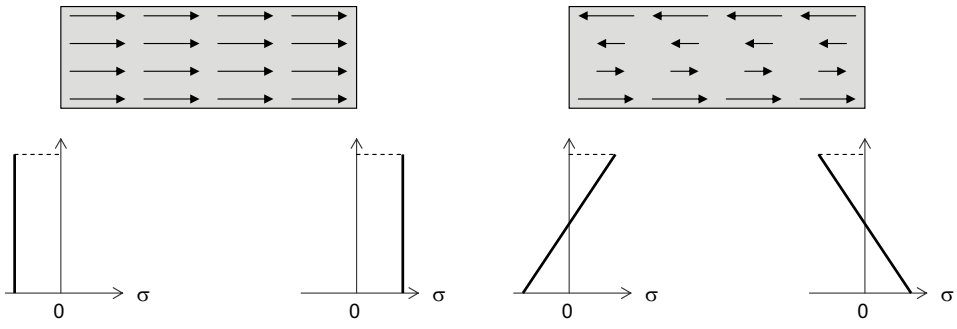

Figure 4.46: The different influence of surface charges in the case of an external uniform magnetic field (left) and a current-induced magnetic field (right) in a thin magnetic sheet. The upper drawings illustrate the magnetization inside the sample, the lower part the magnetic surface pole density σ.

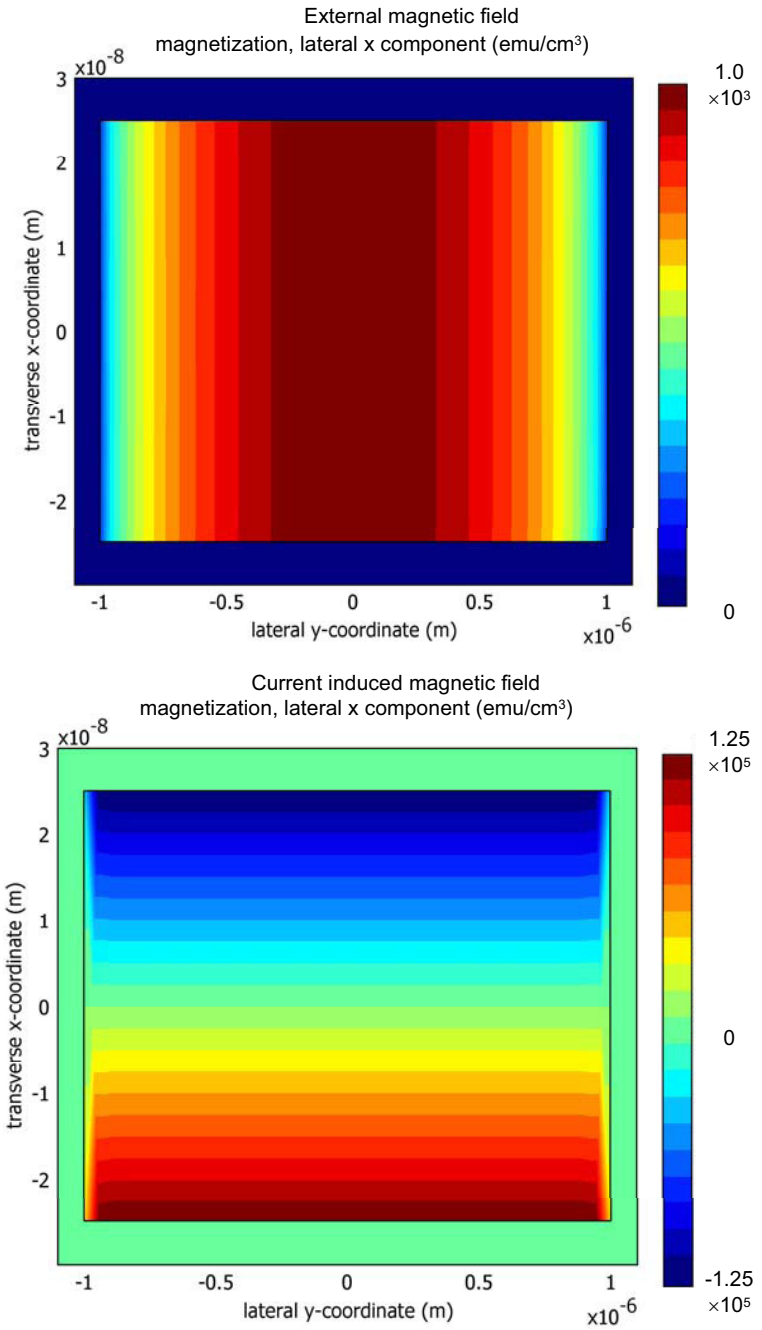

Figure 4.47: Filled contour plots of the lateral magnetization of a $Co_{50}Fe_{50}$ film ($\mu_{r,Co_{50}Fe_{50}}$ = 5000) in an external applied magnetic field (top), and as the response to the current-induced magnetic field (bottom), illustrating the difference in demagnetization effects. Notice the increase by a factor 100 of the maximum value of the lateral magnetization. The scale of abscise and ordinate are different.

– is plotted, while the right picture shows the magnetization due to a current flow in the sample. The length of the arrows is proportional to the magnitude of the local magnetization. We have neglected here the influence of the transverse magnetic field component and the scale of the *x*- and *y*-axis are again different. The corresponding surface pole density $\sigma = \boldsymbol{n} \cdot \boldsymbol{M}$, with $\boldsymbol{n}$ a unit vector normal to the surface, follows immediately and is plotted in the bottom part of figure 4.46. The demagnetizing field at a certain position *r* is influenced by all surface poles, according to the expression [25]:

$$H(r) = \frac{1}{4\pi} \int \int \mathbf{n}' \cdot \mathbf{M}(r') \frac{r - r'}{|r - r'|^3} d^2 r'. \tag{4.28}$$

The specific profile of the surface pole density in the current-carrying thin sheet, therefore yields only small demagnetizing magnetic fields. This should be visible in the magnitude of the magnetization. Indeed, if we place the magnetic strip in a uniform lateral external magnetic field, effects of demagnetization cause the lateral magnetization inside the magnetic strip to vary along the lateral direction with a maximum at the center of the sample, as can be seen in the top part of figure 4.47. The magnetization as a response to a current flow in the strip, plotted on the bottom side of figure 4.47, remains quasi-constant in the lateral direction due to the low demagnetizing fields.[19] The maximum value of the lateral magnetization in the current-carrying case is as much as 100 times larger than in the case of the external magnetic field. Both values can be compared as we have set the external magnetic field strength equal to the highest field value induced by the current flow in the strip. Simulations have been done with the same specifications as the ones used for figure 4.45.

Now, return to the isolator application. Remember from chapter 2 that the non-reciprocal loss shift $\Delta\alpha$ is expressed by the perturbation integral:

$$\Delta\alpha = -\frac{8\pi}{Z_{vac}\lambda} Re \left[\frac{\int \int g(\mathbf{M}) E_x^{(0)} E_z^{(0)} dxdy}{\int \int \left[E_x^{(0)} H_y^{(0)} - E_y^{(0)} H_x^{(0)} \right] dxdy} \right], \tag{4.29}$$

with the gyrotropy *g(**M**)* varying linearly with the magnetization, *g(**M**) = a**M**(x,y)* (below magnetic saturation) and all field values depending on the transverse and lateral coordinates *x* and *y*. This expression shows how $\Delta\alpha$ depends on the magnetization weighted by the electric field product $E_x^{(0)} E_z^{(0)}$. Ideally, the lateral magnetization should therefore be high at positions *x* and *y* where the magnitude of the field product is high. We can assume that $E_x^{(0)} E_z^{(0)}$ decreases monotonously with depth in the ferromagnetic metal film,[20] hence it is advantageous to have a magnetization profile that is maximal at the metal-semiconductor interface. This is exactly the case if the ferromagnetic film itself is used as the electromagnet, as

[19] But obviously goes through zero in the transverse direction.

[20] This assumption is rigorous for the evanescent tail of a guide mode in non-dissipative media. In structures containing absorbing materials the propagation vector has complex values, hence the field profiles in the outer cladding layers are not purely exponential and the product $E_x^{(0)} E_z^{(0)}$ has sign changes in these layers. For simplicity reasons we consider here that the phase of the electric field changes only slowly with depth in the metal, such that $E_x^{(0)} E_z^{(0)}$ has a fixed sign in the the region with non-negligible magnitude.

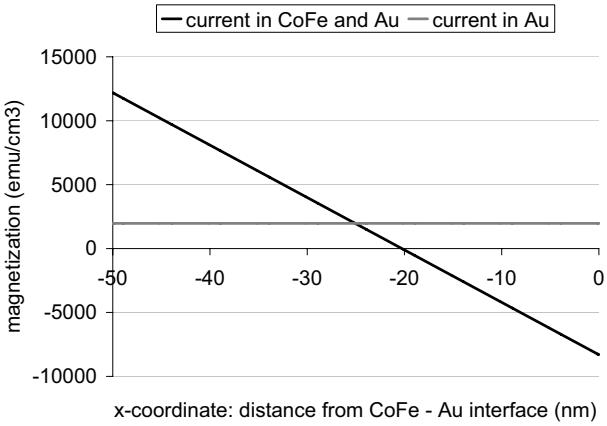

Figure 4.48: Profile of the magnetization in the $Co_{50}Fe_{50}$ film induced by current flowing in both the magnetic and the non-magnetic metal layer (black line) and by current flowing solely through the non-magnetic Au film (gray curve).

can be derived from figure 4.47. It can therefore be expected that this configuration is more efficient than that of a gold-electromagnet in terms of the non-reciprocal absorption shift per unit electromagnet current.
In a practical device, the thin 50nm $Co_{50}Fe_{50}$ film is always covered with a gold strip that is several hundreds of nanometers thick and tens of micrometers wide. This extra metallization layer allows for electrical contacting of the isolator and protects the ferromagnetic layer against oxidization. In other words, a practical optical waveguide isolator has a metal layer configuration that is exactly the limit of an isolator with an integrated electromagnet mentioned earlier. We can conclude from the previous discussion that for this structure there will be two contributions to the magnetization in the magnetooptic metal contact, each with a distinct spatial distribution. The relative importance of each contribution depends on the fraction of the longitudinal current that flows through the top gold layer and through the $Co_{50}Fe_{50}$ layer.

Consider as an example a 2μm-wide and 50nm-thick $Co_{50}Fe_{50}$ film, topped with a 5μm-wide and 400nm-thick gold film. Furthermore, assume a longitudinal current injection of 500mA and a current density in the gold that is three times higher than that in the $Co_{50}Fe_{50}$ due to the higher electrical resistivity of the latter. The corresponding lateral magnetization profile along the thickness of the $Co_{50}Fe_{50}$ film is represented by the black line on figure 4.48. We compare this result to the situation where the 500mA of current is only sent through the gold strip, for which the calculated magnetization profile is described by the grey curve. Due to the difference in sheet resistance and the small dimensions of the ferromagnetic metal strip as compared to the gold layer the amount of current flowing through the $Co_{50}Fe_{50}$ stripe is low. The simulation results show that even in this case the maximum lateral magnetization is more than six times that of a purely gold electromagnet. The plots in figure 4.48 show that the magnetization in the $Co_{50}Fe_{50}$-current case is quasi-symmetric with respect to the middle of the ferromagnetic film. The (minor) deviation from perfect symmetry originates from

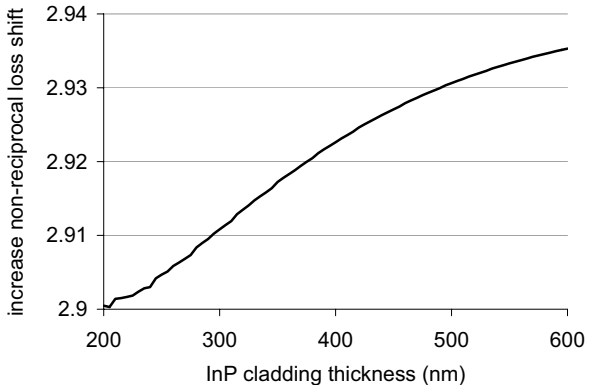

Figure 4.49: Theoretical enhancement of the non-reciprocal loss shift $\Delta\alpha$ by current flowing through the ferromagnetic metal contact of an optical isolator as a function of the InP cladding thickness. The reference value for $\Delta\alpha$ is that for the case of current flowing solely through the non-magnetic Au contact layer.

the contribution of the current flowing through the top gold layer to the magnetization.
To estimate the actual influence of the different magnetization profile formula 4.29 should be evaluated with a x-coordinate dependent gyrotropy *g(M) = aM(x)*.[21] The outcome of such calculations is shown in figure 4.49, where the non-reciprocal loss shift $\Delta\alpha$ is plotted as a function of the InP cladding thickness, with the gold-electromagnet situation as the reference, i.e. $\Delta\alpha_{Au-electromagnet} = 1$. The theoretical performance enhancement of the isolator with an integrated electromagnet from current injection in the ferromagnetic metal contact is almost 300%. The rise of the plot with larger InP thickness can be attributed to the fact that the penetration depth of the guided mode in the metal is smaller, hence the overlap with the region of positive magnetization is relatively larger. In section 4.4.2.4 we look into the optimization of the metal structure so as to optimize the useful magnetization. This simulation example shows that the effect of current flowing through the ferromagnetic layer of the isolator contact can introduce a significant increase of the 'practical' magnetization, hence of the efficiency of the integrated electromagnet. As such it provides a possible explanation for the performance enhancement of the single device mentioned at the start of this section.

4.4.2.3 Electrical behavior

In this electromagnet scheme there are two current flows through the metal structure. On one hand there is the electromagnet current that flows longitudinally from one device facet to the other. On the other hand there is the SOA pump current which distributes through the metal layers before diffusing into the semiconductor. It is important to examine whether the electromagnet current has an influence on the pump current flow and consequently on the longitudinal current

[21] Due to the small lateral demagnetizing fields the magnetization profile is quasi-independent of the lateral y-coordinate, hence 1D calculations can be applied.

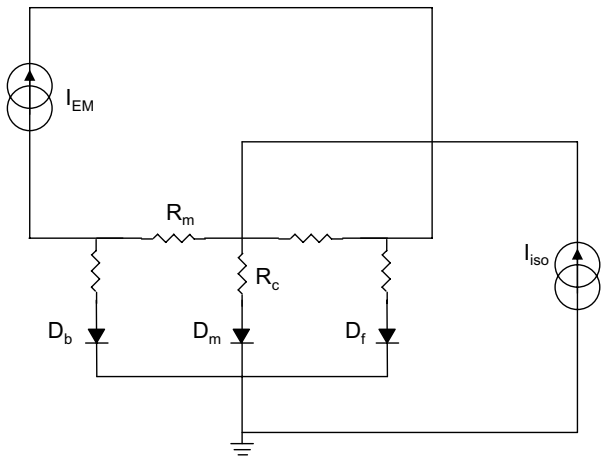

Figure 4.50: Equivalent electrical circuit of an optical isolator with the magnetooptic metal contact serving both as the ohmic electrical contact and as the integrated electromagnet. I_{iso} *and* I_{EM} *correspond to the isolator bias current and the electromagnet current respectively,* R_c *and* R_m *are the metal-semiconductor contact resistance and the resistance of the metal film, and diodes* D_f, D_m *and* D_b *denote the multiple-quantum well amplifying region.*

injection profile in the SOA heterostructure. Consider therefore the equivalent electrical scheme of the optical isolator with the magnetooptic metal film used as the integrated electromagnet (figure 4.50). The current values I_{iso} and I_{EM} denote the isolator bias current and the electromagnet current respectively, R_c and R_m correspond to the metal-semiconductor contact resistance and the resistance of the metal film, and diodes D_f, D_m and D_b denote the longitudinally distributed multiple-quantum well amplifying region. Depending on the electromagnet current I_{EM} the current flowing through each diode changes, as is illustrated in figure 4.51 for a total bias current $I_{iso} = I_{D_f} + I_{D_m} + I_{D_b}$ of 150mA, and resistance values $R_c = 6.0\Omega$ and $R_m = 6.0\Omega$. These last values correspond to the experimental ones mentioned in paragraph 4.3.4.2 for a 2mm long device. Upon a change of the flow direction of the electromagnet current, the diode D_f curve becomes the D_b and vice versa. Notice that with a perfectly conducting metal ($R_m = 0.0$) the influence of electromagnet current is zero.
These calculations show that the additional longitudinal current flow introduces a large inhomogeneity of the current injection in the SOA. As elaborated in section 4.3.4.2 this results in a decrease of the gain at a given pump current level. Additionally, the modification of the injection profile by the electromagnet makes it particulary difficult to asses the operation of the electromagnet. After all, remember that we compare the light emitted at one facet for both electromagnet current flow directions. For a regular electromagnet any change in intensity is due to the non-reciprocal effect. Not in this case however; the injection profile of the SOA changes upon electromagnet flow reversal, with consequently a change of the emitted ASE, even without a magnetooptic effect. The solution is to cha-

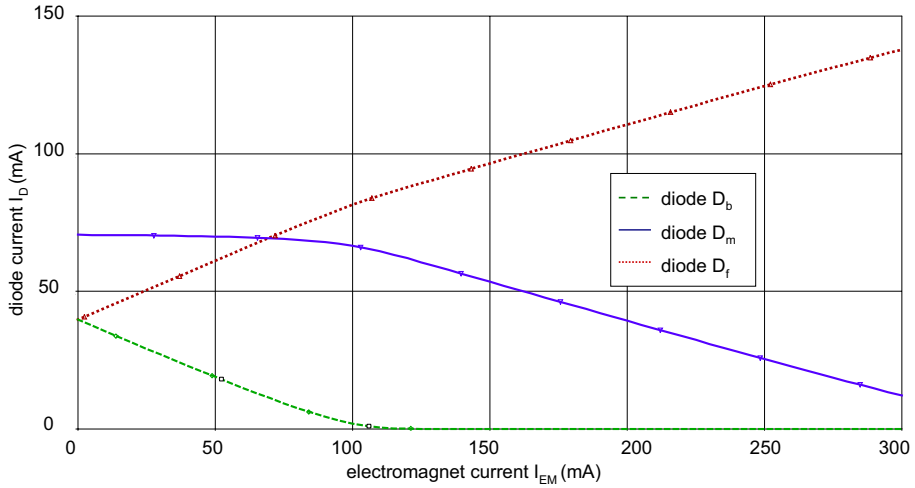

Figure 4.51: Evolution of the current flowing through diodes D_f, D_m *and* D_b *with the longitudinal electromagnet current, flowing from front to back facet. The total isolator pump current* I_{iso} *equals 150mA.*

racterize the devices far above threshold to minimize the influence of the emitted ASE.
One solution for this issue is to inject the isolator current at a multitude of longitudinal positions. As such, the longitudinal pump current flow is limited, with consequently a reduced interaction with the electromagnet current.

4.4.2.4 Design

Earlier, it has been shown how the use of the ferromagnetic metal layer as an integrated electromagnet enhances the generated non-reciprocal loss shift $\Delta\alpha$ per unit of electromagnet current. In this section we explore the limits of this configuration.
From the perturbation formula 4.29 it follows that the magnitude of $\Delta\alpha$ is determined by the overlap of the field product $E_x^{(0)}E_z^{(0)}$ and the magnetization profile. With $E_x^{(0)}E_z^{(0)}$ decreasing monotonously with depth in the ferromagnetic metal film and the magnetization profile being quasi-antisymmetric with respect to the middle of the ferromagnetic film, the integrand that determines the non-reciprocal loss shift changes sign in the middle of the metal layer. In other, words, any light penetrating deep into the metal gives a negative contribution to the value of $\Delta\alpha$. The obvious solution is to increase the thickness of the $Co_{50}Fe_{50}$ layer. Actually, due to the linear magnetization profile every increase of thickness causes an important enhancement of the performance. However, there is a technological constraint on this, as explained in section 4.1; a value of 100nm should be considered as the upper limit on the thickness of the Co_xFe_{1-x} layer. A second possibility for improvement is to increase the portion of current flowing through the ferromagnetic metal. After all, the magnetic field induced in a current carrying structure scales to the current flowing through that structure. The first option is to increase

the thickness of the $Co_{50}Fe_{50}$ layer, but the maximum value is limited. Second method is to reduce the cross-section of the gold contact layer. Finally there is also the possibility to replace the gold by a contact material with a higher electrical resistivity. Both last modifications increase the overall resistance of the metal structure which might lead to temperature related issues.
Assume now a 100nm thick $Co_{50}Fe_{50}$ film and keep the rest of the metal structure identical to that of the example discussed in section 4.4.2.2. For this configuration it can be calculated that an enhancement of the non-reciprocal loss shift of 13.8 can be realized compared to a gold-electromagnet. In other words, the increase of the ferromagnetic metal film thickness from 50nm to 100nm increases the efficiency of the $Co_{50}Fe_{50}$-Au-electromagnet by a factor 3.5.

4.5 Conclusion

In this chapter the practical realization of the amplifying waveguide optical isolator has been discussed. The evolution of the fabrication of the waveguide components has been pointed out, and the different characterization methods have been explained. Next, the development of the isolator has been elaborated in a chronological order, starting from the first-ever demonstration. Continuous improvement of the component's building blocks combined with the increased understanding of the isolator operation have resulted in the demonstration of a device with a performance that exceeds that of the first component by more than a factor 80. The result is a monolithically integratable optical isolator that is transparent in one direction while showing 13dB of loss in the opposite propagation direction. Furthermore, a rate equations model of the component has been developed which allows for the explanation of less-intuitive observations such as the major dependence of the isolation on the pump current. In addition, other aspects such as the spectral dependence and the dynamic behavior have been studied.
The last part of this chapter was dedicated to the development of an isolator with an integrated electromagnet. The design, fabrication and proof-of-principle have been described and an elegant concept for a major improvement has been identified; using the isolator contact itself as the integrated electromagnet, by introducing an extra longitudinal current flow, largely enhances the efficiency of the electromagnet.

Bibliography

[1] Th.G.S.M. Rijks, R.F.O. Reneerkens, R. Coehoorn, J.C.S. Kools, M.F. Gillies, J.N. Chapman, and W.J.M. de Jonge, "Switching field interval of the sensitive magnetic layer in exchange-biased spin valves." *J. Appl. Phys.,* vol. 82(7), pp. 3442–3451 (1997).

[2] M. Vanwolleghem, "Een geintegreerde InP-gebaseerde optische golfgeleiderisolator op basis van ferromagnetische CoFe-contacten, An integrated InP-based Optical Waveguide Isolator Using Ferromagnetic CoFe Contacts." *Ph.D. thesis,* ISBN , 90-8578-013-6, Ghent University, Belgium (2005).

[3] M. Vanwolleghem, W. Van Parys, D. Van Thourhout, R. Baets, F. Lelarge, O. Gauthier-Lafaye, B. Thedrez, R. Wirix-Speetjens, and L. Lagae "Experimental demonstration of nonreciprocal amplified spontaneous emission in a CoFe clad semiconductor optical amplifier for use as an integrated optical isolator." *Appl. Phys. Lett.,* 85, pp. 3980-3982 (2004).

[4] M. Vanwolleghem, W.F.H. Van Parys, D. Van Thourhout, R. Baets, F. Lelarge, O. Gauthier-Lafaye, B. Thedrez, R. Wirix-Speetjens, and J. De Boeck, "Experimental verification of a novel integrated isolator concept." in the Proceedings of 29^{th} *European Conference on Optical Communication,* postdeadline papers 6, pp.78–79, Rimini, Italy (2003).

[5] B. Jensen, in *Handbook of Optical Constants of Solids II*, E. D. Palik, ed., chapter 6 "Calculation of the refractive index of compound semiconductors below the band gap", pp. 125–149, Academic Press (1991).

[6] P. B. Johnson and R. W. Christy, "Optical constants of transition metals: Ti, V, Cr, Mn, Fe, Co, Ni, and Pd." *Phys. Rev. B,* vol. 9(12), pp. 5056–5070 (1973).

[7] G. S. Krinchik, and V. A. Artemjev, "Magneto-optical properties of Ni, Co, and Fe in the ultraviolet visible, and infrared parts of the spectrum." *Sov. Phys.-JETP,* vol. 26(6), pp. 1080–1085 (1968).

[8] A. K. Zvezdin, and V. A. Kotov, *table 10.1* in "Modern Magnetooptics and Magnetooptical Materials." Institute of Physics Publishing, Philadelphia, USA (1997).

[9] W.H. Meiklejohn, and C.P. Bean, "New Magnetic Anisotropy." *Phys. Rev.,* 105, pp.904-913 (1957).

[10] H. Shimizu, and Y. Nakano, "Fabrication and Characterization of an InGaAsP/InP Active Waveguide Optical Ioslator with 14.7dB/mm TE mode Nonreciprocal Attenuation." *J. Lightwave Technol.,* vol. 24(1), pp. 38–43 (2006).

[11] J. Piprek, "Semiconductor Optoelectronic Devices. Introduction to Physics and Simulation." *Academic Press - Elsevier Science,* pp. 89–90 (2003).

[12] C. Henry, R. Logan, F.R. Meritt, and J.P. Luongo, "The effect of intervalence band absorption on the thermal behaviour of InGaAsP laser." *IEEE J. Quantum Electron.,* vol. 19(6), pp. 947–952 (1983).

[13] F. Fiedler, and A. Schlachetzki, "Optical parameters of InP-based waveguides." *Solid State Electron.,* vol. 30(1), pp. 73-83 (1987).

[14] S. Verspurten, J. De Merlier, G. Morthier, D. Van Thourhout, and R. Baets, "All-optical 2R regeneration at 10 Gb/s in a MZI-configuration with one active arm." *Proceedings of the OSA Topical Meetings (Optical Amplifiers and Their Applications Integrated Photonics Research),* p.JWB 13, San Francisco, California, USA (2004).

[15] J. Piprek, P. Abraham, and J.E. Bowers, "Self-Consistent Analysis of High-Temperature Effects on Strained-Layer Multiquantum-Well InGaAsP-InP Lasers" *IEEE J. Quan. Electron.,* 36(3), pp. 366-374 (2000).

[16] J.N. Fehr, M.A. Dupertuis, T.P. Hessler, L. Kappei, D. Marti, P.E. Selbmann, B. Deveaud, J.L. Pleumeekers, J.Y. Emery, and B. Dagens "Direct observation of longitudinal spatial hole burning in semiconductor optical amplifiers with injection." *Appl. Phys. Lett.,* 78(26), 4079 (2001).

[17] J.C. Lagarias, J.A. Reeds, M.H. Wright, and P.E. Wright "Convergence Properties of the Nelder-Mead Simplex Method in Low Dimensions." *SIAM Journal of Optimization,* 9(1), pp. 112-147 (1998).

[18] L.A. Coldren, and S.W. Corzine, "Diode Lasers and Photonic Integrated Circuits." *Wiley, New York* (1995).

[19] M. Takenaka, and Y. Nakano, "Proposal of a Novel Monolithically-Integratable Optical Waveguide Isolator." *in Proc. 11^{th} International Conference on Indium Phosphide and Related Materials, Davos, Switzerland*, pp. 298-292 (1999).

[20] K. H. J. Buschow, P. G. van Engen, and R. Jongebreur, "Magneto-optical properties of metallic ferromagnetic materials." *J. Magn. Magn. Mater.*, 38(1), pp. 1-22 (1983).

[21] "COMSOL, The Unifying Multiphsysics Simulation Environment." *http://www.comsol.com/*

[22] World Gold Council, "Properties of Gold." http:www.utilisegold.com/uses_applications/properties_of_gold/.

[23] T. Sourmail, "Near equiatomic FeCo alloys : Constitution, mechanical and magnetic properties." *Progress in materials science*, 50(7), pp. 816-880 (2005).

[24] R.W. Cross, S.E. Russek, S.C. Sanders, M.R. Parker, J.A. Barnard, and S.A. Hossain, "Size and Self-Field Effects in Giant Magnetoresistive Thin-Film Devices." *IEEE Trans. Magnetics*, 30(6), pp. 3825-3827 (1994).

[25] R. C. O'Handley, equation 2.45 in *Modern Magnetic Materials : Principles and Applications*, (Wiley-Interscience, New York, USA, 2000).

5

Monolithically integrated laser-isolator device

THE fundamental advantage of the amplifying waveguide optical isolator over the traditional garnet-based approach is that the isolator can straightforwardly be integrated with its laser source, in a monolithic way. In this chapter, we will focus on the development of such a monolithically integrated laser-isolator component.

The integrated laser-isolator device is realized in a buried heterostructure technology, in order to show an industrially viable process, as is motivated in the first paragraph of this chapter. We start our discussion with the design of the buried isolator layer structure. Next, we subsequently describe the integration process, the technological difficulties that have been encountered and the modifications done to overcome these issues. Finally, the characterization results on the integrated laser-isolator device are presented.

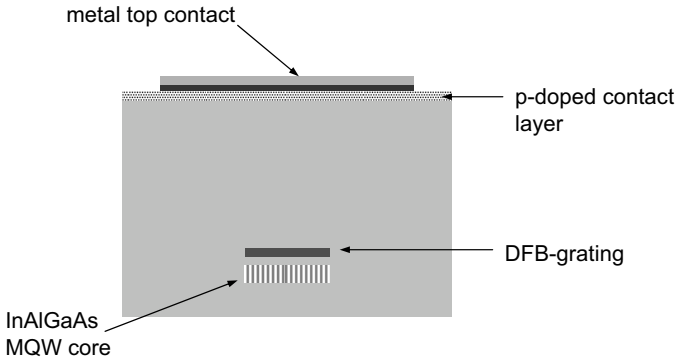

Figure 5.1: Schematic cross-section of a buried heterostructure laser.

5.1 Introduction

In the previous chapters the concept of a TM-mode amplifying waveguide optical isolator has extensively been elaborated. The combination of the development of a high TM-selective gain material, an appropriate choice of the ferromagnetic metal and a good understanding of the design rules of the layer structure has lead to the demonstration of a 2.1mm-long isolator, transparent in the forward propagation direction and showing 13dB loss in the backward direction, for a limited current injection level of 155mA. All of this has been realized in a shallowly etched ridge waveguide configuration. The next step in the development is to prove that such a waveguide structure can monolithically be integrated with a DFB laser source. DFB laser sources are most often based on buried heterostructure (BH) technology, for as BH lasers have merits of low threshold currents, high oscillation frequencies and stable beam pattern characteristics compared to ridge structure lasers. The cross-section of such a BH laser – more in particular a so-called etched mesa buried heterostructure – is schematically drawn in figure 5.1. The amplifying core is limited to a narrow strip, surrounded in both the lateral and the transverse direction by cladding material with a lower refractive index. As such, strong lateral and transverse confinement of the light is ensured.

In order to demonstrate an industrially viable fabrication process and to realize a system compatible device, it was decided to develop the integrated DFB laser-isolator component using a buried ridge stripe (BRS) technology, a technology which has already been transferred to an industrial application scale. A schematic layout of the integrated laser-isolator device is drawn in figure 5.2. The laser and isolator part differ only in the thickness of the InP top cladding, the presence of a grating layer and the composition of the contact metal.
Apart from the industrial compatibility of a buried isolator configuration and the possible reduction of the transparency current, this scheme has additional advantages. First of all, as the top surface of the structure is flat the alignment problems of the ferromagnetic metal – discussed earlier in section 4.1 – are avoided and it is possible to have a wide metal stripe contact. As pointed out in section 2.4, this ensures that the magnetooptic effect is high at magnetic remanence, hence avoiding

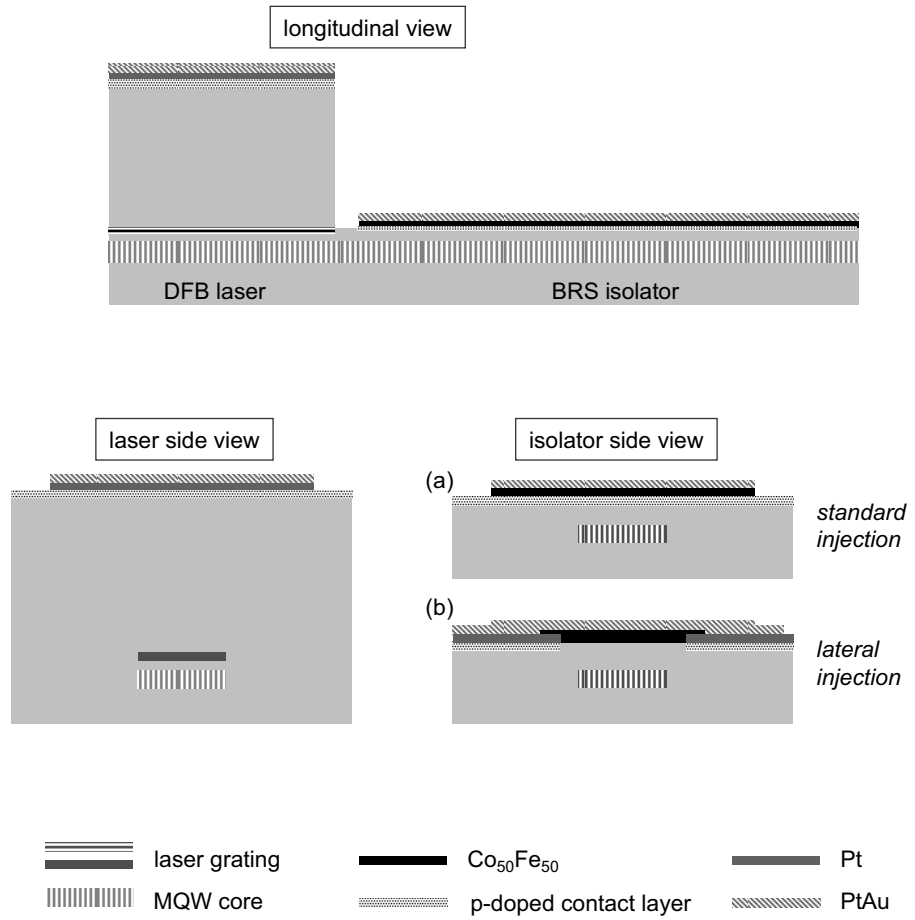

Figure 5.2: Schematic layout of the monolithically integrated laser-isolator device. The illustration at the top shows a longitudinal cross-section, the bottom figures depict a transverse cross-sectional view of the laser (right) and isolator (left) section. Layer structure (a) corresponds to a standard current injection scheme, while (b) shows a configuration for lateral current injection.

the need for an external magnet, either a permanent magnet or an electromagnet. Another issue, related to future applications, is that the BRS technology allows to include coupling adapters, enabling easy packaging of the component.

5.2 Design

As mentioned in chapter 3, the actual design of the isolator layer structure is done by means of 1D slab waveguide simulations. While this slab layer structure is a fairly good approximation of the shallowly etched ridge waveguide isolator, this is not at all the case for the buried ridge stripe device, as the high index contrast in the lateral direction between the amplifying core and cladding makes the structure

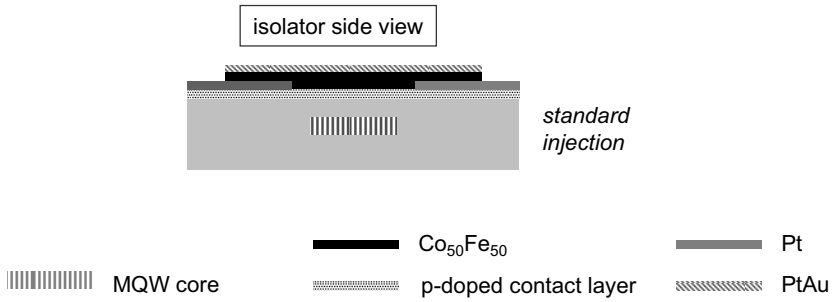

Figure 5.3: Schematic layout of the actual isolator section with the standard current injection scheme.

explicitly two-dimensional. Consequently, in order to really estimate the performance of the buried ridge stripe isolator, additional 2D simulations are inevitable. The design procedure is therefore as follows; first we design the isolator layer structure with the 1D slab solver and afterwards the influence of 2D effects is estimated using the 2D mode solver extended with the perturbation-based algorithm for magnetooptic waveguide simulation (see section 3.5). We distinguish two different current injection schemes for the BRS isolator: standard current injection (figure 5.2(a)) and lateral current injection 5.2(b)). The design of the corresponding layer structures is the subject of this section.

5.2.1 Standard current injection

The most straightforward buried ridge waveguide isolator structure is illustrated in figure 5.2(a). The cross-section is identical to the one of the ridge waveguide isolator except for the fact that the quantum well part is limited in the transverse direction and encapsulated in an InP medium. Furthermore, no waveguide ridge is etched. It has to be remarked that the actual layout of the fabricated isolators with the standard current injection scheme is different from what is shown in figure 5.2(a). A more correct schematic layout of the actual isolators is given in figure 5.3; for the metallization steps, the masks of the lateral current injection scheme have been used but without removing the ternary contact layer on top of the buried ridge. This implies that in a first metallization step a Pt film is deposited, with a window centralized around the buried waveguide core. The window in the Pt film is 2.0μm or 2.5μm wide corresponding to a ridge width of 0.6μm respectively 1μm.

From a 1D slab waveguide point of view, this BRS isolator structure is obviously identical to the ones described in chapter 4. Logically, the same 1D designs as the ones tabulated in table 4.9 are valid here. Simulation of the 2D cross section shows that the width of the etched mesa must be 1μm or less for lateral monomodality. In table 5.1 the theoretical performance figures of a BRS isolator are tabulated. The 2D numbers are found through 2D magnetooptic calculation on a 1μm wide BRS waveguide. In these simulations the current leakage through the p-n homojunctions at the side of the etched mesa has been neglected. This

Layer	Material	D4P (nm)	D3P (nm)
MO metal	$Co_{50}Fe_{50}$	50	50
Contact	$In_{0.54}Ga_{0.46}As$	15	15
Contact	$In_{0.81}Ga_{0.19}As_{0.41}P_{0.59}$	170	100
Cladding	InP	335	400
SCH	$In_{0.86}Ga_{0.14}As_{0.32}P_{0.68}$	33.5	11
Barrier	InAlGaAs	20	20
Well	InAlGaAs	10 x 9	10 x 9
Barrier	InAlGaAs	20 x 9	20 x 9
SCH	$In_{0.86}Ga_{0.14}As_{0.32}P_{0.68}$	13.5	4
Cladding	InP	1000	1000
Substrate	InP		
Parameter		D4P (nm)	D3P (nm)
Transparency current	1D	3.07	3.14
(mA/μm/dB)	2D	3.6	3.7
Length	1D	0.21	0.20
(mm/dB)	2D	0.19	0.19

Table 5.1: Design values and calculated performance figures of the buried $Co_{50}Fe_{50}$ isolator devices with the standard current injection scheme, for two different designs labeled D4P and D3P. In the D4P-calculations 4 parameters have been varied: both SCH layers the InP cladding and the quaternary contact layer, while for the D3P design only the first three have been modified and the quaternary InGaAsP layer thickness is fixed at a value of 100nm. The width of the buried core in the 2D simulations is set at 1μm.

theoretical modeling shows that a buried ridge stripe isolator configuration holds the promise of a significant improvement of the isolator performance. If we compare to the 2D-numbers of table 4.10 for a 2μm ridge waveguide, it immediately becomes clear that both the transparency current and the device length reduce in a BRS-configuration. The origin of this is the enhanced modal confinement in the pumped active region; $\Gamma_{ridge} \approx 0.14$, $\Gamma_{buried} \approx 0.17$. It should be stressed that current leakage in the buried case and absorption in the unpumped active region in the ridge waveguide case are not taken into account in our calculation, hence the actual transparency current levels might be higher.

5.2.2 Lateral current injection

The buried ridge isolator configuration allows for an alternative current injection scheme. In this configuration, current is injected through metal contacts located at the side of the etched mesa. The idea is that the absorbing InGaAs contact layer can then be etched away locally on top of the mesa, as is illustrated in the schematic cross-section of this structure in figure 5.2(b). This should result in a decrease of the modal loss of the TM guided mode, hence an improvement of the isolator performance. Again we have designed the isolator layer structure with the 1D slab solver and subsequently calculated the exact 2D cross-section. From the results tabulated in table 5.2, one can deduce that there is indeed an

Layer	Material	D4P-lat (nm)	D3P-lat (nm)
MO metal	$Co_{50}Fe_{50}$	50	50
Contact	$In_{0.81}Ga_{0.19}As_{0.41}P_{0.59}$	250	100
Cladding	InP	300	420
SCH	$In_{0.86}Ga_{0.14}As_{0.32}P_{0.68}$	40	10
Barrier	InAlGaAs	20	20
Well	InAlGaAs	10 x 9	10 x 9
Barrier	InAlGaAs	20 x 9	20 x 9
SCH	$In_{0.86}Ga_{0.14}As_{0.32}P_{0.68}$	18.5	3
Cladding	InP	1000	1000
Substrate	InP		
Parameter		D4P (nm)	D3P (nm)
Transparency current	1D	2.83	2.94
(mA/μm/dB)	2D	3.39	3.51
Length	1D	0.19	0.19
(mm/dB)	2D	0.17	0.18

Table 5.2: Design values and calculated performance figures of the buried $Co_{50}Fe_{50}$ isolator devices with the lateral current injection scheme, for two different designs labeled D4P-lat and D3P-lat. In the D4P-lat-calculations 4 parameters have been varied: both SCH layers the InP cladding and the quaternary contact layer, while for the D3P-lat design only the first three have been modified and the quaternary InGaAsP layer thickness is fixed at a value of 100nm. The width of the buried core in the 2D simulations is set at 1μm.

improvement of both the the transparency current and the isolator length, but it is it less than 10%.
This novel buried isolator scheme has been patented by our co-workers at Alcatel-Thales III-V Lab [1].

5.3 Technology

In this section we list the different processing steps in the fabrication of the monolithically integrated laser-isolator device. This fabrication has been done by Alcatel Thales III-V Lab.[1] The problems and subsequent technological improvements are discussed. The process flow is illustrated with longitudinal cross-section or top view images.

[1] In the framework of the European Union project IST-ISOLASER.

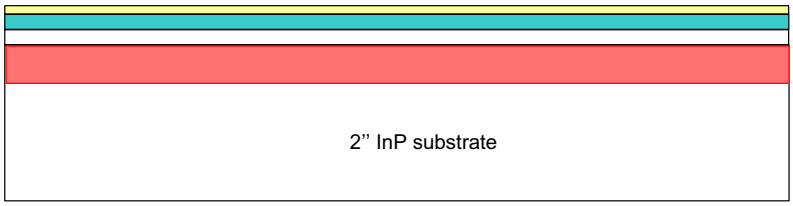

Figure 5.4: Step 1 - MOVPE growth of the basic structure: InP buffer + InAlGaAs MQW + InP spacer + InGaAsP guiding layer (for the grating) + InP cap layer.

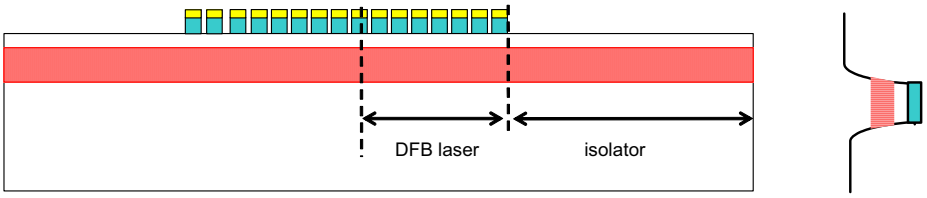

Figure 5.5: Step 2 - definition of the DFB grating: e-beam writing onto PMMA resist and subsequent ICP etching (depth 100nm).

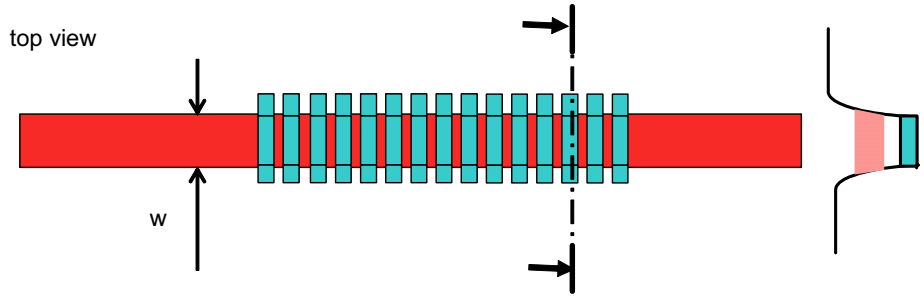

Figure 5.6: Step 3 - BRS stripe definition: dielectric deposition, lithography, plasma etching and soft cleaning. There is no planarizing regrowth on the grating before the stripe etching (= modification compared to a standard DFB process).

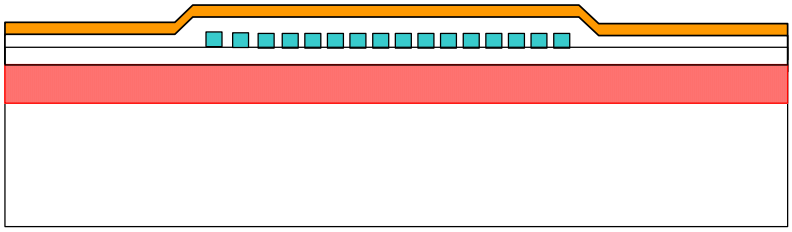

Figure 5.7: Step 4 - shallow BRS MOVPE regrowth of the isolator stripe: InP (thickness ≈ 400nm) + InGaAsP/InGaAs contact layer.

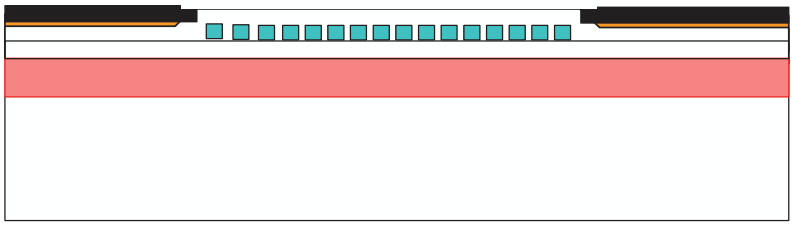

Figure 5.8: Step 5 - isolator capping layer: dielectric deposition, lithography, plasma etching and chemical etching.

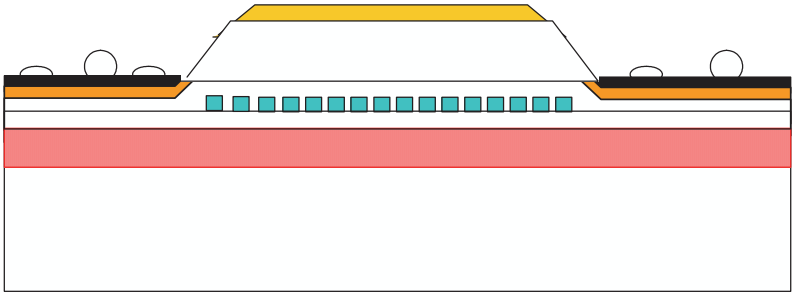

Figure 5.9: Step 6 - selective MOVPE re-growth for the DFB laser: InP + InGaAs contact layer.

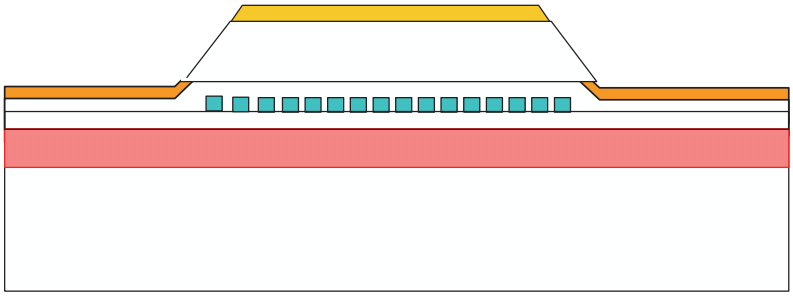

Figure 5.10: Step 7 - wafer cleaning: poly-crystal removal.

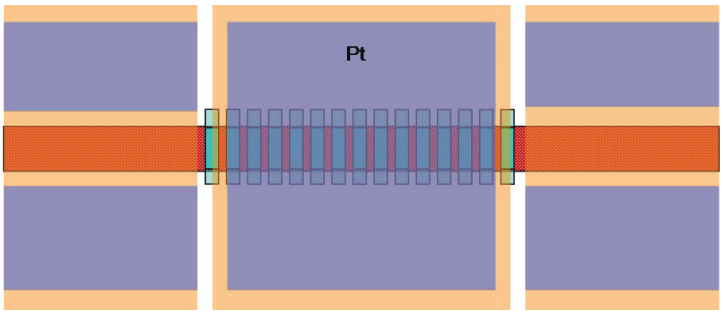

Figure 5.11: Step 8 - ohmic p-type side contact: platinum deposition.

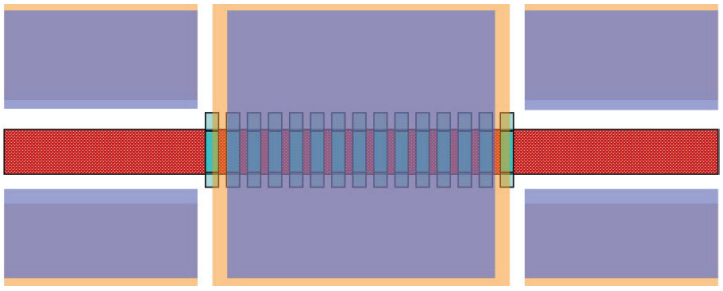

Figure 5.12: Step 9 - contact annealing and InGaAs contact layer removing (in the configuration of lateral current injection).

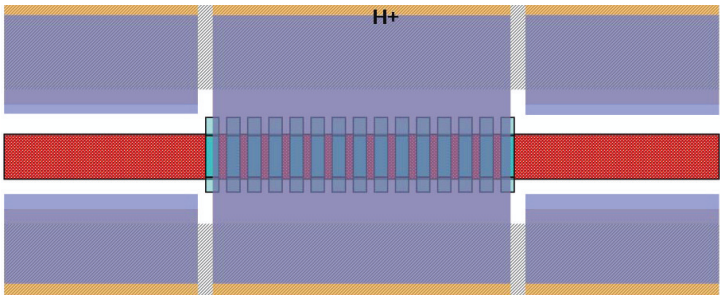

Figure 5.13: Step 10 - proton lateral electric isolation: lithography, implantation and cleaning.

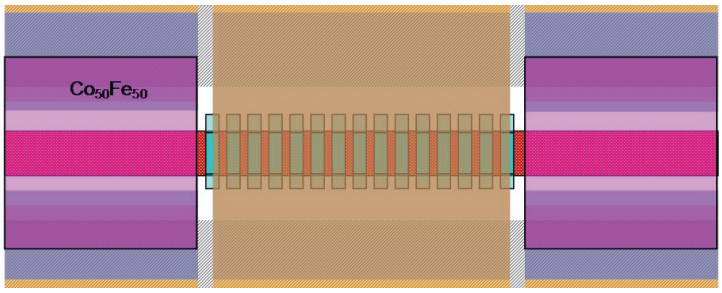

Figure 5.14: Step 11 - $Co_{50}Fe_{50}$ magnetooptic contact: lithography, deposition and lift-off.

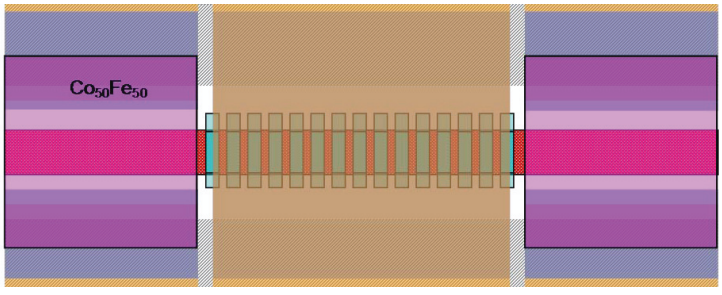

Figure 5.15: Step 12 - titanium-gold metallization and subsequent gold electroplating. Step 13 - wafer thinning and back side metallization.

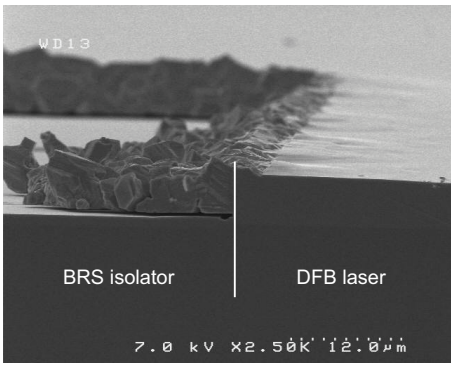

Figure 5.16: Polycrystalline InP grown onto the isolator section, not removed after lift-off step.

A first series of wafers has been processed according to this sequence. Based on the technological results, a number of process-flow adaptations have been made.

Alteration of the choice of dielectric for selective MOVPE regrowth (step 6) Non-uniform adhesion of the silicon nitride dielectric layer used to protect the isolator part during the selective area regrowth (SAG) of the laser section has been encountered. Consequently, large parts of the isolator section have been covered with InP and InGaAs material. The origin of this problem is the large area size of the isolator section; the same dielectric mask is traditionally used for SAG although with a smaller area. For this application silicon nitride is therefore not suitable and instead silicon oxide has been used in the next fabrication attempt.

Selective area etching instead of selective area regrowth Usually, in a selective area MOVPE growth process, all islands of InP polycrystal that have grown onto the dielectric mask can be lifted-off through chemical removing of the dielectric (processing step 7). In the fabrication of the integrated laser-isolator device, with the large difference in InP cladding thickness between laser and isolator part, a thick InP layer needs to be grown selectively at the laser section. This implies a large side contact area between the polycrystal grown onto the isolator section and the monocrystal (re-)grown onto the laser part. The immediate result is that at the edge between the laser and the isolator section an important amount of polycrystalline InP kept sticking to the InP monocrystal and was not removed by the chemical process in step 7 of the process-flow. This is illustrated in figure 5.16. From this observation it can be concluded that selective area regrowth is not the preferred technological method to realize the monolithically integrated laser-isolator configuration sketched in figure 5.2. Therefore it has been decided to modify the process-flow; an InP regrowth step is done at both the laser and the isolator section followed by selective area chemical etching to remove the excess material on top of the BRS isolator part. Translated in terms of the process sequence given earlier, this means that steps 5 to 7 have been altered.

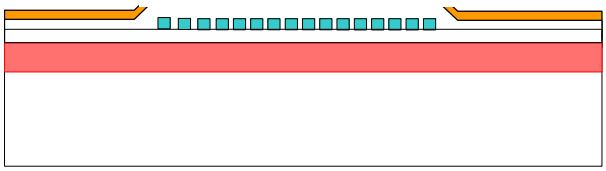

Figure 5.17: Modified step 5 - removal of the isolator contact layer at the laser section: dielectric deposition, lithography, etching and cleaning.

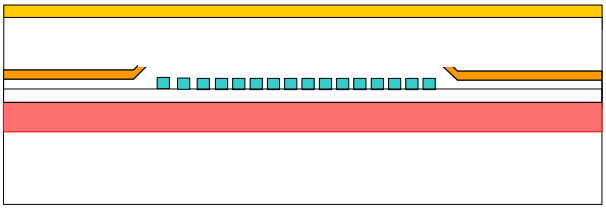

Figure 5.18: Modified step 6 - MOCVD re-growth: InP + InGaAs.

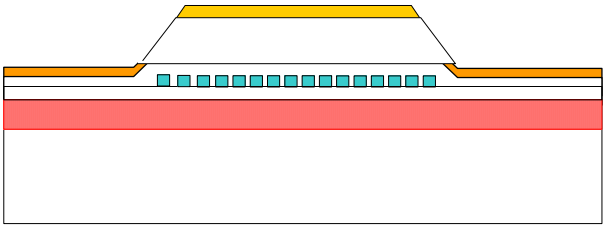

Figure 5.19: Modified step 7 - removal of the previous MOCVD regrowth at the isolator section: dielectric deposition, lithography, chemical etching and cleaning.

Platinum-gold metallization instead of titanium-gold Adhesion problems of the metal films have been encountered when using titanium-gold (TiAu) for the metallization. If instead platinum-gold (PtAu) is used, the adhesive quality is satisfying.

Modifying the process-flow as described has led to the realization of a series of wafers with monolithically integrated laser-isolator devices. A microscope image of a mounted laser-isolator device is given in figure 5.20. The DFB-laser part is wire-bonded to a high frequency (HF) contact to allow for direct modulation. The isolator section is wire-bonded through multiple bonds to a contact pad. The quality of the fabrication has been examined by observation of transverse cross-sections of the integrated laser-isolator component with a scanning electron microscope (SEM). The first row of images of figure 5.21 shows the cross-section of both parts before the metallization steps, the bottom row depicts the fully fabricated device. These pictures clearly illustrate the large difference in thickness of the upper cladding between both parts. No fabrication inaccuracies are visible on the cross-section images of the DFB-laser part and, as is discussed below, characterization confirms that the quality is satisfying. It is however a different story for

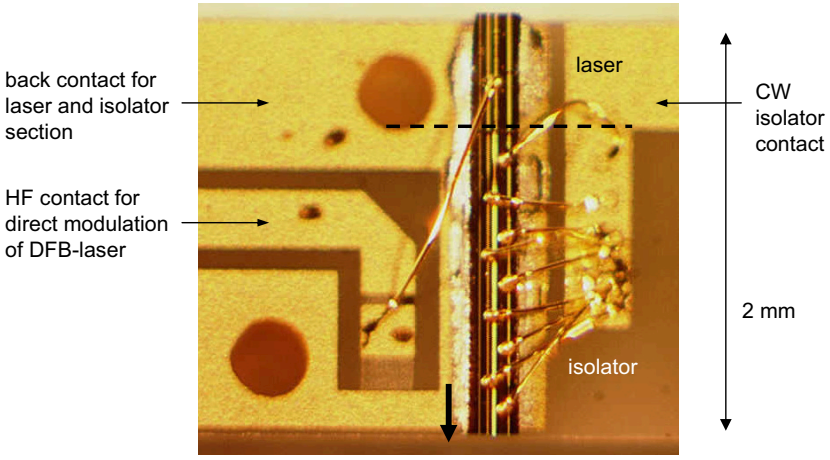

Figure 5.20: Microscope image of a monolithically integrated laser-isolator component, mounted on a high frequency submount.

the BRS isolator part. The planarization of the InP top cladding layer clearly is far from perfect, resulting in a non-flat lateral surface profile. A possible implication for the isolator performance is a decrease of the adhesion of the metal layers. Improved planarization could be achieved using well-known epitaxial solutions; a two-steps regrowth with intermediate etching.
When zooming in onto the isolator cross-section, as illustrated in figure 5.22, another, more serious issue becomes visible, i.e. the interface between the semiconductor and the metal is extremely rough. Given the fact that the magnetooptic Kerr effect is an interface phenomenon, this inaccuracy is expected to deteriorate the performance of the isolator part importantly.

In conclusion, the integration of a DFB-laser with a BRS isolator has been successfully realized – at least from technological point of view. A number of successive modifications to the initial process-flow has been made to enable the integration of a standard BRS section – with an upper cladding thickness of 3μm – with a shallow BRS isolator section with only 400nm of InP upper cladding. In the next section, the actual performance of this laser-isolator component is extensively discussed.

5.4 Characterization

5.4.1 DFB-laser section

We start this section by emphasizing the difference between the fabrication of the integrated DFB-laser section and a standard DFB-process; no planarizing regrowth step has been performed onto the grating before the buried ridge definition and etching (step 3). This step has been dropped in order to retain full control over the thickness of the upper cladding layer of the isolator during the first full wafer regrowth (step 4).

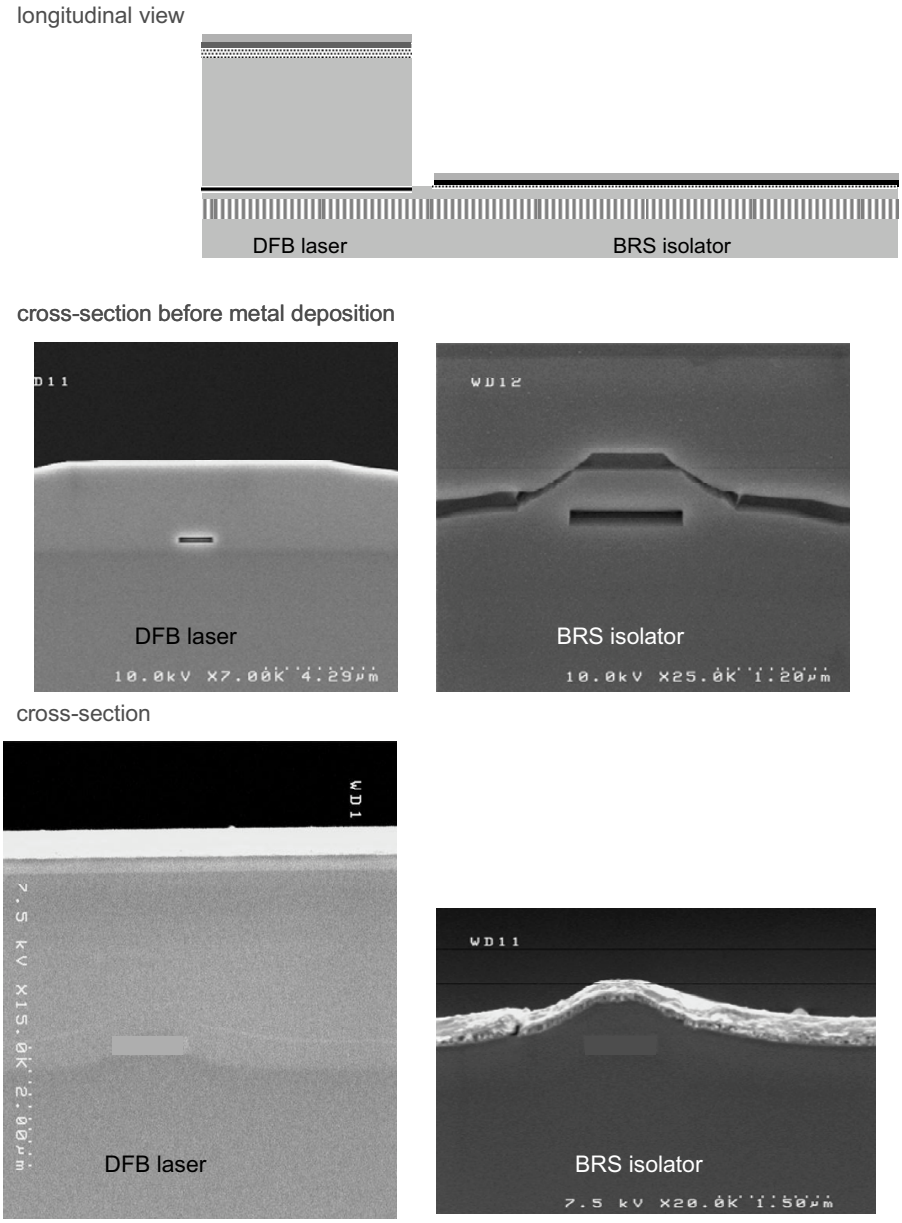

Figure 5.21: SEM images of the monolithically integrated laser-isolator device. Lateral cross-sections of the laser and isolator part illustrate the quality of the fabrication.

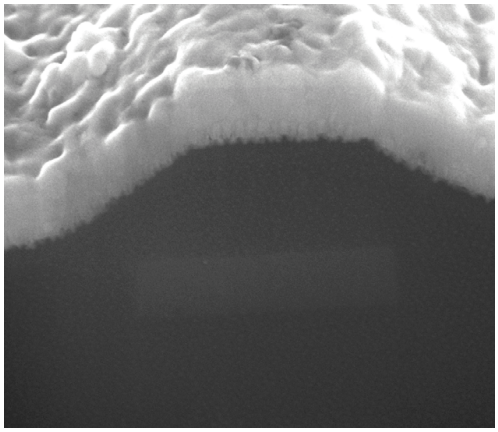

Figure 5.22: SEM-picture of a detail of the cross section of the BRS isolator, illustrating the non-flat surface and the large roughness of the metal-semiconductor interface.

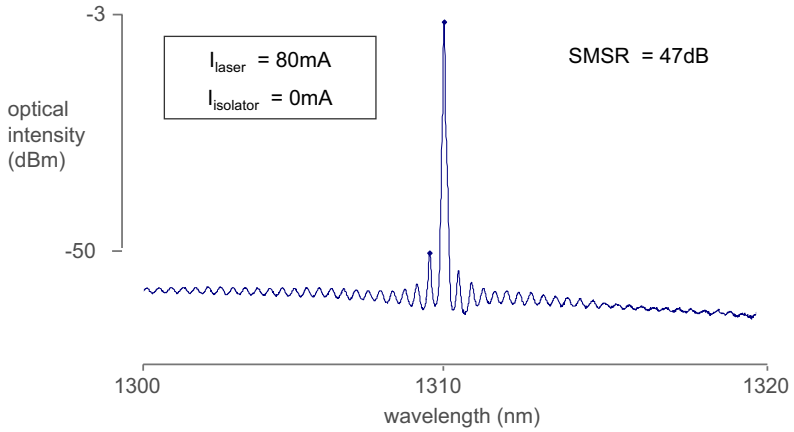

Figure 5.23: Emission spectrum of the DFB-laser section at a bias current of 80mA at 25°C. An optical intensity of -3dBm coupled to a monomode fiber combined with 47dB side mode suppression has been observed.

Despite this modification, good and reproducible performance of the DFB-laser section has been experienced. The characterization has been done by detection of the optical signal at the DFB-laser facet of the integrated laser-isolator component. Lasing has been observed at 4 different emission wavelengths – 1296nm, 1303nm, 1310nm and 1318nm at 25°C – corresponding to different grating pitches. These experimental emission wavelengths match to the calculated values. Longitudinal single mode emission with side mode suppression ratios (SMSR) higher than 33dB and up to 47dB has been observed, as illustrated in figure 5.23 where the emission spectrum of a single mode laser at a bias current of 80mA is shown. Besides, despite the absence of a rear facet anti-reflection coating a good yield has been obtained; 17 out of 33 of the tested lasers emitted longitudinally monomode.

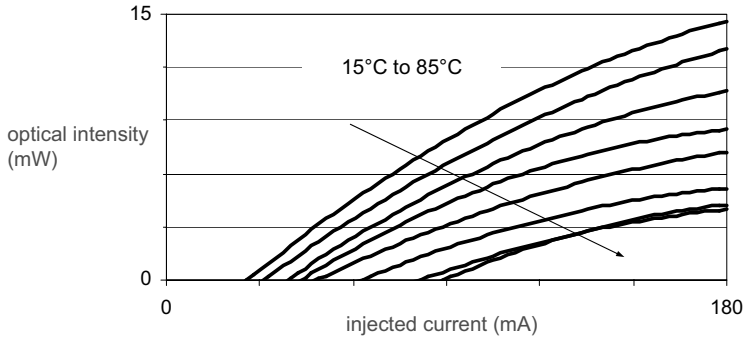

Figure 5.24: Emitted laser power versus injected current for a range of operation temperature values. The optical intensity is detected with a photo diode at the laser facet of the integrated laser-isolator component.

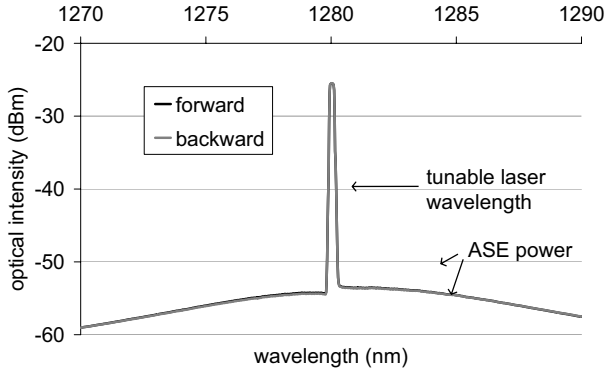

Figure 5.25: Transmission experiment on a stand-alone BRS isolator. Forward and backward signal coincide meaning that no non-reciprocal effect is observed.

Furthermore, as is shown in figure 5.24, the DFB-laser operates up to 85°C and high output intensities – more than 12mW or 10.8dBm at 25°C – have been demonstrated.

5.4.2 BRS isolator part

Before focussing on the integrated laser-isolator device, we wanted to estimate the quality of the isolator part. Therefore, stand-alone isolators, obtained from the laser-isolator component by cleaving off the laser section, have been characterized.
Optical transmission experiments have been performed on these buried isolators, an example of which is shown in figure 5.25. The injected current equals 280mA on a device with a length of 1mm. The tunable laser power was set at 6dBm. The conclusion that can be drawn from this plot is that the 'forward' and 'backward' signal – actually positive and negative lateral magnetization – coincide perfectly, or, in other words, that no non-reciprocal effect can be observed. This has been

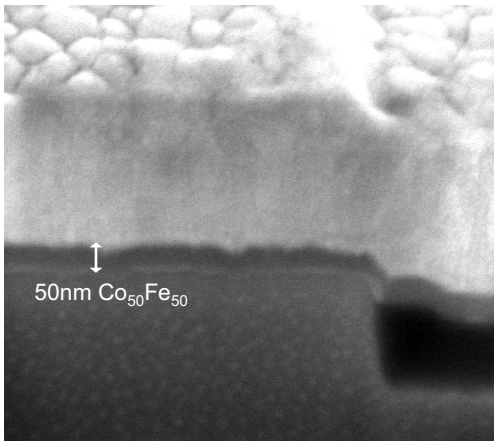

Figure 5.26: SEM-image of a detail of the cross section of a ridge waveguide isolator, illustrating that the different layers in the metal contact can be distinguished.

confirmed by measurements of the amplified spontaneous emitted light under magnetization reversal, as is illustrated below in figure 5.28(a). On the positive side, the transmission experiment of figure 5.25 is a prove of amplification of the light traveling through the device, indicating good waveguiding quality and successful current injection into the buried quantum well core.
To gain insight in the nature of the failure of the magnetooptic effect, a series of experiments have been undertaken. In addition to the bad metal-semiconductor interface quality, the SEM-image of a detail of the isolator cross-section (figure 5.22) learns that the different metal layers forming the metal contact – Pt, PtAu and $Co_{50}Fe_{50}$ – cannot be resolved, which indicates that the $Co_{50}Fe_{50}$ and PtAu layers are intermixed. As a reference, in figure 5.26 a SEM image of a ridge waveguide isolator cross-section is given, where the different metal layers can easily be distinguished.

The point of intermixing of the metals in the contact has further been examined through secondary ion mass spectroscopy (SIMS). This technique uses the process of secondary ion formation by bombarding the surface with a highly collimated beam of (primary) ions. The surface emits material, a fraction of which is ionized. These secondary ions are detected with a mass spectrometer to determine the composition of the surface. The result of a SIMS experiment, with a lateral resolution of 20μm on the isolator surface, is depicted in figure 5.27. It shows that both iron (Fe) and cobalt (Co), the two elements of the ferromagnetic metal film, are indeed present, but it is not possible to quantify the concentration of these elements on the basis of this experiment. It can be deduced that the concentration of Co and Fe is high between the surface (depth = 0μm) and a depth of 420nm into the material. However, the ferromagnetic layer should only be 50nm in thickness and should be located at a depth of approximately 400nm – the thickness of the PtAu layer deposited on top. This is a clear indication of the intermixing of the $Co_{50}Fe_{50}$ film with the PtAu and confirms the assumption made on the basis of the SEM-image (figure 5.22). A positive conclusion that can be made from

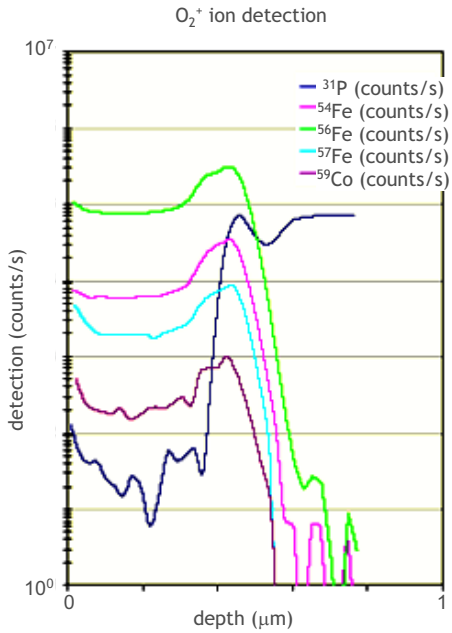

Figure 5.27: Secondary ion mass spectroscopy of the BRS-isolator surface.

the SIMS measurement is that the metal concentration rapidly drops at the depth where phosphor (P) is found, indicating only a minimal diffusion of metal into the semiconductor layers. Besides, the fact that the metal concentrations of Co and Fe are actually different from zero is likely to originate from the non-flat lateral surface and large surface roughness of the metal-semiconductor interface rather than to be an indication of diffusion of metal into the semiconductor layers.

As the intermixing of the ferromagnetic metal with the PtAu contact layer might deteriorate the magnetic properties of the structure the magnetization of the BRS-isolator has been investigated via alternate gradient force magnetometer (AGFM) measurements. These experiments confirm the absence of a magnetic signal – less than 0.5μemu has been observed. It can therefore be concluded that the accidential mixing of the contact metals is probably the main cause for failure of the isolator.
If this is truly the origin, a component on which no PtAu top layer has been deposited should perform better. AGFM measurements on a sample with isolators of this type indicate the presence of a magnetic signal, but the magnitude is 20 times lower than the expected value – 6.5μemu instead of 120.0μemu. Add to this the fact that the TM-polarized ASE has a flat response to a changing magnetic field, as is illustrated in figure 5.28(b) and that on a SEM image of a cross-section no $Co_{50}Fe_{50}$ is visible and it can be concluded that during the end stages of the process-flow the majority of the $Co_{50}Fe_{50}$ film has accidentally been removed, leaving only some $Co_{50}Fe_{50}$ at random positions on the sample.

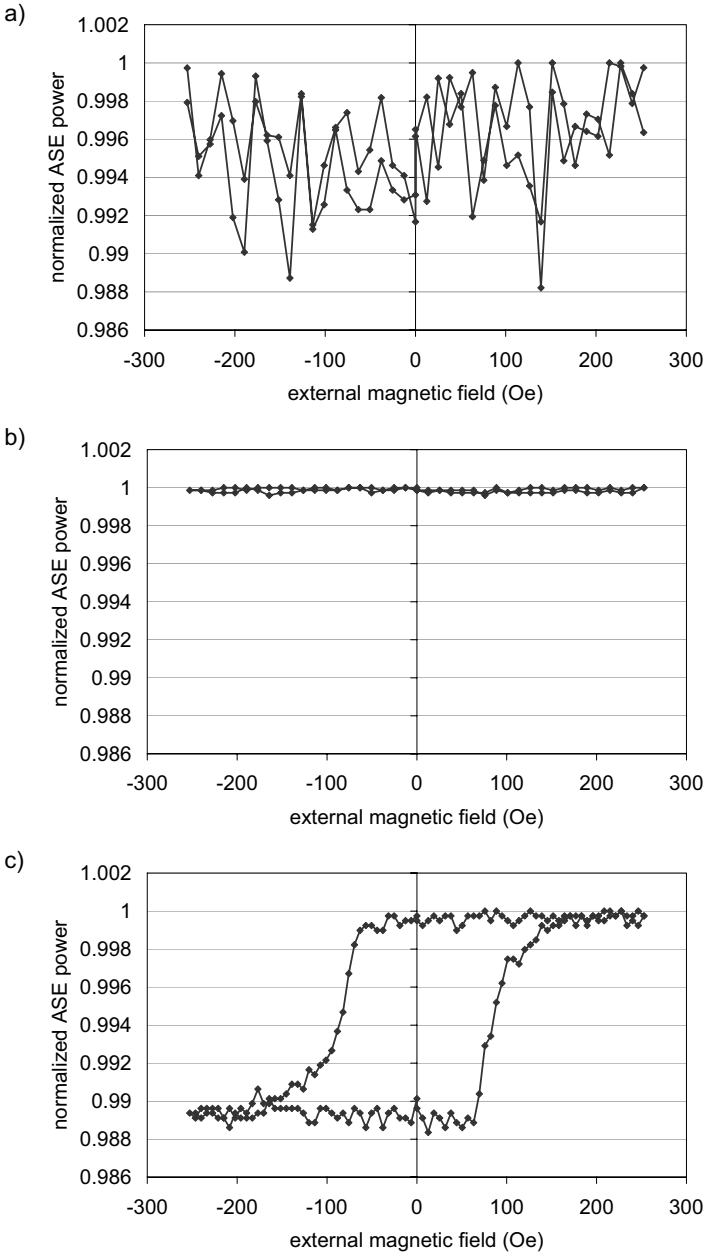

Figure 5.28: Detection of the emitted amplified spontaneous emission (ASE) as a function of an externally applied lateral magnetic field for (a) a fully processed sample, (b) a sample without PtAu contact deposition and (c) a sample with CoFe redeposition. Only in the (c)-case the magnetooptic Kerr effect can be observed.

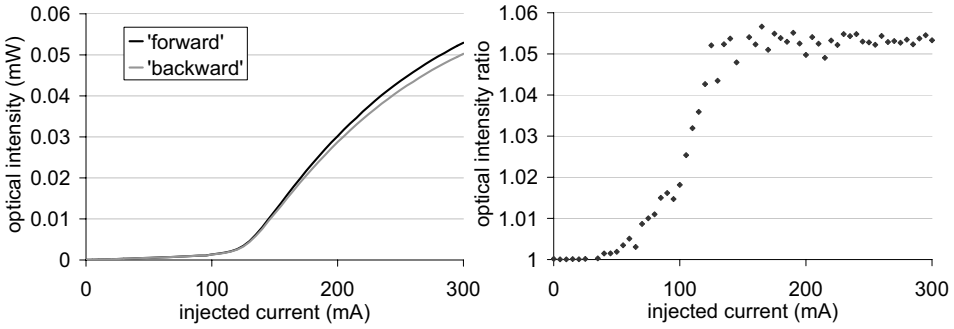

Figure 5.29: Non-reciprocal lasing experiment on a stand-alone buried isolator. The left picture shows the evolution of the output power with increasing bias current for forward and backward propagation. The right graph gives the corresponding power ratio. The ratio of 1.053 corresponds to an optical isolation ratio of 0.91dB/mm.

The logical next step was to repeat the deposition of the ferromagnetic metal on samples without PtAu top layer.[2] The presence of a magnetooptic effect has been tested by evaluation of the emitted ASE while varying the externally applied magnetic field (see section 4.2.1.1). In figure 5.28 a comparison is being made of the outcome of these experiments in the three BRS isolator cases that have just been discussed. We remark that in these measurements the isolator sections of integrated laser-isolator components have been characterized instead of stand-alone isolators. Both perform essentially the same in these experiments as the injected current levels are low compared to the transparency value, hence the rear end of the isolator does not play a role.[3] The current injection equals 200mA, 100mA and 100mA in respectively cases (a), (b) and (c). The (TM-polarized) ASE power has been normalized to drop the (large) difference in absolute emitted intensity. The large amount of noise on the top graph is a result of the very low output power, seriously reducing the precision of the measurement data. These ASE-graphs show that only after repeating the CoFe deposition (case (c)) the optical intensity is significantly modified by the presence of a magnetic field. The hysteresis-shape response of the optical intensity to the magnetic field is clear evidence of the presence of the magnetooptic effect. This is the first (qualitative) demonstration of non-reciprocity on a buried isolator. Now, from this one measurement it is not possible to obtain quantitative data on the magnitude of the magnetooptic effect. Hence, short stand-alone BRS isolators of the (c) type have been cleaved for characterization with the non-reciprocal lasing technique (see section 4.2.1.2). Before

[2]It has to be remarked that at the time of doing this the equiatomic $Co_{50}Fe_{50}$ composition was not available in the sputter system, hence it was opted to go for $Co_{90}Fe_{10}$. Although this choice implies a significantly lower theoretical optical and magnetooptic performance, it should not hinder a proof-of-principle experiment.

[3]In practice the integrated laser-isolator components don't perform identical to stand-alone isolators in terms of the current injection. Current leakage to the DFB-laser section decreases the useful current in the isolator part. This however does only alter the quantitative measurement data, but doesn't affect the qualitative conclusions that can be drawn on the basis of figure 5.28. The electrical quality of the integrated laser-isolator device is discussed in detail in section 5.4.3

we proceed with the discussion of these experiments we remark that from the hysteresis graph of figure 5.28 information can be gathered about the magnetic quality of the deposited CoFe film. Indeed, the hysteresis has a squareness that is close to 1, which, keeping in mind the magnetic principles elaborated in chapter 2, indicates that the 100μm wide ferromagnetic film has a smooth lateral profile without serious cracks.
Figure 5.29 summarizes the results of a non-reciprocal lasing experiment on 495μm long stand-alone buried isolators on which the deposition of CoFe has been repeated. The ratio between forward and backward signal above threshold equals 1.053, which corresponds to an isolation ratio of 0.91dB/mm. The threshold current of 120mA corresponds to a forward transparency current of 88mA, extracted with the help of equation 4.2 with a calculated confinement factor of 0.171. According to 2D simulations of a $Co_{90}Fe_{10}$ BRS device with a D3P layer structure design, the theoretical isolation ratio is 3.5dB/mm combined to a transparency current of 37mA/mm.[4] Comparing these numbers to the experimental values indicate a discrepancy of the isolation by a factor 3.85 and a 4.85 times higher current. The increase of the transparency current is believed to result mainly from current leakage through the p-n homojunction at the side of the buried waveguide core. The combination of a lower isolation and a higher current, together with the very high variation of the performance among nominally identical devices, seems to indicate that the interface between the CoFe contact and the semiconductor material is of inferior quality. In any case, while it is a (minor) success that non-reciprocal lasing has been demonstrated, the experimental results show that a lot of work still needs to be done to obtain a competitive buried optical isolator.

5.4.3 Integrated laser-isolator component

In the previous sections the quality of the two parts of the integrated laser-isolator component has been assessed. Extensive experimental work has proven that the performance level of the DFB-laser section is high, but that alterations to the isolator section have to be made to achieve non-reciprocity. In this section we investigate some issues that are specific for the integrated laser-integrated device.

One of these aspects is the current injection in each of the two parts of the integrated component. Separate pumping of the laser and isolator section is obtained by introducing a gap between the laser gold-contact and the isolator CoFe-contact. This is illustrated in the electron microscope image of figure 5.30, showing a top view of the interface region between both sections with at the top of the picture the laser and below the isolator. The electrical behavior – the I-V relationship – of the isolator section of the integrated device has been investigated experimentally in each of the three improvement stages mentioned earlier: the original processing, devices without PtAu contact deposition and non-reciprocal sections with CoFe redeposition. Remember from section 5.4.2 that only on the last class of devices non-reciprocity has been demonstrated. The corresponding I-V plots are given in figure 5.31. These graphs clearly show that only in the second case, without PtAu contact, the I-V relationship is perfectly diode-like, as it should be. In the two

[4]This should be an underestimate, as the waveguide cladding is not a flat 400nm layer, but instead is narrower at the side of the buried core (see figure 5.21).

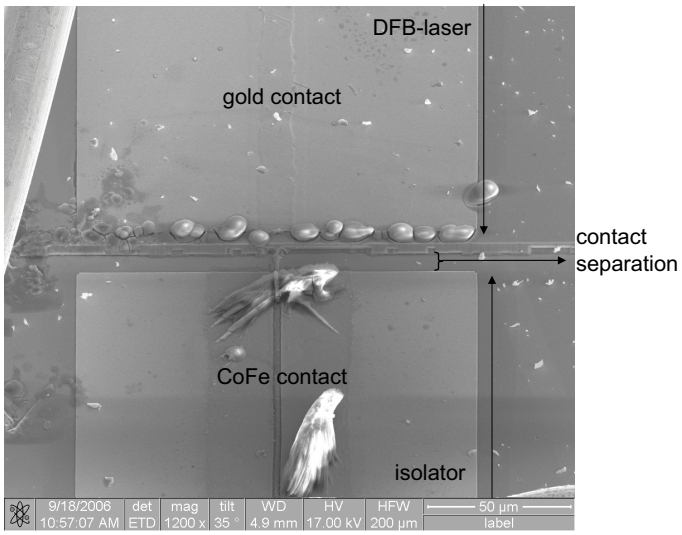

Figure 5.30: Electron microscope image of the integrated laser-isolator device (top view), illustrating the contact separation of the two subcomponents.

other cases the metal deposition seems to cause a current leakage path. We can exclude current leakage to the laser section as in this case the I-V characteristic would remain diode-like. Instead, the deteriorated electrical quality can only be attributed to current leakage over the p-n homojunction at the side of the waveguide core. Question remains why the deposition of an extra metallization layer, either PtAu or CoFe, enhances this current leakage. This can only be caused by an increase of the resistance of the current path through the laser diode with respect to that across the homojunction. Correction of this phenomenon requires a more detailed study of the isolator metal contact. Furthermore, it has been observed that on stand-alone buried isolators with CoFe redeposition, the leakage path becomes less dominant and the CoFe-contacted section has a diode-like I-V plot with the correct voltage jump of 0.95V at the onset of the current injection. This seems to indicate that the leakage paths are localized at certain positions along the isolator section. The inferior contact quality of the isolator section directly results in the degradation of its function as a semiconductor optical amplifier for the optical mode emitted by the DFB-laser section.

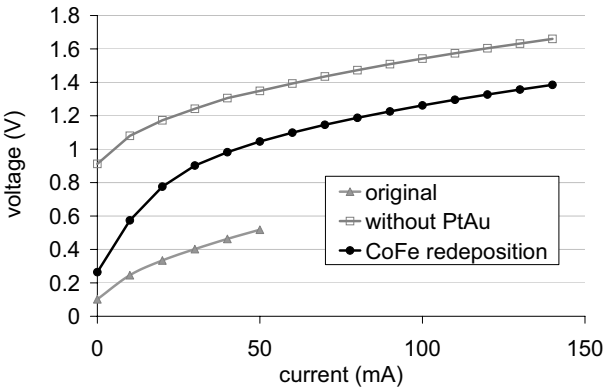

Figure 5.31: Electrical performance of the integrated isolator section. The different graphs correspond to the different stages of the development. Only on the 'CoFe-redeposited' samples non-reciprocal absorption has been demonstrated.

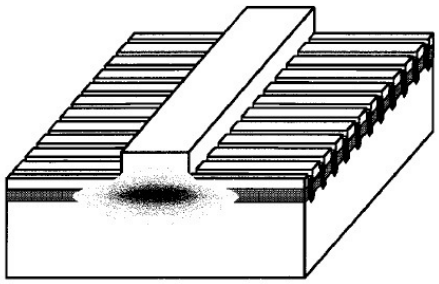

Figure 5.32: Schematic device geometry of a ridge waveguide laser with lateral gratings, providing the optical feedback mechanism. The overlap of the optical wave with the lateral grating is illustrated by the calculated intensity profile on the front facet (after [3])

5.5 Conclusion

This chapter was devoted to the development of a monolithically integrated laser-isolator device. In order to demonstrate the industrial viability of the component, we have opted for a standard DFB-laser integrated with a buried optical isolator scheme. Simulations show that, thanks to the high lateral contrast in such devices, the guiding core width remains limited to 1μm, which lowers the forward transparency current of the isolator. The fabrication of the integrated device has been done in the industrial environment of Alcatel-Thales III-V Lab, and after a series of process modifications, two wafers of monolithically integrated laser-isolator components have been completed. The DFB-laser part was shown to be of good and reproducible quality. For the isolator section, it took us additional study and subsequent processing adaptations before non-reciprocity could be demonstrated. Even then, the performance level is limited. Moreover, the electrical pumping of the isolator section of the integrated device suffers from current leakage phenomena, obstructing the demonstration of the actual monolithically integrated laser-isolator component. As such, it is expected that only extensive investigation of the metal-semiconductor interfaces and the laser-isolator contact separation can solve these problems and enhance the performance.
One possibility to overcome the issues of the buried integrated laser-isolator component is to develop an integration scheme on the basis of a ridge waveguide isolator. A promising configuration for the laser part is a DFB-laser formed by a gold-contacted ridge waveguide with a lateral grating, defined with focussed ion beam (FIB) lithography [2], as illustrated in figure 5.32.

Bibliography

[1] A. Accard, and B. Dagens, "Optical device with integrated semi-conductor laser source and integrated optical isolator." *United States Patent 20070064753*, (2007).

[2] H. König, S. Rennon, J.P. Reithmaier, A. Forchel, J.L. Gentner, and L. Goldstein, "1.55μm single mode lasers with complex coupled distributed feedback gratings fabricated by focused ion beam implantation," *Appl. Phys. Lett.*, 75, pp.1491-1493 (1999).

[3] S. Rennon, L. Bach, J.P. Reithmaier, and A. Forchel, "Complex Coupled Distributed-Feedback and Bragg-Reflector Lasers for Monolithic Device Integration Based on Focused-Ion-Beam Technology." *IEEE J. Sel. Top. Quantum Electron.*, 7(2), pp.306-311 (2001).

6

Alternative applications of non-reciprocity

IN this chapter we investigate alternative non-reciprocal metal-clad waveguide configurations. The knowledge acquired in the previous chapters is used as the basis for this study. We subsequently discuss ring resonator-based isolator structures and passive non-reciprocal waveguide devices.

6.1 Ring resonator-based non-reciprocal devices

In a standing wave cavity, like a Fabry-Pérot cavity, it is not possible to enhance the magnetooptic effect by exploiting resonance in the cavity, because light travels the same distance in forward and backward direction – or equivalently in positive and negative magnetization direction.[1] The situation is completely different in a traveling wave resonator like a ring resonator. In a ring resonator, light propagates only in one direction, clockwise or counterclockwise. With appropriate magnetization of the metal contact on top of the ring, resonating light feels the non-reciprocal loss shift several times and as such the magnetooptic effect is enhanced. In this section we subsequently discuss the simulation of this resonance phenomenon in two different ring resonator configurations, the design of a practical device and its characterization.

6.1.1 Operating principle

We start by discussing the operating principle of ring resonator-based isolators. Consider first a ring resonator with two bus waveguides, as illustrated in figure 6.1(a). The straight waveguides serve as evanescent wave input and output couplers to the ring shaped cavity. If a signal entering port A is on-resonance with the ring, that is if light that has traveled one roundtrip through the ring is in phase with the incoming light, it will exit the structure through port C, called the drop port. In the off-resonance case port B is the output port, called the pass port. Resonance can be seen as the wavelength of the light that fits into the ring, or in other words, that the length of the ring equals an integer number of modal wavelengths. The parameters that determine a reciprocal ring are the power coupling coefficient κ, describing the coupling of the light between straight waveguide and ring, the (possibly complex) effective index of the guided mode and the length of the ring. The ring can be made non-reciprocal if part of the ring waveguide is covered with a laterally magnetized magnetooptic material, in our case a ferromagnetic metal. Obviously the length of this part and the strength of the complex non-reciprocal effective index shift determine the performance. The ratio of the field at the drop port C to that at the input port A can be calculated as:

$$\frac{E_C}{E_A} = \frac{\kappa\sqrt{A_\pm}exp\left(-j\frac{\phi_\pm}{2}\right)}{1-(1-\kappa)A_\pm exp\left(-j\phi_\pm\right)}, \tag{6.1}$$

with

$$\begin{aligned} A_\pm &= exp\left(-\alpha_0\frac{L}{2}\right)exp\left(\pm\frac{\Delta\alpha}{2}\frac{L_{NR}}{2}\right), \\ \phi_\pm &= \frac{2\pi}{\lambda}n_{eff,0}L \pm \frac{2\pi}{\lambda}\frac{\Delta n_{eff}}{2}L_{NR}, \end{aligned} \tag{6.2}$$

and where we have assumed that the power coupling coefficient is identical for both ring-bus couplings. L is the ring circumference and L_{NR} the length of the

[1] This property has been used in the non-reciprocal lasing characterization method, as is elaborated in detail in appendix B.

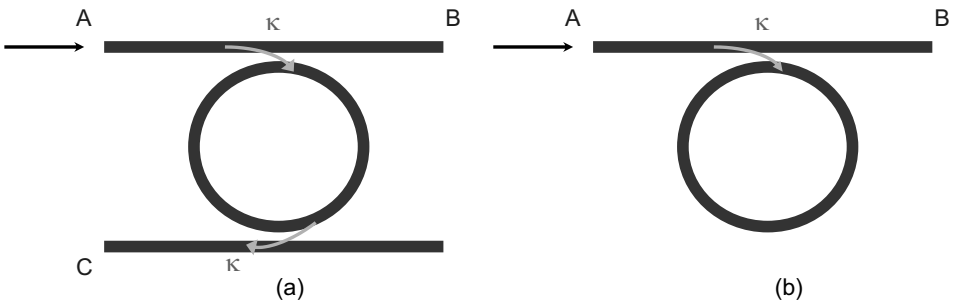

Figure 6.1: Schematic layout of a ring resonator (a) and an all-pass ring (b).

ring waveguide covered with a laterally magnetized ferromagnetic metal. λ is the operation wavelength and $n_{eff,0}$ -$j\frac{\alpha_0\lambda}{4\pi}$ the complex effective index of the unperturbed mode. Δn_{eff} -$j\frac{\Delta\alpha\lambda}{4\pi}$ is the complex non-reciprocal shift and the plus and minus indices correspond to forward respectively backward propagation. We remark that this equation is only valid if the denominator is larger than zero, i.e. below the threshold of the ring-shaped cavity. The optical transmission is obviously directly found as:

$$\frac{I_C}{I_A} = \frac{|E_C|^2}{|E_A|^2}. \tag{6.3}$$

The analogous equations between the pass port B and the input port A are :

$$\begin{aligned} \frac{E_B}{E_A} &= \frac{\sqrt{1-\kappa} - \sqrt{1-\kappa}A_{\pm}exp\,(-j\phi_{\pm})}{1-(1-\kappa)A_{\pm}exp\,(-j\phi_{\pm})}, \\ \frac{I_B}{I_A} &= \frac{|E_B|^2}{|E_A|^2}. \end{aligned} \tag{6.4}$$

From these equations the transmission spectrum of the ring resonator at both pass and drop port can be calculated. Before going into the operating principle of the ring isolator we remark that an alternative ring configuration is the one illustrated in figure 6.1(b), with only one bus waveguide. Such a component is called an all-pass ring. In the absence of loss in the structure all power is transmitted to the pass port. If the ring is not perfectly transparent, a resonance pattern can be observed in the output spectrum which originates from the fact that resonating light passes multiple times through the ring. The field equation for an all-pass ring is:

$$\frac{E_B}{E_A} = \frac{\sqrt{1-\kappa} - A_{\pm}exp\,(-j\phi_{\pm})}{1-\sqrt{1-\kappa}A_{\pm}exp\,(-j\phi_{\pm})}. \tag{6.5}$$

In figure 6.2 the transmission spectra at the drop and pass ports of a two-bus ring isolator and at the pass port of an all-pass ring isolator are given for forward (black) and backward (grey) propagation. In the backward direction C becomes

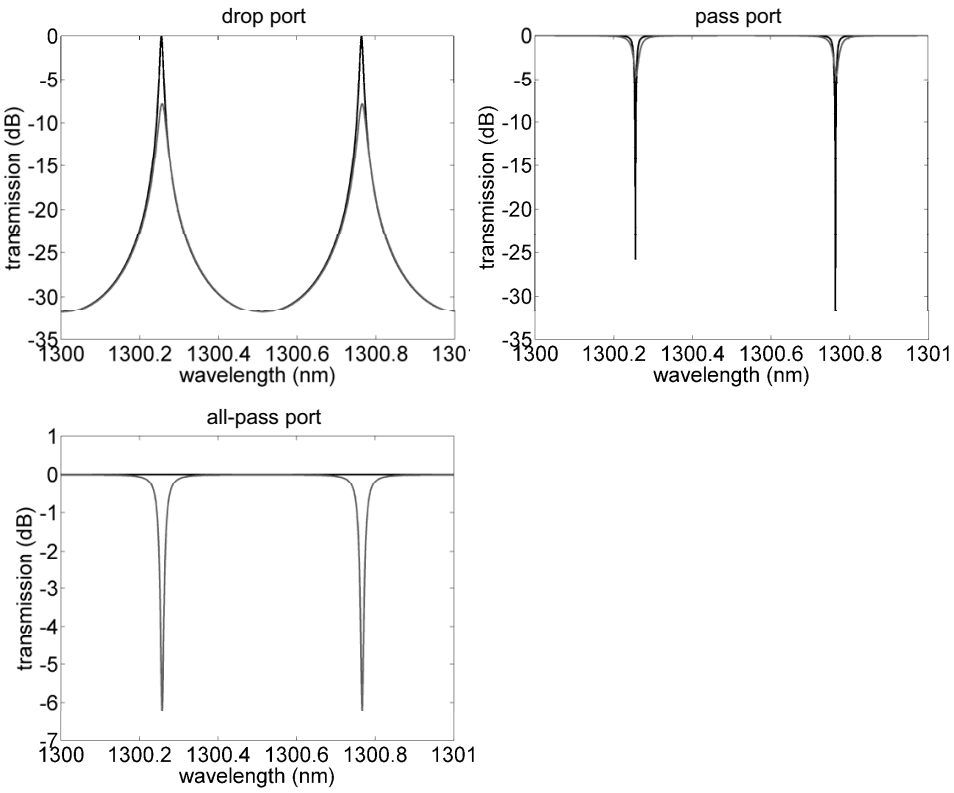

Figure 6.2: Transmission spectra at the drop and pass ports of a ring isolator and at the pass port of an all-pass isolator. The black curve corresponds to forward propagation and the grey to the backward direction.

the input and A the drop port or B the input and A the pass port. The ring parameters are given in table 6.1.1. α_0 has been chosen such that the ring is transparent in the forward propagation direction,[2] which will be the actual working point. The values for the non-reciprocal shift of the effective index correspond to that of the third generation straight waveguide isolators. The optical isolation is the difference in transmission between forward and backward light or between the black and the grey signal in figure 6.2. Clearly, the isolation is only significant at the resonance wavelengths, as in this case the light travels multiple times through the ring. Furthermore, the plotted spectra show that the isolation is mainly due to the non-reciprocal loss shift $\Delta\alpha$ and that the non-reciprocal phase shift Δn, which changes the resonance wavelength, has only a minor effect.
To understand the operating principle of a ring isolator, consider a wavelength at which the resonator is on-resonance. In figure 6.3(a) the transmission to the drop port is plotted as a function of the gain or loss inside the ring, expressed in decibel

[2]With transparency we mean that the material gain compensates all the internal loss in the ring-shaped cavity, but not the coupling loss to the bus waveguide(s).

Symbol	Value
L	1000μm
L_{NR}	100μm
$n_{eff,0}$	3.322
Δn_{eff}	4.73×10^{-5}
$\Delta\alpha$	14.8×10^{-4} μm^{-1}
κ	0.05

Table 6.1: Parameters of the ring isolators used in figure 6.2.

(dB) per roundtrip. This gain value doesn't include the coupling to the bus waveguide(s).[3] The only free parameter is the power coupling coefficient κ, which is varied between 1% and 10%. From these curves the principle of isolation enhancement in a ring resonator can be understood. Assume that the ring is electrically pumped to a level at which the loss per roundtrip for forward propagation is zero. This corresponds to full transmission at the drop port (at the resonance wavelength!). In this case the loss in the backward direction equals the non-reciprocal loss shift. The corresponding transmission, which depends on the coupling coefficient, is exactly the optical isolation. For example for a non-reciprocal loss shift of -2dB per roundtrip the transmission/isolation equals -10dB, -15dB or -27dB for a coupling of 10%, 5% or 1% respectively. In other words, due to the ring resonances the observed optical isolation is largely enhanced compared to a straight waveguide and the enhancement scales inversely with the coupling coefficient.
The same study can be done for the pass port of the two-bus resonator as illustrated in figure 6.3(b). For this port to operate as an isolator the backward loss should be close to zero to obtain low transmission, while in the forward direction gain should be provided in order to have full transmission of the signal. Another option is to operate in an absorbing mode by providing loss in the forward direction while the loss per roundtrip remains zero for backward propagation. This can obviously be done by reversing the magnetic field direction.
The pass port of an all-pass ring isolator has a similar operating principle as can be deduced from 6.3(c). The difference is that at 0dB gain / loss per roundtrip the transmission is complete and that the point of total attenuation varies with the coupling coefficient and is described by:

$$g[dB] = \frac{10}{ln(10)} ln(1-\kappa). \tag{6.6}$$

As such, in the all-pass configuration the non-reciprocal loss shift in the ring should be equal to this value of g, which scales inversely with the coupling coefficient.

In conclusion, designing a ring-based isolator comes down to the calculation of the correct length of the non-reciprocal section of the ring corresponding to a certain power coupling coefficient and – for the drop port operation – a required optical isolation level. An example is shown in figure 6.4, where the non-reciprocal length is plotted as a function of the value of κ for an isolation of 20dB, on the left

[3] That means that at 0dB the ring is at transparency and not at threshold.

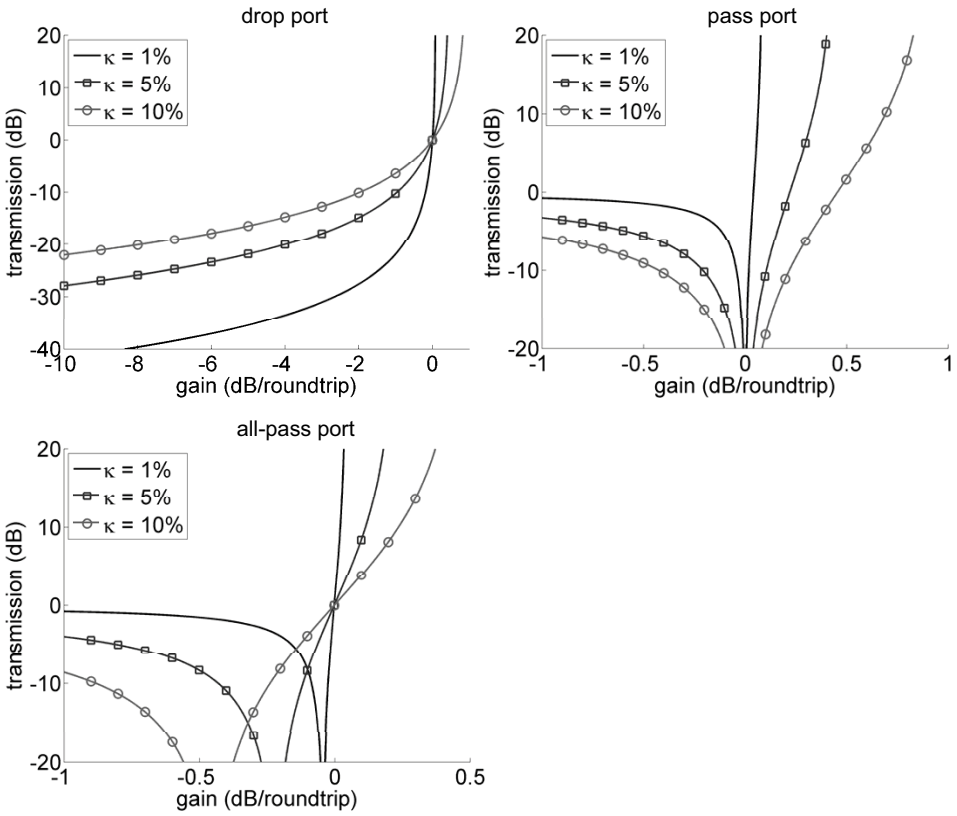

Figure 6.3: Transmission at drop and pass ports of a ring isolator at a resonance wavelength as a function of the gain/loss per roundtrip, illustrating the operating principle of a ring isolator. At the right hand side of the plot the gain is high enough to compensate the coupling loss to the bus waveguide(s) and the threshold of the ring cavity is reached.

for the drop port and on the right for the all-pass configuration. The device is assumed to be transparent in the forward direction and the optical mode parameters are the ones of table 6.1.1.

The (all-)pass port configuration is inherently much more efficient than the drop scheme in terms of the optical isolation enhancement. Its big disadvantage however is that off-resonance wavelengths are not attenuated, hence such an isolator protects only against back-reflected light with these wavelengths. The solution is to cascade a pass port configuration isolator with the drop port of a reciprocal ring resonator with the same resonance wavelengths.

6.1.2 Design

In this section we will translate the general concept of a ring isolator to a practical device. The idea is to fabricate the ring isolator as an all-active component based on the multiple quantum well tensile strained gain material discussed earlier in

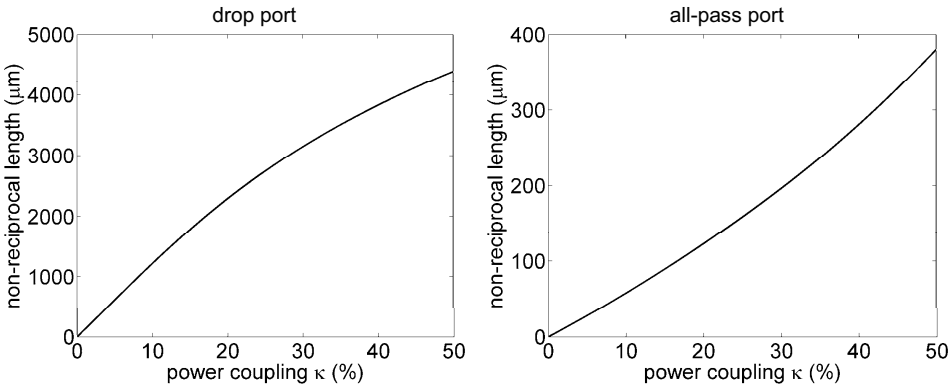

Figure 6.4: Length of the non-reciprocal section as a function of the power coupling coefficient κ corresponding to an optical isolation level of 20dB.

this work. Furthermore, the cladding thickness between the guiding core and the metal contact is the same for the entire structure and equal to the thickness optimized for a straight non-reciprocal waveguide. More in particular the ring isolator wafer material is the same as that of the third generation isolator demonstrators of chapter 4 with a layer structure as tabulated in table 4.9. While this approach implies extra loss in the reciprocal device parts and requires electrical pumping of the bus waveguides, it allows for simple fabrication and avoids active-passive integration and selective area etching/regrowth.

Apart from the optical isolation an important device parameter is the pump current required for transparency of the ring. As it is our purpose to obtain a proof of the principle, the sole design criterion for the injection current is that the ring can be brought to transparency with a realistic amount of current. Once the layer structure has been fixed, this amount of current depends on the length of the reciprocal part of the ring – contacted with a standard Ti/Au contact – the length of the non-reciprocal part of the ring – covered with a $Co_{50}Fe_{50}$/Ti/Au stack – and the radiation loss in the bend sections.
As explained later in this section the free spectral range of the resonator places an upper limit to the total length of the ring of a few millimeters. Keeping in mind the experimental results of chapter 4 and the fact that the internal loss of a Ti/Au covered waveguide is lower than that of a $Co_{50}Fe_{50}$ contacted waveguide, the current required to overcome the metal absorption of the ring should be lower than 200mA, even if the entire ring is covered with the ferromagnetic metal.
The intrinsic radiation loss that occurs in bend waveguides is known to decrease strongly with the bend radius [1]. Furthermore, the radiation loss is heavily dependent on the index contrast between the waveguide core and the side-cladding. As we don't want to etch the quantum wells to avoid large surface defects and the associated scattering loss, the index contrast of the isolator waveguide is small: 0.31% for a 300nm etched ridge waveguide with a third generation layer structure (see table 4.9). For this etch depth a 2μm wide ridge waveguide is TM-monomodal. With the aid of the commercial mode solver FIMMWAVE the rela-

tionship between the bend loss and the bend radius has been calculated, resulting in a lower limit on the bend radius of 150μm. The corresponding minimal ring circumference equals 0.94mm.

As elaborated in section 6.1.1 one of the main parameters that determine the optical isolation in a ring isolator is the power coupling coefficient κ. Remember that the required non-reciprocal length scales with this parameter, hence small values of κ are preferred. This can be obtained via evanescent coupling. Especially in the all-pass configuration the value of the coupling coefficient is important as it determines the roundtrip loss at which the dip in the transmission occurs. As we will elaborate in the next section the all-pass isolator structures have a racetrack geometry. In this type of resonator the 'ring' consists of a cascade of bend and straight waveguides and the coupling between the bus and the ring waveguide mainly happens in a straight section. For this section the simple theory of (symmetric) directional couplers can be used. More in particular we have applied the concept of supermodes. The effective indices of the symmetric ($n_{eff,+}$) and antisymmetric ($n_{eff,-}$) supermodi of the straight coupling section have been calculated with a 2D mode solver for a series of widths of the gap between the bus and the ring ridge waveguide. It has been assumed that the waveguides are electrically pumped to transparency, which would be the actual operation mode of the structure. With these effective index values the power coupling from bus to ring can immediately be calculated as [2]:

$$\kappa = \frac{1}{2} - \frac{1}{2} cos\left(\frac{2\pi}{\lambda}(n_{eff,+} - n_{eff,-})L\right), \tag{6.7}$$

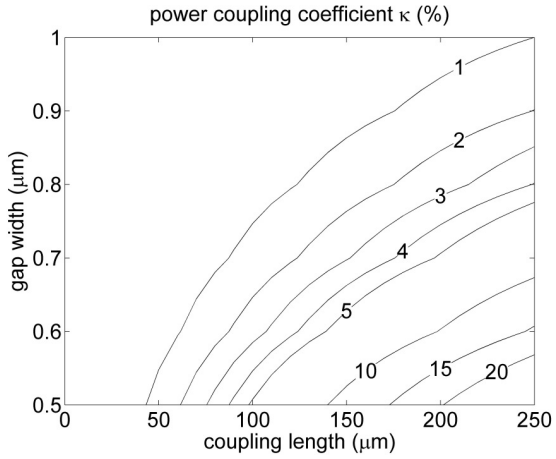

Figure 6.5: Power coupling coefficient κ as a function of the gap width and the length of the straight coupling section.

with L the length of the coupling section. In figure 6.5 the obtained power coupling coefficient κ is plotted as a function of the gap width and the length of the straight coupling section. Additionally there is some coupling between the bus waveguide and the bend sections of the ring. The correction on κ for this has

been calculated by using a cascaded coupler segment method [3], where the bend is segmented in a number of small parts each of which can be considered as a directional coupler. The extra coupling in the bend sections is up to a few percent.

Apart from the optical isolation and the transparency current the resonator is characterized by the free spectral range (FSR) and the full width at half of the maximum (FWHM) of the resonance peaks. The FSR is the distance between two resonance peaks on a wavelength λ or a frequency ν scale. The FSR of a ring resonator is expressed by:

$$FSR_\lambda = \frac{\lambda^2}{n_g L} \qquad FSR_\nu = \frac{c}{n_g L}, \tag{6.8}$$

with n_g the modal group index:

$$n_g = n_{eff} - \lambda \frac{dn_{eff}}{d\lambda}, \tag{6.9}$$

and c the speed of light in vacuum. For example, for a ring length of 1mm the free spectral range of the InAlGaAs-InP resonator isolator equals 90GHz. The FWHM – the spectral width at -3dB of the peak transmission is related to the FSR and can be calculated as [1]:

$$FWHM \equiv \Delta\nu_{-3dB} = \frac{FSR_\nu}{\pi}\left(\frac{1-(1-\kappa)A_\pm}{\sqrt{1-\kappa}\sqrt{A_\pm}}\right), \tag{6.10}$$

with κ the power coupling coefficient and $A_\pm$ defined as in equation 6.2. In figure 6.6 the relative FWHM – the ratio of the FWHM to the FSR – is given as a function of the gain per roundtrip for a number of power coupling coefficients. The FWHM of the resonator decreases as the loss reduces, and becomes zero if there is enough gain per roundtrip to compensate the power coupling to the bus waveguide, i.e. at threshold of the ring laser. Once the FSR and the power coupling coefficient κ have been fixed, the FWHM as a function of the ring loss can be read off such a graph. For a 1mm ring (FSR = 90GHz) with a κ-value of 10% the FWHM at forward transparency equals 3GHz. In a resonator the FWHM limits the maximal data rate the device is compatible with. Its value is related to the cavity photon lifetime τ as:

$$\tau = \frac{1}{2\pi\Delta\nu_{-3dB}}. \tag{6.11}$$

6.1.3 Contact lithography mask set

On the basis of the previous study we have designed and programmed a contact lithography mask set with a variety of two-bus ring isolators and all-pass ring isolators. To minimize reflections at the cleaved facets of the devices, the waveguides are tilted at an angle of 7 degrees with respect to the crystal axes. The ridge width of the straight waveguides has been set at 1.9μm, that of the bend waveguides at 2.1μm. In the racetrack resonators an offset of 0.2μm has been built in to improve the coupling between the straight and the bend sections. As explained before the

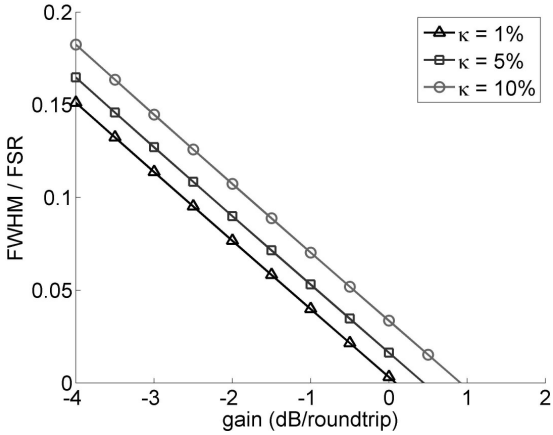

Figure 6.6: Ratio of the FWHM to the FSR as a function of the gain/loss in the ring resonator for power coupling coefficients κ = 1%, 5% and 10%.

lower limit on the bend radius equals 150μm. In addition, we have fixed an upper limit on the resonator length of 2.5mm – which corresponds to a FSR of 36GHz. Two types of all-pass resonators have been included, of which the schematic layout is depicted in figure 6.7. The grey areas are the reciprocal waveguide parts and the black sections are covered with the ferromagnetic metal, hence can be made non-reciprocal. The corresponding magnetization direction M is indicated on the figure. The first type, illustrated in figure 6.7(a), has a racetrack configuration with a straight non-reciprocal section. The power coupling coefficient has been varied between 1% and 20% by an appropriate choice of the gap between the bus and ring waveguides – with a minimum of 0.5μm – and the length of the straight section of the racetrack, as elaborated in the previous section. The corresponding length of the non-reciprocal section follows from equation 6.6:

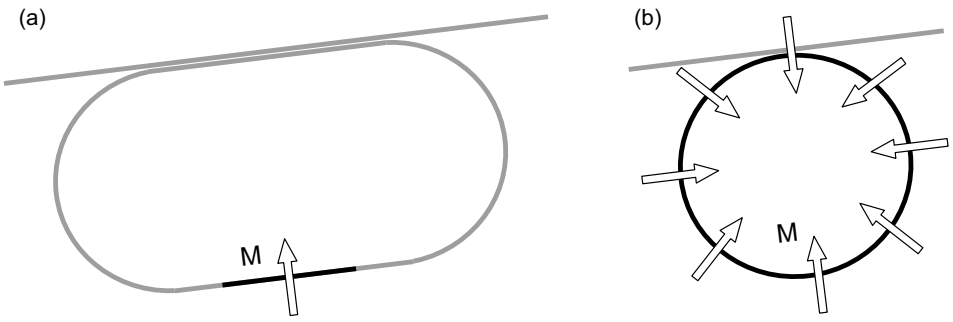

Figure 6.7: Schematic layout of the all-pass ring resonator structures included on the contact lithography mask.

$$L_{NR} = \frac{ln(1-\kappa)}{\Delta\alpha}, \tag{6.12}$$

once the non-reciprocal loss shift $\Delta\alpha$ is known. The second type of all-pass device is one where the complete ring is covered with a ferromagnetic contact. The corresponding required magnetization is radially oriented (see figure 6.7(b)) which can only be realized by integrating a ring-shaped (electro-)magnet on top of the resonator. This type of resonator structure can have a relatively high non-reciprocal loss shift per roundtrip – 3 to 11dB depending on the ring length – and is designed to operate as an unidirectional ring laser; because light traveling in one direction – clockwise or counterclockwise – has a higher internal loss than the counter-propagating light, only in one direction threshold is achieved. As a result, a laser signal is emitted at one single facet of the bus waveguide. The lasing direction can easily be switched by reversing the current flow in the electromagnet. Devices with a ring length varying between 630μm and 1885μm have been integrated on the mask.
The two-bus ring resonators have been designed to operate in the drop port regime. Remember from figure 6.3 that, unlike in the case of pass port operation, there is no zero in transmission for the backward propagating light. Instead, the optical isolation increases with increasing length of the non-reciprocal section, hence this should be maximized. Furthermore, as we want to generate the magnetization by applying an external magnetic field, we prefer a racetrack resonator with on one of the straight sections a ferromagnetic metal contact. The schematic layout of these ring isolators is sketched in figure 6.8. The bend radius has been varied between 150μm and 250μm and resonator lengths between 1100μm and 2500μm have been included.

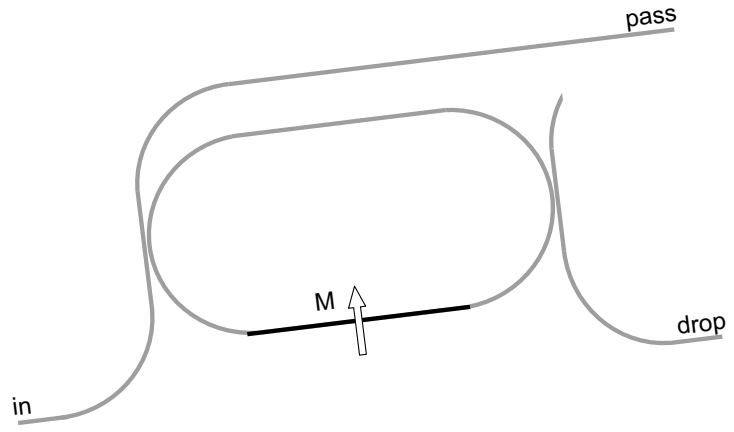

Figure 6.8: Schematic layout of the two-bus ring resonator structures included on the contact lithography mask.

Finally, some of the two-bus ring isolators and all-pass isolators have been placed in cascade to enable attenuation of back-reflected off-resonance wavelengths.

The contact lithography mask consists of 7 layers, corresponding to subsequent processing steps:

- mask layer 1: definition of the non-reciprocal waveguide sections
- mask layer 2: definition of the reciprocal waveguide sections
- mask layer 3: definition of the current isolation layer
- mask layer 4: definition of the second metallization pattern, for electrical contacting of the active waveguides
- mask layer 5: definition of the isolation layer between the waveguide metallization and the electromagnet metal strips
- mask layer 6: definition of the electromagnet metal pattern
- mask layer 7: definition of the pattern for electroplating

A detailed description of the resonator processing sequence with this mask set is given in appendix A. The ridge waveguide definition through etching is done with the metal contacts as the etch mask, a technique that has previously been applied for the straight waveguide isolators. The alignment between mask layers 1 and 2 is therefore a critical step. To deal with this, mask layer 2 overlaps with layer 1 at the non-reciprocal sections. Furthermore, the width of the ferromagnetic metal strips is chosen to be 0.4μm smaller than that of the strips defined by mask layer 2. This is illustrated in figure 6.9. In addition, as we want to electrically contact the bus waveguides separately from the ring, each device has two electrical contact paths defined by mask layer 4. Finally, the width of the electromagnet metal strips has been set at 5μm, which, according to the study of section 4.4, is the optimized value.

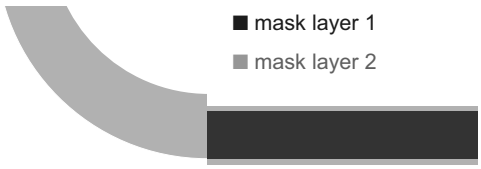

Figure 6.9: Illustration of the overlap between mask layers 1 and 2 to minimize the impact of misalignment.

6.1.4 Fabrication and measurements

With the contact lithography mask set and using the epitaxial wafer material of the third generation straight isolators, ring isolator test devices have been fabricated. The fabricated structures have been inspected by a scanning electron microscope (SEM). In figure 6.10 images of cross-sections at different positions along a ring waveguide are given. The left picture shows the coupling section of a two-bus ring isolator. The widths of the straight bus (left) and bend ridge waveguides (right) are in good correspondence with the design values. The gap between both waveguides is of good quality. One serious fabrication error is the fact that the

BCB current isolation layer is too thick. The implication is that the second metallization layer – light colored on the image – which enables current injection in the structures is almost interrupted at the waveguide ridges, which obviously deteriorates the current injection. This could be avoided by using a less viscous BCB composition. The image on the right of figure 6.10 depicts a cross-section of a non-reciprocal ring section. The additional metal layers with respect to the left picture are clearly visible and so is the electromagnet metal strip on top. Again, the second metallization layer is practically interrupted. Several other fabrication runs have been undertaken but all have failed, for a variety of reasons.

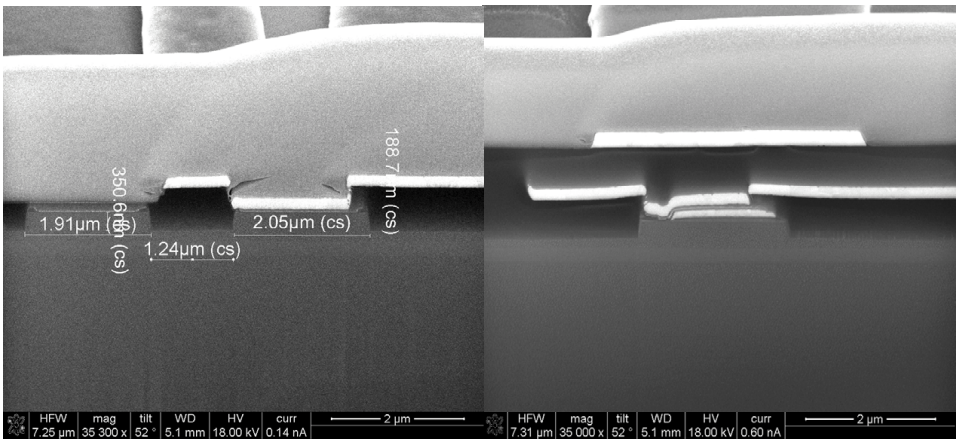

Figure 6.10: Electron microscope images of cross-sections of a ring resonator isolator, with on the left a coupling section and on the right the non-reciprocal part of the ring.

Initially the straight waveguide isolators included on the chip have been characterized in order to compare the fabrication quality with previous runs. The observed optical isolation is the same as that of earlier devices with the same epitaxial material, but the transparency current is a multiple of its former value, as expected on the basis of the SEM images. Next, ring isolator test devices have been characterized both based on their emitted ASE and by inspecting the transmission of a (wavelength tunable) laser signal. However, resonance phenomena have not been observed. This indicates that, despite high pump current levels – up to 700mA for the complete device – the ring remains far from transparency. We believe that this can be attributed to the fabrication error mentioned earlier.

6.1.5 Conclusion

In this section we have developed ring resonator-type isolators. In a drop port configuration its operation is based in the enhancement of the non-reciprocal loss shift in a traveling wave resonator. Using the pass port on the other hand results in a very large optical isolation at the resonance wavelength due to the difference in internal loss of forward and backward – or clockwise and counterclockwise – light in the resonator. The operating principle has been elaborated and all-active

ring-based isolators have been designed. A contact lithography mask set has been developed and used for the fabrication of the first test devices. However, due to a fabrication error the experimental proof-of-principle has not been achieved.

6.2 Passive non-reciprocal devices

An optical isolator is by definition a device which is optically transparent in the forward propagation direction (and absorbing in the opposite direction). This requirement of transparency implies that any internal loss must be compensated by a gain mechanism. In other words, a ferromagnetic metal-clad isolator inherently contains an amplifying core. In practice this limits the choice of an isolator material system to InP and related materials, which have been discussed so far in this work. However, it is interesting to neglect the requirement of optical transparency and look into absorbing non-reciprocal structures. After all, other applications such as a magnetic field sensor can do without optical transparency. This opens up the way to other material systems.
In recent years a lot of optical functionalities have been developed in the silicon on insulator (SOI) material system. This system, of which the structure is illustrated in figure 6.2, is characterized by a very high refractive index contrast between the Si core ($n_{1550nm} = 3.476$) and the surrounding cladding, which is either oxide SiO_2 ($n_{1550nm} = 1.444$) or air. As a consequence, the guided mode is very tightly confinement, hence very small photonic structures can be realized in this system since the bend radius can be decreased down to a few micrometer. In addition, silicon is widely available at relatively low cost and, what is even more important, wafer scale CMOS fabrication techniques can be employed as silicon is the material of electronics. In recent years, essential components for optical communication networks such as wavelength filters [4], heterogeneously integrated micro-disk lasers [5] and photodetectors [6] have been studied and demonstrated. Other applications such as low-cost biosensors [7] also have received attention. Furthermore, as mentioned in chapter 1, SOI has recently been used for garnet-based non-reciprocal phase shifters [8].

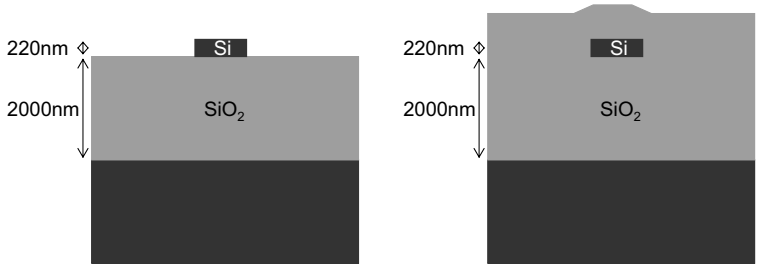

Figure 6.11: Schematic illustration of the structure of silicon-on-insulator, with on the right an air-clad structure and on the left a structure with oxide SiO_2 top cladding.

In this section we investigate SOI as a material system for passive, metal-clad non-reciprocal applications.

	Air cladding	SiO_2 cladding
$Co_{90}Fe_{10}$	5.0%	3.0%
$Co_{50}Fe_{50}$	11.5%	4.5%
Fe	10.0%	6.0%

Table 6.2: Isolation-to-loss ratio of Co_xFe_{1-x} covered SOI waveguides.

6.2.1 Non-reciprocal loss shift

In chapters 2 and 3 we have done an extensive study of the influence of the material choice on the magnitude of the non-reciprocal effect. We remark that the only figure of merit (FoM) suited for passive non-reciprocal devices is the isolation-to-loss ratio $\frac{\Delta\alpha}{\alpha}$ due to the absence of current injection. The non-reciprocal loss shift $\Delta\alpha$ is expressed as:

$$\Delta\alpha = \frac{|g||E_x^{(0)}(x_{i+})|^2}{Z_{vac}|n_{eff}|}\ sin(\angle g + 2\angle E_x^{(0)}(x_{i+})). \tag{6.13}$$

Remember that the value of the isolation-to-loss-ratio depends heavily on the characteristics of the magnetooptic material and the refractive index of the upper and lower waveguide cladding, but is quasi-independent of the thickness of the different layers. In fact, it is especially the sine-factor appearing in the formula of $\Delta\alpha$ that changes largely with the refractive index of the cladding. We refer to figure 3.11 for an illustration of the evolution of this phase-related factor with the material index of the cladding for the three Co_xFe_{1-x} alloys studied throughout this work. Due to this trend, it can be expected that the non-reciprocal characteristics of a high-index contrast system such as SOI differ substantially from those of the InP-based material discussed in the previous chapters.

Consider a SOI waveguide with an opaque Co_xFe_{1-x} film deposited on top. The core thickness and width are 220nm and 500nm respectively. While 1550nm wavelength is the common operation wavelength for SOI systems, 1300nm is considered here, as the magnetooptic constants of Co_xFe_{1-x} are only known in this range. With the waveguide model described in section 3.4 we have calculated the isolation-to-loss ratio. Due to the intrinsically high lateral index contrast these simulations are only accurate if the 2D calculation tool is being used. The results are tabulated in table 6.2. Unsurprisingly we need to make a distinction between a structure with a non-zero SiO_2 oxide top cladding and one where the magnetooptic metal is the actual top cladding. In the latter case the isolation-to-loss ratio values are comparable to the ones found in chapter 3 for InP-based structures,[4] with $Co_{50}Fe_{50}$ the best performing material. With an oxide top cladding a Fe ferromagnetic film leads to the highest isolation-to-loss ratio equal to 6.0%, followed by 4.5% for $Co_{50}Fe_{50}$ and 3.0% for $Co_{90}Fe_{10}$. As such these values are at least a factor two lower than what can be achieved without an oxide cladding.

[4]Keeping in mind the results of section 2.3, this should not come as a surprise. If a metal is directly deposited onto the waveguide core the magnetooptic effect is mainly determined by the refractive index of the core material, while the influence of the substrate index is low. This, together with the fact that the indices of InP and Si are similar explains the calculated isolation-to-loss values.

We can therefore conclude that the high index contrast characteristics of SOI do not lead to an increase of the isolation-to-loss ratio of Co_xFe_{1-x} covered waveguide.

6.2.2 Non-reciprocal phase shift

So far only the imaginary part of the non-reciprocal shift of the effective index has been considered. As discussed in the previous paragraph, this absorption shift is limited on a Co_xFe_{1-x}-SOI structure. A better option might be to apply the real part of the complex shift of the effective index, also called the non-reciprocal phase shift. This effect can be used to realize an optical isolator in a Mach-Zehnder interferometer configuration. With a proper choice of the non-reciprocal phase shift and the reciprocal phase difference between both arms of the interferometer, constructive interference can be achieved in the forward direction and destructive interference for backward propagating light. This principle, which is widely used in ferrimagnetic garnet isolators, has recently been examined for the Co-InGaAsP-InP material system by Shimizu [9]. Another possible configuration is a ring resonator with a magnetized ferromagnetic metal film, where the non-reciprocal phase shift creates a difference in resonance wavelength between clockwise – forward – and counterclockwise – backward – propagation. If this structure is cascaded with another (reciprocal) ring resonator with resonance wavelengths equal to the forward resonance, it makes up an optical isolator. The magnitude of the real part of the non-reciprocal shift Δn can be calculated from the magnetooptic perturbation formula and reads in a simplified form:

$$\Delta n = \frac{\lambda 10^{-4}}{4\pi} \frac{|g||E_x^{(0)}(x_{i+})|^2}{Z_{vac}|n_{neff}|} \, cos(\angle g + 2\angle E_x^{(0)}(x_{i+})). \tag{6.14}$$

The difference with the imaginary effect (equation 6.13) obviously is the cosine factor instead of the sine factor describing the influence of the phase matching between the gyrotropy constant and the transverse electric field component. Immediate consequence is that a structure that maximizes the imaginary part effect minimizes the real part of the effect. The InAlGaAs-InP isolator layer structure with a $Co_{50}Fe_{50}$ metal contact is therefore not at all suited for an interferometer-based isolator. The two options are to shift to a different magnetooptic material or to modify the modal electric field. From our discussion in section 3.2 it follows that none of the three Co_xFe_{1-x} compositions gives rise to a high cosine factor for an InP-based structure. The modification of the cladding material however does have a large impact on the phase relation between the gyrotropy g and the electric field. In figure 6.12 the evolution of the cosine factor which determines Δn is given with varying cladding refractive index. The waveguide core is a 300nm thick layer with refractive index 3.5 and the cladding thickness is 500nm, although the curve appears to be very insensitive to changes of these parameters. This graph shows that a high value of the non-reciprocal phase shift Δn requires a high index contrast between the core and the cladding and that $Co_{50}Fe_{50}$ is the preferred material. This obviously brings us to the SOI material system with a SiO_2 cladding. For example, for a structure with a 100nm thick oxide top cladding covered with

an opaque $Co_{50}Fe_{50}$ film, Δn is 0.00177, which corresponds to a length for a non-reciprocal phase shift of π equal to 368μm. This value is three times better than that for an InP-based structure with the same internal loss.

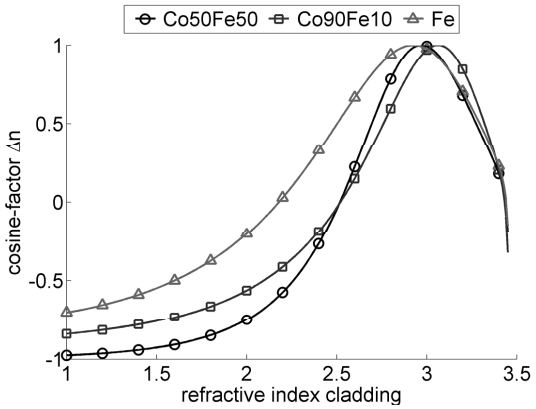

Figure 6.12: Evolution of the cosine factor of equation 6.14 with cladding refractive index, for three different Co_xFe_{1-x} compositions.

However, apart from Δn the absorption caused by the metal plays an important role. After all, if the total internal loss of the passive structure is too high, the device is of no practical use. We consider -40dB to be the upper limit on the loss. Consider a $Co_{50}Fe_{50}$-SOI waveguide of length L. The corresponding loss equals:

$$loss[dB] = \alpha[cm^{-1}]L\frac{10}{ln(10)} \tag{6.15}$$

with α the modal absorption coefficient. With this length a non-reciprocal phase change $\Delta\phi$ corresponds:

$$\begin{aligned} \Delta\phi &= \frac{2\pi}{\lambda}\Delta nL \\ &= Re[\Delta\beta]L \end{aligned} \tag{6.16}$$

with *Re[$\Delta\beta$]* the real part of the complex shift of the propagation constant. Combining equations 6.17 and 6.16 gives:

$$loss[dB] = \frac{\alpha}{Re[\Delta\beta]}\Delta\phi\frac{10}{ln(10)}. \tag{6.17}$$

Now, $\frac{\alpha}{Re[\Delta\beta]}$ is a parameter of the material system and almost independent of the dimensions of the different layers – it is the 'real' equivalent of the isolation-to-loss ratio $\frac{\Delta\alpha}{\alpha}$. For the combined $Co_{50}Fe_{50}$-SOI system its value is around 21.0. In other words, there is a one-to-one relation between the loss of a structure and the non-reciprocal phase change that can be generated. The maximum $\Delta\phi$ corresponding to a device loss of -40dB for the $Co_{50}Fe_{50}$-SOI structure is $\frac{\pi}{7.1}$. This limitation implies that this material system is not suitable for a Mach-Zehnder interferometer-

based isolator as a non-reciprocal phase change of at least $\frac{\pi}{4}$ is required.[5] Also for a ring resonator configuration the ratio of the non-reciprocal phase shift to the internal loss is too small.

6.2.3 Conclusion

Silicon-on-insulator (SOI) is an attractive material system for low-cost photonic applications. We have investigated its suitability for passive metal-clad non-reciprocal devices. With the ferromagnetic metal compositions that are currently known the ratio between the non-reciprocal effect and the absorption caused by the metal is however too small for practical implementation.

[5] In which case both arms contain a $\pm\frac{\pi}{4}$ non-reciprocal part and have opposite magnetization.

Bibliography

[1] M. Hammer, R.H. Kirankumar, and R. Stoffer, "Analytical approaches to the Description of Optical Microresonator Devices." *Microresonators as Builing Blocks for VLSI Photonics: International School of Quantum Electronics,* 39^{th} Course, pp.48-71 (2004).

[2] C.K. Madsen, and J.H. Zhoa, "Optical filter design and analysis: A signal processing approach." *Wiley interscience,* (2000).

[3] A. Bhatnagar, K.R. Suresh Nair, R. Kumar, K. Chalapati, and Y. G. K. Patro, "Study of Cross Coupling in Transition Bends Using Cascaded Coupler Segment Method." *IEEE Photon. Technol. Lett.,* 6(8), pp.1004-1007 (1994).

[4] T. Tsuchizawa, T. Shoji, R. Tamechika, S. Itabashi, and H. Morita, "Microphotonics devices based on silicon microfabrication technology." *J. Sel. Topics Quant. Electron.,* 11(1), pp. 232-240 (2005).

[5] J. Van Campenhout, P. Rojo-Romeo, D. Van Thourhout, C. Seassall, P. Regreny, L. Di Cioccio, J.M. Fedeli, C. Lagahe, and R. Baets, "Electrically pumped InP-based microdisk lasers integrated with a nanophotonics silicon-on-insulator waveguide circuit." *Optics Express,* 15(11), pp.6744-6749 (2007).

[6] M. Rouviere, L. Vivien, X. Le Roux, J. Mangeney, P. Crozat, C. Hoarau, E. Cassan, D. Pascal, S. Laval. J.M. Fedeli, J.F. Damlencourt, J.M. Hartmann, and S. Kolev, "Ultrahigh spreed germanium-on-silicon-on-insulator photodetectors for 1.31 and 1.55 μm operation." *Appl. Phys. Lett.,* 87(23), pp.231109 (2005).

[7] K. De Vos, I, Bartolozzi, E, Schacht, P. Bienstman, R. Baets, "Silicon-on-Insulator microring resonator for sensitive and label-free biosensing." *Optics Express,* 15(12), pp.7610-7615 (2007).

[8] H. Yokoi, T. Mizumoto, and Y. Shoji, "Optical nonreciprocal devices with a silicon guiding layer fabricated by wafer bonding." *Appl. Opt.,* 42(33), pp.6605-6612 (2003).

[9] H. Shimizu, S. Yoshida, and S. Goto, "Semiconductor Waveguide Optical Isolators Towards Larger Optical Isolation Utilizing Nonreciprocal Phase Shift by Ferromagnetic Co." *IEEE Photon. Technol. Lett.,* 20(18), pp.1554-1556 (2008).

7

Conclusion and outlook

7.1 Conclusion

In the introductory chapter we have distinguished a fourfold objective of our research. In the next paragraphs we will review these tasks, and as such formulate the conclusion of our work.

The subject of this research is a monolithically integratable optical isolator. Prior to this work, the proof-of-principle of the theoretical concept had been realized, a joint achievement together with Vanwolleghem. Despite a number of improvements, the amplifying waveguide isolator configuration was merely an academic curiosity at the start of this work. The first main objective was therefore to evolve from a promising concept towards a device suitable for practical applications.
Initially we have distinguished how the evanescent tail of a guided mode of a basic metal-clad waveguide interacts with the magnetooptic metal. We have been able to translate this complex interaction into some fundamental design rules. These findings have served as the criteria for the optimization of two of the main isolator building blocks: the choice of the ferromagnetic metal composition for the magnetooptic contact and the development of an ohmic metal-semiconductor contact structure specifically for the optical isolator. Extensive simulations have subsequently resulted in the design of the actual isolator structure in terms of the dimensions of the different layers.
An isolator demonstrator combining all knowledge has been fabricated. Experiments show an isolation level of 13.0dB combined with 155mA of current required for transparency in the forward propagation direction. This result is remarkable as it is the first - and so far only - demonstration of a transparent monolithically integratable optical isolator. Through interpolation it is possible to compare this result to the first proof-of-principle experiment. Since then the performance level, in terms of the current required for forward transparency, has been increased by more than a factor 80. In addition, an extensive study of other device aspects such as the spectral behavior and the current dependence of the optical isolation has been performed. The main observation is that the amplified spontaneous emission has a large influence on the device operation.

A second part of this work consisted of the realization of an optical isolator with an integrated electromagnet. This provides a solution for the poor magnetic remanence properties of the amplifying waveguide isolator configuration and enables to apply an on-chip magnetic field in an arbitrary direction. After the magnetic design of this structure a proof-of-principle experiment has been successfully performed. The electromagnet current required to generate a magnetic field strong enough to saturate the ferromagnetic isolator contact is however far beyond the acceptable for practical applications. A largely improved configuration has been identified, based on the fact that when current is flowing through the ferromagnetic metal film itself a far more favorable magnetization profile is being generated. An extensive theoretical discussion has been given and it has been supported by an experimental result.

The third objective of this research was the development of an integrated laser-isolator device. The most important advantage of the amplifying waveguide optical isolator scheme is that it can straightforwardly be integrated with a laser source

as both devices have essentially the same structure. In accordance with standard DFB-laser technology, the integrated device has been designed and fabricated in a buried ridge waveguide configuration. Good operation of the laser part has been proven, despite important changes with respect to the standard process flow. After a series of process modifications we have managed to demonstrate the presence of non-reciprocity on the isolator part. Despite these changes the quality of the metal-semiconductor interface remains inferior and the device suffers from current leakage phenomena. These inaccuracies have obstructed the full demonstration of the integrated laser-isolator component.

The last major objective was the exploration of non-reciprocal devices that are based on the amplifying waveguide optical isolator concept but deviate from the straight TM-mode metal-clad semiconductor optical amplifier. These include ring resonator-based isolators and passive non-reciprocal devices.
Resonance of light in a ring-shaped magnetized metal-clad waveguide can be exploited to realize a high performance optical isolator. A thorough theoretical study has been made, a contact lithography mask set has been created and test devices have been fabricated. Due to inferior quality of the current injection in the all-active devices the experimental demonstration of the concept could however not be achieved.
Passive metal-clad non-reciprocal devices are attractive for applications where the optical transparency is not a requirement, such as a magnetic field sensor. The obvious material system is silicon-on-insulator (SOI), characterized by a large index contrast between the core and the surrounding cladding. The non-reciprocal loss shift of a Co_xFe_{1-x}-SOI structure however appears to be limited. The real part of the complex effective index shift – the non-reciprocal phase shift – on the other hand is significantly higher than that on an InP-based device. Calculations indicate that the ratio of the non-reciprocal phase shift to the absorption in the metal is however far too low for practical implementation.

7.2 Outlook

The amplifying isolator concept is today at a point in its evolution that it is no longer just a promising concept but, with the performance still a factor of 6 below the requirements, it is not ready to be transferred to practical applications. After all, an isolator of at least 25dB is required and this device should not consume more than 50mA of current. At the same time the route towards improvement is far from straightforward. In this paragraph we will explore some possibilities to enhance the isolator performance.

The two most natural ways to improve the amplifying waveguide optical isolator are the development of better gain material and the choice of ferromagnetic materials with more optimized optical and/or magnetooptic characteristics. Both are however not obvious at all. There might be some enhancement of the gain performance by introducing even a higher degree of tensile strain or the use of more quantum wells, but with 9 wells at -1.64% of strain we believe we are close to what is possible today. With respect to the ferromagnetic material, it could well be that exists a more suitable composition, but the identification is a laborious task

as accurate experimental determination of the optical and magnetooptic properties is required. A number of materials have been tested in this work and none even gets close to the equiatomic Co_{50} Fe_{50} alloy.

For the Co_{50} Fe_{50} / InAlGaAs-InP ridge waveguide isolator configuration there is no distinctive route to realize the improvement needed for practical application of the amplifying waveguide optical isolator. Remember from the slab waveguide calculations of section 3.4 that even in theory 78.5mA of current per micrometer ridge width is needed for a 25dB isolator, a value which enhances largely for ridge widths below 2μm due to the corresponding decrease of the modal confinement. As such, even when the device fabrication can be optimized so as to lift the discrepancy between experiment and theory, the required level of performance cannot be reached.
One solution could be to replace the InP cladding by a material with a refractive index of 2.45. As calculated in section 3.4.5 this would result in a reduction of the transparency current by 38%. The common materials with a refractive index in that region are however oxides which are electrically insulating. Electrical pumping of the amplifying waveguide core is therefore not possible. First task would therefore be to identify a current conducting material with the appropriate refractive index value. In addition, a fabrication method for such an oxide cladding quantum wells structure needs to be developed. In other words, while it would take some effort to realize this improved isolator structure it should in theory result in a considerable performance increase.

A second option is to continue the development of a buried ridge isolator structure. After all, due to the intrinsically higher lateral contrast than is the case for a shallow ridge waveguide the modal confinement is higher and the ridge width can be reduced without penalty on the transparency current per micrometer width. According to the 2D calculations of chapter 5.2 a buried structure with 1μm core requires 90mA current for 25dB isolation, a value that approaches the required specifications. These specifications however neglect the current leakage over the homojunctions at the side of ridge. Current blocking layers should therefore be built-in, a technique that is well known for buried DFB-lasers. Furthermore, the results of chapter 5 indicate that a more detailed study of the fabrication of the buried isolator structure is required to obtain satisfying performance, both in terms of optical isolation and current injection quality. However, we believe that this buried isolator has the highest potential to be implemented one day in commercial applications.

The third route towards improvement is that of an isolator based on a ring resonator. In chapter 6 it has been elaborated that 25dB of isolation can in theory easily be achieved with a ring-shaped waveguide partially covered with a magnetized ferromagnetic metal film. The practical realization of a ring-resonator isolator requires further research effort. Shifting from all-active waveguides with a thin InP-cladding to structures with passive bus waveguides and/or a thick cladding layer in the reciprocal device parts, might be appropriate to reduce the required transparency current.

A

Isolator fabrication and contact lithography mask set

IN this appendix we summarize the details of the amplifying waveguide optical isolator fabrication. The processing sequences of both straight waveguide and ring resonator-based devices are listed. In addition, the different mask layers of the contact lithography mask set developed in this work are given.

A.1 Waveguide isolator fabrication

The first generations of amplifying waveguide optical isolators have been fabricated using standard SOA/isolator fabrication. The only additional fabrication step is the deposition of the ferromagnetic metal layer. The processing sequence can be summarized as:

1. wafer preparation (natural oxide removal)
2. deposition SiO_x (150 nm) as an etch mask
3. lithography (ridge waveguide)
4. etching of SiO_x: plasma etch (O_2:CF_4)
5. removal of resist
6. reactive ion etch (CH_4:H_2)
7. removal of oxide: wet etch (HF)
8. spinning of polyimide or benzocyclobutene (BCB)
9. lithography: definition of current windows (image reversal)
10. etching of current windows: plasma etch
11. cleaning of exposed semiconductor contact interface (sulfuric acid dip)
12. lithography: definition of 30μm wide lift-off patterns for Co_xFe_{1-x} metallization (image reversal)
13. sulfuric acid dip (diluted 1:10). This extra step is needed because the sample is transferred to the sputter machine in IMEC.
14. deposition of 50nm Co_xFe_{1-x} under magnetic bias ($\perp$ stripes)
15. Joule evaporation of Ti/Au bilayer (40/150 nm)
16. lift-off in aceton
17. optional step: Au plating
18. thinning of the substrate (down to $\sim$ 150μm)
19. deposition back contact AuGe: no anneal (avoiding detrimental damage to the Ohmic properties of the Co_xFe_{1-x} contacts – see the results of section 3.3), no Ni (to avoid any guiding of the magnetic flux lines through the back contact)

Later, we have identified an improved fabrication method. By using 2μm wide ferromagnetic metal stripes as the etch mask for the ridge waveguide definition, accurate covering of the ridge with ferromagnetic metal can be guaranteed. This modified processing sequence is listed below:

1. wafer preparation (natural oxide removal)
2. lithography: definition of 2μm wide resist patterns for Co_xFe_{1-x} metallization (image reversal)
3. deposition of 50nm Co_xFe_{1-x} under magnetic bias ($\perp$ stripes)
4. sputter deposition and Joule evaporation of Ti/Au bilayer (40/150 nm)
5. lift-off in aceton
6. reactive ion etch (CH_4:H_2)
7. spinning of polyimide or benzocyclobutene (BCB)
8. lithography: definition of current windows (image reversal)
9. etching of current windows: plasma etch
10. cleaning of exposed semiconductor contact interface (sulfuric acid dip)
11. lithography: definition of 30μm wide lift-off patterns for second metallization needed for electrical contacting (image reversal)
12. Joule evaporation of Ti/Au bilayer (40/150 nm)
13. lift-off in aceton
14. optional step: Au plating
15. thinning of the substrate (down to $\sim$ 150μm)
16. deposition back contact AuGe

A.2 Fabrication of ring isolators

Next, the different processing steps of ring resonator-based isolator devices are summarized. Reference is made to the corresponding layers of the contact lithography mask.

1. wafer preparation (natural oxide removal)
2. lithography (mask layer 1): definition lift-off patterns for CoFe metallization (image reversal)
3. deposition of 50nm CoFe under magnetic bias ($\perp$ stripes)
4. sputter deposition and Joule evaporation of protective Ti/Au bilayer (40/150nm)
5. lift-off in aceton
6. lithography (mask layer 2): definition lift-off patterns for Ti/Au metallization (image reversal)

7. sputter deposition and Joule evaporation of Ti/Au bilayer (5/20nm)
8. lift-off in aceton
9. reactive ion etch (CH_4:H_2)
10. spinning of benzocyclobutene (BCB)
11. lithography (mask layer 3): definition of current windows (image reversal)
12. etching of current windows: plasma etch
13. cleaning of exposed semiconductor contact interface (sulfuric acid dip)
14. lithography (mask layer 4): definition of lift-off patterns for second metallization needed for electrical contacting (image reversal)
15. Joule evaporation of Au layer (200nm)
16. lift-off in aceton
17. spinning of benzocyclobutene (BCB)
18. lithography (mask layer 5): definition of SOA contact windows (image reversal)
19. etching of contact windows: plasma etch
20. lithography (mask layer 6): definition of lift-off patterns for electromagnet (image reversal)
21. Joule evaporation of Au layer (400nm)
22. lift-off in aceton
23. Au plating (mask layer 7)
24. thinning of the substrate (down to $\sim 150\mu$m)
25. deposition back contact AuGe

Figures A.1 to A.7 depict the different mask layers of the contact lithography mask developed in this work. Apart from the ring resonator-based isolator structures extensively discussed in chapter 6, the mask contains straight non-reciprocal waveguides and the integrated laser-isolator components mentioned in the conclusion of chapter 5.

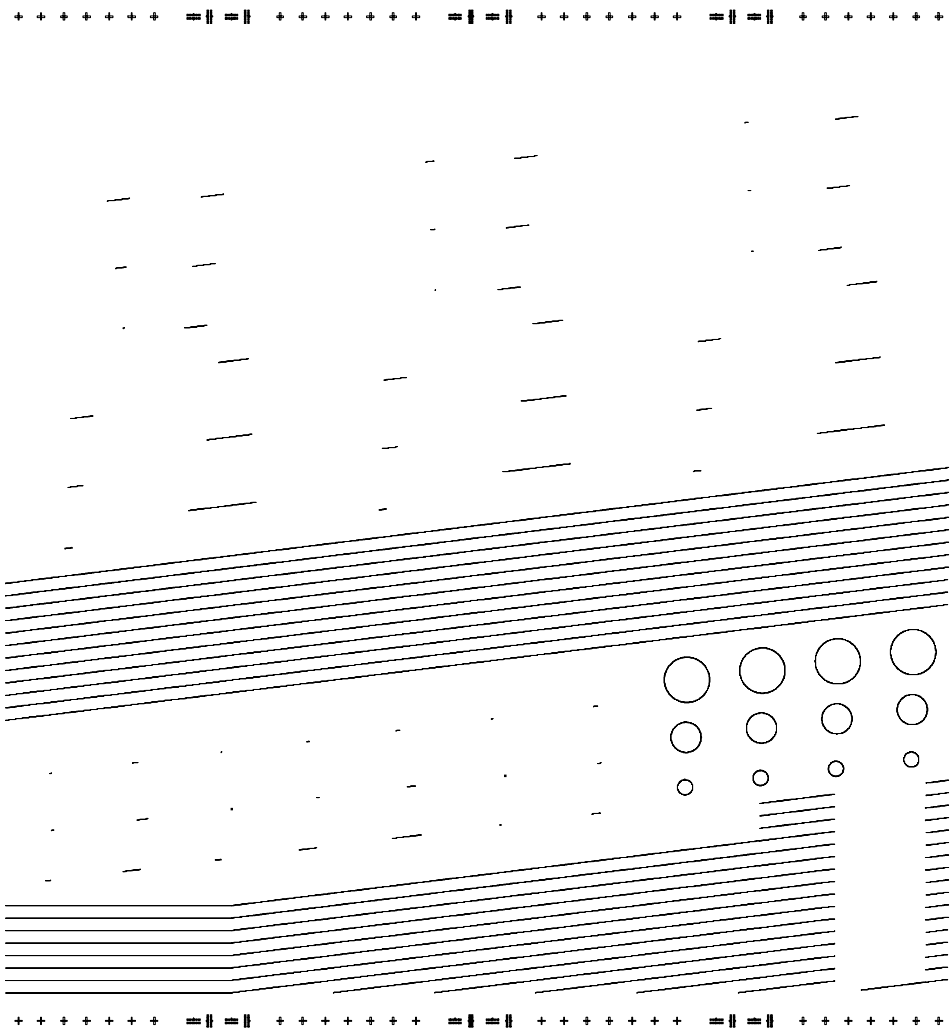

Figure A.1: Mask layer 1: definition of Co_xFe_{1-x} covered waveguides.

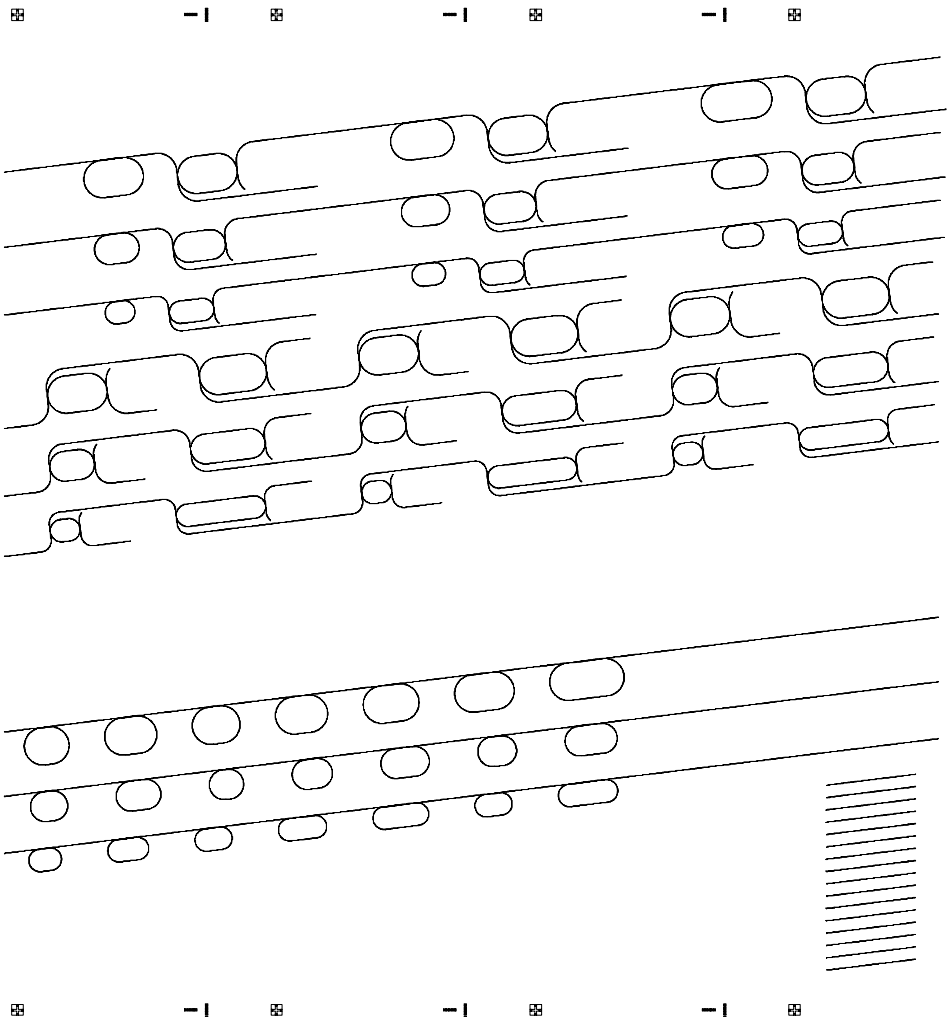

Figure A.2: Mask layer 2: definition of Ti/Au covered waveguides.

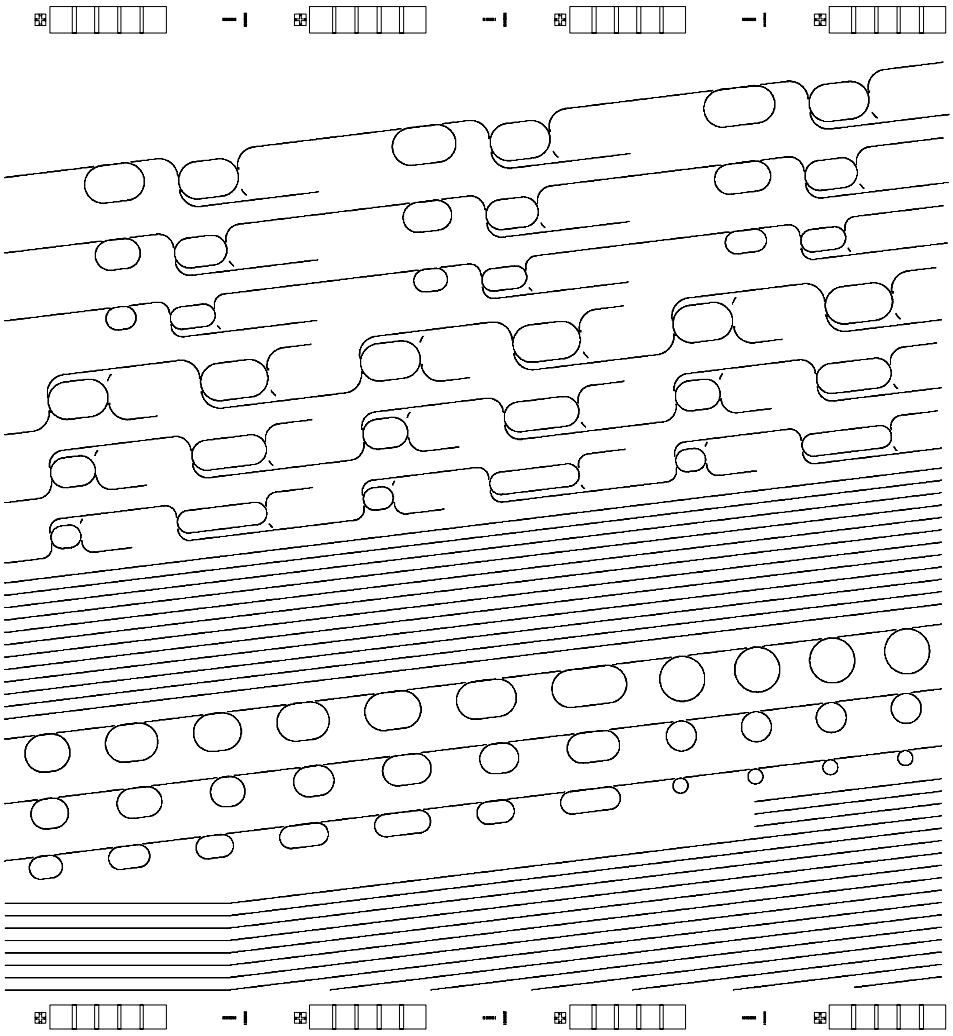

Figure A.3: Mask layer 3: definition of current isolation windows.

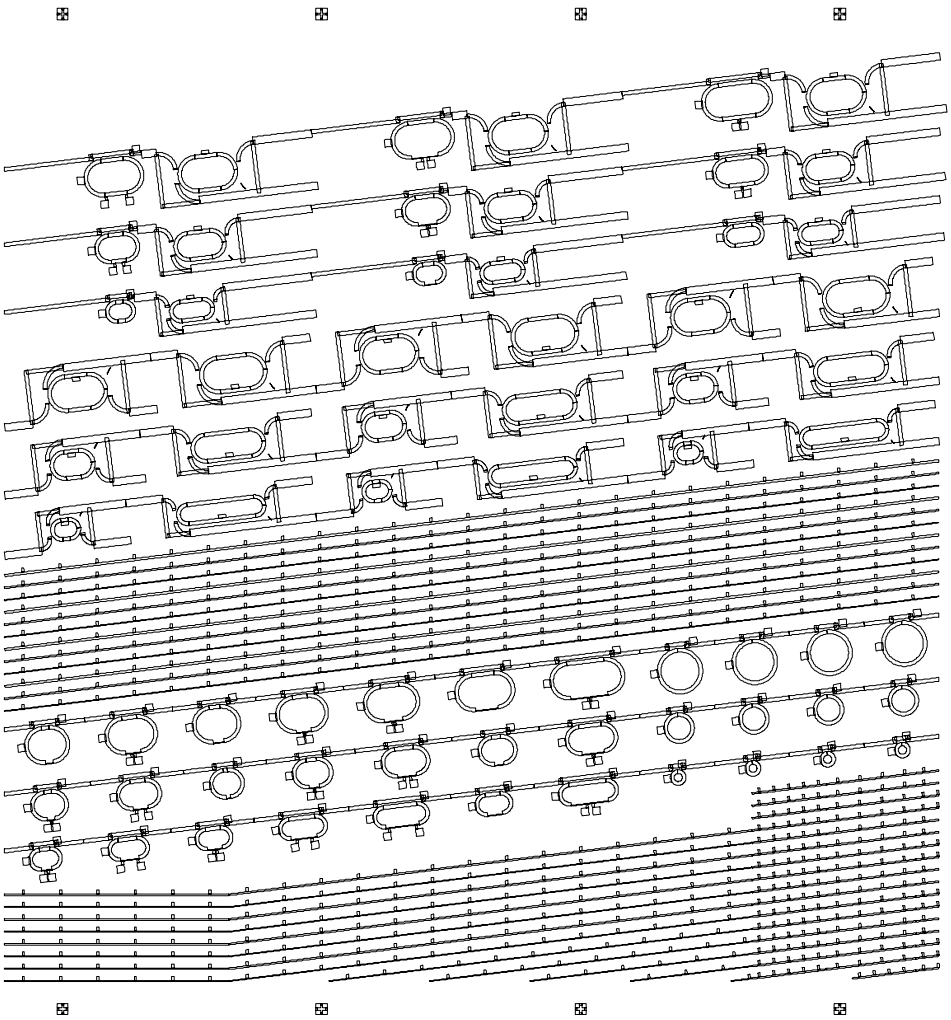

Figure A.4: Mask layer 4: definition of second metallization pattern.

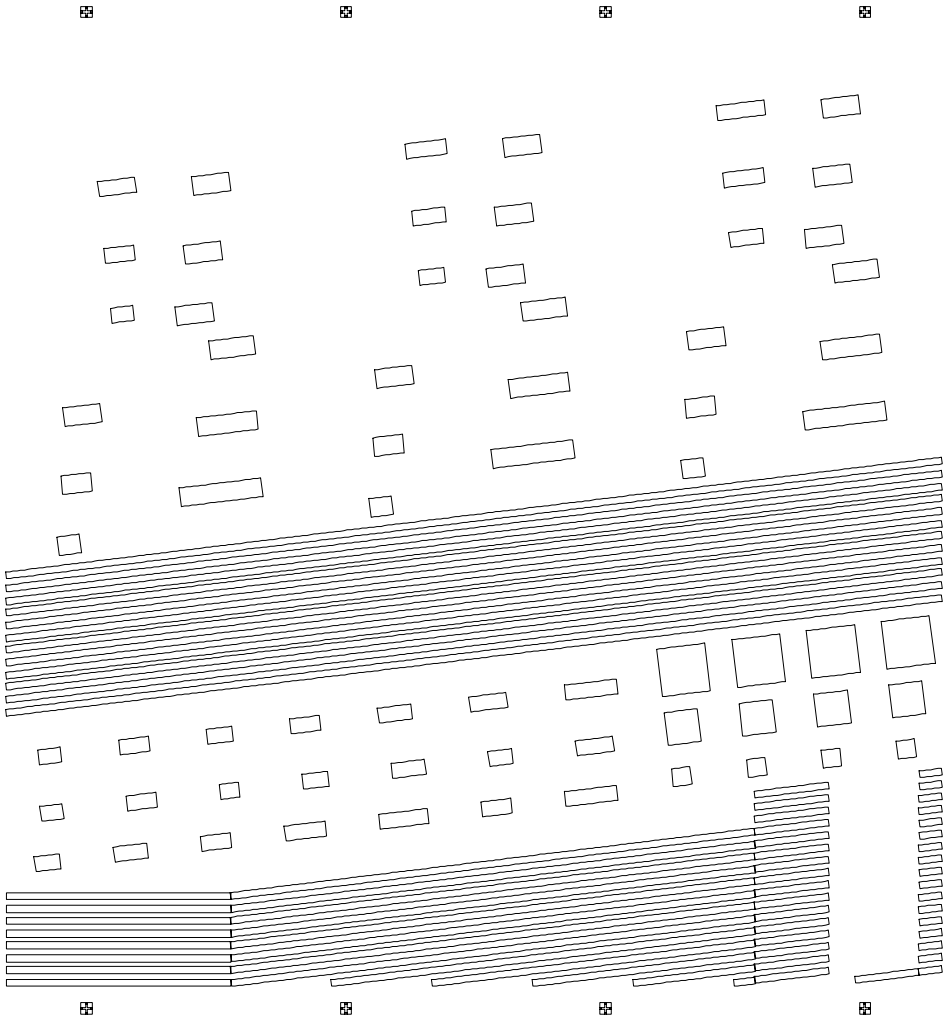

Figure A.5: Mask layer 5: definition of contact windows.

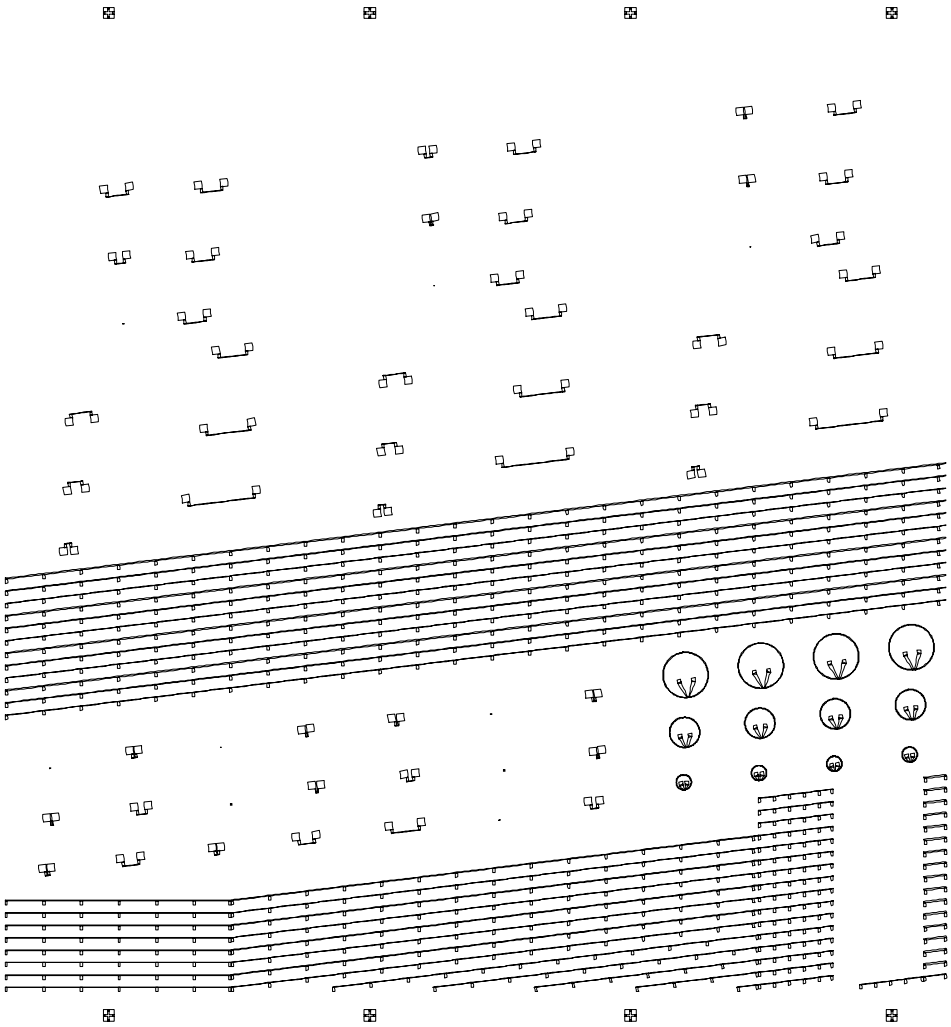

Figure A.6: Mask layer 6: definition of integrated electromagnet pattern.

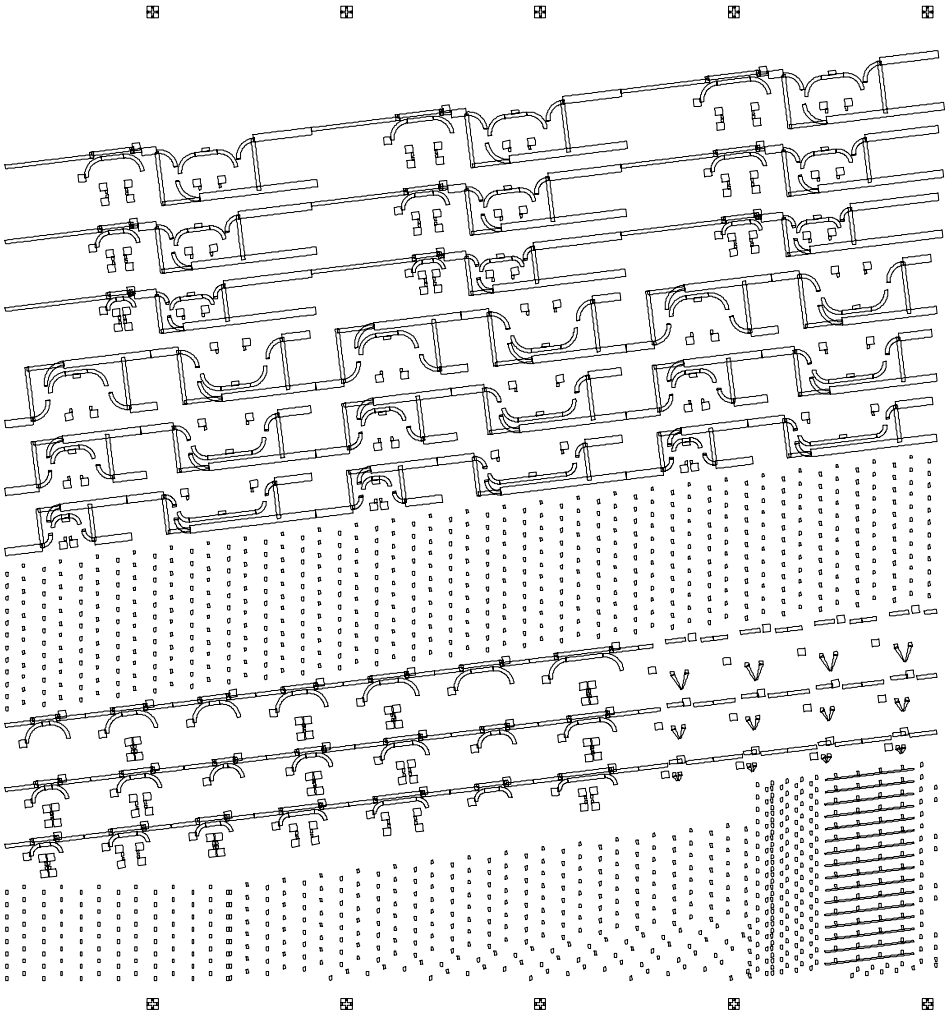

Figure A.7: Mask layer 7: definition of electro-plating pattern.

B

Non-reciprocal lasing: calculation details

IN section 4.2.1.2 a characterization method on the basis of non-reciprocal lasing has been introduced. In this appendix the calculation of the corresponding formulas is given.

B.1 Calculation of equation 4.1

Consider the non-reciprocal Fabry-Pérot cavity sketched in figure B.1. At lasing, the roundtrip amplitude gain of the non-reciprocal cavity equals one, hence the threshold condition reads:

$$\sqrt{R_f R_b}\, exp\left(\frac{G_f L}{2}\right)\, exp\left(\frac{G_b L}{2}\right) = 1, \tag{B.1}$$

with R_f and R_b the reflection coefficients of the forward and the backward facet and L the cavity length. G_f is the modal gain in the forward propagation direction and G_b the analogy for the backward direction:

$$\begin{aligned} G_f &= \Gamma G - \alpha_0 + \frac{\Delta\alpha}{2} \\ G_b &= \Gamma G - \alpha_0 - \frac{\Delta\alpha}{2}, \end{aligned} \tag{B.2}$$

with G the material gain of the amplifying waveguide, Γ the modal confinement in the gain region, α_0 the reciprocal cavity loss and $\Delta\alpha$ the non-reciprocal loss shift. The threshold condition can therefore be rewritten as:

$$\sqrt{R_f R_b}\, exp\left([\Gamma G - \alpha_0]L\right) = 1, \tag{B.3}$$

hence, clearly doesn't contain any non-reciprocal contribution. This originates from the fact that the resonating light travels the same distance in forward and backward direction. Nevertheless, the emitted optical power is not independent of the propagation direction. The emitted power at the forward facet P_f is related to that at the backward facet P_b as:

$$\begin{aligned} P_f &= (1 - R_f)\, P'_f \\ &= (1 - R_f)\, exp\left(G_f L\right)\; P''_b \\ &= (1 - R_f)\, R_b\, exp\left(G_f L\right)\; P'_b \\ &= \frac{(1 - R_f)}{(1 - R_b)}\, R_b\, exp\left(G_f L\right)\; P_b. \end{aligned} \tag{B.4}$$

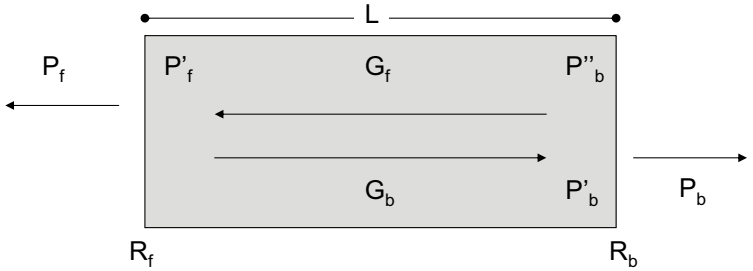

Figure B.1: Schematic layout of the non-reciprocal Fabry-Pérot cavity.

By combining this result with the threshold condition (B.3), the ratio of the forward emitted power to the backward emitted power becomes:

$$\begin{aligned} \frac{P_f}{P_b} &= \frac{(1-R_f)}{(1-R_b)}\, R_b\, \frac{1}{\sqrt{R_f R_b}}\, exp\left(\frac{\Delta\alpha}{2}L\right) \\ &= \frac{(1-R_f)}{(1-R_b)}\, \sqrt{\frac{R_b}{R_f}}\, exp\left(\frac{\Delta\alpha}{2}L\right). \end{aligned} \tag{B.5}$$

If we assume that both facet reflection coefficients are equal,[1] this expression reduces to:

$$\rho \equiv \frac{P_f}{P_b} = exp(\frac{\Delta\alpha L}{2}). \tag{B.6}$$

This formula gives us a very simple method to extract the value of the non-reciprocal loss shift $\Delta\alpha$ – and hence the isolation ratio IR – with only the cavity length and the output power ratio ρ as input parameters:

$$\begin{aligned} \Delta\alpha[1/mm] &= \frac{2}{L[mm]} ln(\rho) \\ IR[dB/mm] &= \frac{10}{ln(10)} \frac{2}{L[mm]} ln(\rho). \end{aligned} \tag{B.7}$$

B.2 Calculation of formula 4.2

From the experimental value of the threshold current an estimate of the transparency current of the device can straightforwardly be obtained. The threshold condition reads:

$$\Gamma G_{thresh} = \alpha_0 + \alpha_{mirror} \tag{B.8}$$

with G_{thresh} the material gain needed to achieve threshold, Γ the confinement of the optical mode in the quantum wells, α_{mirror} the mirror loss and α_0 the modal loss in the absence of a magnetic field, related to the forward internal loss α_{fw} as:

$$\alpha_{fw} = \alpha_0 - \frac{\Delta\alpha}{2} \tag{B.9}$$

with $\Delta\alpha$ the total non-reciprocal absorption shift. The experimental gain-current density relation of the amplifying core relates to any loss term α as:

$$\alpha = -\Gamma G = -\Gamma G_0 ln\Big(\frac{J}{J_0}\Big) \tag{B.10}$$

[1] Due to the difference in modal profile of forward and backward propagating light the reflection coefficients are actually not identical. As this is however a second order effect, our assumption is a valid approximation.

With this the threshold condition can be rewritten as:

$$\Gamma G_0 ln\Big(\frac{J_{thresh}}{J_0}\Big) = \Gamma G_0 ln\Big(\frac{J_{transp,fw}}{J_0}\Big) - \frac{\Delta\alpha}{2} + \alpha_{mirror} \tag{B.11}$$

with J_{thresh} and $J_{transp,fw}$ respectively the threshold current density and the forward transparency current density. Both $\Delta\alpha$ and J_{thresh} – via I_{thresh} – can be determined experimentally. The mirror loss is known to be related to the cavity length L and the facet reflectivity R, of which we can assume that it is identical for both device facets:

$$\alpha_{mirror} = \frac{1}{L} ln\Big(\frac{1}{R}\Big). \tag{B.12}$$

Equations B.11 and B.12 directly lead to an expression for the forward transparency current $I_{transp,fw}$:

$$I_{transp,fw} = dLJ_0 exp\Big[ln\Big(\frac{I_{thresh}}{dLJ_0}\Big) + \frac{\Delta\alpha}{2\Gamma G_0} - \frac{1}{\Gamma G_0 L} ln\Big(\frac{1}{R}\Big)\Big] \tag{B.13}$$

with d the width of the waveguide ridge.[2]

[2]Actually d is the effective width of the ridge waveguide, taking into account the lateral current spreading.

C

Isolator measurement setups

IN this appendix we elaborate on the details of the different characterization setups that have been used to characterize the amplifying waveguide optical isolators.

C.1 Isolator measurement setups

The TM-mode amplifying waveguide optical isolator basically is a semiconductor optical amplifier (SOA) of which the properties depend on the propagation direction of the light, if a non-zero lateral magnetization is present in the ferromagnetic metal contact. With lateral direction we mean perpendicular to the light propagation and parallel to the layer surfaces. Ideally this device would work in magnetically remanent regime, but for the characterization we apply an external magnetic field. For the experiments performed in the frame of this work, we employed basically two different measurement setups. For both the heart of the setup is the photonic chip mounted on a sample holder. These devices are cleaved and possibly provided with anti-reflection coatings on the waveguide facets. The electrical pumping of the SOA is done via probe needles placed on the front and back contact of the active device. The temperature of the chip is controlled and stabilized with a thermoelectric cooler (TEC).

The first, and most frequently used setup, is equipped with an external electromagnet of which the magnetic field can be varied continuously between -825Oe and +825Oe by means of a voltage source,[1] where changing the sign obviously means reversing the magnetic field direction. This enables to measure magnetic hysteresis curves like those depicted in figures 4.4 and 4.5. Light emitted at one facet of the current drive device is captured with an objective lens and coupled into an optical power meter after it has propagated through a free-space polarization filter. This setup is illustrated in figure C.1(a). Apart from the hysteresis measurements, the non-reciprocal lasing experiments can also be done. Remember that in principle the light intensities emitted at both facets need to be compared. However, this requires that the coupling efficiencies between chip and detector are identical at both sides, which is extremely difficult to realize. The fact that the magnetooptic effect is symmetric with respect to the zero-magnetization state provides a solution. An equivalent experiment is to compare the light intensities emitted at one facet for a magnetization in both lateral directions ($\boldsymbol{M}$ = +M and $\boldsymbol{M}$ = -M). As it is the ratio of both intensities that contains the useful information, the requirement for the identical coupling is eliminated.
An analogous setup can be used to perform transmission measurements. At the input side, we need a TM-polarized laser signal. An external cavity tunable laser is normally used, to choose the signal wavelength at the peak of the SOA gain spectrum. Moreover, using a tunable laser enables to study the spectral dependence of the isolator device. Coupling of the signal to the chip is done with a lensed fiber. The input polarization is fixed at TM with the aid of fiber optic polarization controller which utilizes stress-induced birefringence to alter and control the polarization state [1]. The laser signal emitted by the input lensed fiber is coupled to the output objective lens, propagates through the free-space polarization filter and is detected with the optical power meter. The pass-polarization of the free-space polarization filter is fixed at TE and the polarization controller is adjusted so as to obtain a minimal intensity on the power meter. The input fiber is

[1] Notice that we work in CGS units instead of SI units, as is usual in the field of magnetism. Remember that the relation between the magnitude of a magnetic field in A/m (SI) and in Oersted Oe (CGS) is: $1\text{A/m} = 4\pi 10^{-3}\text{Oe}$

not polarization-maintaining, hence the polarization state can change if the fiber is manipulated. Therefore, as illustrated in figure C.2, during this calibration, the input fiber is lifted just above the surface of the photonic chip. This entire procedure ensures that the light coupled to the photonic chip is TM-polarized. At the detection side, once the input polarization is calibrated, the objective lens is replaced by a lensed fiber connected to a spectrum analyzer. After all, the output light is a mixture of amplified spontaneous emission (ASE) and the transmitted signal. As we primarily want to examine the influence of the magnetooptic effect on the transmitted signal, an optical spectrum analyzer is required to split both contributions. At both facets the coupling between fiber and chip is optimized using active alignment. The SOA-based device is injected with current and the lensed fiber position adjusted such that the detected optical intensity is maximized. A mechanical optical switch is used in the 'input' light path to switch between the alignment measurement and the actual transmission experiment. On this transmission measurement setup, illustrated in figure C.1(b), all static characteristics of the non-reciprocal waveguide devices can be examined. For dynamic characterization, it needs to be extended with a modulator, an oscilloscope, bit-error-rate tester,...
This setup actually has no significant disadvantages, as opposed to the one discussed later. The main difficulty has been to avoid magneto-mechanical phenomena; due to the intrinsic switching of the magnetic field, mechanical parts of the setup might shift, with as a result the variation of the fiber-to-chip coupling with magnetic field direction and magnitude. By using materials with a low magnetic permeability such as aluminium, copper and plastics, magneto-mechanical influences have been eliminated.

For some of our experiments, another setup has been used.[2] This setup effectively measures the difference between light propagating in opposite directions for a fixed magnetic field. The lateral magnetic field is generated by a 1000Oe permanent magnet. The setup is sketched in figure C.3. Light from a tunable laser is coupled to one of the chip facets, propagates through the magnetized device, is picked up at the opposite facet and detected on a spectrum analyser or a power meter. This is repeated for the opposite propagation direction on the chip. Mechanical optical switches and optical circulators control the light path.[3] Again lensed fibers are used for the fiber-to-chip coupling. The input polarization is controlled with fiber-optic polarization controllers, and one in each input light path is required. To fix the polarization at TM, we rely on the wavelength difference of the gain peak of TE and TM polarization in strained quantum well gain material, which is the direct result of the valence band splitting (see chapter 3). To illustrate this, the photoluminescence spectra of the InAlGaAs-InP tensile strained multiple quantum well material is shown in figure C.4, for different values of the tensile strain. The lower wavelength peak corresponds to heavy hole-electron (hh-c) recombination, which contributes mainly to TE-polarization, while the higher wavelength peak is that of the light hole-electron (lh-c) recombination process,

[2]Measurements have been performed at the Research Center for Advanced Science and Technology at the University of Tokyo, Japan, in the frame of a collaboration with the research group of Nakano. This is the same group that invented the concept of an amplifying waveguide optical isolator [2].

[3]An optical circulator is a device with three or more ports which has the functionality that a signal fed into any port is transferred to the next port only.

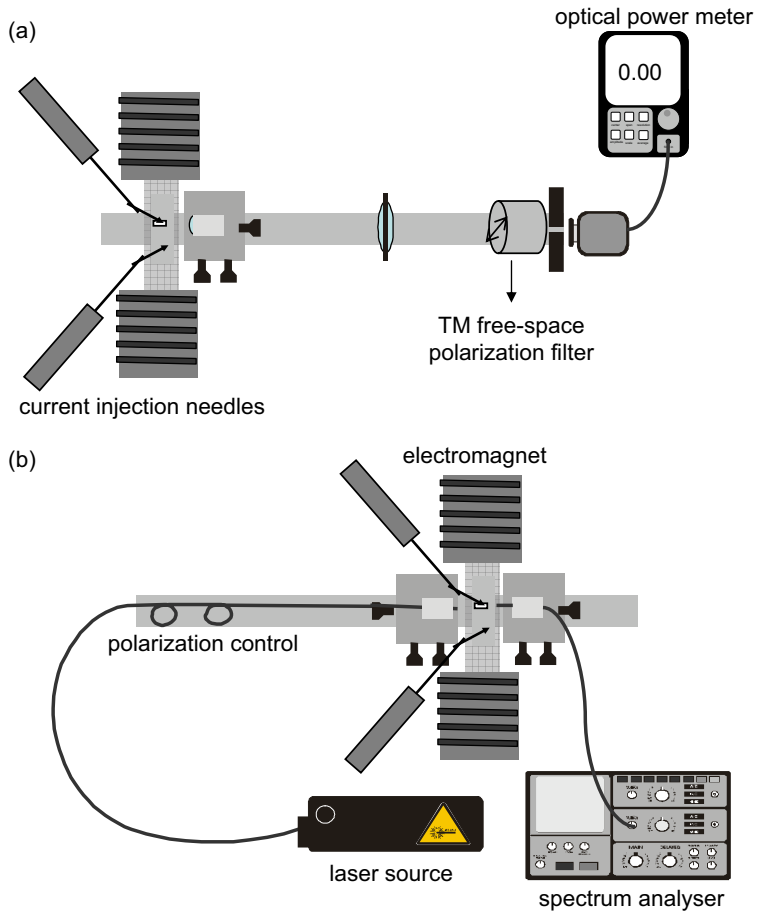

Figure C.1: Schematic illustration of the experimental setup on which the majority of the measurements have been done.

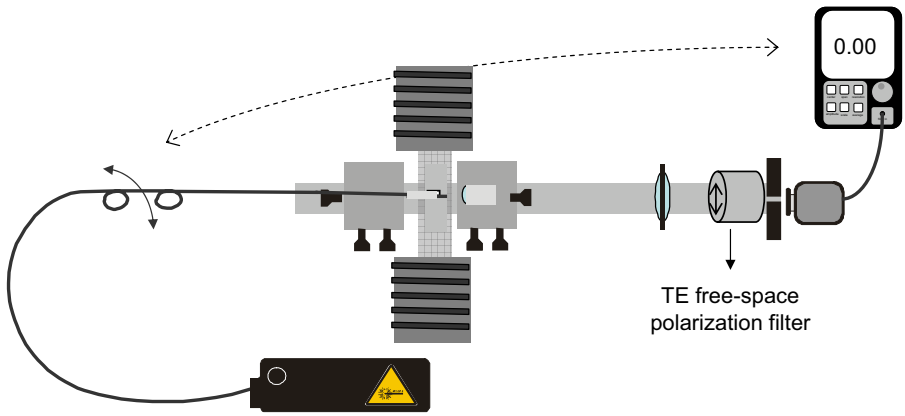

Figure C.2: Schematic illustration of the polarization calibration procedure.

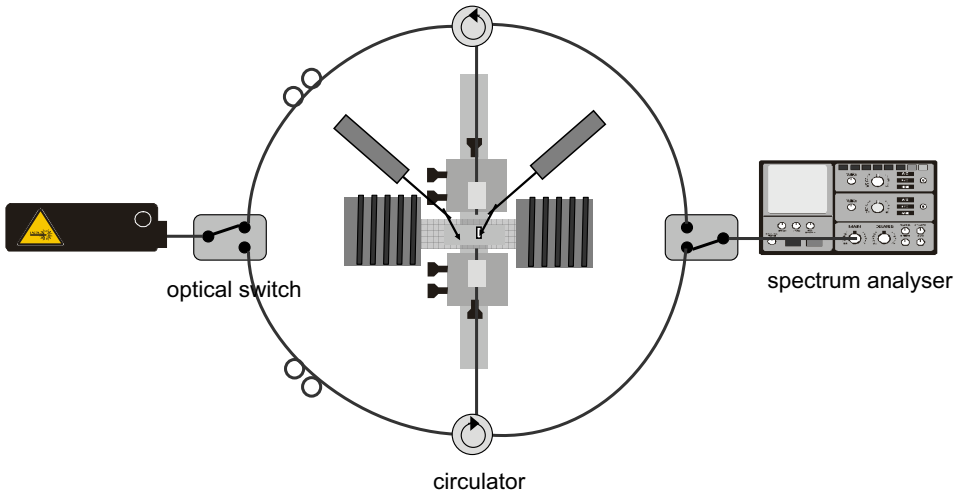

Figure C.3: Schematic illustration of the experimental setup used during the collaboration with Nakano.

which mainly determines the TM-gain. Optimization of the fiber-to-chip coupling is again done with active alignment.
The disadvantages related to this setup are all related to the different paths followed by the light in forward and backward direction. The detected signals can only be compared if the coupling loss (at two facets), the circulator loss, and other losses along the fibers are identical, which is very difficult to achieve. In a purely reciprocal device, the coupling loss at both facets can be (approximately) equalized by adjusting the fibers so that the detected (ASE) power is the same, if necessary corrected for the difference in circulator and other losses. This is however, not at all the case for a magnetized non-reciprocal component, as the ASE emitted at both facets is essentially different.[4] In addition, specifically for our non-reciprocal devices, the current injection in the longitudinal direction is inhomogenous (see section 4.3.4.2), when pumped with a single needle on the top contact. This causes another difference of the optical intensity between both facets. Another issue is to ensure that the input signal polarization is identical for transmission in forward and backward direction. All these deviations can in principle be measured separately and be corrected for in the alignment stage of the transmission experiment. However, it makes the measurements laborious and seriously increases the risk of errors. Despite the difficulties, we have been able to reproduce the results obtained on the first setup. Furthermore, the experiments related to the dynamic performance, elaborated later in this chapter, have been done on the last setup

[4]Installing the permanent magnet after the alignment procedure is not an option as this has too much influence on the position of the different mechanical parts.

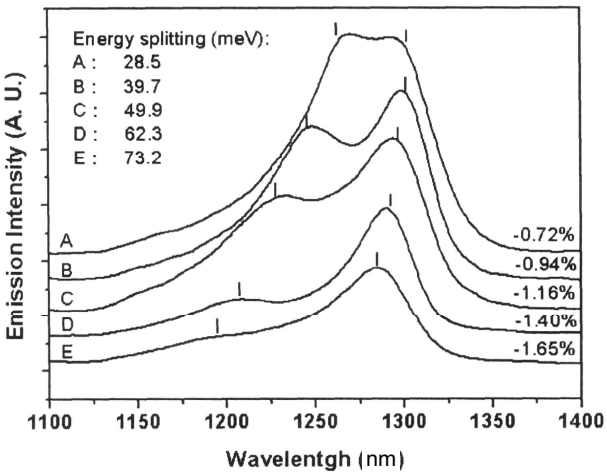

Figure C.4: Room-temperature photoluminescence spectra of the InAlGaAs-InP tensile strained multiple quantum wells for various strain values. The two peaks in the spectra, corresponding to the hh-c and lh-c recombinations, illustrate the splitting of the gain peak between TE- and TM-polarization.

Bibliography

[1] H. C. LeFevre, "Single-mode Fiber Fractional Wave Devices and Polarization Controllers." *Electron. Lett.*, 16(20), pp.778-780 (1980).

[2] M. Takenaka, and Y. Nakano, "Proposal of a Novel Monolithically-Integratable Optical Waveguide Isolator." *in Proc. 11^{th} International Conference on Indium Phosphide and Related Materials, Davos, Switzerland*, pp. 298-292 (1999).